Electronic Structure Study of Copper-containing Perovskites

Mark Robert Michel

University College London

A thesis submitted to University College London in partial fulfilment of the requirements for the degree of Doctor of Philosophy, February 2010.

I, Mark Robert Michel, confirm that the work presented in this thesis is my own. Where information has been derived from other sources, I confirm that this has been indicated in the thesis.

Mark Robert Michel

Abstract

This thesis concerns the computational study of copper containing perovskites using electronic structure methods. We discuss an extensive set of results obtained using hybrid exchange functionals within Density Functional Theory (DFT), in which we vary systematically the amount of exact (Hartree-Fock, HF) exchange employed. The method has enabled us to obtain accurate results on a range of systems, particularly in materials containing strongly correlated ions, such as Cu^{2+}. This is possible because the HF exchange corrects, at least qualitatively, the spurious self-interaction error present in DFT.

The materials investigated include two families of perovskite-structured oxides, of potential interest for technological applications due to the very large dielectric constant or for Multi-Ferroic behaviour. The latter materials exhibit simultaneously ferroelectric and ferromagnetic properties, a rare combination, which is however highly desirable for memory device applications.

The results obtained using hybrid exchange functionals are highly encouraging. Initial studies were made on bulk materials such as $CaCu_3Ti_4O_{12}$ (CCTO) which is well characterised by experiment. The inclusion of HF exchange improved, in a systematic way, both structural and electronic results with respect to experiment. The confidence gained in the study of known compounds has enabled us to explore new compositions predictively. Interesting results have been obtained, and we have been able to identify new materials of potential interest, which represent clear new targets for future experimental studies.

Acknowledgements

I'd like to dedicate this thesis to the loving memory of the most caring and selfless person I ever knew, my mother, Lauren Michel. Of course I wish that you were here to see this, but wherever you are, I hope that you are proud.

During my time at UCL I have been fortunate enough to work with some amazing people of whom it would be rather churlish not to acknowledge. In particular I would like to thank Alastair, Paul, Kim, Aisha, Luis, Martin, Vladimir, Martijn, Gareth, Alexei, Scott, Steven and Antonio for their good friendship and generosity with their time. Most of all I would like to thank my supervisor, Dr. Furio Cora, for his unbelievable patience and incredible level of support, without which this PhD would not have been possible.

I would like to acknowledge my family for their love and support throughout my studies. In particular I would like to thank my Grandmother for not giving up on me through school and my Uncle for enabling get to University.

I am hugely grateful to Prof. Richard Catlow for giving me the opportunity to undertake this PhD and would like to thank EPSRC for funding.

Chapter 1 - Introduction

This thesis is mostly concerned with the computational study of a class of isostructural materials, known as perovskites. Perovskites have the general composition ABZ_3, where A and B are two different cations, and Z an anion, and receive their name from the mineral perovskite $CaTiO_3$. Perovskites have attracted much attention since the discovery of ferroelectricity in barium titanate ($BaTiO_3$) in 1945. Research on perovskites has led to the discovery of many interesting electronic properties. These include large dielectric constants, magnetic phases, colossal magnetoresistance (CMR) behaviour as well as conducting, semi-conducting and superconducting properties. The majority of these properties are not only interesting from an academic point of view, but also play a key role in technological applications. If we consider for example materials exhibiting large dielectric constants, these are currently the key component for the miniaturisation of integrated circuits. It is the magnitude of the dielectric constant that will ultimately determine the miniaturisation of microelectronic circuits that are ubiquitous in consumer electronics. Other examples of practical applications of perovskites include ferroelectric materials in memory devices and superconductors in medical imaging equipment. Of particular interest are perovskites which display two or more of the above properties; one such example are magnetoelectric materials, which display an interplay of ferroelectric and ferromagnetic properties. Availability of magnetoelectric compounds opens up new applications, for instance the ability to store data magnetically as well as electronically. Some perovksites like $BiMnO_3$ and $SeCuO_3$ are among the few known examples of magnetoelectric compounds.

The range of useful properties exhibited by members of the perovskite family is vast, and will be discussed in more detail in chapter 4, with some attention to the electronic properties that enable these.

Several perovskites are already implemented in devices used today. However, many materials which display potentially useful properties are not yet able to be exploited due to a lack of understanding at the atomic level. A large amount of research is targeted at not only rationalising observations and known effects in perovsites, but also to design new compositions with novel electronic behaviour.

During this PhD we have studied several perovskites which display fascinating electronic properties. The first material studied in detail is $CaCu_3Ti_4O_{12}$ (CCTO) which displays one of the largest known dielectric constants. This makes it the ideal choice for device miniaturisation, however, the origin of such a high dielectric constant is still debated and hence we aimed to validate current theories. This study extends from CCTO to other isostructural materials, some known experimentally, such as $CaCu_3Ge_4O_{12}$ and $CdCu_3Ti_4O_{12}$, but others studied here for the first time (eg. $SrCu_3Zr_4O_{12}$). The second class of materials studied in this thesis makes reference to Copper Selenite ($SeCuO_3$) which has recently been shown to display magnetoelectric properties.

Despite the very large number of perovskite-structured materials known, there are still gaps in the perovskite literature where adequate explanations have not been provided for some observed properties, or where potential new perovskite structures have not yet been synthesised. In some cases, synthesis requires extreme or at least unusual conditions; for example $SeCuO_3$ can only be achieved under pressure, while phases with anions other than oxygen are air sensitive, or may require long and expensive synthesis conditions. It is increasingly common to assist experimental synthesis with computational studies, both to select the target materials for particular application areas, and also to understand the conditions at which the target solid is stable. Indeed computational chemistry has now become an indispensable tool in materials sciences, and it is this tool that we have taken advantage of during the PhD.
Our studies have involved performing quantum mechanical calculations on the structural and electronic properties of copper containing perovskites. These studies have been performed using the CRYSTAL06 code which has allowed us to apply hybrid-exchange functionals in density functional theory (DFT); this methodological choice is linked to the systematic failure of pure DFT functionals in describing well localised electronic states, such those of the d^9 Cu^{2+} ions.

As mentioned earlier, a section of this thesis is dedicated to discussing the properties of CCTO. The crucial feature of this perovskite is the large dielectric constant, k. This measurable observable describes the response of the solid to an applied electric field; in practice, an insulating solid polarises and screens the applied field. The dielectric

constant is the proportionality constant between applied and total (applied minus screening) fields. In the general case, the response is directional, and the dielectric constant is represented by a 3x3 tensor; in an isotropic case with polarisation parallel to the applied field, the tensor reduces to a constant, k. An alternative operational way to define k is by considering a non-conducting material between the two plates of a capacitor, the latter being a combination of two conductors carrying charges of equal magnitude and opposite sign. By placing a dielectric between the plates, the capacitance increases by a dimensionless factor, k, known as the dielectric constant. This constant varies from one material to another. The potential difference between the plates of a capacitor, if ΔV is the value in vacuo, is reduced to $\Delta V/k$ when a dielectric is introduced. We thus find that the advantages from introducing a dielectric are an increase in capacitance and maximum operating voltage.

To describe the microscopic origin of the effect on introducing a dielectric we must consider the electric dipole moments. The electric dipole consists of two charges of equal magnitude but opposite sign separated by a given distance. If a uniform external field is applied to the dipole, the dipole experiences a torque which brings it into line with the field. However, we can distinguish between the cases of polar and non-polar molecules. Molecules are said to be polarised when a separation exists between the average position of the negative charges and the average position of the positive charges in the molecule. This condition is always present in some molecules eg. water and are thus known as polar molecules. Molecules that do not posses a permanent polarisation are called non-polar.

Let us consider the case of a dielectric made up of polar molecules placed in the electric field between plates of a capacitor; the dipoles are randomly oriented in the absence of an electric field. Where an external field due to charges on the capacitor plates is applied, a torque is exerted on the dipoles causing them to partially align with the field. The dielectric can then be described as polarised. The temperature and magnitude of the applied field with determine the degree of alignment.

If molecules of the dielectric are non-polar, the field due to the plates produces some charge separation and an induced dipole moment. These moments tend to align with the field and hence the dielectric is polarised. Therefore, we can polarise a dielectric with an external field regardless of whether the molecules are polar or non-polar.

Thus, when a dielectric material is placed between plates of a capacitor, the capacitance increases by the dielectric constant due to a decrease in the magnitude of the electric field and to a corresponding decrease in the potential difference between the plates. The decrease in the magnitude of the electric field arises from an internal electric field produced by aligned dipoles in the dielectric. The "normal" value of the dielectric constant varies with the type of material: a protic solvent like water has a dielectric constant of 80, aprotic solvents (hexane) have dielectric constant of ~2, while ionic solids vary in the range of 50-100. Ceramic samples of CCTO instead have been found to have a giant dielectric constant of $k \sim 10^5$, hence the practical interest in the material. The atomic-scale behaviour that originates this giant k is however still under discussion.

All the materials investigated in this thesis contain late transition metal ions, such as Cu^{2+}. The local environment of these ions in the crystal is strongly affected by as electronic distortion, first studied in 1937 by Hermann Arthur Jahn and Edward Teller[1], while at UCL Chemistry, and now commonly known as the Jahn-Teller effect. The mechanism behind this distortion is briefly discussed here. The Jahn-Teller Theorem states that a non-linear molecule in a degenerate electronic ground state distorts in such a way as to remove the electronic degeneration. The Jahn-Teller effect is most commonly encountered in octahedral complexes of the transition metals and is common in Cu^{2+} containing systems. The d^9 configuration of Cu^{2+}, in octahedral coordination, gives three electrons in the two degenerate e_{2g} orbitals. This gives a doubly degenerate electronic ground state and results in a distortion along one of the axes (consisting in an elongation of the bond along the z-axis).

In octahedral systems the distortion is most pronounced when an odd number of electrons occupy the e_g orbitals (ie. in d^9, low spin d^7 and high spin d^4 complexes, all of which have doubly degenerate ground states). This is due to the e_g orbitals involved in the degeneracy pointing directly at the ligands, so distortion can result in a large energetic stabilisation. Technically this effect should also occur when there is a degeneracy due to the electrons in the t_{2g} orbitals (ie. configurations such as d^1 or d^2, both of which are triply degenerate). However, the effect is much less noticeable, as the bonding between the metal t_{2g} orbitals and the ligands is of π type, and with less efficient overlap than that of σ type between the metal e_g orbitals and the ligands, resulting in a much smaller energy lowering of the distorted geometry. In tetrahedral

complexes, Jahn-Teller distortions are also small, due to the poor overlap between metal and ligands orbitals.

Much of the work of this thesis looks into the rationalisation of the different magnetic ground states (AFM or FM) exhibited by the systems studied. One of the most popular theories to rationalise whether the magnetic interaction between two open-shell ions in a crystal is ferro- or antiferro-magnetic, is that derived by P Anderson, J Goodenough and J Kanamori[2], now known as the Anderson-Goodenough-Kanamori (AGK) rules. These rules apply to interatomic spin-spin interactions between two atoms, each carrying a net spin, that are mediated by virtual electron transfers directly between the atoms (direct exchange) and/or between a shared anion and the two open-shell ions (superexchange). A virtual electron transfer occurs between overlapping orbitals of electronic states that are separated by an energy E. Orthogonal orbitals do not overlap, so there is no electron transfer and the resulting interaction is ferromagnetic; it is responsible for the Hund highest-spin rule for the free atom or ion. The AGK rules state that superexchange interactions are antiferromagnetic where the virtual electron transfer is between overlapping orbitals that are each half-filled, but they are ferromagnetic where the virtual electron transfer is from a half-filled to an empty orbital or from a filled to a half-filled orbital. The AGK rules extend to predict an exact crossover angle within an M-O-M bridge which defines the point at which a system exhibits ferro or anti-ferromagnetism. This angle is ~135°; such a value is of interest in this thesis because an isostructural series of perovskites, $(Se_xTe_{1-x})CuO_3$, has equilibrium Cu-O-Cu angles[3] that cross the limiting valued predicted by the AGK rules, and it is of interest to link how the measured (or calculated in our case) magnetisation of the solid varies as a function of the Cu-O-Cu angles.

The plan of the thesis is as follows: in Chapter 2 we introduce some concepts of crystallography which allow us to understand the models which are used to represent the structure of the perovskites studied in this work and the effect that this can have on their properties. In Chapter 3 we introduce the theories and models available to perform calculations on crystalline solids and justify the most appropriate for our particular studies. Chapter 4 looks at basis sets, why they are necessary and the factors which influence the choice of one over another. There are many computational codes which

incorporate the theories outlined in Chapters 2-4; in chapter 5 we discuss the code chosen for this PhD and outline some of the tools it contains which have been of particular use. Chapter 6 then provides a short review on the family of perovskites which outlines the structural and electronic properties of some known examples. This examines the literature which is relevant to this PhD and is designed to help put the following results chapters into context. We then move on to Chapter 7 where the structural and electronic properties obtained from bulk and surface calculations on several isostructural perovskites of the form $AA'_3B_4Z_{12}$ (eg. CCTO) are presented. In Chapter 8 we present the results of bulk calculations on several Cu-containing perovskites of the ABZ_3 form, using $SeCuO_3$ as a reference compound. In this chapter we are particularly interested in electronic and magnetic properties, and the effect of cation substitution on the A and B site and anion substitution on the Z site of the pervoskite structure. In chapter 9 we present an overall conclusion of this work and we also highlight our suggestions for potential future work.

Chapter 2 - Crystalline Solids and Surfaces

In this chapter, some definitions and notations of crystallography are outlined. The aim here is to introduce the models used for the study of the bulk and surfaces of the materials investigated during this PhD. It should be noted that this discussion is limited to crystalline solids.

2.1 Crystal Lattices

A crystal lattice is a mathematical concept, which can be described as an infinite pattern of points, each of which has the same surroundings in the same orientation. In 3-dimensions, if any lattice point is chosen to be the origin, the position of any other lattice point can be defined by the vector $\vec{T}$ such that:

$$\vec{T} = m\vec{a} + n\vec{b} + p\vec{c} \qquad (2.1)$$

where a, b and c are vectors often known as basis vectors, which form a parallelepiped that defines the unit cell of the lattice. These vectors describe the length of each side of the unit cell (a_0, b_0 and c_0) and, together with the angles between them, are collectively known as the unit cell parameters. These angles are called α, β and γ, where α lies between b and c, β lies between a and c and γ lies between a and b. The unit cell is not a unique entity, it is chosen conveniently to reveal a crystal's underlying symmetry. In equation (2.1), m, n and p are any rational numbers.

There are 14 possible lattices (in 3-dimensions) which are known as Bravais lattices (or sometimes direct lattices). These have been illustrated in Figure 2.1.

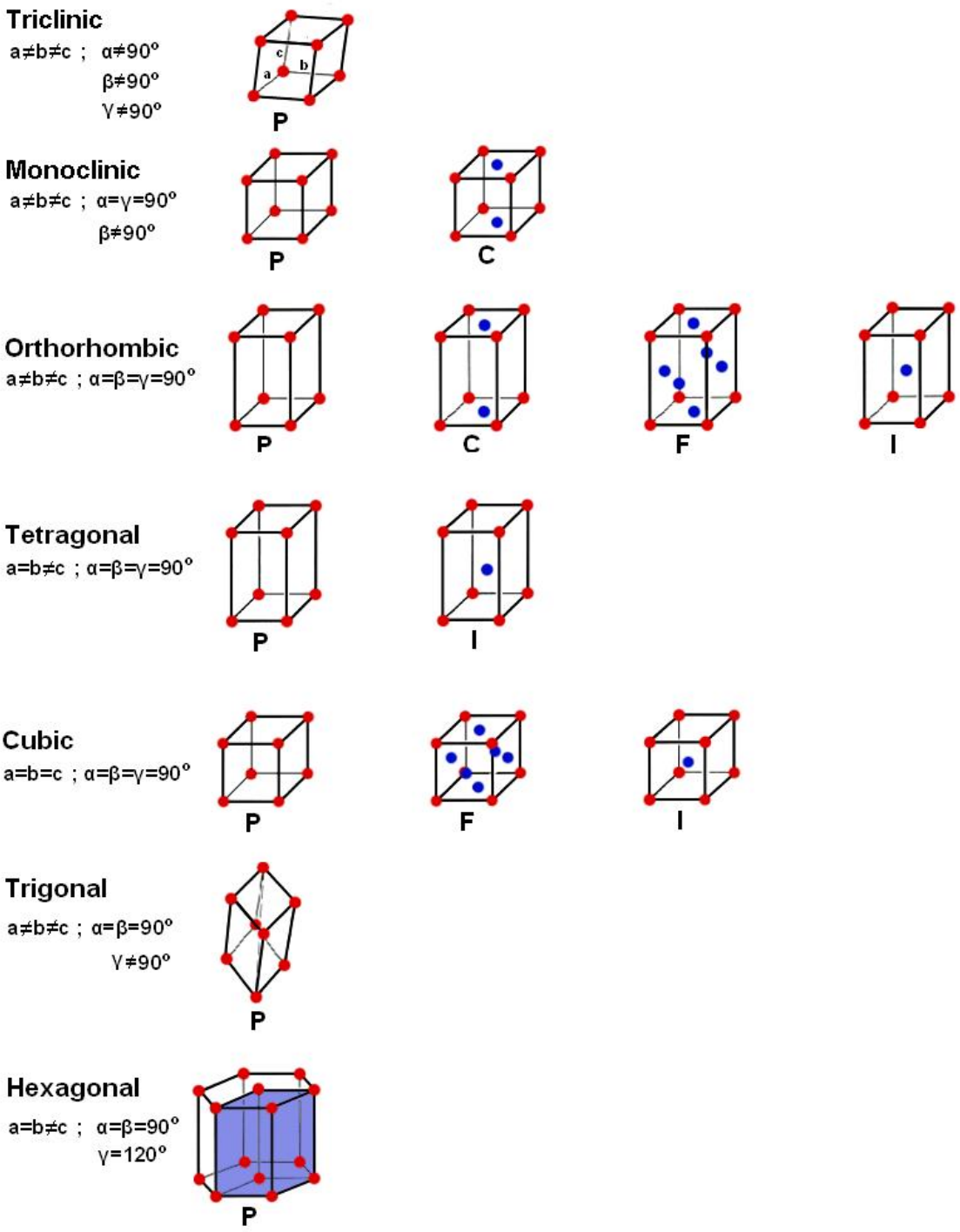

Figure 2.1 The Bravais lattices. The a, b and c directions are as shown in the Triclinic case. Image adapted from ref. [4].

There are 7 different classes of a, b, c, α, β and γ that are needed to define all of the Bravais lattices. These are labelled in Figure 2.1.

The Bravais lattices are further denoted by the number of lattice points contained in a unit cell. The simplest is known as the primitive lattice and is denoted as P in Figure

2.1. This is the smallest type of unit cell and the only one which contains only one lattice point. A unit cell that contains lattice points in the corner and in the centre of the cell (2 lattice points) is known as body-centred unit cell and is labelled I. A unit cell containing lattice points in the centre of each its faces (4 lattices points) is called a face-centred unit cell and is labelled F. There are also unit cells containing a lattice point on one of the face centres which is called A-face centred if the faces cut the a-axes, B-face centred if the faces cut the b-axes and C-face centred if the faces cut the c-axes.

2.2 Crystal Structures

The Bravais lattices allow any crystal structure to be built by positioning one or more atoms on each lattice point. The atom or atoms that sit on each lattice point are usually called the basis or the motif. This is the smallest fragment of the crystal structure that, when repeated, can create the whole structure. The motif, for example, could be an atom or a molecule. Therefore, a crystal structure is formed of both a lattice and a basis. It is important to note here the distinction between the crystal lattice and crystal structure. A crystal lattice is simply a lattice of points in space formed by repeating units, a purely mathematical concept. The crystal structure is formed by placing a basis down on each point of a lattice. An identical arrangement and orientation of the basis is found at each lattice point. Hence the crystal is formed by repeating the basis in space according to a given Bravais lattice.[5]

The axes used to describe the crystal structure are the same as those outlined so far. The position of an atom within the unit cell can be described by fractional coordinates. These provide a position which is a fraction (in each direction) of the unit cell lengths, a_0, b_0 and c_0. So for example if we have an Oxygen atom at position (½, ½, ½) it is located halfway along the a axis, halfway along the b axis and halfway along the c axis, ie. it is located in the centre of the unit cell.[6]

So far, we have seen how a unit cell can be constructed from one of fourteen different Bravais lattices by adding an atom or a set of atoms to each lattice point known as a basis. An entire crystal structure can then be constructed by repeating this unit cell in 3-dimensions. Therefore, one can build a crystalline system by defining the unit cell type

(eg. Tetragonal), the unit cell parameters (a_0, b_0, c_0, α, β and γ) and the fractional positions of all the unit cell atoms.

We will now see how there are several symmetry operations available which lead to the existence of a finite number of classes known as point and space groups.

2.3 Symmetry, Point Groups and Space Groups

A solid, such as a crystal structure, can be classified in terms of the collection of symmetry elements that can be attributed to the given shape. Its internal symmetry can be described by the combination of axes of rotation and mirror planes. It is a collection of such symmetry operations, applied to a point in space (leaving one point fixed), that is given the name of a point group. The various possible symmetry elements under consideration are inversion centre, reflection plane, rotation axis and rotation-inversion axis. It should be noted that translation plays no part here since it does not leave one point fixed. The combination of these symmetry elements leads to 32 possible crystallographic point groups.

As aforementioned, one can place a basis of atoms or molecules on the points of a Bravais lattice. It follows that adding these introduces more and more possible combinations of symmetry operations. The number of possible Bravais lattices, together with the various point groups, give a total of 230 different space groups. That is to say that by considering the combinations of the 32 point groups, the screw axes (simultaneous rotation and translation), glide planes (combination of a reflection and a translation in a plane) and the different Bravais lattices we arrive at 230 space groups. We can then attribute a particular real crystal to one of these space groups. Each group is represented by a combination of numbers, letters and symbols which are chosen to represent the symmetry elements of the structure.[7]

The space group provides much information about a system including the type of unit cell and all or some of the fractional coordinates of the atoms in the cell. To fully build the crystal structure one must additionally known the type of atoms within the cell, the unit cell parameters and the fractional coordinates of the atoms that are not fixed by the space group symmetry.

2.4 Miller Indices

The facets and internal planes through a crystal lattice or structure can be described by Miller Indices. If a unit cell of a crystal is defined by vectors $\vec{a}$, $\vec{b}$ and $\vec{c}$, then any crystal plane that intercepts the axes proportional to a/h, b/k and c/l respectively is denoted by its Miller indices (hkl). These indices describe not just one plane, but all parallel planes. The values of h, k and l are multiples of the unit cell lattice parameters, a_0, b_0 and c_0. Therefore, the set of planes which lie parallel to the unit cell edge is given the relevant h, k or l value zero. Some examples of these Miller indices are the 001, 110 and 111 planes which are illustrated in Figure 2.1. The 001 indices represent the set of planes that lie parallel to the a-axes and b-axes and intersect the unit cell at position 1c. Planes cutting the a-axes and b-axis at 1a and 1b are the 110 planes, and planes cutting the a-axes, b-axes and c-axes at 1a 1b and 1c are called the 111 planes. Indices of higher multiples of the axes exist, for example, the 122 planes will cut the unit cell edges at 1a, 1/2b and 1/2c.

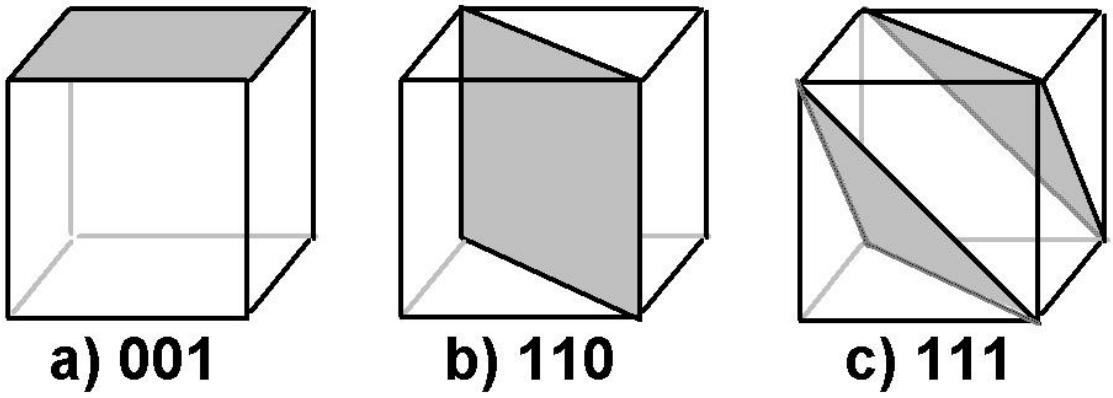

Figure 2.2 Examples of some Miller indices of lattice planes a) 001, b) 110 and c) 111

2.5 Reciprocal Lattice and Reciprocal Space

For each Bravais lattice, a corresponding reciprocal lattice may be postulated which possesses the same symmetry. Where the Bravais lattice may be described as existing in real space, the reciprocal lattice exists in reciprocal space. This idea was created in order to simplify the process of describing the physical properties of many systems.

To derive the reciprocal lattice we define new lattice vectors $\vec{a}^*, \vec{b}^*, \vec{c}^*$ whose directions are perpendicular to the end faces of the Bravais lattice unit cell. The lengths of these new lattice vectors are the inverse of the perpendicular distance from the lattice origin to the end faces of the Bravais lattice unit cell. The reciprocal lattice points are associated with a set of planes described by the Miller indices (hkl). The position of the (hkl) spot in the reciprocal lattice is related to the orientation of these planes and the spacing between them, d_{hkl}. In fact the lengths of the vectors of the reciprocal space can be written as:

$$a^* = \frac{1}{d_{100}}, b^* = \frac{1}{d_{010}}, c^* = \frac{1}{d_{001}} \tag{2.2}$$

For example, the cubic, tetragonal and orthorhombic lattices are equivalent to:

$$a^* = \frac{1}{a_0}, b^* = \frac{1}{b_0}, c^* = \frac{1}{c_0} \tag{2.3}$$

For crystals possessing different symmetries the relationship between the Bravais and reciprocal lattice is more complex; this detail is not relevant to this PhD. The important point to note is that the use of reciprocal space allows the physical properties of many systems to be more easily described.

Just as the Bravais lattices have primitive cells, there is also a primitive cell of a given reciprocal lattice. This is called the first Brillouin zone.

2.6 K-Points and the Brillouin Zone

In order to understand the concepts of the next chapter it is convenient to introduce the concept of k-points here. There are an infinite number of k-points in the Brillouin zone. Electronic structure calculations performed on crystalline solids require the evaluation of integrals over the Brillouin zone, that cannot be performed analytically. This problem is overcome by the fact that k-points that are sufficiently close together contain similar information; we can therefore replace the integration with a summation over a finite

number of k-points. The amount of points required to obtain converged properties will depend on the size and nature of the system. For example, metallic systems tend to require more k-points (to capture the shape of the Fermi surface properly) than a large band-gap insulator. A common recipe for choosing the number of k-points was that developed by Monkhorst and Pack[8], which is particularly well suited for metallic systems, but is applied more generally to all crystalline solids.

2.7 Modelling Solids and Surfaces

We have now seen how a crystalline solid can be constructed by applying translational and point symmetry operations to a finite number of atoms describing its unit cell. During this PhD we have been interested in studying both bulk materials as well as their surfaces. Let us now discuss how this can be done in practice by making use of the concept of periodic boundary conditions (PBC).

2.7.1 Bulk Calculations

For the majority of this PhD, calculations were performed on the bulk properties of materials; an explicit description of each atom of a typical solid would involve calculations on a large amount of atoms, of the order of Avogadro's number ($\sim 6 \times 10^{23}$). Calculations on this scale are clearly not computationally feasible. We also have the issue of surface effects. Unless the chosen bulk size is adequately large (too large to simulate) the ratio between the number of surface atoms and total number of atoms would be large enough to cause surface effects to be more important than they should.

These problems are overcome by the application of periodic boundary conditions (PBC) which enable crystalline solids to be characterised in a more manageable way. In this way a unit cell is chosen including the minimal number of atoms which contains the whole symmetry of the system. This is used with the lattice vectors indicating the size of the unit cell and the direction of replication to reproduce an infinite crystalline structure. This cell is able to interact with an infinite lattice of identical image cells

surrounding it in each Cartesian direction (leaving no surfaces). Any movement or action from an atom in the main cell is replicated precisely by the equivalent atoms in the surrounding 'image' cells. Here we have a situation where each particle interacts, not only with other particles in its cell but with their images in nearby cells. This is advantageous as information about the atoms in each cell do not need to be stored. It is only necessary to store information on the molecules in the unit cell. If an atom were to leave the cell there would be an equivalent atom entering from the opposite side. Therefore the entire solid is reproduced by just repeating this unit cell in all Cartesian directions.

2.7.2 Surface Calculations

The ability to perform calculations on surfaces and interfaces is extremely beneficial as this is where the most interesting properties are often observed. Surfaces are often complex and difficult to characterise experimentally. Therefore computational methods are extremely important in calculating properties of surfaces.

The surface of a crystalline solid can be described by the Miller indices that define the crystal plane exposed, as introduced in section 2.4. However, Miller indices do not fully define the surface structure.

Real surfaces are semi-infinite systems and therefore it would not be efficient to perform calculations of properties in this way. One way of modelling the surface involves representing two dimensional surfaces of a crystal as slabs of the material. Here, the crystal is considered as a stack of planes perpendicular to the surface (the direction perpendicular to the surface is usually indicated as z in surface studies) and a slab of finite thickness is cut out. Periodic boundary conditions are applied in the x and y planes of the material. Perpendicular to the slab the boundary condition is that the wavefunction decays to zero at a large enough distance from the slab. This is the method utilised during this PhD. An alternative representation of surfaces consists in using slabs separated by a finite layer of empty space, thus restoring 3D periodicity. This has not been of interest during this work and we will therefore not go into these details.

2.8 Magnetic Structures

Magnetic order in bulk materials and their surfaces can have a large effect on the crystal structure. Let us therefore discuss magnetism and how it is incorporated into the crystallographic structures discussed above.

It is possible to occupy positions of a crystal lattice with any element, some of which may contain unpaired electrons. As a result of the spin on these atoms we are presented with the phenomenon of magnetism where each atom has a magnetic dipole associated with it. These dipoles can exist with different alignments such as paramagnetic, ferrimagnetic, ferromagnetic (FM) or anti-ferromagnetic (AFM).[9] Paramagnetic compounds have magnetic dipoles which are completely unaligned in random directions. A ferromagnetic structure is one that undergoes a phase transition from a high temperature phase that does not have a macroscopic moment to a low temperature phase that has a spontaneous magnetisation. This spontaneous magnetisation remains even in the absence of an applied magnetic field. This is due the randomly aligned magnetic dipole moments of the atoms in the paramagnetic high temperature phase tending to line up in the same direction. This is shown in Figure 2.3 along with two other possible orderings, AFM and ferrimagnetic. Ferromagnetism has been successfully rationalised by two theories, the Curie-Weiss localised-moment theory[10] and the Stoner band theory of magnetism[11]. Weiss proposed that a "molecular field" acts to align magnetic moments and we now understand this to be the quantum mechanical exchange energy (see Chapter 3) which causes electrons with parallel spins (and therefore with parallel magnetic moments) to have a lower energy than electrons with anti-parallel spins. It is below a cut-off tempertature known as the Curie temperature, T_c, that the molecular field of a material is so strong that it remains magnetised even in the absence of an applied magnetic field (the analogous cut-off for AFM materials is known as the Neel temperature, $T_{N,}$ ie. the temperature above which an AFM material becomes paramagnetic).

In an AFM structure the magnetic dipole moments of the atoms are ordered anti-parallel to one another. This leads to a net zero magnetisation and hence they are not as sought after for technological applications. There can often be more than one type of AFM arrangement available to a structure. For example, the magnetic dipoles can alternate in direction along the 111, 110 or 001 planes. Ferrimagnets are similar to AFM materials

in that the dipoles align antiparallel. The difference is that in a Ferrimagnet some of the dipole moments are larger than others so the material has a net overall magnetisation; hence these can be useful for device implementation.

When describing an AFM structure it is not always possible to use the same unit cell as used for an isostructural paramagnetic or diamagnetic unit cell. For example if there are three magnetic ions in a unit cell it is not possible to have an equal number of spin up and down ions. Therefore a multiple cell must be created. In this example a double unit cell is the best solution from a computational point of view where the cell is doubled along one direction. This allows for three alpha and three beta spin and hence a proper AFM magnetic structure.

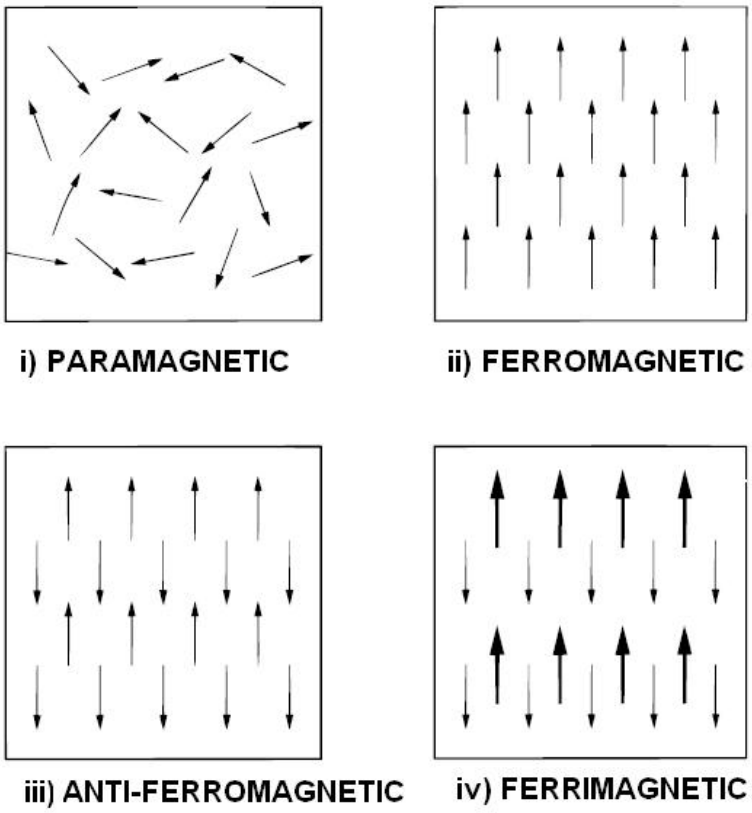

Figure 2.3 Example of the possible ordering of dipoles in magnetic structures. Image adapted from ref. [12].

Chapter 3 - Theoretical Methods

3.1 Quantum Mechanics

The properties of the materials being researched during this PhD strongly depend on the electrons in the system and need therefore to be addressed by quantum mechanical methods. Such techniques enable us to probe the electronic structure of a given system by solving the Schrödinger equation. The electron-electron interation makes this a difficult task as the unknown electron density of the system depends on itself, a problem known as many-body interaction. It has been tackled by several methods over the years, of which the two principle techniques applied to solids are Hartree-Fock (HF) theory and density functional theory (DFT). Both form an integral part of the work performed here, and they will be discussed in some detail in the following sections.

In quantum mechanics it is the wavefunction that holds all of the physical information about a system. This is not measurable and can only be obtained by solving the time-independent Schrödinger equation[13]:

$$H\psi(\underline{r},\underline{R}) = E(\underline{R})\psi(\underline{r},\underline{R})$$

where:

$$H = -\frac{\hbar^2}{2m}\sum_i^n \nabla_i^{\,2} + \sum_i^n \sum_I^N \frac{Z_I e^2}{4\pi\varepsilon_0 r_{Ii}} + (e-e) \qquad (3.1)$$

In this equation the wavefunction, ψ, depends on the set of locations, $\underline{R}$ of the nuclei and the electronic coordinates, $\underline{r}$. H is the Hamiltonian, ie. the quantum mechanical operator that corresponds to the internal energy of the system. The terms in the definition of H (3.1) correspond to the kinetic energy of the electrons, the electron nuclei attraction and electron-electron interaction (with Coulomb and exchange components and indicated here simply as e-e). It may also contain a Coulomb internuclear repulsion term, but under the Born-Oppenheimer approximation (electrons move faster than nuclei and adapt instantly to a given nuclear configuration) the nucleus-nucleus repulsion can be treated as an additive classical term and removed from the Schrödinger equation.

In principle the Schrödinger equation (3.1) can be solved to obtain the desired properties of a given system. However, in practice, this is not straightforward: the potential experienced by each electron is influenced by all other electrons within a given system. Therefore, the problem lies in the equations which need to be solved, depending upon each other. The problem applies to systems of all sizes, from molecules to solids with the only exception of one electron systems which are obviously of limited practical interest.

During this PhD we are interested in techniques which solve the many body problem for solids, which contain a number of atoms of the order of the Avagadro number (10^{23}). Solving the Schrödinger equation directly for all electrons is clearly impossible, and approximations need to be made in order to make this task feasible. In fact, this task is impossible for even a two electron system and even in this case approximations need to be made.

The motivation for solving this problem is clear when it is realised that once the electronic wavefunction and electronic energy are calculated, a wealth of other useful information about a given system is achievable.

Techniques to solve the many-body problem have been suggested and introduce approximations in the Schrödinger equation. Those that we have applied in our work are based on a mean-field approximation that factorises the many-body equation into a set of one-electron equations, in which each electron of the system moves in the mean-field generated by all other particles. These are the HF and DFT theories discussed below.

3.2 Hartree-Fock Theory

The electron-electron potential energy in (3.1) is the main complication in electronic structure calculations. The first step here is to neglect this feature and define a new wavefunction, ψ°, in which the electron-electron energy has been neglected[14]. We can then say that:

$$H^\circ\psi^\circ = E^\circ\psi^\circ$$

where:

$$H^\circ = \sum_{i=1}^{n} h_i \qquad (3.2)$$

In (3.2) h_i is known as the one-electron Hamiltonian for electron i. If we split the n-electron equation (3.2) into n one electron equations we can express ψ° as a product of n one electron wavefunctions of the form, $\phi_a^o(\underline{r},\underline{R})$. ϕ_a^o is thus a solution of:

$$h_i\phi_a^o(i) = E_a^o\phi_a^o(i) \tag{3.3}$$

In this equation E_a^o is the energy of one electron in orbital a, given by the product of an orbital wavefunction and spin functional. The overall energy, E°, is the sum of the one electron energies and the overall wavefunction will be expressed as a product of one-electron wavefunctions:

$$\psi^o = \phi_a^o(1)\phi_b^o(2)...\phi_z^o(n) \tag{3.4}$$

The assumption that the wavefunction can be built from a product of single electron wavefunctions is an approximation and does not satisfy the Fermi-Dirac statistics (also resulting in the Pauli exclusion principle[15]). This principle forbids the existence of two fermions at the same point in space with the same quantum numbers. It more specifically states that the total wavefunction (including spin) must be antisymmetric with respect to the interchange of any pair of electrons. To solve these problems the n-electron wavefunction can be written not as a simple product of one-electron spin orbitals, but as a Slater determinant[16] built on the n spin orbitals. The Slater determinant ensures that the Pauli principle is obeyed and can be written as:

$$\psi = \frac{1}{\sqrt{(n!)}}\begin{vmatrix} \phi_a^o(1) & \phi_b^o(1) & ... & \phi_z^o(1) \\ \phi_a^o(2) & \phi_b^o(2) & ... & \phi_z^o(2) \\ ... & ... & ... & ... \\ \phi_a^o(N) & ... & ... & \phi_z^o(N) \end{vmatrix} \tag{3.5}$$

which is anti-symmetric under the interchange of any pair of electrons. The overall wavefunction can therefore be written as:

$$\psi^o(\underline{x},\underline{R}) = \left(\frac{1}{n!}\right)^{-\frac{1}{2}} \det\left|\phi_a^o(1)\phi_b^o(2)...\phi_z^o(n)\right| \tag{3.6}$$

We have so far neglected the electron-electron interactions but any treatment of the electronic structure of a system must include this effect. The mean-field approximation treats the electron-electron interactions in an average way. This means that each electron moves in the electrostatic field due to the nuclei, and feels the effect of the average distribution of the other n-1 electrons. The combination of factorisation of the wavefunction into one electron orbitals and the mean field approximation gives rise to the Hartree-Fock (HF) method[17-20]. The HF wavefunction is given by a Slater determinant of the form of (3.6), in which electron-electron energy interactions are treated in an average way. We then use Variational theory, which involves minimising the Rayleigh ratio:

$$\xi = \frac{\int \psi^*(\underline{x},\underline{R}) H \psi(\underline{x},\underline{R}) d\underline{x}}{\int \psi^*(\underline{x},\underline{R}) \psi(\underline{x},\underline{R}) d\underline{x}} \tag{3.7}$$

to derive the spin orbitals that yield the best n-electron determinantal wavefunction. This minimisation must be done under the constraint that spinorbitals be orthonormal. The lowest value of the Rayleigh ratio is identified with the ground state electronic energy for the selected nuclear configuration, $\underline{R}$. The Hartree-Fock equations for the individual spin orbitals are given by:

$$f_i \phi_a(i) = \varepsilon_a \phi_a(i) \tag{3.8}$$

where:
$$f_i = h_i + \sum_u \left[J_u(i) - K_u(i)\right] \tag{3.9}$$

Solving equation (3.8) yields the spinorbitals $\phi_a(i)$ of energy ε_a, f_i is the Fock operator. In equation (3.9) we have a sum over all spinorbitals, u, while J_u and K_u are the Coulomb operator and exchange operator respectively:

$$J_u(1)\phi_a(1) = j_0\left[\int \phi_u^*(2)\frac{1}{r_{12}}\phi_u(2)d\underline{x}_2\right]\phi_a(1) \tag{3.10}$$

$$K_u(1)\phi_a(1) = j_0\left[\int \phi_u^*(2)\frac{1}{r_{12}}\phi_a(2)d\underline{x}_2\right]\phi_u(1) \tag{3.11}$$

In (3.10), J_u, represents the Coulombic interaction of electron 1 with electron 2 in the orbital ϕ_u. In (3.11), K_u, takes into account the effects of spin correlation. In both equations we have:

$$j_0 = \frac{e^2}{4\pi\varepsilon_0} \tag{3.12}$$

From equation (3.9) we have the average potential energy of a given electron (in this case electron i) in the field due to all other electrons. As clear from (3.10) and (3.11), the unknown electron wavefunction ϕ also enters the definition of forces. The HF equations must be solved iteratively via a self-consistent field (SCF) method. In this method, a trial set of spinorbitals is formulated to construct the Fock operator which are then used in the HF equations to produce a new set of spinorbitals. These new spinorbitals are put back through the method and the cycle continues until some numerical convergence criteria is satisfied.

In solving these equations we will in theory end up with an infinite number of spinorbitals ϕ_u with energy, ε_u. In practice we can only solve these equations for a finite number, m, of spinorbitals with $m \geq n$ (n is the number of electrons in the system). When the SCF cycles are complete these m spinorbitals are arranged in order of increasing orbital energy with the n lowest energy spinorbitals called occupied orbitals and the other called virtual orbitals. The Slater determinant built from the occupied spinorbitals is the HF ground state wavefunction, denoted as Ψ_0.

In closed-shell systems we can assume that the spatial components of the spinorbitals are the same for each pair of electrons. If we have n electrons there are then ½n spatial orbitals each doubly occupied by electrons in spin up (α) and spin down (β). This gives a total wavefunction known as a restricted HF wavefunction (RHF).

For open shell systems we can still treat the electrons in restricted formalism, forcing the spatial wavefunction for doubly occupied orbitals to be identical for spin up and down electrons, in a method called ROHF.
However, the ROHF approximation often leads to an inaccurate variational ground state energy. Open shell systems can be better treated using an unrestricted HF (UHF) formalism in which the eigenstates for α and β electrons are solved independently. The one disadvantage of the UHF method is that UHF wavefunction is not an eigenfunction of the spin operator, S^2.

For practical implementations, we need to define a basis that can be used to describe the spin-orbitals ϕ_a. Let us consider a basis set of M basis functions, θ_j. ϕ can be defined as a linear combination of these basis functions, θ, whose coefficients, c_{ji}, are unknown:

$$\phi_i = \sum_{j=1}^{M} c_{ji}\theta_j \tag{3.13}$$

The problem of calculating the wavefunction is equivalent to finding the coefficients, c_{ji}. Using the matrix representation of operators f and h in the basis set, θ, equations (3.8) and (3.9) can be re-written as:

$$\sum_{j=1}^{M} F_{ij}c_{ja} = \varepsilon_a \sum_{j=1}^{M} S_{ij}c_{ja} \tag{3.14}$$

where: $F_{ij} = \int \theta_i^*(1)\, f_1 \theta_j(1) d\underline{r}_1$, $S_{ij} = \int \theta_i^*(1)\theta_j(1) d\underline{r}_1$

In these equations S is the overlap matrix and F is the Fock matrix. Equation (3.14) is known as the Roothaan equations. We can write in matrix notation:

$$\mathbf{FC} = \mathbf{SC}\varepsilon \tag{3.15}$$

where ε is an MxM diagonal matrix of the orbital energies $\varepsilon_{a,}$ and **C** is an MxM matrix composed of elements c_{ja}. Introducing a transformation matrix, **X**, to generate an orthonormal basis set from our initial basis set, equation (3.15) can be rewritten as:

$$\mathbf{F'C'} = \mathbf{C'}\varepsilon \tag{3.16}$$

where

$$\mathbf{F'} = \mathbf{X}^{\dagger}\mathbf{FX} \tag{3.17}$$

and

$$\mathbf{X} = \mathbf{S}^{-\frac{1}{2}} \tag{3.18}$$

The solution to (3.16) is obtained via an SCF approach, a cyclic procedure, outlined in Figure 3.1, that is repeated until the specified convergence criteria is met.
The choice of a suitable basis set is discussed in Chapter 4.

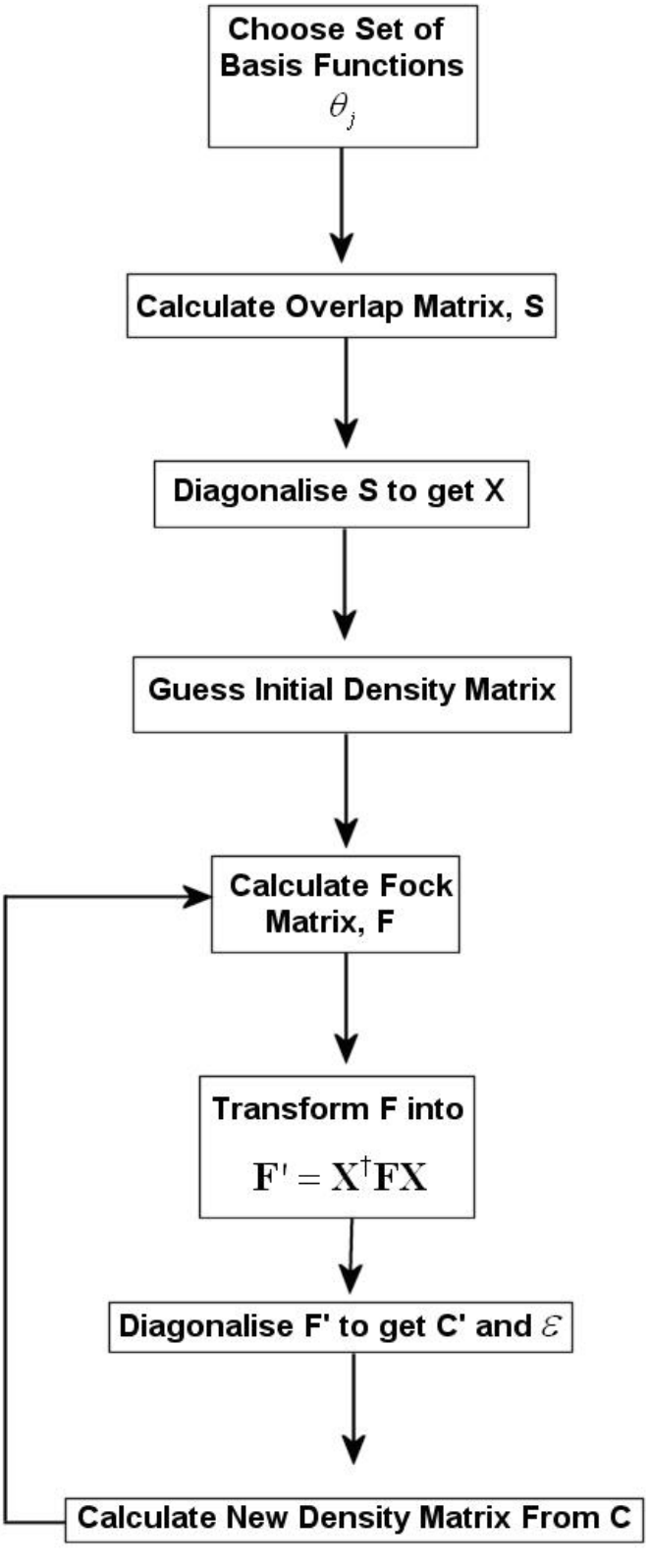

Figure 3.1 Schematic description of the HF SCF cycle procedure. The last procedure is repeated until some convergence criteria is met.

3.2.1 Limitations of HF theory

The HF ground state wavefunction does appear to be theoretically very sound and gives satisfactory results in many cases, however it does have limitations which have led to the development of new methods. Among these limitations is the fact that HF does not take into account the correlation existing between the movements of the electrons due to the independent particle model upon which it is based. The correlation energy, E_{corr}, is defined as the difference between the exact energy of the system and that calculated by the HF approximation at the HF limit (with an infinite basis set).

$$E_{corr} = E_{exact} - E_0^{HF} < 0 \tag{3.19}$$

Several methods, known as post-HF theories build on the HF wavefunction to generate more accurate solutions and account for the correlation energy. A separate alternative to study the electronic structure of a given system is represented by Density Functional Theory (DFT), which has been applied extensively in this thesis work and will be discussed in the next section.

Before examining DFT however, it is important to mention that the accuracy of post-HF techniques is achieved at the expense of a large computational effort. For a system described by M basis functions, the cost of a HF calculation is proportional to M^4 while post-HF methods scale with even higher powers of M (at least 5); by contrast DFT scales as M^3 and is therefore the method of choice for large systems.

3.3 Density Functional Theory (DFT)

In the late 1920's L. H. Thomas[21] and E. Fermi[22] took a different approach to Hartree in solving the many body problem. Instead of working with the wave function, they considered utilising a physical observable to determine the ground state properties of a system. Knowing that the Hamiltonian depends only on the positions and atomic numbers of the nuclei and the total number of electrons, it became obvious that a useful physical observable would be the electron density ρ (the main advantage being that the

density is a function of three coordinates only, whereas the wavefunction depends on 3N coordinates). By integrating the density over all space we find the total number of electrons, N:

$$N = \int \rho(r) dr \tag{3.20}$$

So on one hand we have Hartree-Fock theory, which utilises the wavefunction, and on the other we have density functional theory (DFT) which uses the electron density as its fundamental variable. The two quantities are related, with the density given by the square of the wavefunction.

One of the first attempts at solving the many problem using the electron density as the fundamental variable is given by the Thomas-Fermi theory. This method started by considering a system of non-interacting electrons with uniform density, acted on by a potential, V(r). The total energy is formed of the kinetic energy and potential energy parts:

$$E_{Tot} = E_{kin} + E_{pot} \tag{3.21}$$

For a uniform electron gas, the total energy can be expressed as:

$$E_{tot} = \frac{\hbar^2 \alpha}{m} \int \rho(\underline{r})^{\frac{5}{3}} d\underline{r} + \int V(\underline{r}) \rho(\underline{r}) d\underline{r} \tag{3.22}$$

where $\alpha = \frac{3}{10}(3\pi^2)^{\frac{2}{3}}$.

This expression for the total energy only depends on the total electronic density, ρ. It is said to be a functional of the density.

We must now add further terms to include the effect of electron-electron interactions. This has several components, first the coulomb interaction given by:

$$E_{Cou} = \frac{e^2}{8\pi\varepsilon_0}\iint \frac{\rho(r)\rho(r')}{|\underline{r}-\underline{r}'|}drdr' \tag{3.23}$$

where a factor of one half has been included to eliminate over counting.

The second contribution to the electron-electron interaction is exchange. Unlike the Hartree Fock method, where the exchange energy is evaluated exactly, exchange is approximated in Thomas-Fermi theory. In the uniform gas of interacting electrons the exchange energy per unit volume of position is described by[23, 24]:

$$\varepsilon_X = -\frac{e^2\beta}{4\pi\varepsilon_0}\rho(\underline{r})^{\frac{4}{3}} \tag{3.24}$$

If we then integrate over the whole system the exchange energy is:

$$E_X = -\frac{e^2\beta}{4\pi\varepsilon_0}\int \rho(\underline{r})^{\frac{4}{3}} d\underline{r} \tag{3.25}$$

Correlation is defined as the difference between the exact electron-electron interaction, and the contributions from Coulomb and exchange terms given by (3.23) and (3.25). It can also be expressed as a functional of ρ. An example is that proposed in 1938 by Wigner[25]:

$$E_C = -0.056\int \frac{\rho(\underline{r})^{\frac{4}{3}}}{0.079+\rho(\underline{r})^{\frac{1}{3}}} d\underline{r} \tag{3.26}$$

It is however, convenient for now to leave the correlation energy in general terms, and simply denote it as E_C. We can then express the total energy as:

$$E_{tot} = \frac{\hbar^2 \alpha}{m} \int \rho(\underline{r})^{\frac{5}{3}} d\underline{r} + \int V(\underline{r}) \rho(\underline{r}) d\underline{r} + \frac{e^2}{8\pi\varepsilon_0} \iint \frac{\rho(r)\rho(r')}{|\underline{r} - \underline{r}'|} dr dr' - \frac{e^2 \beta}{4\pi\varepsilon_0} \int \rho(\underline{r})^{\frac{4}{3}} d\underline{r} + E_C$$

(3.27)

It is important to note that (3.23), (3.25) and (3.27) describe a homogenous electron gas in which energies are obtained locally. This idea is at the basis of the local density approximation (LDA), discussed in more detail in section 3.3.2.

We need to minimise the total energy under the condition that the number of electrons in the system is constant. ie. $\int \rho(\underline{r}) d\underline{r} = N$. This means we minimise such that, $\frac{\delta Etot}{\delta \rho(\underline{r})} = \mu = \text{constant}$.

This minimisation is not straightforward as we are dealing with a function whose argument is also a function and therefore known as a 'functional'. We therefore use the mathematical theory of functional differentiation together with the theory of Lagrange undetermined multipliers, to obtain the chemical potential, μ, as:

$$\mu = \frac{\hbar^2 \alpha}{m} \frac{5}{3} \rho(\underline{r})^{\frac{2}{3}} + V(\underline{r}) + \frac{e^2}{4\pi\varepsilon_0} \int \frac{\rho(\underline{r}')}{|\underline{r} - \underline{r}'|} d\underline{r} - \frac{e^2 \beta}{4\pi\varepsilon_0} \frac{4}{3} \rho(\underline{r})^{\frac{1}{3}} + \mu_C \qquad (3.28)$$

If we group all but the first term and denote it as the effective potential, $V_{eff}(\underline{r})$, then we can see the difference between a system of non-interacting electrons and a system of interacting electrons are as follows:
for non-interacting electrons we can write:

$$\mu = \frac{\hbar^2 \alpha}{m} \frac{5}{3} \rho(\underline{r})^{\frac{2}{3}} + V(\underline{r}) \qquad (3.29)$$

while for interacting electrons we incorporate the last three terms of equation (3.28) into an effective potential $V_{eff}(\underline{r})$, yielding:

$$\mu = \frac{\hbar^2 \alpha}{m} \frac{5}{3} \rho(\underline{r})^{\frac{2}{3}} + V_{eff}(\underline{r}) \tag{3.30}$$

We can see here that the difference between the two cases lies in a modification of the potential.

The Thomas-Fermi theory gives correct results only in limited circumstances. It predicts the dependence of the total energy on the number of electrons, N, as being monotonic, but it neglects chemical bonding effects between atoms. Its historic merit is to point the way to DFT.

3.3.1 Hohenberg-Kohn Theorems and Kohn Sham Equations

The fundamental idea at the basis of the Thomas-Fermi theory is that the energy of a given system can be described exclusively in terms of its electronic density. Thirty years later the mathematical proof of this concept was established by P. Hohenberg and W. Kohn[26]. This proof was split into two theorems discussed below.

Let us consider a collection of an arbitrary number of electrons and nuclei, enclosed in a large box and moving under the influence of an external potential V(r) and the mutual interaction. The Hamiltonian of such a system can be described as:

$$\hat{H} = \hat{T} + \hat{U} + \hat{V} \tag{3.31}$$

where the first term is the kinetic energy, the second describes the electron-electron interaction and the third is the interaction of electrons with the nuclei and the external potential.

The first Hohenberg-Kohn theorem[26] states that the external potential is univocally determined by the electronic density, besides an additive constant. A uniform shift in V(r) by an arbitrary constant has no physical effect. This is best proved by turning the

statement around and prove this is true via *reductio ad absurdum*. It was indeed shown that it is impossible for two different potentials (differing by more than an additive constant) to give the same ground state density, ie. if $V(\underline{r}) - V'(\underline{r}) \neq \mathrm{c}$ then we end up with different ground states.

The first Hohenberg-Kohn theorem proves that all properties of a system can be calculated from its electronic density, but does not show us how to calculate the density of a system. Hohenberg and Kohn's second theorem shows us that the density obeys a variational principle, ie. given an external potential V(r), the electronic density of the system is the one that minimises the energy (subject of course to the constraint of describing the correct number of electrons). Since the ground state energy, ie. the expectation value of $\hat{H}$ given by equation (3.31), is a functional of the density, $\rho(\underline{r})$, also the single contributions to $\hat{H}$ can be expressed as functionals of $\rho(\underline{r})$. We therefore have:

$$E_g[\rho(\underline{r})] = \int V(\underline{r})\rho(\underline{r})d\underline{r} + F[\rho(\underline{r})] \tag{3.32}$$

where

$$\hat{F} = \hat{T} + \hat{U} \tag{3.33}$$

represents the kinetic energy and electron-electron interactions. $F[\rho]$ is a universal functional, valid for any number of particles and any external potential. Because the fundamental quantity is the electron density, the method based on Hohenberg-Kohn (HK) theorems is also known as DFT.

If $F[\rho]$ was a known and relatively simple functional of ρ, determining the ground state energy and density, in a given external potential, would be rather easy. It would only require the minimisation of a functional of the three dimensional density function. However, the functional form of F is unknown, and the main limitations of DFT consist

in providing accurate enough working formulations of F. Let us now see how such working formulations can be achieved.

Because of the long range Coulomb interaction, it is convenient to separate out from $F[\rho(\underline{r})]$ the classical Coulomb energy between electrons and write:

$$F[\rho(\underline{r})] = T[\rho(\underline{r})] + U[\rho(\underline{r})] \tag{3.34}$$

where T[ρ] is the kinetic energy of a system of non-interacting electrons and U[ρ] is the interaction energy. The energy can then be expressed as:

$$E_{tot}[\rho(\underline{r})] = \int V(\underline{r})\rho(\underline{r})d\underline{r} + T[\rho(\underline{r})] + U[\rho(\underline{r})] \tag{3.35}$$

The true ground state is found by minimising with respect to $\rho(\underline{r})$, using a Lagrange multiplier to constrain the number of electrons, to obtain:

$$\frac{\delta E_{tot}}{\delta\rho(\underline{r})} = V(\underline{r}) + \frac{\delta T[\rho(\underline{r})]}{\delta\rho(\underline{r})} + \frac{\delta U[\rho(\underline{r})]}{\delta\rho(\underline{r})} = \mu \tag{3.36}$$

We can also introduce an effective potential:

$$v_{eff}(r) = V(\underline{r}) + \frac{\delta U[\rho(\underline{r})]}{\delta\rho(\underline{r})} \tag{3.37}$$

from which (3.36) can be written as:

$$\frac{\delta T[\rho(\underline{r})]}{\delta\rho(\underline{r})} + v_{eff}(\underline{r}) = \mu \tag{3.38}$$

The constant (chemical potential) comes from the fact that we minimise under the constraint that the number of electrons is constant.

By making explicit the electron-electron interaction in $U[\rho(\underline{r})]$, the energy for a system of interacting electrons is given by:

$$E_{tot}[\rho(\underline{r})] = \int \rho(\underline{r})V(\underline{r})d\underline{r} + T[\rho(\underline{r})] + \frac{e^2}{8\pi\varepsilon_0}\iint \frac{\rho(\underline{r})\rho(\underline{r}')}{|\underline{r}-\underline{r}'|}d\underline{r}d\underline{r}' + E_{xc}[\rho(\underline{r})] \quad (3.39)$$

In practice, the kinetic energy functional $T[\rho(\underline{r})]$ for the system of interacting electrons is approximated by the solution for a system of non-interacting electrons; while the term $E_{xc}[\rho(\underline{r})]$ contains all the terms that are not exactly known. It takes into account the difference between the kinetic energy functional for the non-interacting system and the equivalent functional for the interacting system, the exchange interaction between electrons and the electron-electron correlation energy. It is usually referred to as exchange and correlation energy.

The Kohn-Sham method defines a practical way to solve the DFT equations; it introduces a one-electron Hamiltonian in the same form of the Schrödinger equation, that yields one-electron orbitals ψ_n as solutions of the one-electron Kohn-Sham equation.

$$\frac{-\hbar^2}{2m}\nabla^2\psi_n(\underline{r}) + v_{eff}(\underline{r})\psi_n(\underline{r}) = \varepsilon_n\psi_n(\underline{r}) \quad (3.40)$$

and:

$$\rho(\underline{r}) = \sum_n |\psi_n(\underline{r})|^2 \quad (3.41)$$

The theory on which DFT is based is formally exact however it relies on the knowledge of the exchange and correlation functional whose exact definition is unknown. The most important step is therefore to decide on a suitable approximation for $E_{xc}[\rho(\underline{r})]$. The main aims of modern DFT are in defining ever more accurate approximations for E_{xc}, a topic discussed in section 3.3.2.

The Kohn-Sham equations yield the mathematical framework for finding the ground state density and energy of a many-body electron problem using standard independent particle methods. These equations are solved self-consistently, in the same way as discussed earlier for the HF method. The procedure is schematically shown in Figure 3.2. The first step is to guess the electron density, $\rho(\underline{r})$, and use it to calculate the effective potential $v_{eff}(\underline{r})$. The Kohn-Sham equation can then be solved to obtain the occupied one electron orbitals, ψ_n, which in turn define a new density ρ_{out}. This procedure is then repeated until we achieve self-consistency, ie. $\rho_{out}(\underline{r}) = \rho_{in}(\underline{r})$ to within a chosen numerical accuracy[27].

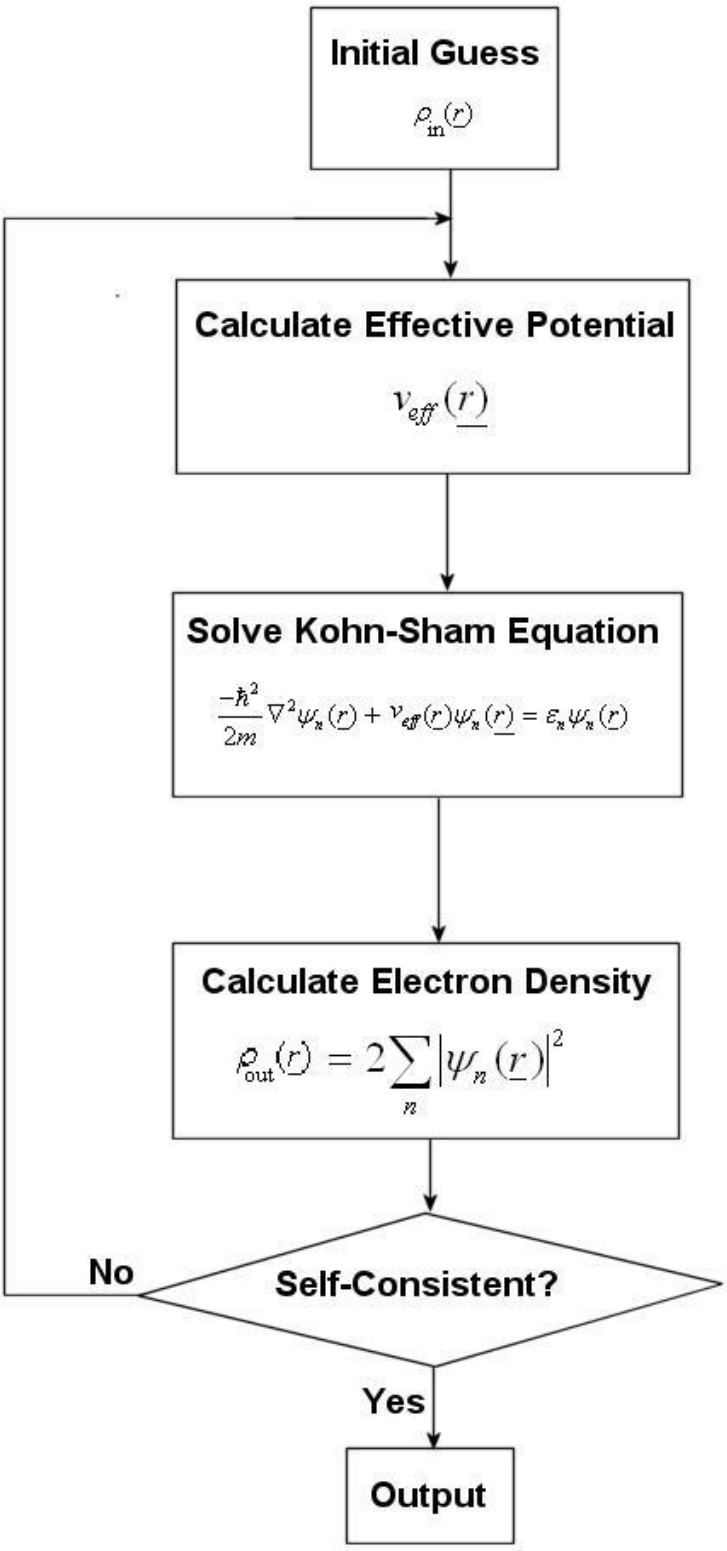

Figure 3.2 Schematic description of the SCF cyclic procedure in solving the Kohn-Sham equations.

3.3.2 Exchange and Correlation Functionals

The main aim of modern DFT is in making ever improving approximations to the exchange-correlation functional, $E_{xc}[\rho(\underline{r})]$, of the Kohn-Sham equations. The simplest of these is known as the local density approximation (LDA)[26]. The main idea behind the LDA was to consider an inhomogeneous electric system as locally homogeneous, and then use, at each point in space, the exchange and correlation hole corresponding to the homogeneous electron gas (known to a very good accuracy) with the same density. The exchange-correlation energy is simply calculated by integrating over all space with the exchange-correlation energy density at each point assumed to be the same as in the homogeneous electron gas with that density.

In a real non-uniform system described by electronic density $\rho(\underline{r})$, at each $\underline{r}$ there is an exchange-correlation energy given by $\varepsilon_{xc}[\rho(\underline{r})]\rho(\underline{r})$. The total exchange-correlation energy can be described by:

$$E_{xc}[\rho(\underline{r})] = \int \varepsilon_{xc}[\rho(\underline{r})]\rho(\underline{r})d\underline{r} \qquad (3.42)$$

This is the local density approximation (LDA). Despite its simplicity, the LDA is in fact able to achieve relatively accurate results for metallic solids with delocalised electrons. It does however have several shortcomings. In atoms where the electrons are quite localised the electronic densities are poor. Binding energies are consistently overestimated, and bond distances underestimated, in the LDA compared to experimental values. Another shortcoming of the LDA is that the local formulation of the energy expression does not account for the electronic redistribution in bonds, excluding chemistry from the functional expression.

The next generation of functionals were aimed at solving the problem of the inhomogenities in the electronic density that are present within the LDA functional. This was done by expanding locally the functional dependence of E_{xc} on $\rho(\underline{r})$ to include gradient and higher order derivatives. In general, a gradient expanded exchange-correlation energy can be expressed as:

$$E_{xc}[\rho(\underline{r})] = \int \varepsilon_{xc}[\rho(\underline{r})]\rho(\underline{r})F_{xc}[\rho(\underline{r}), \nabla\rho(\underline{r}), \nabla^2\rho(\underline{r}), ...]d\underline{r} \qquad (3.43)$$

where F_{xc} is a factor that modifies the LDA functional to consider the variation of $\rho(\underline{r})$ at the reference point. Methods that include the gradient of the density in r are known as generalised gradient approximations (GGA), while functionals that contain second derivatives of $\rho(\underline{r})$ in r (and eventually a correction to the kinetic energy functional) are called meta-GGA. The dependence of $E_{xc}[\rho(\underline{r})]$ on the gradient (or higher) derivatives of $\rho(\underline{r})$ is done in a parametric way. GGA functionals are still local in a mathematical definition, and do not account for non-local effects at longer ranges.

Higher order expansions of (3.43) have been developed, but it was learnt that these expansions can easily violate some of the conditions required for the exchange and correlation holes (such as the negativity of the exchange density or the self interaction cancellation). It was Perdew[28] who showed that by including these conditions to functionals that originally did not, yielded an excellent improvement in the exchange energies. The definition of GGA functionals is not unique, and a very large number of GGA functionals have been proposed (often referred to as a functional zoo). These functionals differ both in the number of parameters they contain (of course, a large number of parameters increases the flexibility but may limit transferability) and how they are calculated.

In general terms GGA functionals have been obtained via two different methods: in one case the dependence of the functional on the gradient of the electronic density is performed via analytic functions, whose parameters are fitted to experimental data such as structural parameters, formation energies, thermochemical data etc. Clearly, in this case, the quality of results for classes of molecules or solids different to the reference data cannot be guaranteed. The second method is to determine the dependence of the functional on the gradient via some exact sum rules.

A widely used GGA exchange functional was developed by Becke in 1988[29]. Here he used the method of fitting parameters to experimental data. This is commonly used in conjunction with a correlation functional derived completely independently from the LDA in 1988 by Lee, Yang and Parr (LYP)[30]. Together these exchange and correlation functionals form the commonly used BLYP functional.

Another well known family of GGA functionals is that proposed by Perdew, in which the most used choice, at present, is the formulation proposed by Perdew, Burke and Ernzerhof[31] (PBE) in 1996. The PBE functional is very satisfactory from a theoretical point of view as it includes many of the conditions for the exchange-correlation hole sacrificing only those deemed energetically less important. It is a functional derived without containing any fitting parameters. During this PhD, only the LDA, BLYP and PBE functionals have been considered.

In general it has been found that the GGA's improve upon binding and atomic energies and bond lengths and angles over the LDA. However the performance of these functionals varies depending on the materials under study. For example, semi-conductors are marginally better described within the LDA than in GGA, except for the binding energies. GGA's are known to not satisfy some asymptotic behaviour and therefore there is a limit in the accuracy that the GGA's can achieve. The main reason for this is that the non-locality of the exchange term is not fully taken into account. However, in systems with well localised electrons a problem known as the self-interaction error, discussed in more detail in section 3.3.3, plays a major part in limiting the accuracy of the functionals. Neither the LDA or GGA functionals compensate for the self-interaction error. This self-interaction error is a large limitation of DFT and one which we need to consider very carefully when choosing the appropriate method for the calculations performed during this PhD. Therefore, the self-interaction error is important to be understood and hence this problem is discussed in a separate section.

3.3.3 Limitations of DFT – the self interaction error

Much of the work to be performed in this PhD is aimed at the study of 'strongly correlated' materials displaying unusual electronic and magnetic properties. The problem in describing strongly correlated systems with standard DFT lies in the self-interaction. In a true system, each electron interacts with every other electron other than itself. In HF and DFT all electrons are described as having a Coulomb interaction with all others, but also with themselves, via the Hartree term. The Coulomb interaction of one electron with its own electron density is commonly referred to as "self-interaction".

This term has a non-local mathematical formulation. In HF theory this is corrected by the exchange term, which exactly cancels the spurious Coulomb self-interaction. However in DFT we have a correction via the exchange functional that doesn't exactly cancel the Coulomb interaction of each electron with its own charge density. This systematic error of DFT results in most cases in small qualitative errors in the solution; it does however have catastrophic consequences for systems with well localised electronic states. Such failure is linked to the functional form of the spurious self interaction term, which is proportional to:

$$\frac{\rho(r_1)\rho(r_2)}{r_{12}} \tag{3.44}$$

and scales as $1/r_{12}$.

When r_{12} is small (localised electrons) the error is large; in practice, the DFT energy is lowered by reducing r_{12} ie. by increasing electronic localisation. In strongly correlated systems, this change is often accompanied by a change of the ground electronic state from insulating to conducting, and large errors in the calculated electron density and energy. Obviously, the inability to estimate the correct ground electronic state for a class of systems is a serious drawback of DFT.

The self-interaction problem is tackled by a number of methods that try to introduce an orbital-independent, non-local term in the DFT equations, that eliminates the spurious self-interaction effects. One such method is given by hybrid HF/DFT functionals, where a fraction of HF exchange can be combined to the DFT to compensate for the spurious self-interaction, and is discussed in more detail in section 3.5. It should be noted that the exact amount of HF exchange to be included in the hybrid depends on the system of study and on the particular observables we aim to calculate. The effect this has on the ability to reproduce experimentally derived data is interesting to study and will be looked at during this work.

3.4 Wavefunctions vs Densities

The fundamental difference between HF and DFT is that DFT optimises (in a variational sense) the electron density, while HF optimises a wavefunction. To

determine a particular molecular property using DFT, we need to know how this property depends on the density. However, to determine the same property using a wavefunction we need to know the correct quantum mechanical operator. This leads to an advantage of HF over DFT as there are more well characterised operators then there are generic property functionals of the density.

Another of the main factors that could influence the choice of one method over the other lies in the computational efficiency of the two. If the number of basis functions used to represent the orbitals is N, DFT scales no worse than N^3. This is faster than HF theory by a factor of N and significantly better than other methods that, like DFT, include electron correlation[32]. With regards to correlation, DFT is clearly superior as correlation is not included at all in the HF method.

3.5 Hybrid DFT/HF Methods

Within strongly correlated systems we have discussed how the lack of self-interaction correction to the Hartree term is a limitation to the accuracy that can be achieved by LDA and GGA functionals. Only when an explicit orbital dependence is included in the DFT formulation can the electron self-interaction be corrected. This problem has been tackled via several methods such as the self-interaction corrected (SIC) LDA[33, 34], exact exchange (EXX)[35] functionals and the LDA+U[36] method. Hybrid density functionals are another way to correct the self-interaction error. Hybrid functionals make use of the HF theory, in which the self-interaction cancellation between Coulomb and exchange contributions is exact. Combining DFT and HF formulations of the exchange forces provides a method of reducing the extent of the self-interaction error. For the work carried out in this PhD, it is this HF-DFT method that we make use of. The advantage of this method lies in its convenience. As the one electron forms of HF and DFT in the Kohn-Sham formulism (3.40) hold the same shape, it is straightforward to combine the two. This way we are taking advantage of computational tools that are already in place, although hybrid exchange cannot be justified on first-principles, and needs an empirical treatment.

The first hybrid exchange functional was introduced by Becke who made use of the adiabatic connection formula to show how to continuously transform the HF into the DFT formulation of the exchange functional. The exchange and correlation functional in hybrid exchange methods can be generally written as:

$$E_{xc}^{hyb} = \alpha E_x^{HF} + (1-\alpha)E_x^{DFT} + E_c^{DFT} \tag{3.45}$$

Here the parameter α is varied in order to achieve the most accurate result for a given system or observable. The first hybrid exchange formulations are the Becke half and half functional where α=0.5[37], and the three-parameter B3LYP functional[38] (that was actually first derived as B3PW, but transferred from the PW to the LYP correlation functional without changes). The parameters of B3LYP, including α, have been fitted to structure and thermochemistry of molecular databases. Attempts to define α from first principles also exist, such as the PBE0 hybrid exchange proposed by Perdew.

Inclusion of the HF exchange in order to accomplish, to some extent, self-interaction correction into the DFT formalism has reportedly achieved a noticeable improvement in results over standard DFT. While hybrid exchange functionals are now accepted as the best performing DFT choice for molecules, the situation is still less clearly defined for solids. A first systematic attempt at assessing the performance of hybrid DFT for solids is described by Cora et al.[39]. In this extensive review, the properties of hybrid exchange functionals in describing crystalline solids was presented, with a particular emphasis on transition metal compounds. A consistent study of the structural and electronic properties of several compounds was performed for a range of HF-DFT hybridisation steps. Clear trends were found in these properties with the most important being that the inclusion of HF exchange increases the degree of electronic localisation in the solution. This causes a systematic increase in the ionicity of the materials, a systematic decrease of the lattice parameter and increase of the elastic constants and bulk moduli. The important result was that whenever HF and standard (LDA/GGA) DFT functionals yield systematic errors with opposite sign with respect to experiment, “the formulation of hybrid functionals improves the accuracy of the calculations”. This is the case for band gaps, magnetic coupling constants, phonon spectra and all properties that depend on the extent of electronic localisation at perfect or defective lattice sites. It was found that this was particularly important at lattice defects that break

the translational symmetry of the crystal as, in this case, non orbital-dependant DFT functionals appear unable to localise the defect states. This is true of even simple matrices as MgO. Importantly it was also found that the best percentage of HF exchange included in the formulation differs depending on a combination of the system and property under investigation. High weights of HF exchange always ensured convergence of the solution to the correct ground electronic state which was not always true of low HF components (<20% HF exchange). Generally the optimum weight of HF exchange for a solid-state specific hybrid functional is higher than the 20% optimised in the B3LYP formulation for molecular species and much closer to Becke's half and half hybrid with 50% HF exchange.

The hybrid HF-DFT functionals are now the most accurate available[40], they are the method of choice for quantum mechanical calculations in particular in strongly correlated systems. In this thesis work we shall build on results presented in ref.[39], to consider new solids and observables of practical interest.

Chapter 4 - Basis Sets

In the description of the Quantum Mechanical methods given in Chapter 3, a difficulty has been neglected. To solve the Hartree Fock or Kohn-Sham equations in practice, we must produce a mathematical representation of the one electron orbitals. This is accomplished via the definition of basis functions, $\theta_j(r)$, that describe real space. The ensemble of function θ_j chosen is called a basis set. The HF or KS orbitals can be written generically as a linear combination of these basis functions:

$$\phi_i(r) = \sum_{j=1}^{M} c_{ji}\theta_j(r) \tag{4.1}$$

Here there is a sum running over all basis functions up to the size of the basis set, M, and c_{ji} are the expansion coefficients of the i^{th} orbital. To obtain the exact electronic wavefunction it would require a complete basis set; in practice an infinite number of basis functions, which is not computationally possible. Therefore, a suitable choice of finite basis set needs to be used. There are several forms of basis set of which the most commonly used to study solids are planewaves and Gaussian-type orbitals, described in the following subsections.

4.1 Plane Wave Basis Sets

In a periodic system there are an infinite number of electrons; by using Bloch's theorem we can treat this infinite system of electrons as a system of periodically repeated unit cells where equivalent electrons in neighbouring cells are related to one another by a phase factor.

$$\Psi_{j,k}(\underline{r}) = u_j(\underline{r})e^{i\underline{k}.\underline{r}} \tag{4.2}$$

where

$$u_j(\underline{r}+1) = u_j(\underline{r}) \tag{4.3}$$

$\underline{k}$ is a wavevector confined to the first Brillouin Zone and $u_j(\underline{r})$ is a periodic function which describes the periodicity of the potential (in this case the periodicity of the crystal lattice). It is clear from equation (4.2) that a suitable choice of basis set is formed by plane waves $e^{i\underline{k}.\underline{r}}$, which directly satisfy Bloch's theorem, and have the added advantage of being orthonormal, making the calculation of integrals required in the Schrödinger or Kohn-Sham equations trivial.

In general, any function in real space can be written as the Fourier transform of a function in reciprocal space. Due to the periodicity of $u_k(\underline{r})$ there are two implications. First, the vectors of this Fourier transform are restricted precisely to the reciprocal lattice vectors, $\underline{G}$. Secondly, the Fourier transform becomes a Fourier series[41]. The wavefunctions for the different eigenstates, j, can be written as:

$$\phi_{j,k}(\underline{r}) = e^{i\underline{k}.r}\sum_{G} c_{j,k} + \underline{G}e^{i(\underline{k}+\underline{G}).\underline{r}} \tag{4.4}$$

In theory one requires an infinite number of k-points, but in practice the values of the wavefunction at two points in reciprocal space are identical if sufficiently close. One can then therefore calculate the wavefunction using a finite number of k-points. Furthermore, a free electron with wavevector ($\underline{k}$+$\underline{G}$) has energy:

$$E_c = \frac{h^2(\underline{k}+\underline{G})^2}{8m\pi^2} \tag{4.5}$$

This means that the size of a basis set formed by plane waves can be defined by just one parameter, the cutoff energy. The advantage over other forms of basis set is that the size can be adjusted via just one parameter. The truncation of the basis set will ultimately lead to an error in the computed physical quantities but the advantage is that this error can be decreased by just increasing the cutoff energy. In other forms of basis sets where the basis functions are not orthogonal, such as with Gaussians, increasing the number of basis functions can lead to over completeness.

The problem with Plane Waves is that they are solutions to the Schrödinger equation in the presence of a constant potential. Close to the atomic nuclei the external potential is far from constant and cannot be described by a single Plane Wave. Therefore a large number of Plane Waves must be used to describe these regions correctly. One solution to this issue is to describe the region with rapidly varying density around the nuclei with a Pseudopotential (see section 4.3).

4.2 Gaussian Basis Sets

In 1950 S.F. Boys[42] made a big step in making computational calculations more feasible with the introduction of Gaussian-type orbitals. Gaussians have the great advantage that all the three and four centre Coulomb integrals can be computed analytically. The Gaussian-type orbitals are of the form:

$$\theta_{ijk}(\underline{r}-\underline{r}_c) = (x-x_c)^i (y-y_c)^j (z-z_c)^k e^{-\alpha|\underline{r}-\underline{r}_c|^2} \qquad (4.6)$$

In this equation (x_c, y_c, z_c) are the Cartesian coordinates of the centre of the Gaussian at r_c, α is a positive exponent and i, j and k are non-negative integers. The numbers i, j and k determine the angular dependence of the Gaussian, they are related to the angular quantum number of the solutions of the H atom. When they sum to zero we have an s-type Gaussian, when they sum to one we have a p-type and when they sum to two we have a d-type Gaussian and so on. The biggest advantage of GTO's is that the product of two Gaussians at different centres is equivalent to a single Gaussian function centred at a point between the two. Therefore the two-electron integrals (necessary to compute both HF and DFT Hamiltonians) on three and four different atomic centres can be calculated analytically. One disadvantage of GTO's lies in the fact that they are not orthonormal, and may give rise to spurious effects, such as the one known as the basis set superposition error (BSSE)[43]. Two atoms in a spatial proximity will have overlapping basis functions, resulting in atoms "borrowing" basis functions from nearby atoms to describe their own electronic density, thus achieving a better variational description in molecules (or solids) than when isolated. Therefore, as a result of the

BSSE, the basis set quality will depend on the geometry of the system, which can be particularly problematic.

The Gaussian basis functions contain exponents α that can be optimised variationally; given a number of Gaussian functions, they can therefore be chosen to be of optimal form for the system under investigation. The basis sets with their optimised exponents can then be used for performing calculations. The simplest type of basis set is called a minimal basis set where one function is used to represent each of the occupied orbitals of a given atom. The problem with the minimal basis sets is that they are not flexible enough to describe molecules and solids where electrons participate in chemical bonding and become polarised. Therefore, we need extensive basis sets to achieve better accuracy. We can improve upon this situation in two ways; the first is by using double-zeta or triple-zeta basis sets. Here each basis function in the minimal basis set is replaced by two or three basis functions respectively. There is also a split-valence basis set which is a compromise between achieving a better accuracy than with a minimal basis set but also reducing the larger computational cost required with double and triple-zeta basis sets. This describes each valence atomic orbital by two basis functions while each inner-shell atomic orbital is represented by a single basis function. The second way of improving the basis set quality, known as adding polarisation functions, is to add Gaussians which describe orbitals which are unoccupied in the atom in order to provide an accurate description of polarisation.

The relative simplicity of the algebra of Gaussian functions makes them a favourite basis set; however, they are too smooth (they have zero derivative at the origin) in correspondence of the nuclei. The correct solutions for the H atoms, to which atomic orbitals make reference, are discontinuous at the nucleus where the wavefunction has a cusp. This situation is reproduced by an exponential decay, $e^{-\alpha r}$. A basis function of this form is referred to as a Slater type orbital. However, multi-centre integrals cannot be calculated analytically with Slater orbitals. A solution consists in combining Gaussian and Slater-type orbitals: for each AO, especially in the core region, we use not a single GTO, but a linear combination of GTO's, in such a way as to reproduce the nuclear cusp, but retaining the possibility of calculating integrals analytically. Such linear combinations of Gaussians are known as STO-nG, where n indicates the number of Gaussian-type orbitals combined linearly to reproduce one Slater-type orbital.

Another method is to use fixed linear combinations of primitive Gaussians, where the coefficients and exponents are optimised to reproduce the atomic ground state orbitals at a level of theory, such as HF. These are known as contracted Gaussian-type orbitals.
As the contraction coefficients are fixed, contraction basis functions are most useful to represent core orbitals. A large advantage of contracted Gaussian-type orbitals is that they count as a single basis function and hence the size of the Hamiltonian matrix is enormously reduced.

4.3 Pseudopotentials

Pseudopotentials were developed with the aim of keeping the simplicity of the plane wave approach but attempting to solve the problem of the non-constant potential close the nuclei. This was first tackled by considering the fact that most properties of crystals depend mostly on the valence electrons and very little on the core electrons. There is also very little overlap between their respective wavefunctions. We can therefore say that the distribution of the core electrons does not change if the atoms were moved to a different chemical environment. The most common pseudopotential approach is therefore one where the core electrons are assumed to be frozen and the core electron distribution of the isolated atom is kept in the crystal environment. Here we immediately have the useful advantages of having less eigenstates of the HF and KS equations to be calculated and less electrons have to be treated. This treatment also largely reduces the energy scale meaning that energy differences between atomic configurations are numerically more stable.
Pseudopotentials are therefore based on two observations; firstly, the core states are not crucial for describing chemical bonding and secondly, a good description of the wave functions inside the core region is not absolutely necessary. The idea of replacing the ionic core potential with a pseudopotential came into light. Here the nucleus is described together with its core electrons to simplify the approach.
Pseudopotentials can be employed with plane waves, but also with the Gaussian-type orbitals discussed previously.

Chapter 5 - Choice of Computational Code

In Chapter 3 we have seen that mathematical tools exist for solving the many-body problem. These have now been incorporated into several computational codes which allow the user to perform Quantum mechanical calculations on molecules, solids and surfaces. Some of these include WIEN2k[44], VASP[45-47] and GAMESS-UK[48]. In this PhD, the CRYSTAL06[49] code has been used, which has been developed primarily at the University of Torino and the Daresbury Laboratory. CRYSTAL06 is used to compute the electronic structure of periodic systems within Hartree Fock (HF) and Density Functional Theory (DFT). The code also allows the use of several exchange and correlation functionals as well as HF and DFT hybrid mixing. This code was chosen largely for this feature, as it is the platform that offers the most efficient implementation of hybrid exchange for systems described under periodic boundary conditions. This PhD has involved studying strongly correlated materials, and the implementation of hybrid HF to DFT mixing has been shown provide improved accuracy without greatly increasing computational cost. To date, most studies of the structural and electronic properties of perovskite materials have been performed using hybrid functionals built on the Becke exchange with the LYP correlation functional (the B3LYP case optimised for molecules being a special case of this series). In this work we studied the effect of using various 'user defined' hybrid functionals on the prediction of electronic and structural properties of copper containing perovskites.

CRYSTAL06 allows the use of many tools to assist in obtaining the required data from first principles calculations. Some of the tools which have been important and used throughout the calculations performed in this PhD are outlined in the following subsections.

5.1 Self-consistent mixing techniques

We have seen, in section 3.3.1, how the Kohn-Sham equations are solved self-consistently. However, one cannot simply take the output density after one cycle and put it directly into the next cycle. We can see this if we first denote the deviation from

the correct density at any cycle as δn. We can then say that the error in the output density to linear order in the error in the input, near the solution, is given by:

$$\delta n^{out} = n^{out} - n = (\tilde{\chi} + 1)(n^{in} - n) \tag{5.1}$$

where:

$$\tilde{\chi} + 1 = \frac{\delta n^{out}}{\delta n^{in}} = \frac{\delta n^{out}}{\delta v^{in}} \frac{\delta v^{in}}{\delta n^{in}} \tag{5.2}$$

The function, $\tilde{\chi}$, can be calculated. Clearly the best choice for the new density is one that would make the error zero[27]. If we know all parts of (5.1) then it can be solved to find the ground state density, n:

$$n = n_i^{in} - \tilde{\chi}^{-1}(n_i^{out} - n_i^{in}) \tag{5.3}$$

If (5.3) were exact we would arrive at the solution and the SCF cycle would stop, but it is not exact.

The CRYSTAL06 code allows the use of two different mixing techniques which have been used throughout this PhD, linear mixing and the Broydon method.

5.1.1 Linear Mixing

The simplest approach to calculating the best fraction of the output density to put back in for the next cycle, is known as linear mixing. This expression enables the calculation of an improved density to put back in as n_{i+1}^{in} at cycle $i+1$:

$$n_{i+1}^{in} = \alpha n_i^{out} + (1-\alpha) n_i^{in} = n_i^{in} + \alpha(n_i^{out} - n_i^{in}) \tag{5.4}$$

which only works if α<1.

5.1.2 Broyden Mixing

There are several iterative methods currently available to improve SCF convergence. One of the most sophisticated methods developed is Broyden's quasi-Newton-Rhapson method[50, 51]. The main advantage of this technique is that the self-consistent procedure is generally completed with far fewer iterations than that achieved with linear mixing. Here, at each iteration i, the input density for the next cycle is given by an equation analogous to (5.3) except that $\tilde{\chi}$ is replaced by the approximate Jacobian:

$$n_{i+1}^{in} = n_i^{in} - J_i^{-1}(n_i^{out} - n_i^{in}) \qquad (5.5)$$

The Jacobian is determined using the secant equation (finite difference equation); see reference [52] for further information.

Since then Srivastava[53] improved upon this by deriving a method that avoids NxN matrix storage issues as well as multiplications. With this method only m vectors of length N are required where m is the number of iterations. Although this method proved successful it does have one drawback, as it not only allows the current iteration to update the inverse Jacobian, but it can also override information from previous iterations arbitrarily with information from the current iteration. Vanderbilt and Louie[54] created a modified version of Broyden's method in which information from all previous cycles is included. This method showed improvements over the standard Broyden method but does not address the problem of NxN matrices. It was Johnson[55] who modified this method to eliminate the problem of the large NxN matrices to obtain a similar computational scheme to Srivistana. Here the advantages of both the methods are incorporated into one. Figure 5.1 shows a comparison of the linear mixing and Broyden methods in converging on energy. In this case we can see how the Broyden method approaches the convergence energy difference much faster than the smoother linear mixing approach (using Broyden the convergence criteria is satisfied in under 70 cycles where the linear mixing method needs more than 600 iterations).

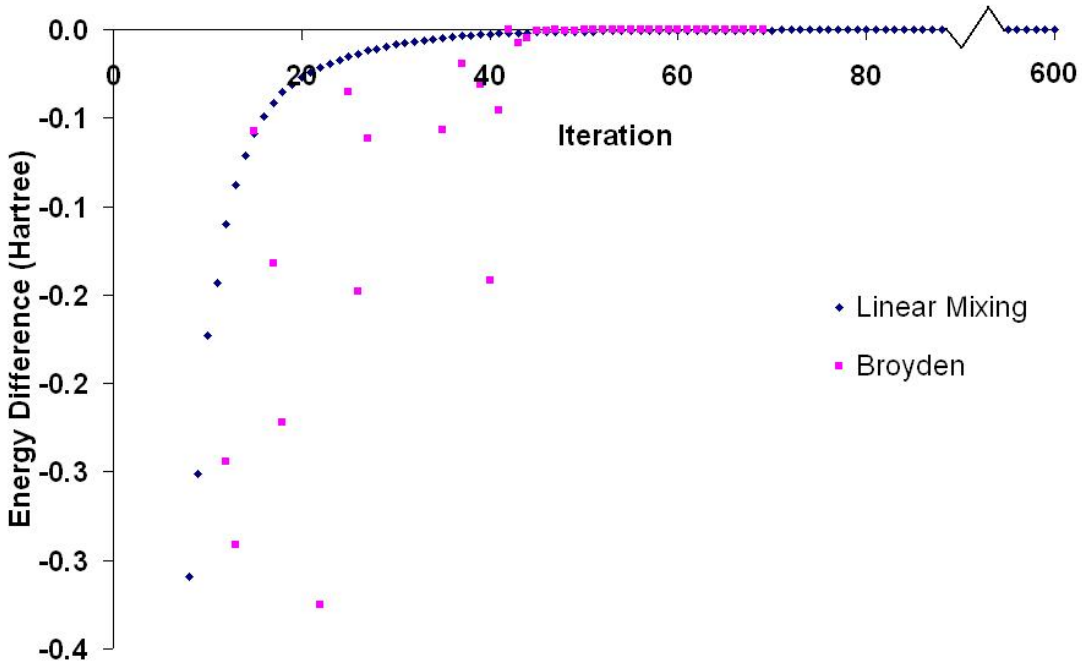

Figure 5.1 Convergence on energy using the Broyden and linear mixing methods under the same convergence criteria. This is an example from one of our calculations on $CoSeO_3$.

5.2 Analysis of the Electronic Density

Much information can be gained from the electronic wavefunction resulting from a calculation performed using CRYSTAL06. In particular, the density of states and Mulliken charges have been of interest during this work. These are outlined below.

5.2.1 Population Analysis

One of the possible ways in which the electronic wavefunction can be analysed is to calculate a population analysis. This is beneficial as the derivation of the atomic charges allows a simple description of the bonding in the system examined. Various methods have been developed to perform such analysis. In general we can distinguish two types of charges, static and dynamic.

The static charges are usually based on the partitioning of the ground state electronic density in contributions attributed to the various atoms. While for an isolated atom the charge is a well defined concept, it is not the same for a polyatomic system, where the result obtained depends on the arbitrary choice made during the attribution of an electron to a certain atom.

On the contrary, the dynamic charges are directly connected to the change of polarization resulting from an atomic displacement. As this change of polarization is in theory measurable in experiments (ie. in infrared spectroscopy intensities), a dynamic charge is easily interpretable.

During this PhD we have been interested in static charges for which we have used the method known as the Mulliken population analysis.

5.2.2 Density of States

It can be frequently useful to obtain information regarding the density of states (DOS) of a given system. The DOS describes the number of states at each energy level that are available to be occupied. It can be given as unit energy, E, or per unit volume, Ω.

$$\rho(E) = \frac{1}{N_k} \sum_{i,\underline{k}} \delta(\varepsilon_{i,\underline{k}} - E) = \frac{\Omega_{cell}}{(2\pi)^d} \int_{BZ} d\underline{k} \delta(\varepsilon_{i,\underline{k}} - E) \qquad (5.6)$$

In (5.6) $\varepsilon_{i,\underline{k}}$ is the energy of an electron (or phonon). (5.6) is the number of independent particle states per unit energy.

The DOS can be combined with the Mulliken population analysis to yield contributions from single atoms (or orbitals) to the energy states in a given interval; this is known as projected DOS or p-DOS.

5.2.2.1 Mulliken Charges

This method of population analysis was developed in 1955 by Mulliken[56] and can be readily applied to calculations employing local basis sets, such as STO's and GTO's.

This analysis provides the total effective number of electrons in each atomic orbital and thus the values for the effective charge on each atom. This is done by calculating the atomic charge in each element of the density matrix P_{ij} and dividing it equally among the two atomic orbitals involved i and j. The electronic charge in each atom is then the sum of the contributions from all the atomic orbitals of its basis set. Let us see how this is done in practice.

First, the electrons are divided up amongst the atoms according to the degree to which different atomic orbital basis functions contribute to the overall wavefunction[32]. If we write the total number of electrons, N, as:

$$N = \sum_j \psi_j(\underline{r})\psi_j(\underline{r})d\underline{r} \tag{5.7}$$

and use the expansion of ψ_j in terms of atomic orbitals defined in Chapter 4 - we obtain:

$$\begin{aligned} N &= \sum_j \sum_{r,s} c_{jr}\phi_j(\underline{r})c_{js}\phi_s(\underline{r})d\underline{r} \\ &= \sum_j \left(\sum_r c_{jr}^2 + \sum_{r \neq s} c_{jr}c_{js}S_{rs} \right) \end{aligned} \tag{5.8}$$

In (5.8) r and s index basis function ϕ, and S is the overlap matrix derived in section 3.2; c_{jr} is the coefficient of basis function r in the molecular orbital j. Mulliken suggested that the electrons associated with the single basis functions in (5.8) belong only to the atom relevant to that basis function. Electrons shared between basis functions are placed equally on the two atoms corresponding to r and s. If we also divide the basis functions up over atoms, k, we can calculate the atomic population, N_k via:

$$N_k = \sum_{j \in k} \left(\sum_{r \in k} c_{jr}^2 + \sum_{r \in k, s \in k} c_{jr}c_{js}S_{rs} \right) \tag{5.9}$$

Consequently we can then define the Mulliken partial atomic charge:

$$q_k = Z_k - N_k \tag{5.10}$$

where Z is the nuclear charge.

This method is obviously just an approximation and hence has shortcomings. Firstly, we have assumed that each basis function can be associated with an atomic centre. Therefore if we use basis functions that are not centred on the nuclei it is not applicable. Secondly, the Mulliken method is heavily basis set dependent, but provides useful qualitative information on bonding in the system studied.

Chapter 6 - Perovskites

A perovskite is any material with the same crystal structure as that of the natural mineral, calcium titanium oxide ($CaTiO_3$), originally found in the ural mountains of Russia in 1839 by Gustav Rose. This mineral was named after the Russian mineralogist, L. A. Perovski.

Perovskites have the general formula ABZ_3, where A and B are cations of different sizes (A larger than B) and Z is the anion. The B ions can be 3d, 4d or 5d transition metal ions taking an octahedral coordination. The perovskite structure is displayed by many oxides, several of which have technological applications. The properties required for such applications are strongly dependent on the coordination and connectivity of ions in the perovskite structure, making it important to be well understood.

6.1 Structure and Distortions

In this section we first discuss the ideal perovskite structure, before moving on to look at deviations from the ideal form and the reasons behind these structural distortions. Distortions within the perovskite structure reduce the symmetry, which is essential for producing the interesting magnetic and electric properties observed in eg. the ferroelectric tetragonal form of $BaTiO_3$[57]. There are many reviews of perovskites, with examples being found in the following references [58-62]. In this chapter we describe a sample of the literature on perovskites with the aim of highlighting some of the most interesting and relevant work to set out the context of this PhD and assist with the understanding of the following chapters.

The ideal perovskite structure crystallises with cubic symmetry in the Pm3m space group. The A cation in the perovskite structure is 12-coordinated and the B cation is 6-coordinated. The structure can be looked at as being a network of corner shared BZ_6 octahedra where all B-Z-B angles are 180^o. However, it is common to have deviations from the ideal structure and stoichometry. In fact the ideal perovskite structure is quite rare and even the mineral perovskite itself has some distortion. The idealised perovskite

cubic structure is typified not by $CaTiO_3$ but by $SrTiO_3$ (space group Pm3m, a=3.905Å). This is displayed below in Figure 6.1. In $SrTiO_3$, Sr^{2+} occupies the A site in 12 fold coordination and Ti^{4+} ions are on the B site forming a 3D corner sharing network of TiO_6 octahedra.

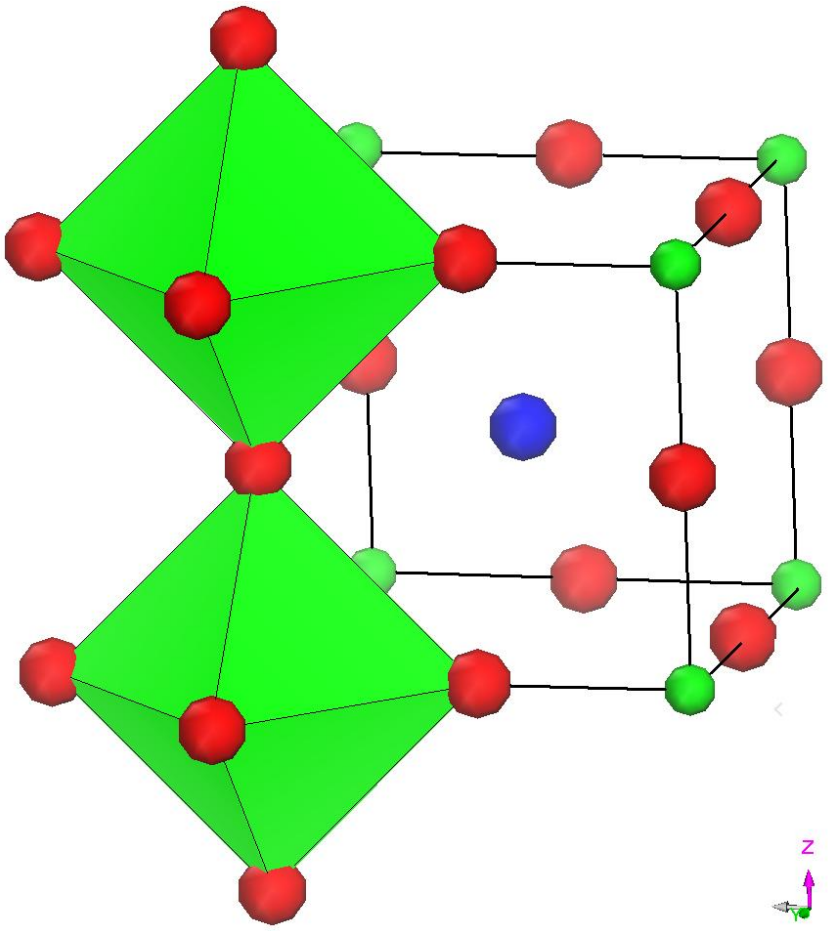

Figure 6.1 Ideal cubic structure of the perovskite $SrTiO_3$. The corner sharing TiO_6 octahedra is visible as are the Sr^{2+} ions in twelve fold coordination, shown in blue.

The anion, Z in the perovskite structure is often oxygen, but perovskites containing other anions such as F^-, Cl^- or S^{2-} are also known.

Partial occupation of the A or B site is also a possibility. For example, partial occupation of the A site is realised in the cubic tungsten bronzes A_xWO_3 (A=alkali metal, $0.3 \leq x \leq 0.93$). This is discussed later.

As mentioned earlier, it is common to observe perovskites which display deviations from the ideal structure. There are several factors that can drive distortions in the perovskite lattice which we shall now discuss. Firstly, the deviation can be rationalised

by size effects. In this case structural distortions are dictated by the ratio of A and B ionic sizes, and electronic configuration of the metal ions. Two main distortion types are observed, one linked with the off-centering of the B ions in the BZ_6 octahedra, the other with tilting of the BZ_6 octahedra in the structure. If we first consider the ideal cubic case, the lattice parameter a_0 is related to the ionic radii, R_A, R_B and R_0 by the following equation:

$$a_0 = \sqrt{2}(R_A + R_0) = 2(R_B + R_0) \tag{4.1}$$

This allows us to define the Goldschmidt tolerance factor, t, as:

$$t = (R_A + R_0)/\sqrt{2}(R_B + R_0) \tag{4.2}$$

which rationalises the distortion. Cases with $t < 1$ give rise to tilting modes, while materials with $t > 1$ show B off centering modes. The ideal cubic phase requires t=1.
The ideal perovskite $SrTiO_3$ has a tolerance factor very close to the ideal value of 1 which explains its stability in the cubic phase. Another example of a perovskite with t=1 is $KFeF_3$. Examples of perovskites with t<1 include $CaTiO_3$, $GdFeO_3$ (t=0.81) and $SrZrS_3$. This occurs due to a smaller than ideal A cation, which causes a tilting of the BZ_6 octahedra. Such a distortion leads to a closing up of the dodecahedral interstices. The A cation may also relax towards a side of the dodecahedral interstice to further reduce the AZ equilibrium bond distance. Examples of perovskites with a tolerance factor >1 include instead $BaZrO_3$, $BaNiO_3$ and $CsGeCl_3$ where t=1.04, 1.13 and 1.03 respectively. This situation is achieved by combining a large A and small B ion, which leads to a contraction of the BZ_6 octahedra. In this case hexagonal variants of the perovskite structure are also stable, which include some degree of face sharing between BZ_6 octahedra leading to the formation of cavities where the A ions fit better. $BaNiO_3$ can be said to be of ideal hexagonal type with only hexagonal stacking of the close packed layers. However, many perovskites exist with different sequences of hexagonal and cubic close packed layers.

It should be noted here that the tolerance factor equation assumes purely ionic bonding. As perovskites are not truly ionic, the tolerance factor serves only as an estimate.

Symmetry lowering distortions in perovskites may also be dictated by electronic effects, such as Jahn-Teller distortions of open shell transition metal ions. Perovkites containing ions with an odd number of electrons in the e_g orbitals for instance will experience this effect, including high spin d^4 Mn^{3+} and Fe^{4+} and d^9 ions eg. Ni^{3+} and also Cu^{2+}. Structural distortions driven by Jahn-Teller active ions at the B site are known for several perovskites; an example is $AMnO_3$ (where A=Ln, Pr and Nb). Here, Mn^{3+} ions with high-spin $3d^4$ configuration are subject to a Jahn-Teller distortion that causes an axial elongation of the MnO_6 octahedra. An extreme case of Jahn-Teller distortion is given by d^9 ions such as Cu^{2+}. Cu^{2+} are rare in perovskite materials, though examples exist such as $CaCu_3Ti_4O_{12}$ (CCTO) and $CuSeO_3$ (which are of central interest to this thesis) where the strong stability of the Cu^{2+} in square planar coordination drives the structural distortion. In CCTO the Cu^{2+} ions occupy the 12 coordinated sites and drive a tilting of the TiO_6 octahedra to achieve this coordination environment. In $CuSeO_3$, instead, Cu^{2+} is in the octahedral sites, and originates a Jahn-Teller distortion of the CuO_6 octahedra. We can also observe distortions of perovskites containing either a d^0 transition metal (Ti^{4+}, Nb^{5+}, W^{6+} etc.) or a lone pair cation (with a polarisable s^2 outer valence shell occupied, such as Pb^{2+}, Bi^{3+}, Sn^{2+}, Se^{4+}, Te^{4+} etc.) where the distortion has been attributed to second order Jahn-Teller effects[63-69]. For octahedrally coordinated d^0 transition metals, the empty d orbitals of the metal mix with the filled p orbitals of the ligands upon off centering of the metal in its coordination octahedron. In the case of lone pair cations it is believed that the interaction of the s and p-orbitals of the metal cation with the oxide anions is critical for lone-pair formation[70-75]. This has an important consequence on the structure as the lone pair pushes the cation off-centre in the 12 coordinated sites, generating an electric dipole in the structure. An example of the latter distortion is observed in $CuSeO_3$ where the lone pair of the SeO_3^{2-} ions creates SeO_3 trigonal pyramidal units. The distortion observed in $CuSeO_3$ is thus due to a combination of the lone pair chemistry of Se^{4+} and the stability of Cu^{2+} in square planar environment.

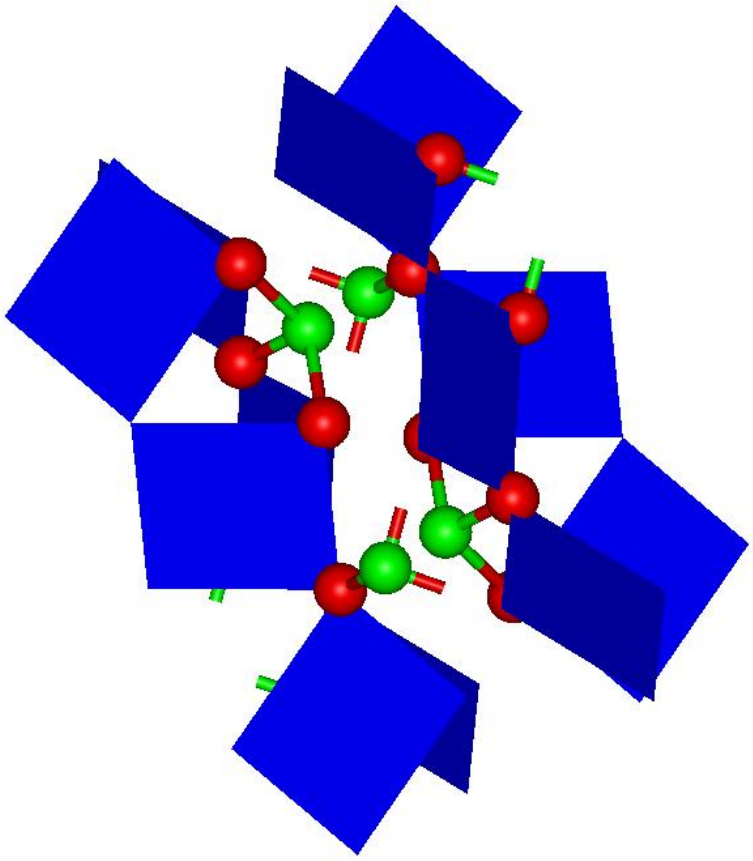

Figure 6.2 The unit cell of $CuSeO_3$, displaying the square planar coordination of Cu^{2+} (blue) and the SeO_3 trigonal pyramidal units (oxygen in red and selenium in green).

Another factor that can cause distortions in perovskites involves changing the composition from the ideal ABZ_3. Possibilities for this lie in anion or cation deficiencies. Examples of A ion deficient materials are common in the family of bronzes, obtained by partial intercalation of alkali metal or other very electropositive ions (A) in the empty dodecahedral interstices of group 6 trioxides (WO_3 and β-MoO_3). The bronzes have the composition A_xBO_3. An interesting example of these is Na_xWO_3 as by increasing x, and hence the fraction of W reduced to 5+ oxidation state, leads to an increased conductivity. Conductivity, in the W bronze, Na_xWO_3 is controlled by the single parameter, x[76], which is a simple example of how the electronic properties of perovskites can be controlled by chemical modification. An example of Z deficient perovskite can be found in $SrFeO_{3-x}$[77, 78] which is often substoichiometric due to the presence of O vacancies. Anion vacancies can in general be achieved by doping with low valent ions, partial reduction of the transition metal or by heating a sample in a

reducing environment. It has been shown that the oxygen content in $SrFeO_{3-x}$ varies between 2.5 and 3 (ie. x ranges between 0 and 0.5); x also corresponds to the fraction of Fe ions in 3+ oxidation state. At high values of x the oxygen vacancies order so that FeO_5 pyramids are formed. The $SrFeO_{3-x}$ compounds are examples of defect perovskites important for oxygen ion conduction since the process of vacancy hopping is the most common mechanism for this property.

Because the perovskite structure is very common among transition metal compounds, it is relatively easy to form solid solutions in which either (or both) the cation positions are occupied by 2 or more types of ions. Such solid solutions can be disordered, for instance in a number of compounds with interesting dielectric properties such as PZT ($PbZr_{1-x}Ti_xO_3$) and PMN ($PbMg_{1/3}Nb_{2/3}O_3$)[79] or ordered. The latter case is found in the class of double perovskites, $A_2BB'Z_6$ that contain stoichiometric amounts of the two B ions which are strictly alternating in the octahedral sites, with examples such as Sr_2FeMoO_6[80] and Bi_2MnNiO_6 or K_2NeAlF_6. Ordered solid solutions at the A site are also known, with a relevant example being CCTO. Here the A sites are occupied by ¼ Ca and ¾ Cu ions in long-range ordered alternation. In CCTO it is possible for the octahedra to tilt in such a way that there exists a square planar coordination for three quarters of the A cations explaining the observed stability of the 3:1 ratio of Cu^{2+} and Ca^{2+} ions. In this case the Cu atoms are four coordinated with the O atoms and a square is formed with a Cu atom at the centre. To produce the square planar A sites a large tilt is needed; in CCTO the Ti-O-Ti angles are reduced from the ideal180^o to 141^o.

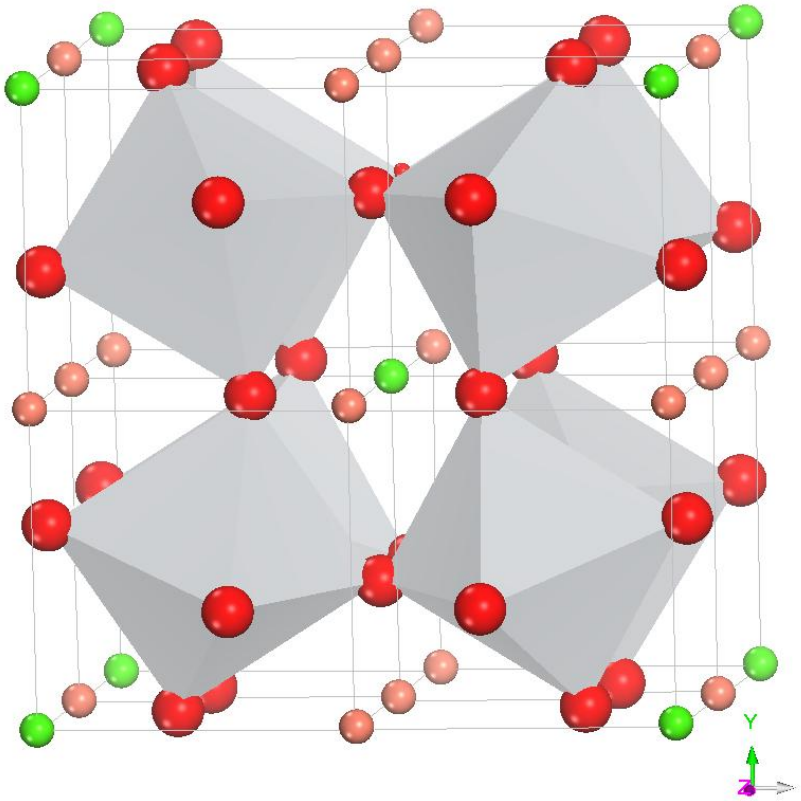

Figure 6.3 Perovskite structure of CCTO showing the tilting of the octahedra. The Calcium and Copper atoms in green and pink sit on the A and A' sites respectively. The Titanium atoms are on the B site in grey (in the middle of the octahedral) and the Oxygens atoms occupy the Z sites in red.

6.2 Properties of Perovskites

We have seen how the variations in structure in terms of defects and distortions combined with the perovskites ability to accommodate nearly every element of the periodic table can give rise to a great variety of structures. In turn many exhibit some interesting and often unique properties, that can be modified by any of the structural distortions or chemical modifications discussed in section 6.1 above.

6.2.1 Dielectric Properties

The dielectric properties of perovskites have been studied in detail since the discovery that perovskites such as $BaTiO_3$ and $PbTiO_3$[81] possess unusually high dielectric constants. This feature is desired for, amongst other things, capacitative components in

microelectronics. The high dielectric constant of $PbTiO_3$ and $BaTiO_3$ is based on collective polar displacements of the metal ions (on the B site of the perovskite) with respect to the oxygen sublattice and hence is linked to ferroelectricity.

Another group of perovskite-structured materials which exhibit large dielectric constants of practical interest are known as relaxor ferroelectrics. These are examples of disordered solid solutions, such as $PbZn_{1/3}Nb_{2/3}O_{3-x}PbTiO_3$[82] and $PbMg_{1/3}Nb_{2/3}O_{3-x}PbTiO_3$ (PMN), which not only show large dielectric constants but also a pronounced frequency dispersion and a variation of the dielectric constant as a function of temperature.

Giant dielectric constant materials have now found great importance for use in device implementation eg. as metal-oxide semi-conducting field effect transistors (MOSFET's). In such cases the dielectric constant will ultimately determine the miniaturisation of such components. It is the perovskite $CaCu_3Ti_4O_{12}$[83] that currently displays the largest known dielectric constant of $\sim 10^4$-10^5[84-86]. The mechanism behind this property is not yet clear, with a barrier layer capacitor model being one of the possible origins claimed in the literature. Another example is the Li-ion conductor compound $La_{0.67}Li_{0.25}Ti_{0.75}Al_{0.25}O_3$[87].

6.2.2 Ferroelectricity, Ferromagnetism and Multifeorroicity

A ferroelectric crystal exhibits a spontaneous electrical polarisation that can be switched by the application of an electric field. Such behaviour is observed in $BaTiO_3$, $SrTiO_3$[88] and $KNbO_3$[89] as well as other perovskites. In the case of $BaTiO_3$, this behaviour can be attributed to the t>1 factor (t=1.06). which means that the Ti^{4+} ion is slightly too small for the octahedral void of the structure, and can rattle in the octahedral interstice. Neighbouring Ti^{4+} ions will undergo similar displacements resulting in the formation of a net dipole and a macroscopic polarisation if the ferroelectric state is long range ordered. Ferroelectric materials have two stable minima where the macroscopic polarisation is in opposite directions which can be switched via the application of external electric fields. These two states can be denoted 0 or 1 which recalls the Boolean algebra based on the binary arithmetics on which computers are built. A single bit of memory can be based on a 0 or a 1 and hence ferroelectric materials find use in memory

devices[90]. The study of these materials has increased rapidly over the last decade due to the realisation that such phenomenon can be hugely beneficial for device implementation. Other than in memory devices such applications include tranducers (due to their piezoelectricity) and capacitors (due to their high dielectric permittivity)[12].

A ferromagnetic crystal exhibits instead a spontaneous magnetisation, which arises through the presence of open shell transition metal ions with with parallel spin polarisation, and can be switched by the application of a magnetic field. Similarly to materials displaying ferroelectric behaviour, ferromagnetic materials have received attention over the last decade due to their potential use in technological applications. This behaviour has been observed in several perovskites, including $CuSeO_3$. As well as displaying ferroelectric behaviour, $BiMnO_3$ has also been confirmed to be ferromagnetic in the same phase. Such a material is described as being multiferroic. Nickel iodine boracite $Ni_3B_7O_{13}I$ was the first ferromagnetic ferroelectric material to be discovered[91]. This was followed by a synthesis of several more multiferroic boracite compounds.

Multiferroic magnetoelectrics are extremely rare. An explanation for this lies in the fact that, in general, the transition d metal ions (which are essential for magnetism) reduce the tendency for off-centre ferroelectric distortion. Therefore, an additional structural or electronic driving force must be present for ferroelectricity and ferromagnetism to exist simultaneously[12]. Magnetoelectric Multiferroics are heavily sought after as these combined properties open up a whole new set of possibilities for technological application. As well as being a ferromagnet, $CuSeO_3$ has also been claimed to display ferroelectricity, and hence is classed as a multiferroic[92].

6.2.3 Semi-Conductivity, Conductivity and High T Superconductivity

Many perovskites exist that exhibit a range of interesting and useful conducting properties. For example $KNbO_3$ exhibits semi-conducting properties. Many perovskites have been found to display conducting properties which can be rationalised by examining the electronic configuration of the B ion. eg. $SrTiO_3$ with d^0 Ti^{4+} ions is insulating since it does not have any electrons in the conduction band. On the other

hand $LaNiO_3$ with the d^7 Ni^{3+} and $LaCuO_3$ with d^8 Cu^{3+} are both conductors. A particularly interesting example is $LaCoO_3$ where the d^6 configuration will cause a split in the conduction band between the filled t_{2g} and the e_g orbital leading to an insulator at the ground state.

High temperature superconductivity presents a fascinating area of perovskite research since the discovery, decades ago, that some pervoskites exhibit superconductivity at high temperatures (high T_c). In fact the structure of high T_c cuprates contain perovskite structured sub-units which are responsible for the electronic properties.

The first discovered high T_c was the perovskite-related material $La_{2-x}Ba_xCuO_4$[93].

The perovskite structure is clearly common to a range of multifunctional materials of which a few representative examples are summarised in Table 6.1.

Table 6.1 Examples Perovskites exhibiting some of the many intereting physical properties available to the structure. The table includes some potential practical applications of such materials.

Structure	Physical Property	Possible/Actual Application
$PbZe_{1-x}Ti_xO_3$	Piezoelectric	Ultrasound
$CaCu_3Ti_4O_{12}$	Dielectric	Resonators
$Pg_3MgNb_2O_9$	Dielectric	Capacitors
$BaTiO_3$	Ferroelectric	Computer Memory
$SeCuO_3$	MultiFerroic	Memory Devices
$Ba_{1-x}La_xTiO_3$	Semi-Conductor	Transistors
$Y_{0.33}Ba_{0.67}CuO_{3-x}$	Superconductor	Medical Imaging
$SrTiO_3$	Insulator	Microelectronics
$BaInO_{2.5}$	Ionic Conductor	Electrolyte in Solid Oxide Fuel Cells
$Ba_2MgTa_2O_9$	Highest Melting Point	Space Craft

Chapter 7 - $AA_3'B_4Z_{12}$ Type Perovskites

7.1 $Cu_3CaTi_4O_{12}$ (CCTO)

The main aim of modern microelectronics has been to deliver increasingly smaller, faster and cheaper devices. These devices are made from semiconductors using a process known as photolithography, a process used in microfabrication to selectively remove parts of a thin film or the bulk of a substrate by using light to transfer a geometric pattern from a photomask to a light-sensitive chemical on the substrate. The semi-conductor industry as a whole has relied on the continuous improvement in circuit performance. For this to happen, the components of these circuits have had to achieve a continuous reduction in size. In particular it has been decrease in the size of the key component, the metal oxide semi-conductor field effect transistor (MOSFET) which has enabled the use of more transistors on a given chip and hence increased power and speeds[94]. A MOSFET consists of two semi-conducting parts separated by a dielectric insulator (or gate dielectric). There are more complex designs, but for the purposes of this chapter the simple schematic displayed below adequately describes the MOSFET design.

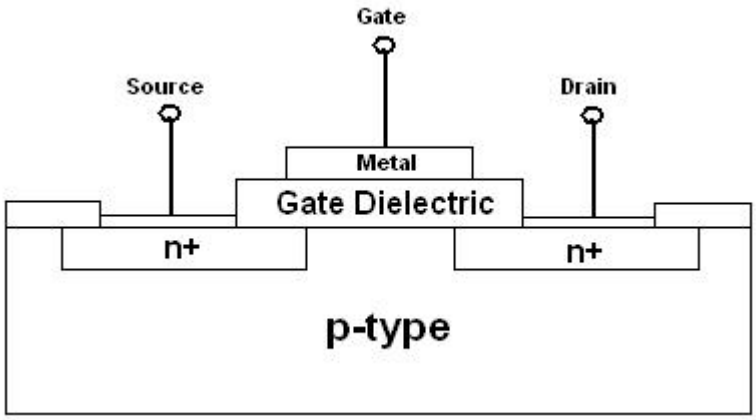

Figure 7.1 Pictorial representation of an N-channel MOSFET. The gate dielectric is located below the metal gate contact.

The gate dielectric material that has allowed the success in miniaturisation so far has been silicon dioxide, SiO_2. The transistors have decreased in size owing to the reduction in thickness of the silicon dioxide gate down to about 1.5nm. A limitation to this reduction has now been reached in the form of leakage current flowing through the structure of the metal-oxide semiconductor via a quantum mechanical tunnelling mechanism[95, 96]. Furthermore, it has been shown that the tunnelling probability increases exponentially as the thickness of the silicon dioxide is reduced[97]. This material has therefore run its course as the material of choice for capacitive componentry. In order to decide on the best way forward it is best to start by looking at the capacitance of a parallel plate capacitor (the gate oxide in a MOSFET can be modelled as such). The capacitance, C, is given by:

$$C = \frac{k\varepsilon_0 A}{t} \tag{7.1}$$

where ε_0 is the permittivity of free space (a constant), A is the capacitor area, k is the relative dielectric constant of the material used (eg. silicon dioxide) and t is the thickness of the capacitor oxide insulator. As we have now reached a limit for reducing t, another way to increase the capacitance is to use a material with a higher k value. For this reason there have been many recent efforts in investigating potential high-k gate dielectrics. As a number of oxides with the perovskite structure are known for their remarkable ability to exhibit high dielectric constants, these have been heavily targeted as new gate dielectric materials. However, dielectric constants higher than 1000 are mostly associated with field induced phase transitions at morphotropic phase boundaries, and the magnitude of k displays a peak as a function of environmental conditions such as temperature, which is clearly not ideal for most applications.

The perovskite-related oxide $CaCu_3Ti_4O_{12}$ (CCTO)[83] has recently attracted attention, due to the material (in ceramic forms) showing an extraordinarily high dielectric constant at room temperature of about 10^4-10^5[84-86]. This high k value also shows good stability over the large temperature range from 100 to 600K. The dielectric constant abruptly drops by three orders of magnitude to a value of around 100 upon lowering the temperature below 100 K. This reduction of k shows a Debye-like relaxation with a single relaxation time. No structural or ferroelectric transition has been

observed in this temperature range, which is unlike common ferroelectric ceramics. The absence of ferroelectric like distortions has been attributed to the tilting of TiO_6 octahedra for the accommodation of the unusual square planar Cu ions on the A sites.

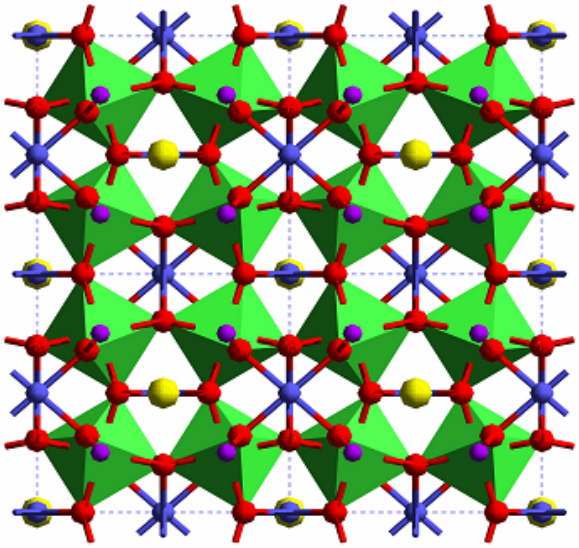

Figure 7.2 Image of CCTO displaying the tilting of the TiO_6 octahedra (in green).

It has been suggested that the dielectric behaviour of CCTO is intrinsic (where the drop would be measured in a perfectly stoichometric, defect-free, and single-domain crystal of CCTO), while others believe it is due to extrinsic effects, such as twin boundaries structure, Maxwell-Wagner relaxation[98], as well as barrier layer capacitor (BLC) effects. Amongst the proposed mechanisms, arguments in support of intrinsic effects have almost been eliminated, and it is the BLC model that has proved most popular. However, the atomic level mechanism for the BLC behaviour is yet to be confirmed. The BLC requires semi-conducting grains separated by insulating boundaries. BLC's are of use in assisting the miniaturisation of circuits due to their small size and large capacitance[99, 100]. It is the semi-conductive $BaTiO_3$ that has largely dominated the field of BLCs, with fabrication enabling one to obtain extremely high capacitance per unit area. To obtain BLCs, a two step sintering process is required: firstly the ceramics are sintered into a semi-conductive state by firing them in a reducing atmosphere. The surfaces of the semi-conductive discs can be reoxidised to form surface BLC's by either annealing the semiconducting ceramics in air or in oxygen atmosphere at a temperature lower than the sintering temperature. Otherwise, some metal oxides can be printed on

the surfaces of the semiconducting ceramics and then diffused into the grain boundary to create an insulating boundary layer, leading to a second phase BLC[101]. The second phase BLC's contain all the desired features of a good capacitor. However, there are some rather large drawbacks of this type of capacitor, including poor reproducibility and complicated multistage processing routes required. If the high dielectric constant of CCTO can be confirmed to be due to the BLC model and hence associated with an intrinsic feature of the crystal structure, this would mean that BLC's could be formed without needing to apply the aforementioned two step sintering process. The main advantage of CCTO in this respect is that the electrical microstructure can be developed in a single processing step in air.

The structure of CCTO was determined from neutron powder diffraction data fourty years ago[102] and has since been confirmed and refined in the space group Im3 (No. 204)[84]. CCTO's crystal structure is body-centred cubic with four $ATiO_3$ perovskite units per primitive cell. Here, Calcium and Copper share the A site, Titanium occupies the B site and Oxygen is on the Z site. The CCTO structure is shown in Figure 7.3.

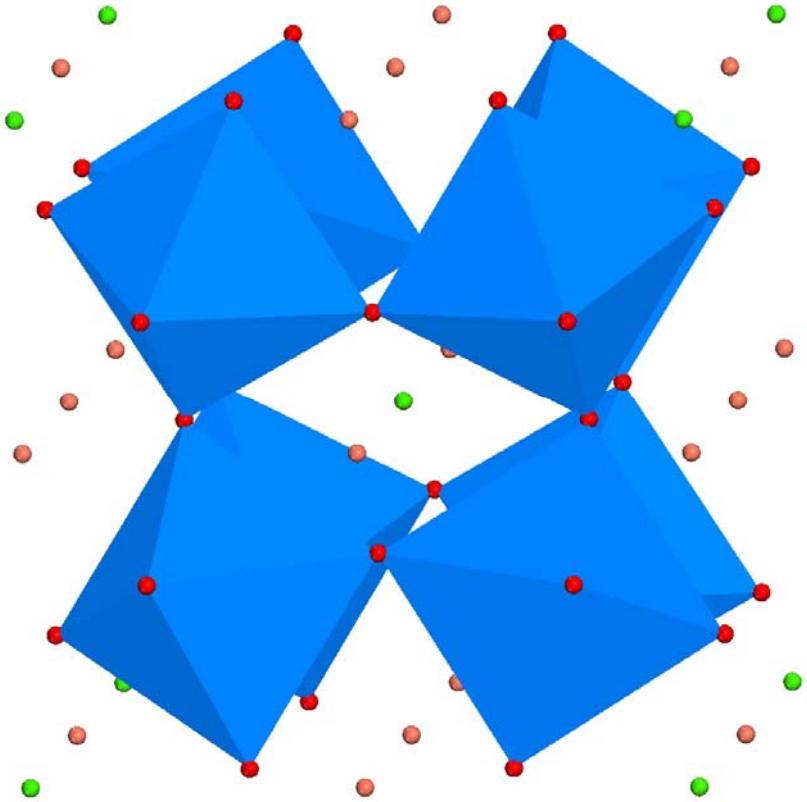

Figure 7.3 Unit cell of the body centred cubic perovskite CCTO, in the Im3 space group. The TiO_6 octahedra are shown in blue. Ca ions in green and the Cu ions are in pink.

From neutron diffraction experiments, CCTO has been confirmed as an antiferromagnetic insulator, with a Neel temperature T_N=25K and Weiss constant, θ_w=-34K. The 40 atom crystallographic unit cell is also the primitive cell of the spin structure, which is double the primitive 20 atom cell of a non-magnetic CCTO structure.

7.1.1 Computational Study of Bulk CCTO

As clear from the discussion of section 7.1, the structural and electronic features of bulk CCTO are well known by experiment. However, its electronic properties leading to the high dielectric constant and possibly to BLC effects are less well understood. One of the aims of our study was to obtain a complete set of quantitative data on the structural and electronic properties of CCTO. The study was performed using CRYSTAL06, which enables the use of hybrid functionals within DFT. Cu^{2+} is a typical 'strongly correlated'

ion, with well localised electronic states which provide a challenge for local DFT; CCTO is therefore suitable to test hybrid exchange functionals. Throughout this study I have used three different DFT formulations, namely the LDA, BLYP[29, 30] and PBE[31] exchange-correlation functionals. It is known that, despite its simplicity, the LDA produces accurate results for properties of metallic solids. However it has been reported to overestimate binding energies by up to 20-30% and severly underestimate bond distances for insulating solids resulting in over compressed geometries. GGA functionals such as PBE and BLYP were designed to improve on the weaknesses of the LDA but do fail to tackle the self interaction problem, which is addressed by the inclusion of the orbital-dependent HF exchange.

HF, DFT and various exchange-correlation functionals have different abilities in reproducing experimentally derived properties of materials. We therefore aim to produce a complete set of data for bulk CCTO, covering a full range of HF to DFT mixing for the LDA, PBE and BLYP exchange-correlation functionals. We then aim to understand the trends produced from the calculations and perform a quantitative comparison to experimentally derived values for different properties of CCTO. In particular we want to conclude on the best hybrid exchange functionals for producing accurate lattice parameters and bond distances, magnetic coupling constants (Neel Temperatures) and Bulk moduli. Given that different fractions of HF to DFT mixing and hybrid functionals will perform differently in describing various properties of bulk CCTO, it is a range of initial starting conditions that we wish to conclude on. We can then use this information to enable a more efficient study of more complex situations such as the surfaces of CCTO. By ultimately looking at the surfaces of CCTO we hope to shed further light on the mechanism behind the observed dielectric constant, and to confirm speculations and atomic level mechanisms responsible for the BLC behaviour.

7.1.1.1 Computational Details.

The DFT exchange-correlation contribution was evaluated by numerical integration over the unit cell volume. Radial and angular points of the grid were generated through Gauss-Legendre radial quadrature, and Lebedev two-dimensional angular point distributions. A pruned grid with 75 radial and 974 angular points was used for all

calculations. Truncation thresholds of (10^{-7}, 10^{-7}, 10^{-7}, 10^{-7}, 10^{-14}) were employed for the selection of integrals in the Coulomb and exchange series[103], while SCF convergence thresholds were set to 1.0×10^{-7} Hartree for both eigenvalues and total energies. These convergence thresholds ensure high numerical accuracy for the calculations[103, 104]. Geometry optimizations were repeated until internal consistency was achieved upon restart, and have been checked against the root-mean-square (RMS) and absolute value of the largest component for both gradients and nuclear displacements[49]. The Gaussian basis sets used to describe the crystalline orbitals were obtained from the online library of CRYSTAL06[105] and are included in the appendix. The initial lattice parameter and fractional coordinates of the unit cell were those derived experimentally by Subramanian et al[84].

Integration of the wavefunction in the irreducible Brillouin Zone (IBZ) of reciprocal space is required to calculate the electron density; this integration is replaced by a numerical sum over a finite number of k points. It is necessary to make an appropriate choice on the number of k points required as to limit computational expense but represent the properties as accurately as possible retaining numerical accuracy[49]. Test calculations using the PBE hybrid functional with 40% HF exchange were performed using Pack-Monkhorst grids for integration in reciprocal space, with k-point nets of 4 x 4 x 4 and 8 x 8 x 8; results are displayed in Table 7.1. It can be seen that the structural and electronic properties are identical in the two cases. It is therefore sufficient to use a 4 x 4 x 4 k point sampling grid, which is the value chosen for all our subsequent calculations.

Table 7.1 Comparison of the structural and electronic properties of CCTO using two different k point grids. Calculations performed using hybrid exchange built on the PBE functional with 40% HF exchange. a_0 is the equilibrium lattice parameter in Å; X_O and Y_O are the fractional coordinates of the O ions (the other coordinates are fixed by space group symmetry); R is the equilibrium bond distances in Å; ΔE is the energy difference between FM and AFM structures in mH; q are the net atomic charges and Spin are the spin atomic charges both in |e| for each ion calculated with a Mulliken partition scheme.

k-points	a_0	X_O	Y_O	R_{Cu-O}	R'_{Cu-O}	R_{Ca-O}	R_{Ti-O}	ΔE	q_{Cu}	q_o	q_{Ti}	$Spin_{Cu}$	$Spin_O$
4x4x4	7.356	0.3024	0.1809	1.971	2.761	2.592	1.947	0.00018	1.74	-1.43	2.54	0.798	0.028
8x8x8	7.356	0.3024	0.1809	1.970	2.761	2.593	1.947	0.00017	1.74	-1.43	2.55	0.802	0.029

7.1.1.2 Geometry Optimisations for the FM and AFM phases of bulk CCTO

Calculations on the bulk structure of CCTO were performed using the LDA, PBE and BLYP exchange-correlation functionals each with a variable fraction of HF exchange, ranging from 0% to 100% in 20% increments. Such calculations are not computationally expensive, but as it is likely that there will be a smooth change of the calculated properties as a function of the fraction of HF exchange, a more extensive sampling of hybrid exchange mixing is unlikely to be necessary.

The FM and AFM structure of CCTO were both studied for the complete range of hybrid functionals, in order to conclude on the most stable magnetic phase and provide an FM and AFM energy difference to enable the calculation of the magnetic coupling constants. Full geometry optimisations have been performed for both FM and AFM magnetic structures; however the equilibrium geometry of the two phases is usually identical to within the numerical thresholds used in our geometry optimisations.

The results for this extensive set of calculations are reported in Table 7.2-7.7. All values are displayed as a function of HF exchange (HF%). Gaps in the results are present due to the difficulty in converging calculations using high fractions of HF exchange in the AFM phase.

Table 7.2 Results for the FM phase of bulk CCTO, using hybrid exchange functionals built on the LDA functional. Symbols and units as in table 7.1.

HF%	a_0	X_O	Y_O	R_{Cu-O}	R'_{Cu-O}	R_{Ca-O}	R_{Ti-O}	ΔE	q_{Cu}	q_o	q_{Ti}	$Spin_{Cu}$	$Spin_O$
0	7.307	0.3038	0.1763	1.927	2.766	2.567	1.945	5.81	1.57	-1.31	2.34	0.531	0.106
20	7.309	0.3032	0.1782	1.940	2.757	2.570	1.940	0.88	1.64	-1.37	2.44	0.669	0.074
40	7.315	0.3028	0.1799	1.953	2.750	2.576	1.938	0.25	1.72	-1.41	2.52	0.777	0.034
60	7.325	0.3022	0.1814	1.966	2.747	2.582	1.937	0.08	1.78	-1.47	2.62	0.859	0.033
80	7.336	0.3016	0.1827	1.979	2.745	2.587	1.937		1.81	-1.50	2.69	0.901	0.023
100	7.349	0.3011	0.1839	1.991	2.745	2.593	1.937		1.84	-1.54	2.76	0.927	0.018

Table 7.3 Results for the AFM phase of bulk CCTO, using hybrid exchange functionals built on the LDA functional. Symbols and units as in table 7.1.

HF%	a_0	X_O	Y_O	R_{Cu-O}	R'_{Cu-O}	R_{Ca-O}	R_{Ti-O}	q_{Cu}	q_o	q_{Ti}	$Spin_{Cu}$	$Spin_O$
0	7.306	0.3039	0.1761	1.926	2.766	2.566	1.945	1.56	-1.31	2.34	0.497	0.088
20	7.309	0.3032	0.1782	1.940	2.757	2.571	1.940	1.63	-1.36	2.44	0.667	0.075
40	7.315	0.3028	0.1799	1.953	2.750	2.577	1.938	1.72	-1.42	2.53	0.783	0.051
60	7.325	0.3022	0.1814	1.966	2.747	2.582	1.937	1.78	-1.47	2.62	0.860	0.035

Table 7.4 Results for the FM phase of bulk CCTO, using hybrid exchange functionals built on the BLYP functional. Symbols and units as in table 7.1.

HM%	a_0	X_O	Y_O	R_{Cu-O}	R'_{Cu-O}	R_{Ca-O}	R_{Ti-O}	ΔE	q_{Cu}	q_o	q_{Ti}	$Spin_{Cu}$	$Spin_O$
0	7.523	0.3030	0.1786	2.001	2.836	2.646	1.996	3.15	1.57	-1.33	2.41	0.557	0.094

20	7.462	0.3028	0.1797	1.991	2.807	2.627	1.978	0.55	1.65	-1.39	2.49	0.692	0.069
40	7.414	0.3025	0.1807	1.985	2.783	2.612	1.962	0.18	1.73	-1.43	2.56	0.795	0.041
60	7.374	0.3021	0.1817	1.981	2.764	2.600	1.949	0.08	1.78	-1.47	2.63	0.865	0.032
80	7.339	0.3017	0.1825	1.978	2.748	2.588	1.938	0.05	1.81	-1.50	2.69	0.903	0.023
100	7.309	0.3014	0.1830	1.974	2.734	2.578	1.929		1.84	-1.53	2.74	0.925	0.018

Table 7.5 Results for the AFM phase of bulk CCTO, using hybrid exchange functionals built on the BLYP functional. Symbols and units as in table 7.1.

HF%	a_0	X_O	Y_O	R_{Cu-O}	R'_{Cu-O}	R_{Ca-O}	R_{Ti-O}	q_{Cu}	q_o	q_{Ti}	$Spin_{Cu}$	$Spin_O$
0	7.522	0.3030	0.1785	2.000	2.836	2.645	1.996	1.57	-1.33	2.41	0.537	0.087
20	7.462	0.3028	0.1797	1.991	2.807	2.627	1.978	1.65	-1.39	2.49	0.690	0.070
40	7.414	0.3025	0.1807	1.985	2.783	2.612	1.962	1.72	-1.43	2.57	0.797	0.048
60	7.374	0.3021	0.1817	1.981	2.764	2.600	1.949	1.78	-1.47	2.63	0.865	0.033
80	7.339	0.3017	0.1825	1.978	2.748	2.588	1.938	1.82	-1.50	2.69	0.903	0.025

Table 7.6 Results for the FM phase of bulk CCTO, using hybrid exchange functionals built on the PBE functional. Symbols and units as in table 7.1.

HF%	a_0	X_O	Y_O	R_{Cu-O}	R'_{Cu-O}	R_{Ca-O}	R_{Ti-O}	ΔE	q_{Cu}	q_o	q_{Ti}	$Spin_{Cu}$	$Spin_O$
0	7.456	0.3031	0.1786	1.982	2.810	2.623	1.978	3.25	1.59	-1.34	2.41	0.563	0.092
20	7.401	0.3027	0.1798	1.975	2.783	2.606	1.961	0.57	1.66	-1.39	2.49	0.699	0.067

40	7.356	0.3024	0.1809	1.971	2.761	2.592	1.947	0.18	1.74	-1.43	2.54	0.798	0.028
60	7.320	0.3020	0.1818	1.968	2.743	2.580	1.935	0.07	1.79	-1.47	2.62	0.869	0.030
80	7.286	0.3015	0.1827	1.965	2.727	2.569	1.924		1.83	-1.50	2.68	0.906	0.022
100	7.256	0.3014	0.1835	1.962	2.711	2.561	1.914		1.85	-1.53	2.73	0.928	0.017

Table 7.7 Results for the AFM phase of bulk CCTO, using hybrid exchange functionals built on the BLYP functional. Symbols and units as in table 7.1.

HF%	a_0	X_O	Y_O	R_{Cu-O}	R'_{Cu-O}	R_{Ca-O}	R_{Ti-O}	q_{Cu}	q_o	q_{Ti}	$Spin_{Cu}$	$Spin_O$
0	7.455	0.3031	0.1785	1.981	2.810	2.623	1.978	1.59	-1.34	2.40	0.543	0.085
20	7.401	0.3027	0.1798	1.975	2.783	2.606	1.961	1.66	-1.39	2.49	0.697	0.068
40	7.356	0.3024	0.1809	1.970	2.761	2.592	1.947	1.74	-1.44	2.56	0.803	0.047
60	7.320	0.3020	0.1819	1.968	2.743	2.580	1.934	1.79	-1.47	2.62	0.870	0.032

Let us now discuss these results, highlighting trends and commenting on how the calculated data compare to experiment.

7.1.1.3 Structural Properties

Table 7.2-7.7 provide structural data for CCTO calculated using the hybrids built on the LDA and GGA (BLYP and PBE) functionals over a complete range of HF to DFT hybrid exchange mixing for the FM and AFM phases. Firstly we examine the trend in the equilibrium lattice parameter, and compare the results with the experimentally derived value. The structure is imposed in these calculations to belong to the Im3 cubic

body-centered space group as derived from experiment. We have however performed Γ-point phonon calculations after each geometry optimisation to confirm that this choice is a proper minimum with respect to symmetry lowering distortions. Depending on the choice of functional and amount of HF used, the equilibrium lattice parameter is predicted to range between 7.523 and 7.256Å, and is shown in Figure 7.4.

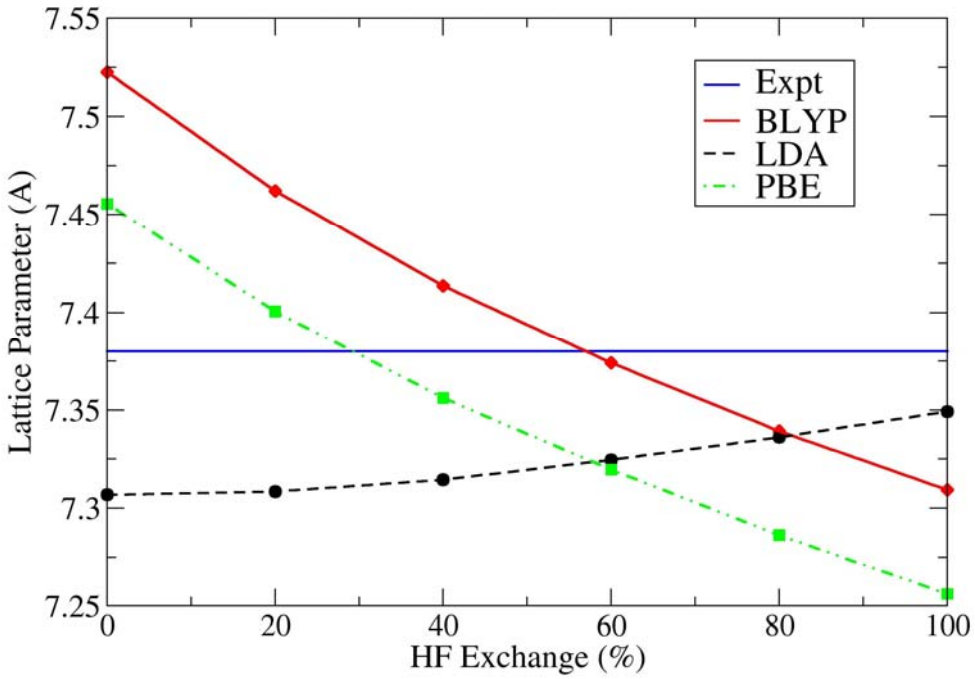

Figure 7.4 Equilibrium lattice parameter against the fraction of HF exchange for the BLYP, PBE and LDA functionals.

Here we can see that the LDA functional, having never been tested in hybrid functionals before, over-compresses the geometry and lets it expand slightly as the component of HF exchange is increased. It can be seen that the LDA never actually allows the lattice parameter to expand enough to achieve the experimental value of 7.391Å[84]. This is a very different behaviour to the two hybrids built on the GGA functionals, which can be seen to overestimate the lattice parameter at the pure DFT limit, and to compress the geometry as the component of HF exchange is increased. It can also be seen from the above graph that the BLYP and PBE functionals show trends which are identical, but shifted by a constant magnitude due to the BLYP functional overestimating the lattice parameter more than PBE. It is also interesting to see that the LDA shows a much smaller change in lattice parameter over the range of HF exchange than that of the GGA functionals.

It should be noted here that the trends show very smooth curves for all results; hence sampling at 20% increments in the fraction of HF exchange was sufficient to extract the required information.
It is clear from Figure 7.4 that the best range of hybrid functionals in reproducing the known experimental lattice parameter of CCTO lies within the BLYP and PBE functionals at a fraction of HF exchange of approximately 30-60%.

To further analyse the structure we now discuss the equilibrium bond distances. The Ti cations are sixfold coordinated by equidistant oxygens, with a bond length (R_{Ti-O}) predicted to be between 1.914 and 1.996Å depending on the functional and amount of HF exchange used. The Ca atoms are surrounded by 12 equidistant oxygens, with bond distances (R_{Ca-O}) predicted in the range 2.561-2.646Å, again depending on the functional and amount of HF exchange. This regular environment is as expected for A cations in the ideal perovskite structure. However, the tilted octahedra do result in a very different environment for each Cu ion, which is coordinated by a planar arrangement of 4 nearest neighbour O atoms with distances between 1.926-2.001Å (R_{Cu-O}), 4 oxygens at a distance of between 2.711-2.836Å (R'_{Cu-O}) and 4 oxygens at a much further distance of more than 3Å, which we do not discuss here. The exact prediction depends on the choice of exchange-correlation functional and amount of HF included in the theory.
To examine these trends the Cu-O, Ti-O, and Ca-O bond distances have been displayed in Figure 7.5, Figure 7.6 and Figure 7.7.

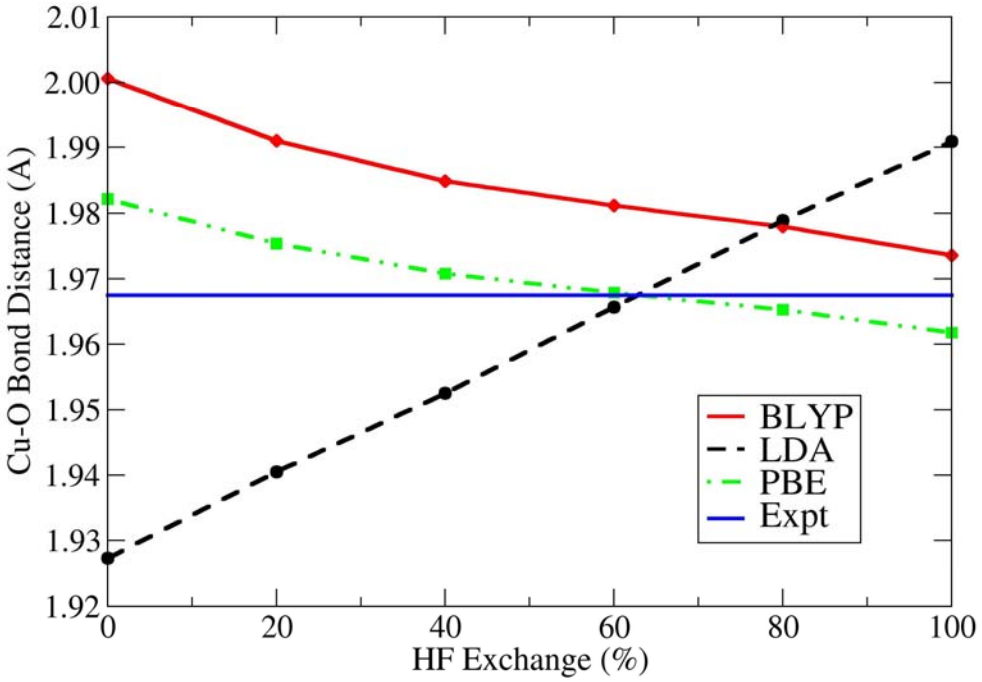

Figure 7.5 Shortest Copper-Oxygen bond distances against the fraction of HF exchange for the difference hybrid functionals examined.

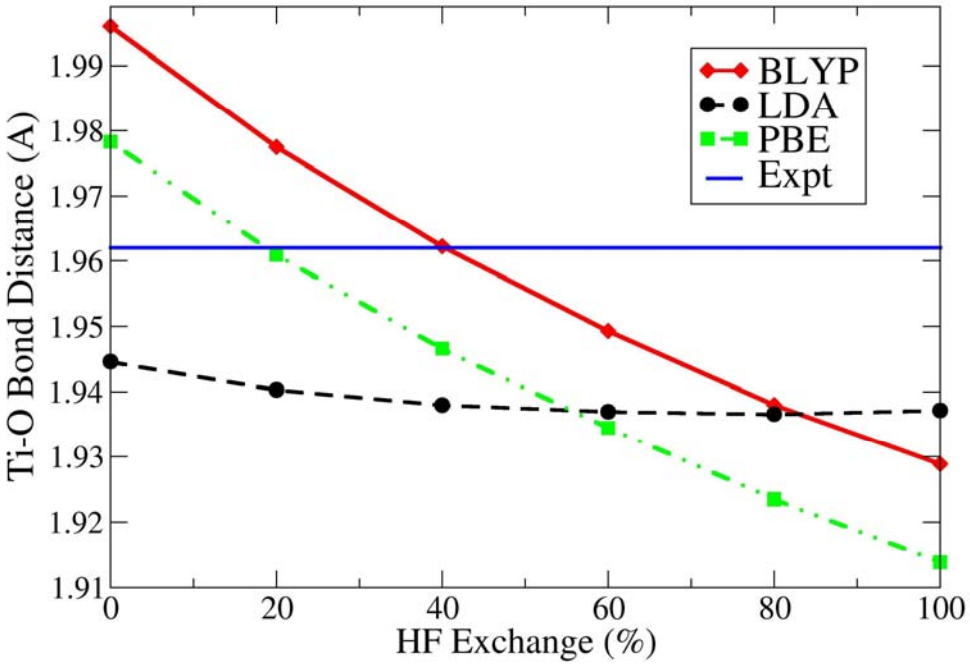

Figure 7.6 Titanium-Oxygen bond distances against the fraction of HF exchange for the different hybrid functionals examined.

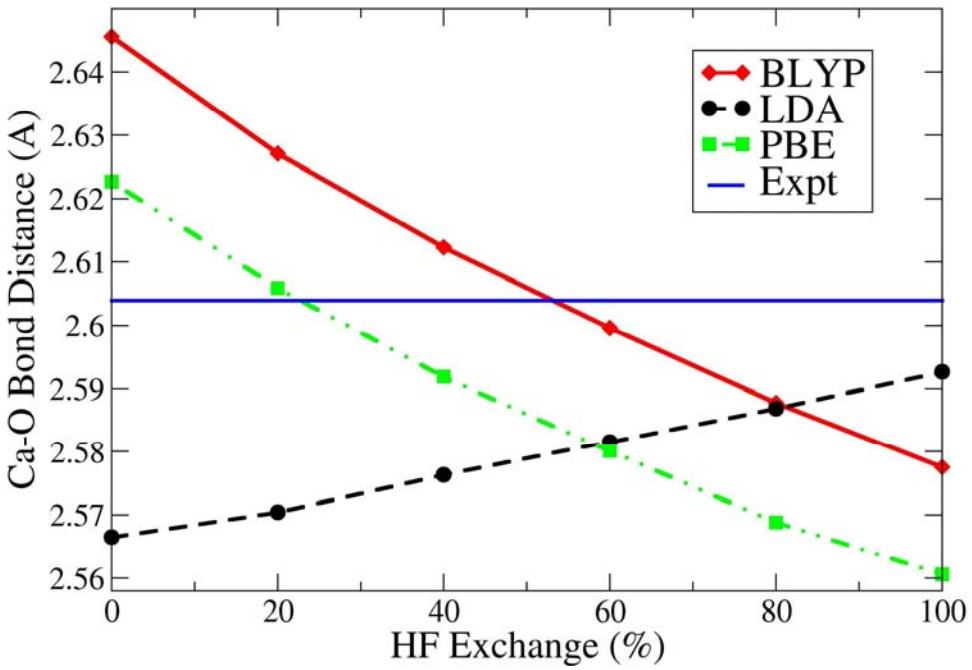

Figure 7.7 Calcium-Oxygen bond distances against the fraction of HF exchange for the different hybrid functionals examined.

The corresponding Cu-O, Ti-O and Ca-O bond distances obtained via experiment[84, 102] are 1.968, 1.961 and 2.604Å respectively, and are marked by the continuous horizontal lines on the above graphs.

It is clear that despite reports of the LDA producing good results for metallic solids with delocalised electrons, it tends to underestimate bond distances in materials with well localised electronic states such as in CCTO.

It can be seen here that the different bond distances show trends different from the lattice parameter and from each other as a function of HF exchange. Most noticeably, the Ti-O bond distance is underestimated with respect to experiment by the LDA, but instead of allowing the distance to expand as more HF is introduced we see a change of opposite sign.

Individual bond distances are best reproduced by different hybrid functionals with differing amounts of HF exchange. Therefore the most accurate formulation to reproduce experimentally derived structural data must be obtained as a compromise among cell and fractional parameters. As the equilibrium lattice parameter has been discussed above, let us now examine the bond distances, starting with Cu-O. From Figure 7.5 it can be seen that this is reproduced using the LDA and PBE hybrid functionals with approximately 60% HF exchange. Similarly from Figure 7.6 and

Figure 7.7 it can be deduced that the BLYP and PBE functionals best describe the Ti-O and Ca-O bond distances between approximately 20-40% and 20-60% HF exchange respectively.

It is also of interest to compare the ratio of the Ca-O/Ti-O, Cu-O/Ti-O and Ca-O/Cu-O bond distances, in order to see the effect of the HF exchange on the relative size of the ions. As commented earlier in Chapter 4, relative ionic sizes play a fundamental role in describing distortions of the perovskite structure via the tolerance, t and are therefore of interest also for CCTO.

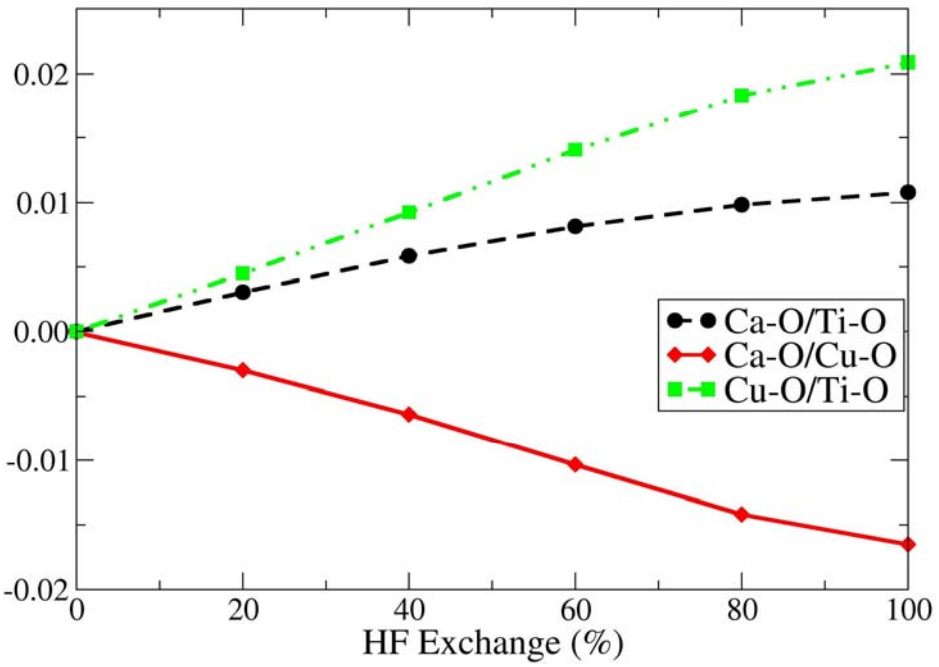

Figure 7.8 Changes of the Ca-O/Ti-O, Cu-O/Ti-O and Ca-O/Cu-O ratios of bond distances as a function of HF exchange calculated using the BLYP functional, with respect to the pure DFT limit, taken as reference.

It can be seen in Figure 7.8 that there is a relative increase in size of the calcium and copper ions, with respect to titanium, as more HF exchange is introduced. This is due to the self-interaction in DFT; in this case, the self interaction affects the electron density on the oxygen, which is delocalised over the covalent Ti-O bonds as opposed to the calcium or copper ions which are more ionic. As a consequence the titanium ions in the pure DFT solution acquire electron density and appear relatively large in size. The introduction of HF exchange corrects for this effect, leaving less d electrons on the

titanium ion, and leading to a relative decrease in the size of titanium compared to copper/calcium. This finding is consistent with studies of other perovskite structures such as Barium Titanate[39], and is confirmed by a Mulliken population analysis of the electron density (Table 7.2-7), which shows that titanium becomes increasingly more ionic on increasing the HF exchange component.

Having successfully converged bulk calculations for CCTO, the bulk modulus of the material was then studied. This was obtained by calculating the total energy as a function of unit cell volume and by fitting the calculated energy values to the 3rd order Birch Murnaghan equation of state (EOS)[106]. The study was done by performing several calculations, each with a fixed lattice parameter at values chosen in increasing steps of 0.05Å around the value deduced from the full geometry optimisations. This set of calculations was repeated using each of the hybrid functionals discussed earlier.

An example of an energy-volume curve, from which the bulk moduli were derived, is shown in Figure 7.9 for the $F_{0.6}$PBE functional. Throughout the range of results, steps were taken to reduce numerical noise; the numerical accuracy achieved can be clearly seen in the smoothness of the curve in Figure 7.9.

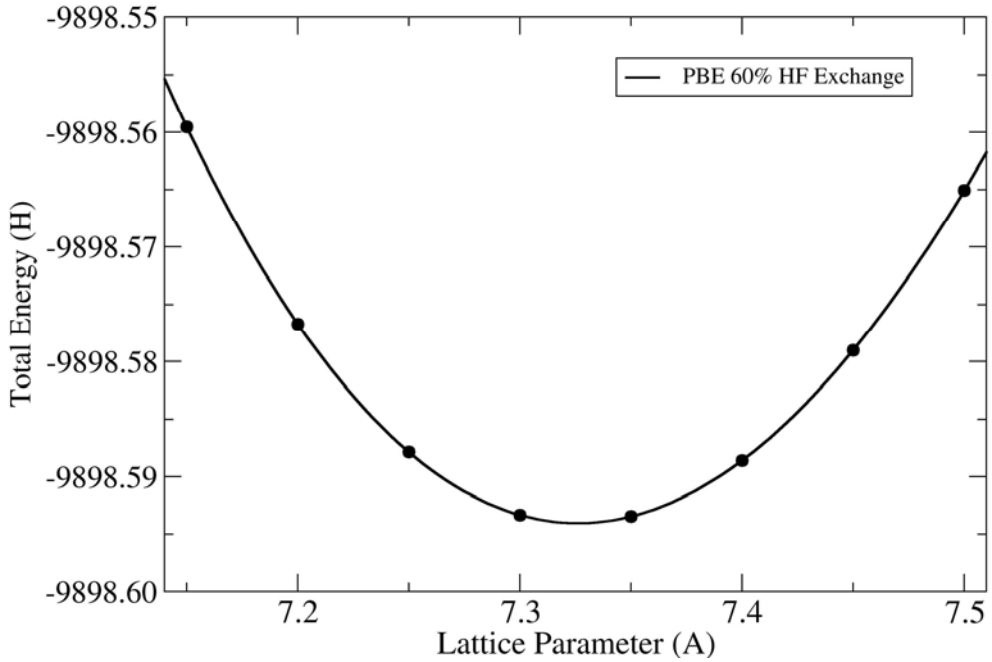

Figure 7.9 Total energy against lattice parameter using PBE with 60% HF exchange.

Fitting data similar to those of Figure 7.9 for the full range of hybrid functionals (BLYP, PBE and LDA) provided the bulk modulus data, displayed in Figure 7.10.

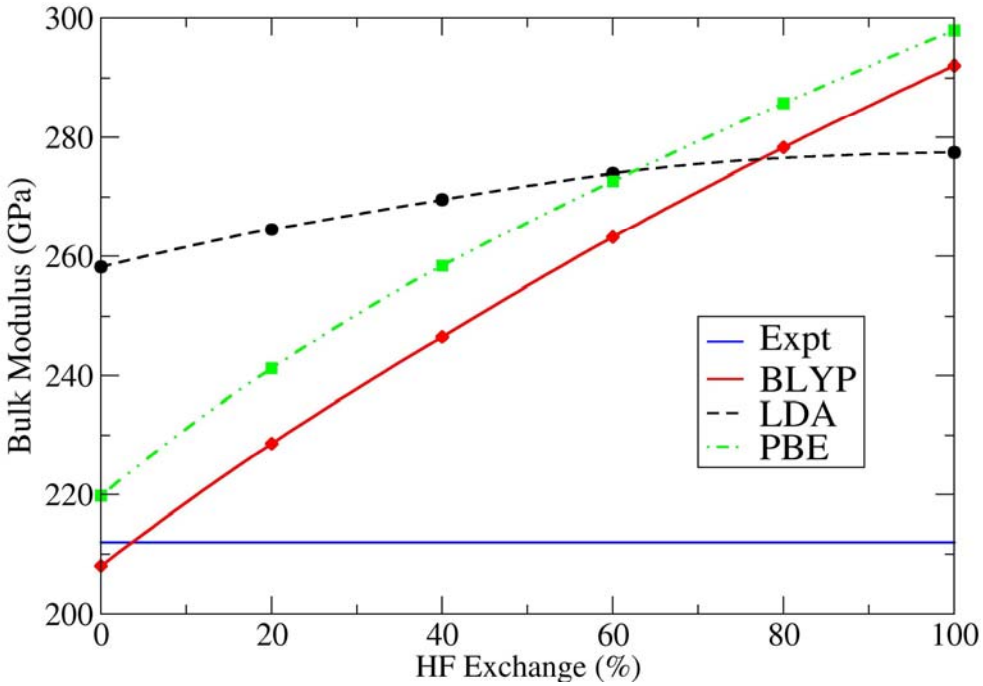

Figure 7.10 Bulk modulus of CCTO as a function of HF exchange for the BLYP, PBE and LDA hybrid functionals.

The values predicted by the LDA series are clearly overestimated and show little change on varying the fraction of HF exchange; the overestimation is associated with the overbinding of the LDA. In contrast the BLYP and PBE functionals show an increase in bulk modulus on increasing the fraction of HF exchange. The LDA has been shown previously in this report, to expand on various bond distances and the equilibrium lattice parameter with increasing HF. Since the value of B is defined as:

$$B = \frac{1}{V_0}\frac{\partial^2 E}{\partial V^2} \tag{7.2}$$

and is inversely proportional to the equilibrium volume, an expansion of V_0 would be expected to cause a decrease of B. We notice however that the bulk modulus increases, indicative of the lower electronic polarisability and hence higher electronic hardness on increasing HF exchange.

7.1.1.4 Electronic Properties

Let us now discuss the electronic structure of CCTO. All the values discussed in this section refer to the equilibrium structure for each of the hybrid functionals examined. Firstly, it can be seen in the columns reporting the spin on the copper and oxygen ions in Table 7.2-7.7, that the spin is most evenly spread out over the atoms for the pure DFT solution; as we increase the percentage of HF exchange the spin is increasingly localised on the copper. For example, let us consider Table 7.6, which reports the FM phase of CCTO using the PBE exchange-correlation functional. For 0% HF exchange we have a spin of 0.56|e| localised on the copper and 0.09 on each of the oxygen atoms; at 100% HF most of the spin is on the copper (0.93 unpaired electrons) with only 0.017 unpaired electrons on the oxygen atoms. This is due to the fact that the solution with a localised charge is unstable in DFT because of the self-interaction error and the energy is lowered by delocalising charge, leaving us with a metallic solution, which is the incorrect ground state.

This trend can be seen pictorially by plotting a spin density map in the plane containing one copper and its four nearest oxygen ions. The spin density map, in Figure 7.11 below, shows how the spin on the copper and oxygen atoms varies as the percentage of HF to DFT mixing is increased. Note the smaller number of isodensity lines on the oxygens for the solution with 100% HF exchange compared with the 0% case.

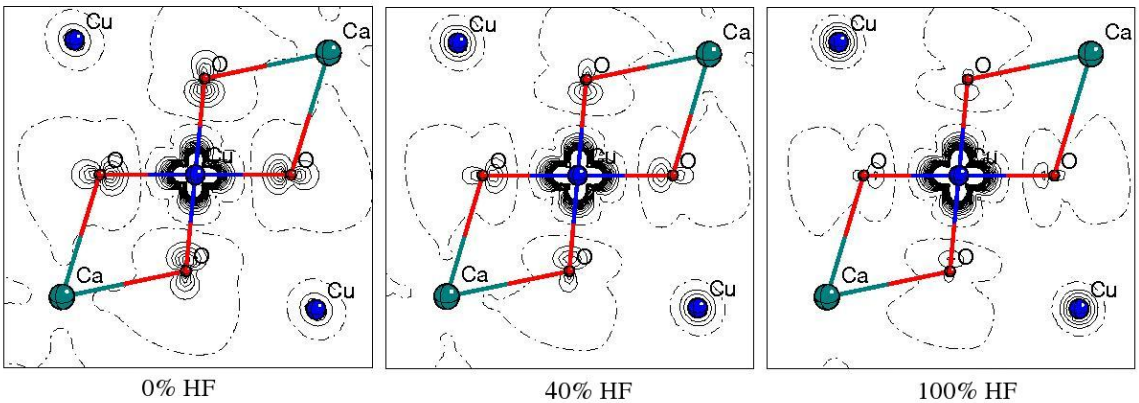

Figure 7.11 Spin density maps for increasing HF to DFT mixing using the PBE hybrid functional. Isodensity density lines drawn between -0.1 and 0.1 au. at intervals of 0.01.

The magnetic structure is a second observable influenced by the spin localisation. Magnetic superexchange is defined as the electronic interaction between two spin polarised ions mediated by a common ligand[107]. In CCTO we have copper ions interacting with one another via a central oxygen ion. In DFT, this interaction is overestimated as it gives a more covalent distribution, which allows a more efficient superexchange. This can be readily seen in tables 7.2, 7.4 and 7.6, in the column reporting energy differences (ΔE) between the AFM and FM phase. In the pure DFT solution the energy difference is greatest and it decreases as more HF exchange is introduced, moving closer to the correct solution until it then begins to overcorrect. This can be seen more clearly in Figure 7.12 below.

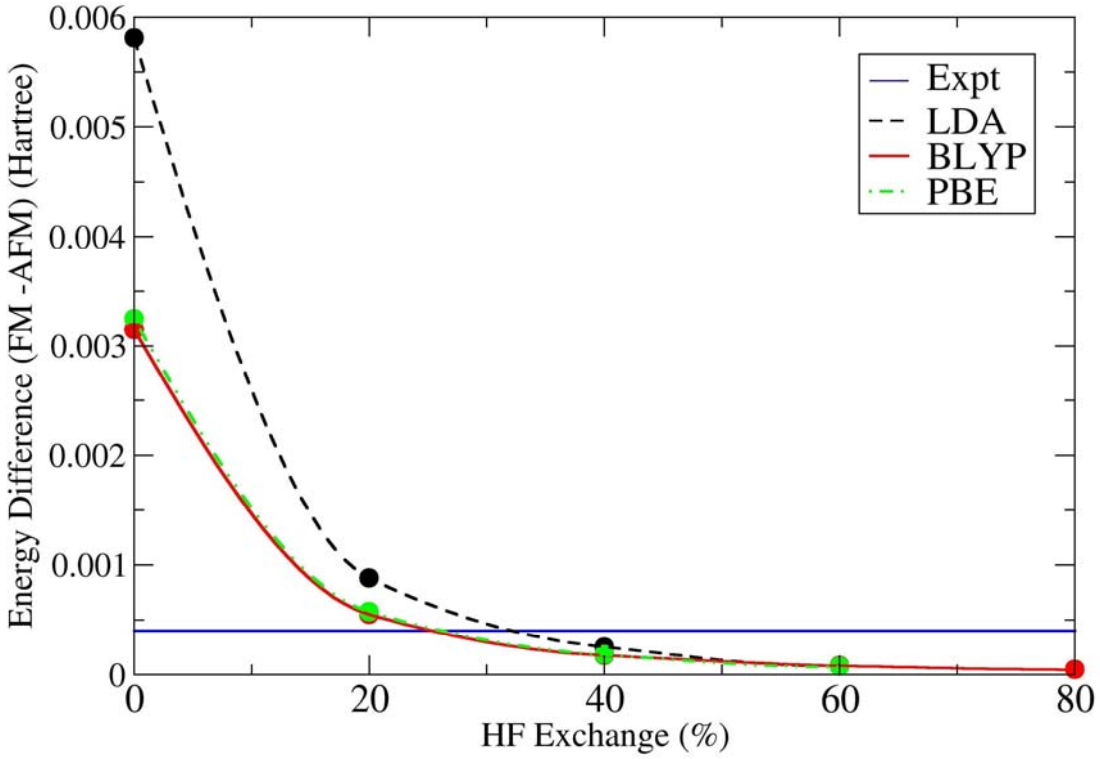

Figure 7.12 AFM and FM energy difference against the fraction of HF exchange for the BLYP, PBE and LDA functionals.

Here we can also see that the two GGA exchange-correlation functionals show almost identical results, while the LDA overestimates the experimental value more than the GGA's. We should note here that this is the typical dependence of ΔE on the HF fraction that we expect to see for a superexchange type of interaction[39].

The experimental value of the energy difference between FM-AFM phases has been derived using the mean field approximation for the Neel temperature (known from transport, Raman and neutron diffraction experiments as 25K)[108-110]. From Figure 7.12 it is possible to see that the FM-AFM energy difference is reproduced most accurately at around 25-30% HF exchange by all three hybrid functionals.

From the change in FM and AFM energies reported in Table 7.2-7 it is possible to deduce the coupling constant of CCTO and therefore the Neel temperature predicted by the theory.

The magnetic order temperature can be derived using the Ising model and using the spin for Cu^{2+} as ½. The energy of the different magnetic phases is given by:

$$E = E_0 + \sum_{i,j} J_{ij} S_i^z S_j^z = E_0 + \sum_{ij} \pm \frac{1}{4} J_{ij} \tag{7.3}$$

where E_0 is the reference energy of a hypothetical phase in which the spin-spin interaction is excluded and i and j are nearest neighbour magnetic ions, that interact with an effective magnetic coupling constant J_{ij}.
Since each pair of nearest neighbour ions in the FM phase have parallel spins and in the AFM phase they have antiparallel spins, the energy for FM and AFM states can be expressed as:

$$E_{FM} = E_0 + \frac{n}{4} J_{ij} \tag{7.4}$$

$$E_{AFM} = E_0 - \frac{n}{4} J_{ij} \tag{7.5}$$

where n is the number of nearest neighbour pairs of Cu ions in each unit cell. Further neighbours do not need to be included as the coupling constant J decreases rapidly with the distance between the ions i and j.

In the CCTO unit cell there are three copper atoms, each of which has four nearest Cu neighbours, giving twelve pairs which needs to be halved to count each interaction only once. By subtracting equations (7.4) and (7.5) and by replacing n=6 we have:

$$\Delta E_{FM-AFM} = \frac{3x4x0.5}{2} J_{ij} = 3J \tag{7.6}$$

The AFM energy used here is the one corresponding to a primitive unit cell of material, consisting of one $CaCu_3Ti_4O_{12}$ formula unit.

As mentioned previously, Transport, Raman and Neutron diffraction experiments indicate that CCTO has a Neel temperature of 25K. The experimental J value can then be extrapolated from this by using the mean field approximation for temperature induced magnetic order and taking into account thermal fluctuations[111] leading to the following equation:

$$T_N \approx \frac{2.25S^2 J}{k_b} \tag{7.7}$$

where the spin, S, on Cu^{2+} is ½.

It should be noted that, from the results analysed so far the electronic properties of CCTO are described almost identically by the three hybrid functionals throughout the range of Hartree Fock exchange. Atomic charges, spin and the change in AFM to FM energies are deduced to be very similar when described by BLYP, PBE and the LDA. Therefore we can say that it is only the percentage of HF exchange which is important in describing the electronic properties of a material, in contrast to the equilibrium structure discussed earlier, which showed a clear dependence both on the fraction of HF exchange and the type of exchange-correlation functional used.

If we take the BLYP functional as an example, throughout the range of 0-100% HF exchange, equation (7.7) predicts the Neel temperature to be in the range of 2-100K. The most accurate description is obtained using the $F_{0.2}$BLYP, which gives T_N=22K. As

the energies we are dealing with are relatively small, it follows that there may be large numerical errors associated with calculations which use them. Therefore the Neel temperature predicted from QM calculations and the mean field approximation can be considered as reasonably accurate for a wide range of HF exchange, covering between 20 and 60% HF percentage.

It has been suggested in the literature[112] that the AFM ordering of spins in CCTO can be attributed to a superexchange involving Cu-O-Ti-O-Cu paths as displayed in Figure 7.13.

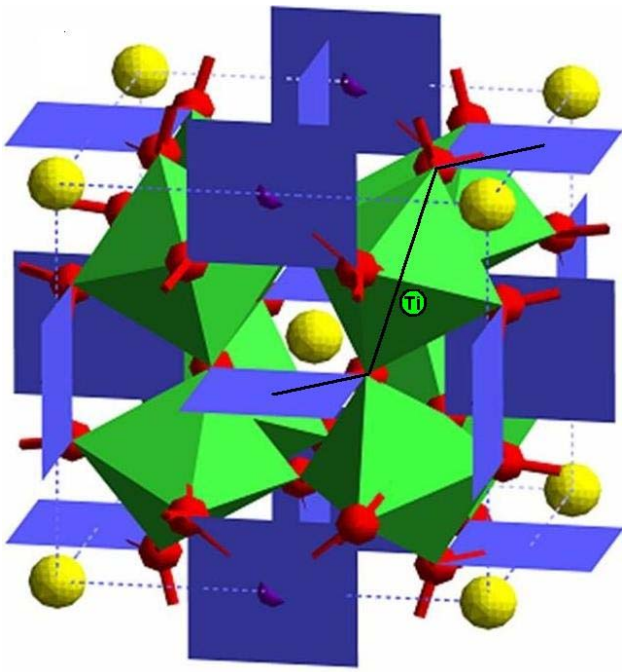

Figure 7.13 Unit cell of CCTO displaying the Cu-O-Ti-O-Cu superexchange mechanism proposed as the reason for an AFM ground state. The Cu atoms are in square planar coordination with oxygen and are displayed in blue. The Ti^{4+} ions are in octahedral coordination with oxygens and are displayed in green.

However our calculations show that this is unlikely to be the case since the spin moment localised on the Ti^{4+} cation is negligible. This can be seen in the spin density plot calculated using the $F_{0.4}$PBE functional, shown in Figure 7.14, which indicates that Ti is inactive in the spin-coupling mechanism.

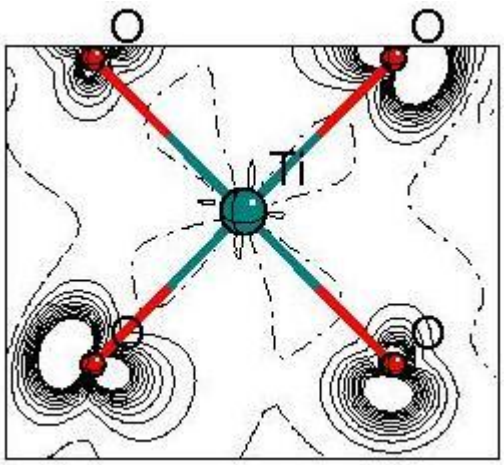

Figure 7.14 Spin density on the Ti^{4+} ions of CCTO which are pictured looking down the 001 planes of the cubic unit cell. This was calculated using the $F_{0.4}$PBE functional. Isodensity lines drawn between -0.1 and 0.1 au. in intervals of 0.01.

Let us now discuss the density of states (DOS) plots, which can provide useful information on band gaps, and composition of states in the valence and conduction bands. Figures 7.15-7.18 show the calculated density of states for CCTO; we limit here to the range of HF exchange between 20 and 60% as this is when the calculated structure and electronic properties find better correspondence to experiment.

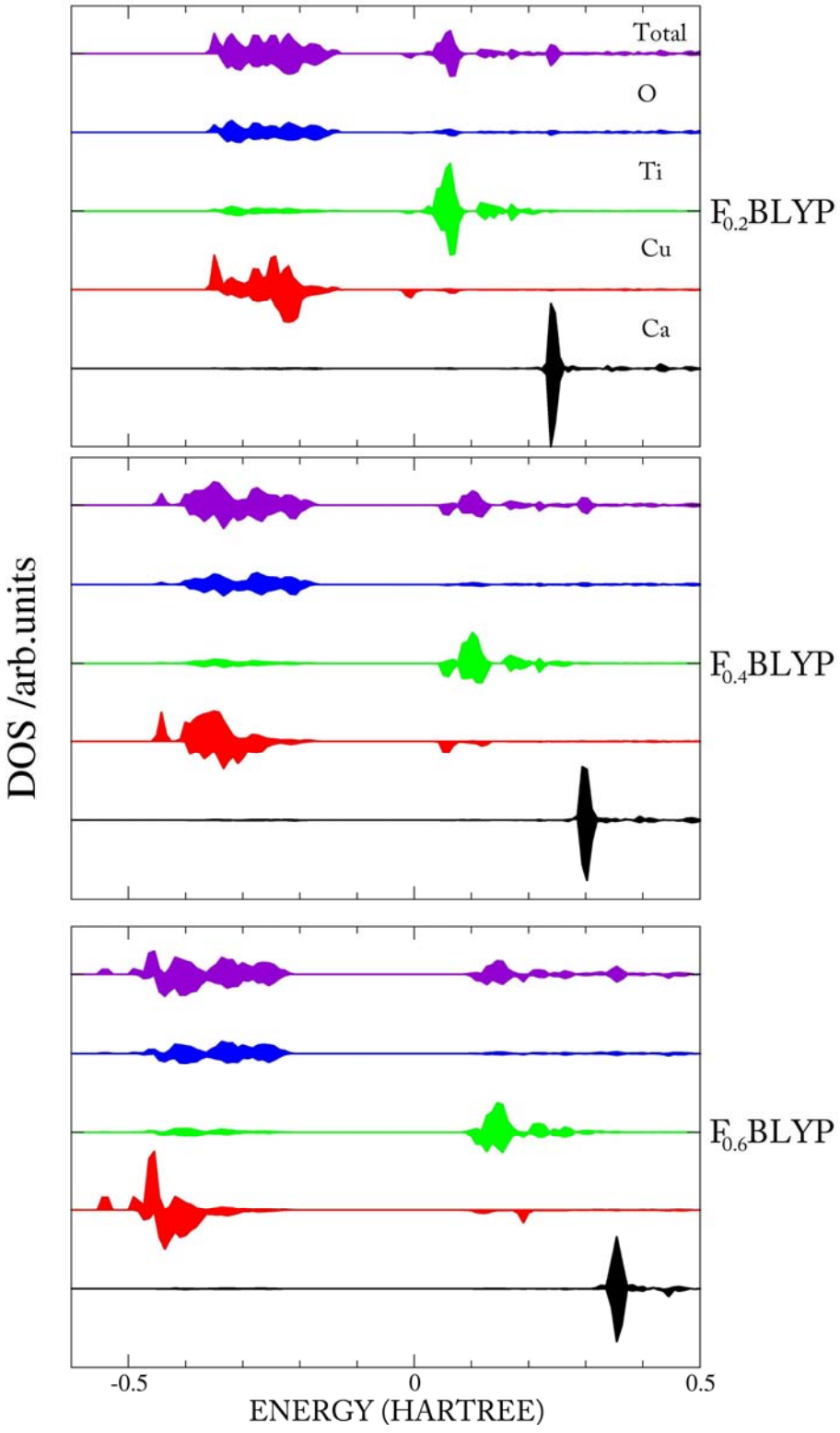

Figure 7.15 Density of States of bulk CCTO using the BLYP hybrid functional at 20, 40 and 60% HF exchange from top to bottom. The projected DOS on the Ca, Cu, Ti and O basis set, and the total DOS are shown, with total divided by ten for ease of presentation.

It should be noted here that the states at the top of the valence band are predicted to be mostly from the oxygen atoms at 60% HF exchange; however, when the amount of HF is reduced, the copper atoms appear to make more of a contribution. The main composition of the DOS at the bottom of the conduction band is predicted to come from the titanium atoms with 60% HF exchange, changing to copper when the amount of HF in the formulation is reduced. In fact the results predict the minimum energy excitation to move from copper-copper to oxygen-copper and oxygen-titanium transitions at 20, 40 and 60% HF exchange respectively. Figure 7.15 also shows how these calculations predict the occupied copper d states to shift down in energy, overlapping the oxygen 2p states when using more and more HF exchange. The solid changes therefore from a Mott Hubbard type insulator at 20% HF exchange to a charge transfer material at 60% HF exchange. Similar trends are observed for each of the DFT functionals examined, ie. BLYP (Figure 7.15), PBE (Figure 7.17) and LDA (Figure 7.18).

The empty d states on the copper atoms can be seen in the energy range between approximately 0 and 0.2 Hartree. This is presented more clearly in Figure 7.16, which is an expansion of the bottom of the conduction band for the hybrid BLYP functionals.

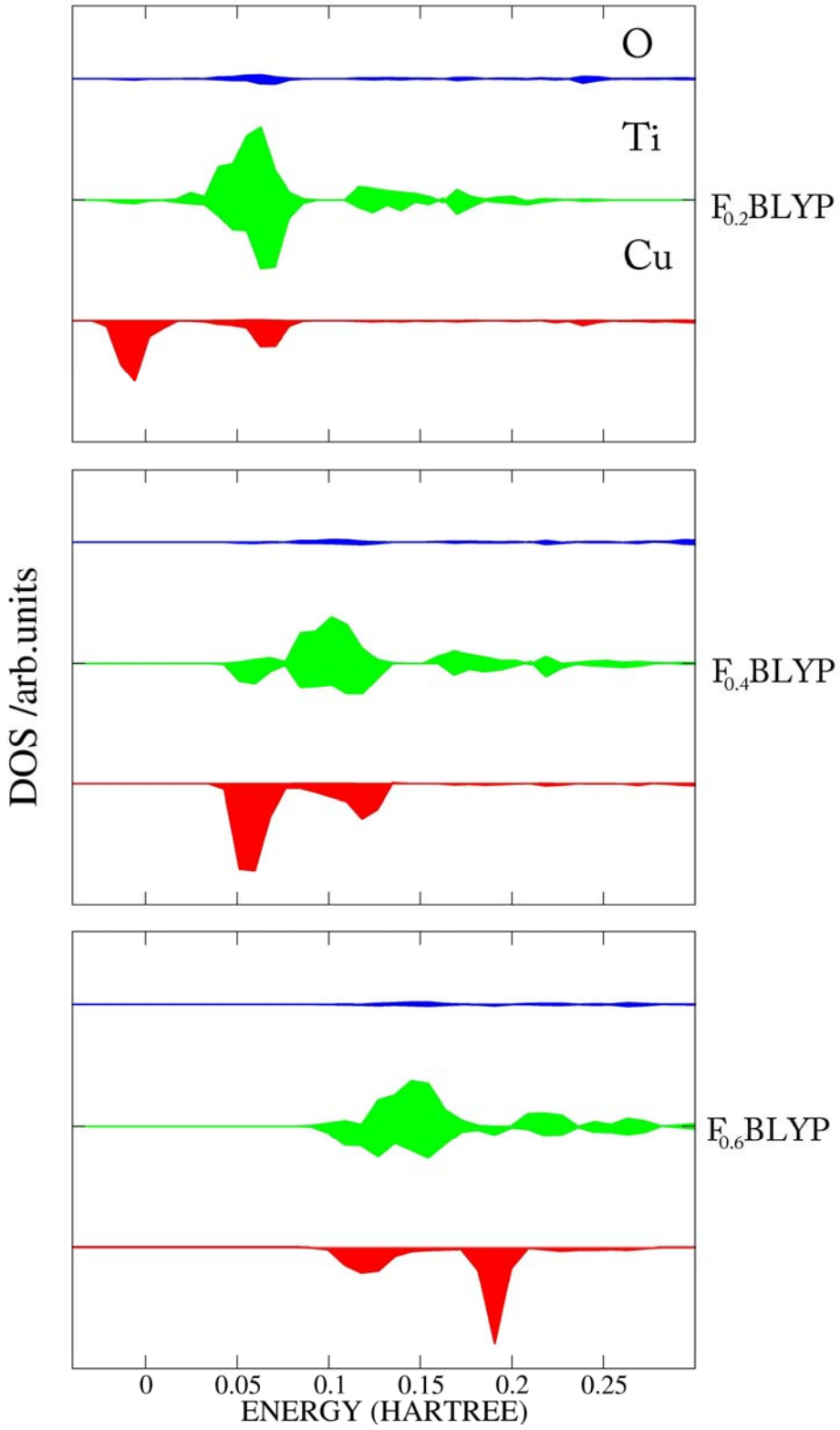

Figure 7.16 Density of states of CCTO bulk using the BLYP hybrid functional at 20, 40 and 60% HF exchange in the energy range of -0.05 – +0.3 Hartree (bottom of the conduction band).

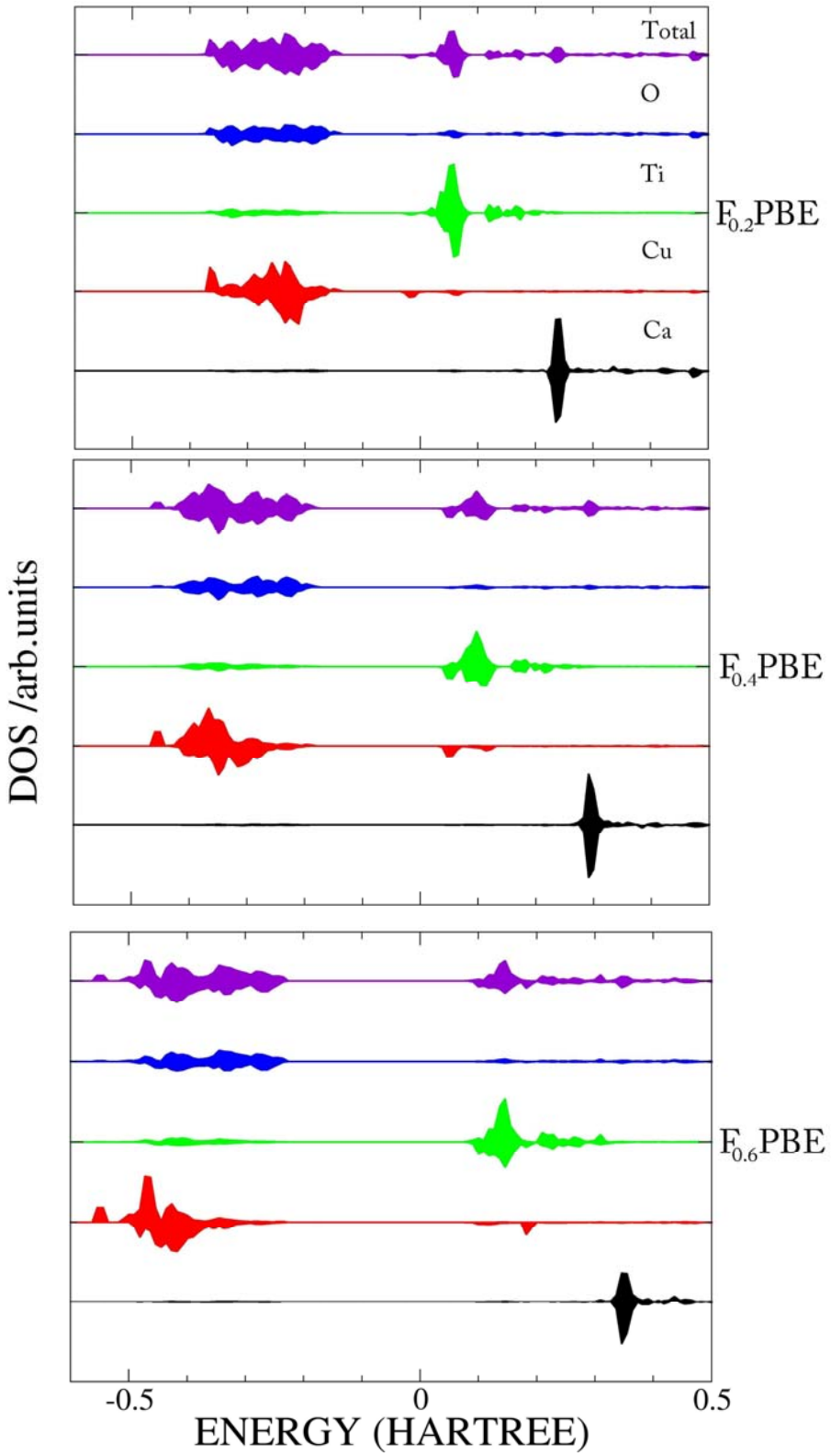

Figure 7.17 Density of States of CCTO bulk using the PBE hybrid functional at 20, 40 and 60% HF exchange from top to bottom. The projected DOS on the Ca, Cu, Ti and O basis set, and the total DOS are shown, with the total divided by ten for ease of presentation.

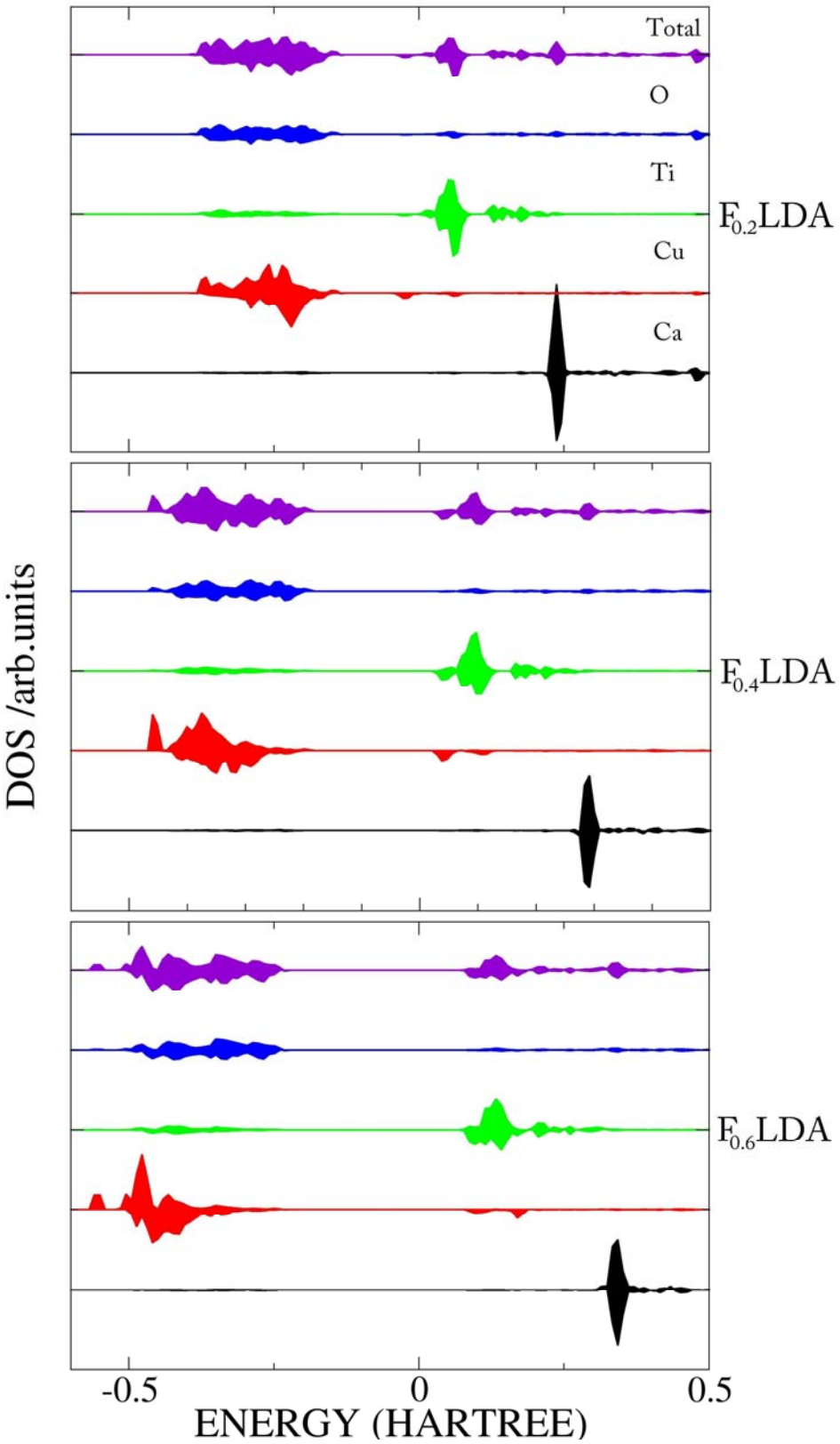

Figure 7.18 Density of States of CCTO bulk using the LDA hybrid functional at 20, 40 and 60% HF exchange from top to bottom. The projected DOS on the Ca, Cu, Ti and O basis set, and the total DOS are shown, with the total divided by ten for ease of presentation.

Figures 7.15, 7.17 and 7.18 provide further evidence for the similarity observed in the electronic properties of CCTO between the hybrid functionals built on the BLYP, PBE and LDA. For example, the band gap can be seen to increase as more HF exchange is introduced for the range of hybrid functionals used. The value of the band gap has similar magnitude in each case. The empty d states on the copper atoms also appear to shift in an almost identical way, independently of which local exchange-correlation functional is used for the DFT component. As an example of the magnitude of the band gap of CCTO; the gap calculated with the $F_{0.4}$PBE functional is 6.19eV.

7.1.1.5 Conclusions on bulk CCTO

It is clear from our results that the choice of functional in DFT affects the prediction of the electronic and structural properties of a given system (in this case CCTO).

It should be noted first that our choice of sampling different hybrid exchange functionals at discrete increments of 20% in the fraction of HF exchange is sufficient, as the results show smooth trends.

The predicted electronic properties of CCTO show similar behaviour throughout the range of HF to DFT hybrid exchange mixing for the PBE, LDA and BLYP hybrid functionals. This suggests that for future calculations the choice of DFT functional is non-critical, but a good choice concerning the fraction of HF exchange is. In contrast, the structural properties of CCTO over the range of HF exchange displayed quite different behaviour depending on the choice of exchange-correlation functional. The LDA initially predicts an overcompressed geometry, allowing it to relax at a rate which is not rapid enough to reach the experimentally derived lattice parameter as the amount of HF exchange is increased. The two hybrids built on the BLYP and PBE GGA functionals do succeed in predicting the experimental value of structural properties such as the lattice parameter and copper-oxygen bond distances, starting from an oversized geometry and reducing it until it is eventually over compressed as more HF exchange is introduced. Even though the BLYP and PBE functionals show a similar trend, BLYP overestimates the PBE values of the lattice parameter throughout the range of HF exchange, and the shortest copper-oxygen bond distance is overestimated by 0.08Å and 0.02Å respectively at the pure DFT limit. The choice of DFT functional, in the role of

reproducing experimentally derived structural properties of CCTO, is therefore important.

Individual properties of CCTO, both structural and electronic, are described best using hybrid functionals with differing amounts of HF exchange. However, for each observable investigated here, hybrid exchange functionals always show a closer match to experiment than predicted by the corresponding pure-DFT study. In order to assess the best-performing functional it is necessary to find a suitable compromise in the description of each individual property. In this respect we note that the difference in the total energy of the FM and AFM structures is best predicted using hybrids with approximately 20% HF exchange. The bulk modulus is generally overestimated and is only described accurately using BLYP with almost pure DFT. The most accurate prediction for the lattice parameter and bond distances is made when using either PBE at approximately 20-30% HF exchange or BLYP at approximately 60% HF exchange. The LDA does not correctly describe the lattice parameter but makes an accurate prediction for the copper-oxygen bond distance at 80% HF exchange.

Overall, the best compromise corresponds to hybrid exchange functionals built on the GGA exchange and correlation formulations of BLYP and PBE and a fraction of HF exchange between 20% and 60%.

7.1.2 Surface Calculations

The ability to study surfaces and interfaces is important as many interesting observations are made there. In the particular case of CCTO, the BLC model suggested to explain the high dielectric constant requires us to understand the electronic structure of surfaces and interfaces. Surfaces are typically complex, defective and often poorly characterised. Therefore, theory has a major role to play in characterising their properties.

In order to investigate the unusual dielectric properties of CCTO, its surface was studied computationally using the same techniques employed for studying the bulk material and discussed earlier. The primary aim of these calculations was to deduce the correct ground electronic state of CCTO surfaces. All surface calculations have been performed

on the FM phase of CCTO, since it is computationally less expensive than the AFM phase, and it has been shown in the bulk to have an identical equilibrium structure. Only the functionals that have been found as best performing in the study of bulk CCTO will be employed here for the CCTO surfaces. These correspond to hybrid-exchange formulations built on the BLYP GGA description and including a fraction of HF exchange between 20% and 60%. This range is justified by our bulk calculations as it was shown to be the best performing in terms of reproducing experimentally derived properties on the bulk of CCTO. It was also concluded that the choice of exchange-correlation functional, on which the hybrids were built, made little difference in terms of reproducing the electronic properties of the bulk. Therefore, only one of the two GGA functionals employed for bulk CCTO will be employed here to study the electronic properties of the surface.

The calculations were performed taking the external 001 surface as the plane of study. A condition for surface stability is the absence of electric dipoles perpendicular to the surface; this is satisfied by the 001 orientation of CCTO in which subsequent planes have composition alternately of $CaCu_3O_4$ and TiO_2, as shown in Figure 7.19. Each of these 001 planes is charge neutral. The 001 surface of CCTO can be cleaved to expose either a $CaCu_3O_4$ plane or a TiO_2 one; in our work we have initially chosen the first option as it is here that the surface chemistry of the Cu^{2+} ions is most likely to affect the properties.

Due the increased expense of surface, compared to bulk calculations it is important to choose an appropriate slab thickness; the slab should however include enough layers to yield converged surface properties.

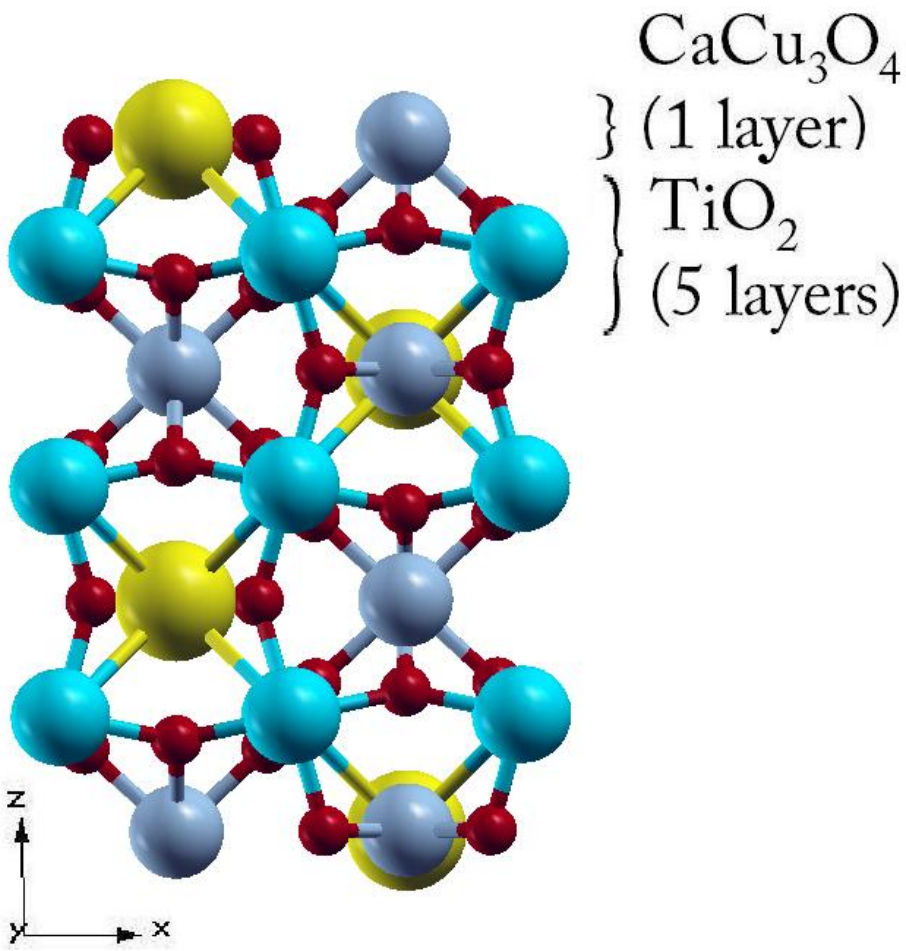

Figure 7.19 001 planes of the CCTO structure in the z direction.

In a surface study, CRYSTAL groups the atoms according to their coordinate (z) perpendicular to the surface orientation. When the CCTO unit cell is oriented in such a way as to have the z coordinate perpendicular to the surface orientation (001 in our case), the atoms of the $CaCu_3O_4$ plane appear at the same z coordinate, while the TiO_2 layer has each atom at slightly non equal z values due to the tilting of the TiO_2 octahedra. In CRYSTAL terminology, each TiO_2 001 plane comprises of 5 atomic layers.

We performed calculations in which both slab surfaces terminate in a $CaCu_3O_4$ layer, and the slab comprises either a plane of symmetry or an inversion operation at the centre. This choice is essential to avoid the appearance of dipole moments perpendicular to the surface. The cations of the outermost layer are arranged as shown in Figure 7.20. The surface unit cell has three Cu ions in the outermost layer, which are labelled as Cu(2), Cu(3) and Cu(4). We compared initially the results obtained with slabs 19 and 25

atomic layers thick (corresponding to approximately 11.1 and 14.8 Å) to examine the convergence of surface properties.

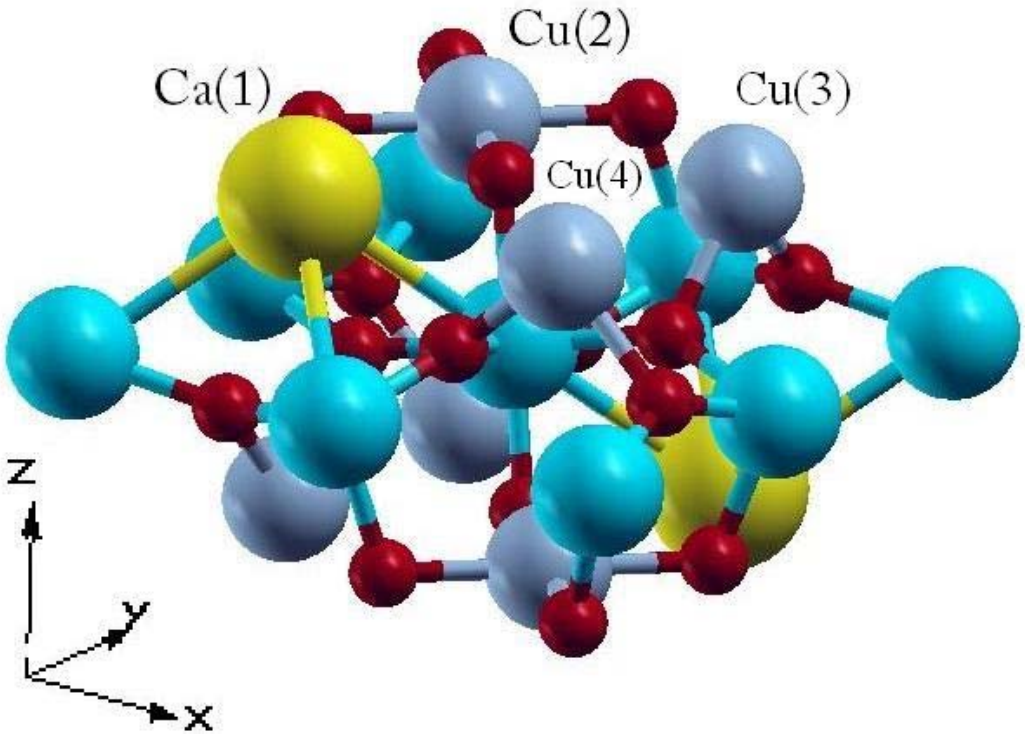

Figure 7.20 Outermost layers at the cleaved 001 surface of CCTO; the Cu and Ca ions exposed at the surface are labelled Ca(1), Cu(2)-Cu(4).

The structural and electronic properties calculated for the two slab thicknesses are almost identical. For example, if we examine the structural data calculated using the $F_{0.4}$BLYP functional, the calcium, copper and titanium to oxygen bonds exposed at the surface were predicted to be 2.61, 1.98 and 1.96Å respectively with both slab thicknesses. The change in position of the three outermost surface coppers with respect to the unrelaxed surface is also very similar using both slab thicknesses: the Cu (3) and Cu (4) atoms drop into the surface by 0.38Å and 0.24Å respectively for a 19 layers slab, and 0.39Å and 0.24Å respectively for a 25 layer slab. The Cu (2) atom is predicted to move outwards from the surface by 0.03Å and 0.02Å for slabs 19 and 25 layers thick respectively.

With respect to the electronic properties, we can see in the form of a DOS plot (Figure 7.21) that the outermost Cu and O ions have very similar contributions in the 19 and 25 layer slabs.

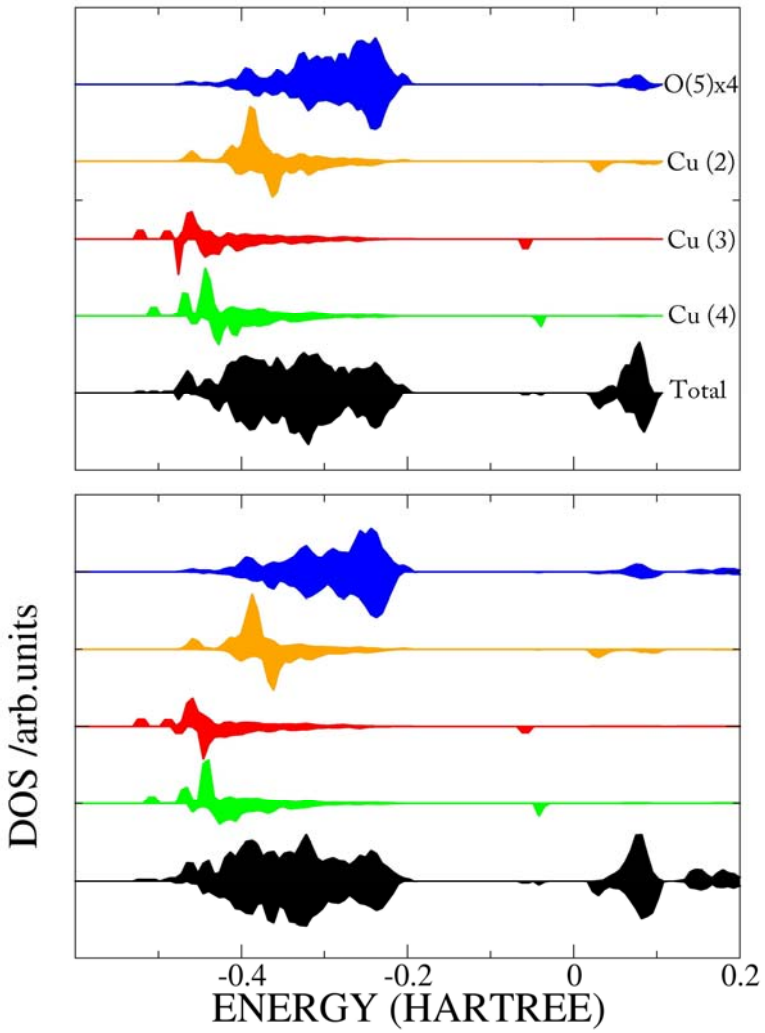

Figure 7.21 Calculated DOS of the 001 surface of CCTO using the BLYP hybrid functional with 40% HF exchange using 19 (bottom) and 25 (top) layer slabs.

The number of unpaired electrons on the three outer Cu^{2+} ions and their atomic spins were identical in 19 and 25 slab layer models. Using 19 layers the net charges were predicted to be 1.718, 1.531 and 1.606|e| while with 25 layers we derived 1.718, 1.532 and 1.606 for Cu (2), Cu (3) and Cu (4) respectively. The spin on these outermost surface coppers was predicted to be 0.788, 0.588 and 0.666|e| using a 19 layer slab and 0.788, 0.588 and 0.666|e| for the 25 layer slab.

The above data show that surface properties have converged for the 19 atomic layer thick slab, and therefore all subsequent studies have been performed with this slab.

Similar to the bulk study, the 001 surface has been investigated with different hybrid exchange functionals; following the bulk results, however, we limit to the range of 20-60% HF exchange and only the BLYP (GGA) DFT functional.

The calculations were performed allowing both structural and electronic relaxation to take place, but the lattice parameters were contrained to those obtained in the bulk calculations (for each functional), as the surface periodicity of a true material is dictated by the lattice parameters of the underlying bulk material.

7.1.2.1 Surface Relaxation

Let us now begin by discussing the structural results. The structure of the first six layers of the surface is presented pictorially in Figure 7.20 where the local environment of the outermost surface coppers can be seen. The Cu (2) ion retains all four short Cu-O bonds of the bulk environment, and is in a square planar environment, while Cu (3) and Cu (4) have just two short Cu-O bonds each oriented away from the surface. In addition, two of the intermediate Cu-O bonds are cleaved in the Cu(3) environment, and two of the long Cu-O bonds for Cu(4). All three copper atoms sit at the same height when the surface is unrelaxed.

Let us now examine the relaxed surfaces. Employing the $F_{0.2}$BLYP hybrid functional, the Cu (2) ion in the optimised structure is predicted to have 4 equidistant nearest neighbour oxygens at 1.88Å, Cu (3) has two short bonds of 1.86Å whilst Cu (4) has two short 1.88Å bonds. The Cu (2) is predicted to stay at its original surface position but Cu (3) and Cu(4) are predicted to drop below the surface by 0.59Å and 0.23Å.

When using the $F_{0.4}$BLYP hybrid functional the Cu (2) is predicted to have 4 equidistant nearest neighbour oxygens at 2.00Å, Cu (3) has two short bonds of 1.80Å whilst Cu (4) has two short 1.85Å bonds. The Cu (2) atom is predicted to move out of the surface by 0.03Å with the Cu (3) and Cu (4) atoms moving into the surface by 0.38Å and 0.24Å respectively upon surface relaxation.

When the $F_{0.6}$BLYP hybrid functional is used the Cu (2) is predicted to have 4 equidistant nearest neighbour oxygens at 1.98Å, Cu (3) has two bonds of 1.98Å whilst Cu (4) has two short 1.82Å bonds. The Cu (2) atom is predicted to move outwards from

the surface by 0.04Å with the Cu (3) and Cu (4) atoms moving into the surface by 0.21Å and 0.24Å respectively. The differences observed with the three functionals are much larger than expected from the early study of bulk CCTO and may indicate a different chemical behaviour of the Cu ions in the three cases.

Let us now discuss the electronic properties, starting with those performed using the F-$_{0.2}$BLYP hybrid functional. The net atomic charges for the copper ions 2, 3 and 4 were predicted to be 1.670, 1.084 and 1.457 respectively. It must be stressed here that we do not expect to achieve formal charges, but these values seem to imply a non equal charge for coppers 2-4. This is corroborated by the spin charges of 0.057, 0.005 and 0.492|e|, where the very small value on Cu(2) and Cu(3) is not compatible with the open shell d^9 configuration of Cu^{2+}. The two Cu involved may possibly have formed a Cu-Cu bond at the surface or disproportionated into Cu^{1+} and Cu^{3+}. The former option is disproved by the negligble Cu(2)-Cu(3) overlap population of 0.000|e| and by their very different net charges. The disproportionation is instead supported by the DOS projected onto the three surface Cu ions (Figure 7.22). The presence of one empty state in both α and β spin levels for Cu(2) shows that this ion is now in 3+ oxidation state, while Cu(3) has no empty d level and is therefore in oxidation state +1. Such a disproportionation is consistent with atomic relaxation, total and spin charges listed in the above structural analysis. The local environment of the three surface copper ions could be the reason behind the disproportionation: the different coordination number of Cu(2) with four nearest neighbour oxide ions at short distance and Cu(3) with only two short bonds splits the relative energy of the respective d levels by a sufficient amount to seed the electron transfer from Cu(2) to Cu(3).

Once we have identified the surface redox behaviour described above, a number of new calculations have been undertaken, with different initial oxidation states for the surface and sub-surface Cu ions; they all converged in the same sequence of Cu^{3+}, Cu^{1+}, Cu^{2+} discussed above, thus increasing our confidence that this is the ground electronic state for the (001) surface. We also performed a study forcing the SCF convergence to a Cu^{2+}, Cu^{2+}, Cu^{2+} surface configuration. This is possible by constraining the number of unpaired electrons in the solution. We found that the Cu^{3+}, Cu^{1+}, Cu^{2+} disproportionation was more stable by 0.362eV. By symmetry there is a disproportionation at both upper and lower surfaces of our slab model and hence the

disproportionation energy of 0.362eV corresponds to that of both surfaces and the disproportionation energy per pair of Cu ions is of 0.181eV. All calculated surface energies will be presented as energy differences for the whole slab (ie. summing the contributions from upper and lower surfaces) throughout this thesis.
The study of disproportionated surfaces with the $F_{0.2}$BLYP functional is further extended to examine the effect of the lattice parameter on the tendency for the surface to disproportionate. This is discussed in section 7.1.2.3.

We now discuss the results using the $F_{0.4}$BLYP functional. Let us examine first the predicted net atomic charges and spins. For coppers 2, 3 and 4 the net charges were predicted to be 1.718, 1.531 and 1.606 and the spins were 0.788, 0.588 and 0.666|e|. In this case the Cu 2-4 arrangement is predicted to be Cu^{2+}, Cu^{2+}, Cu^{2+} and no disproportionation is observed, although the non equal coordination environment of the three copper ions at the surface does effect net and spin charges.

Finally we examine the results from calculations using the $F_{0.6}$BLYP functional. The net atomic charges are predicted to be 1.708, 1.032, 1.717|e| for Cu 2, 3 and 4 respectively, from which we expect to have a Cu^{2+}, Cu^{1+}, Cu^{2+} arrangement.
As Cu^{1+} is closed shell we expect it to have no spin density. The calculation predicts a spin of 0.788, 0.004 and 0.788 on coppers 2, 3 and 4 respectively confirming the Cu^{2+}, Cu^{1+}, Cu^{2+} arrangement. With this arrangement we need one hole for charge balance. The spin charges on the four surface oxygen ions are high (~0.310), so the spin has been put here. Further evidence for the existence of this arrangement is found from the DOS plot in Figure 7.22. This DOS plot shows how copper 3 is the main contributor to the top of the valence band and its levels are shifted at a higher energy compared with the other Cu ions at the surface. This situation is consistent with a reduced Cu^{1+} state of the copper. Using the $F_{0.6}$BLYP functional we observe therefore a charge transfer from the surface oxygens to one of the surface copper ions.
The presence of defect states in the band gap, both in the disproportionated surface obtained with 20% HF exchange and with O to Cu charge transfer achieved using 60% HF exchange, indicates clearly that electron trap states are associated with CCTO surfaces. The n-type semi-conductivity of bulk CCTO is therefore expected to be

destroyed at surfaces, as required for the BLC model for the high dielectric constant of CCTO.

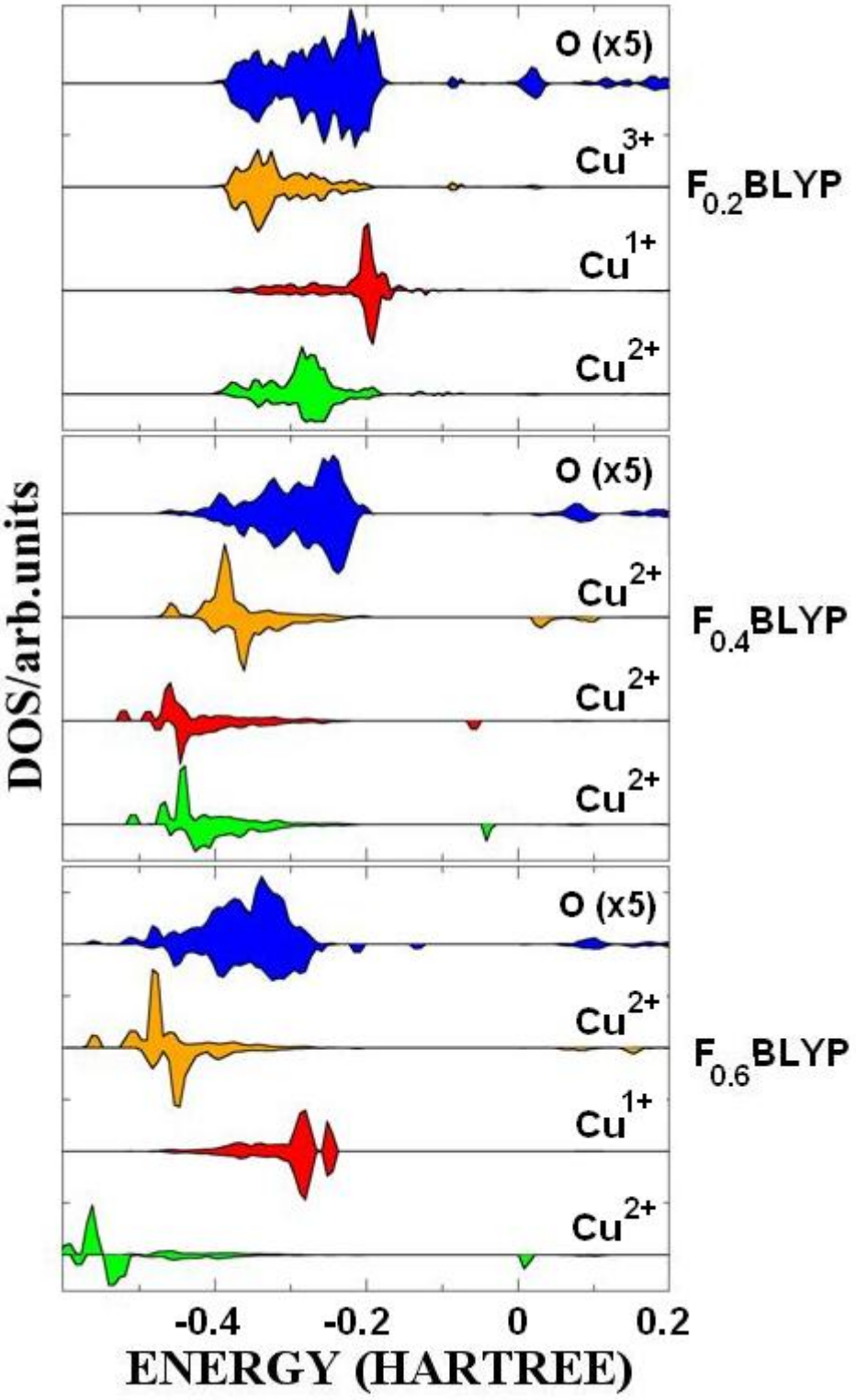

Figure 7.22 DOS Calculated for the 001 Surface of CCTO using the BLYP functional with 20-60% HF exchange.

7.1.2.2 TiO_2 Termination of the 001 Surface

In the previous section we have observed a redox chemistry at the 001 surface of CCTO. We have discovered that surface effects are very sensitive to the choice of theory and we have proposed that they could be due to the way in which the surface has been cleaved. In all of the aforementioned surface calculations, the surface has been cleaved to expose three Cu ions at the outer surface. This leaves one Cu remaining in square planar coordination with four oxygens at a short distance and the other two surface coppers with just two short Cu-O bonds each. In order to investigate the possibility that the observed surface effects are due to the way in which the surface is cleaved, we performed a new set of calculations leaving a TiO_2 (001) layer (shown in Figure 7.19) exposed at the top and bottom layer. These calculations were performed using $F_{0.2}$BLYP, $F_{0.4}$BLYP and $F_{0.6}$BLYP functionals. All computational details remained the same and a slab of 23 layers of thickness (12.2Å) was used (closest to the 19 layer slab used in previous calculations for the new surface cleavage). The Cu ions are now in the subsurface layer and are fully coordinated.

No disproportionation or charge transfer involving the Cu ions in the surface was observed, independently of what theory we use. This is consistent with the model that the surface redox activity of CCTO is due to the local environment of the outermost Cu ions when the surface is cleaved to expose Cu. The result we obtain here is a Cu^{2+}, Cu^{2+} and Cu^{2+} electronic configuration for the equivalent Cu ions that are found to disproportionate in our previous calculations. The DOS for these calculations clarify this result and are displayed in Figure 7.23.

Subramanian et al.[84] first proposed that the origin of the high dielectric constant observed in CCTO is a barrier layer mechanism related to the ceramic microstructure. Sinclair [113] et al. later provided evidence for the barrier layer model via in depth analysis of the materials microstructure obtained by impedance measurements, however the subject is still a matter of controversy. The results we have presented here provide a strong case for the high dielectric constant being rationalised by a barrier layer capacitor model. In the previous section we have reported evidence of redox chemistry being present at the 001 surface of CCTO which would generate defect states in the surface band gap. These would trap mobile charge carriers at the surface and therefore support the proposed BLC model. The results presented here, where TiO_2 layers are exposed at

the surface, indicate clearly that a disproportionated surface would most likely require Copper containing layers to be exposed. We therefore expect that the terminating layer in the stable surfaces are important to the materials dielectric properties. The schematic of Figure 7.24 outlines how our model supports the BLC model.

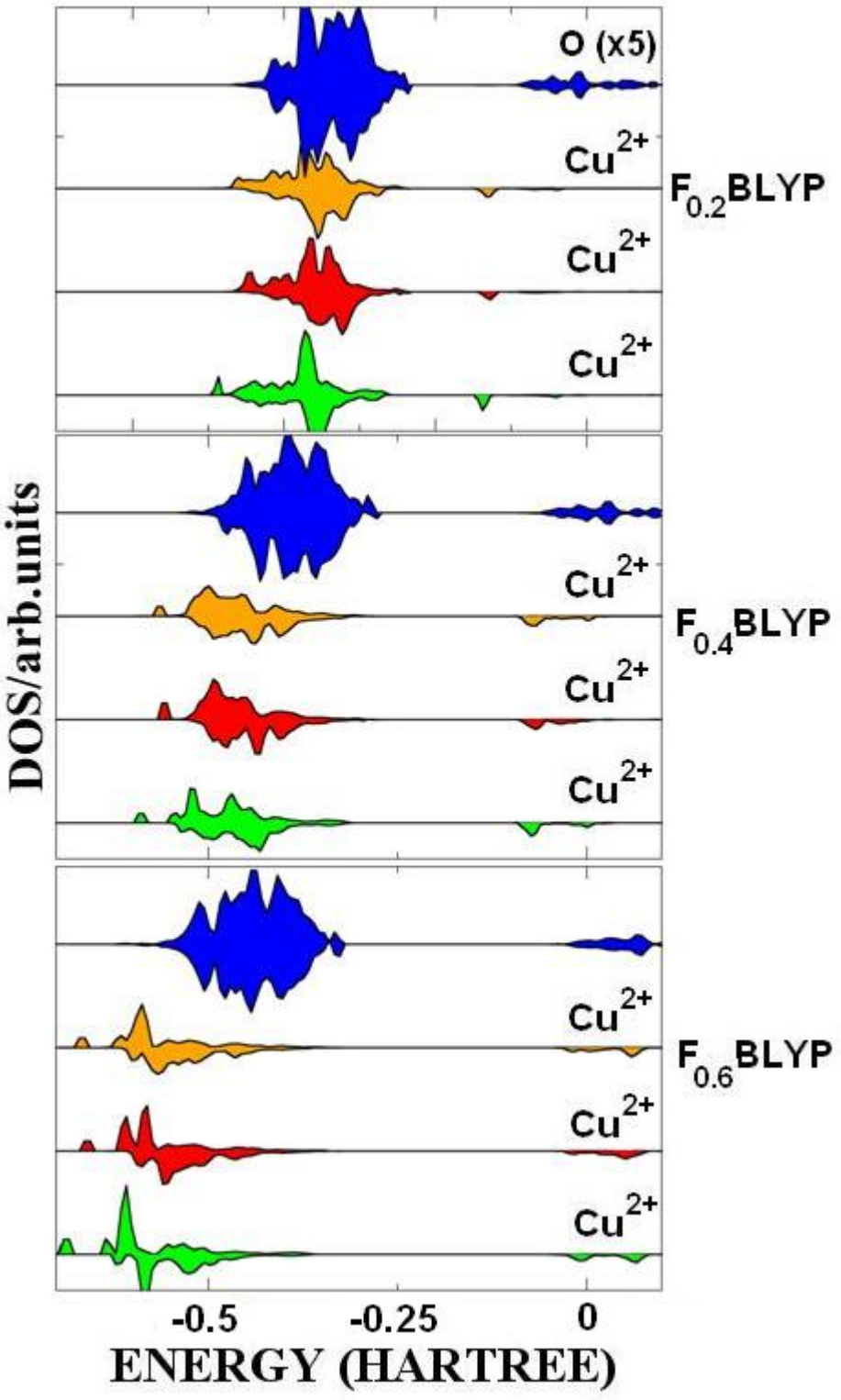

Figure 7.23 DOS for the 001 Surface of CCTO cleaved to expose TiO_2 units. These calculations have been performed using the BLYP functional with 20, 40 and 60% HF exchange.

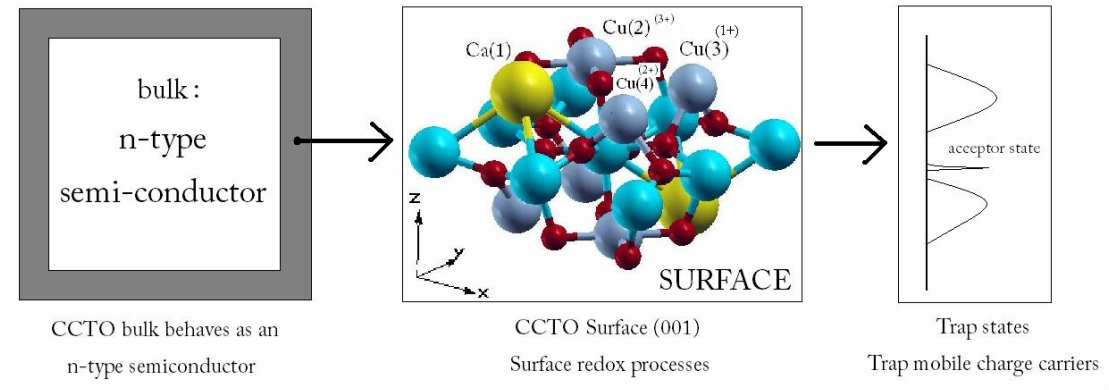

Figure 7.24 Schematic showing how the observed chemistry at the 001 surface of CCTO supports the IBLC model.

7.1.2.3 Effect of Lattice Constant on Surface Electronic Properties

In section 7.1.2 we have shown evidence for a self disproportionation of Cu ions at the 001 surface of CCTO, and have shown how this effect is due to the different coordination environment of the outermost Cu ions generated by the surface cleavage. The crystal-field splitting of the Cu^{2+} d levels may be expected to depend on the distance between Cu and its neighbouring oxygens, and in practice on the lattice parameter of the solid. The latter may be varied experimentally by doping, for instance replacing a fraction of the Ca^{2+} ions with smaller Mg^{2+} or larger Sr^{2+} ions. Reports exist that such modifications of the composition do indeed influence the effective dielectric constant of doped CCTO ceramics[114-117], and it is therefore of interest to understand the effect of a change in the lattice parameter on the stability of the surface disproportionation investigated earlier.

We performed surface calculations (with Cu exposed at the surface) on the 001 surface of CCTO at varying lattice parameter between 7.35Å and 7.55Å. The rest of the geometry was allowed to relax in each case. The initial geometry for each calculation was taken from a geometry optimisation on the bulk structure at fixed lattice parameter. For each lattice parameter two calculations were performed. In one, the electronic configuration was started at the stable Cu^{3+}, Cu^{1+} and Cu^{2+} disproportionation discussed earlier and the other was held to Cu^{2+}, Cu^{2+} and Cu^{2+} for Cu(2), Cu(3) and Cu(4) respectively (Figure 7.20). From this set of data, we can investigate the dependence of

disproportionation on the lattice constant. These calculations were all performed using the $F_{0.2}$BLYP, as this is the choice of theory that predicted the surface disproportionation in our original calculations. The results are shown in Figure 7.25 below.

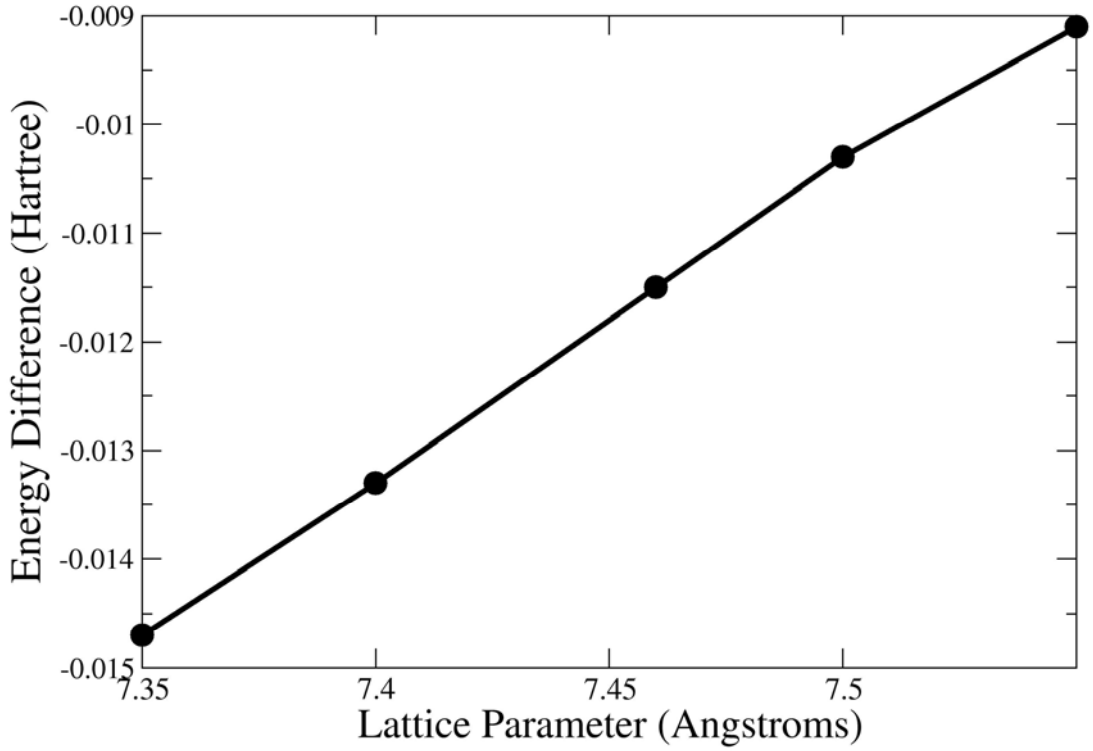

Figure 7.25 Energy difference between calculations converged with surface Cu ions in configuration 2^+, 2^+, 2^+ and those converged to the disportionated 3^+, 1^+, 2^+ state against the lattice constant.

These results confirm the disproportionated 001 surface as the stable ground state for CCTO over a range of lattice parameters; they also show a clear dependence of disproportionation energy on lattice spacing, thus confirming our analysis that the driving force for disproportionation is the different crystal field splitting of the Cu^{2+} levels at the different surface sites. Increasing the lattice parameter of CCTO makes the outermost surface Cu ions less likely to disproportionate, and vice versa. The more we compress the structure, the more the surface is likely to disproportionate. By extrapolating from these results, we predict that a 2+,2+,2+ surface will be more stable when the lattice parameter exceeds approximately 7.86Å, well above the equilibrium

value for CCTO of 7.384Å, but also larger than any change than can be achieved by doping CCTO.

7.1.2.4 Conclusions on the CCTO 001 surface

The 001 surface of CCTO was studied using a slab model, with a thickness of 19 layers. The BLYP functional was employed with three different amounts of HF exchange ($F_{0.2}$BLYP, $F_{0.4}$BLYP and $F_{0.6}$BLYP) and the surface chemistry was predicted to be different in each case. Redox chemistry was observed using 20% HF, yielding Cu^{1+}/Cu^{3+} ions at the surface, 40% predicted a Cu^{2+}, Cu^{2+}, Cu^{2+} arrangement of the outermost surface coppers, and using 60% we observed charge transfer from oxygen to copper. The observed behaviour is attributed to the local environment of the copper atoms. This theory is backed by our calculations on the 001 surface of CCTO where Ti is exposed at the surface. These calculations show that when Cu is not directly exposed at the surface and all Cu ions are in square planar coordination with four short Cu-O bonds, no disproportionation is observed. We also observed that if we compress the lattice parameter of CCTO the surface becomes more likely to disproportionate.

It is clear the way we define forces has a big impact on the surface electronic structure. However, an active redox chemistry of the CCTO surface is common to all three hybrid functionals in our work.

The stability of different copper oxidation states enables a rationalisation of the colossal dielectric constant experimentally observed in CCTO ceramics. The redox chemistry generates defect states in the band gap at the surface, which effectively trap any mobile charge carrier at the surface, thus supporting the internal barrier layer capacitor model (BLC) as the origin of the dielectric properties.

In the following sections we shall perform studies into materials isostructural to CCTO, such as $CdCu_3Ti_4O_{12}$ (CdCTO) and $CaCu_3Ge_4O_{12}$ (CCGO) and investigate their surface chemistry. The former (CdCTO) has a dielectric constant (K) of 409[84] while the dielectric constant of the latter (CCGO) has not yet been reported in the literature. Comparing calculated results for isostructural materials that do and do not display colossal dielectric screening may shed further light onto the origin of this behaviour.

7.2 $CdCu_3Ti_4O_{12}$ (CdCTO)

Here and in the following sections, we discuss a number of materials isostructural to CCTO, that have been investigated during this PhD. One example of these is $CdCu_3Ti_4O_{12}$ (CdCTO)[83, 84, 102]. CdCTO has the same crystal structure as CCTO but yet displays a different dielectric constant of 409[118]. The difference between CCTO and CdCTO ceramics has been addressed in several studies, with the goal of shedding light on the mechanism driving the high dielectric constant of CCTO. Holmes et al.[118] for example, compared the optical conductivity of CCTO and CdCTO. The only real difference they discovered was the extent of the charge transfer from Ca/Cd to O atoms, which cannot account for the large difference in dielectric constant. He et. al.[119] looked at the lattice dielectric response of CCTO and CdCTO from first principles. They concluded that there was no fundamental difference in their intrinsic properties. Also, Ma et. al.[120] looked at CdCTO under pressure (up to 55.5GPa) and compared its compressibility to that of CCTO. Again this work did not unveil the mechanism that effects the different permittivity.

The structure of CdCTO is well known and has been refined to the Im3 space group. Just like CCTO, it exhibits a perovskite like supercell structure with two elements (in this case Cd and Cu) on the A sites, Ti on the B site and O in the Z site. CdCTO is also an AFM insulator[121] and thus requires a double unit cell to accommodate its spin structure.

7.2.1 Bulk CdCTO

In section 7.1 we reported the computational study of the bulk structure and surface properties of CCTO. We found that the electronic structure of the 001 surface depends on the choice of theory. However, we do observe some redox chemistry which can rationalise the giant dielectric constant in CCTO by supporting the proposed BLC model. We acknowledge that the observed effect could be related to the way in which the surface has been created by cleaving the bulk to expose three Cu ions in differing

coordination environments. For this reason we have studied the surface of CdCTO which is isostructural to CCTO but does not exhibit such a large dielectric constant.

As for CCTO, also for CdCTO we first studied the bulk material using a range of hybrid functionals in order to deduce the best definition of forces in bulk CdCTO, and then apply to the description of the surface. The range of functionals used and the computational details are the same as outlined in section 7.1.1, and results of geometry optimisations on the bulk solid are summarised in Table 7.8-Table 7.10 below. The symbols and units are as in Table 7.1.

Table 7.8 FM Results for the hybrids built on the LDA functional. All symbols and units are as in Table 7.1.

HM%	a_o	X_o	Y_o	R_{cu-o}	R'_{cu-o}	R_{cd-o}	R_{ti-o}	ΔE	q_{cu}	q_o	q_{ti}	$spin_{cu}$	$spin_o$
0	7.312	0.3062	0.1773	1.921	2.752	2.587	1.948	6.13	1.58	-1.27	2.32	0.525	0.096
20	7.312	0.3051	0.1791	1.935	2.746	2.587	1.943	0.94	1.64	-1.33	2.41	0.663	0.074
40	7.317	0.3044	0.1802	1.947	2.742	2.589	1.940	0.26	1.71	-1.38	2.50	0.775	0.051
60	7.326	0.3035	0.1826	1.961	2.740	2.592	1.939	0.09	1.77	-1.43	2.57	0.853	0.034
80	7.338	0.3027	0.1833	1.975	2.739	2.596	1.938	0.05	1.81	-1.47	2.64	0.900	0.024
100	7.351	0.3020	0.1847	1.988	2.740	2.600	1.938	0.03	1.84	-1.50	2.71	0.927	0.018

Table 7.9 FM Results for the hybrids built on the BLYP functional. All symbols and units are as in Table 7.1.

HM%	a_o	X_o	Y_o	R_{cu-o}	R'_{cu-o}	R_{cd-o}	R_{ti-o}	ΔE	q_{cu}	q_o	q_{ti}	$spin_{cu}$	$spin_o$
0	7.529	0.3051	0.1797	1.996	2.823	2.666	1.999	3.26	1.57	-1.30	2.41	0.552	0.095
20	7.466	0.3045	0.1806	1.987	2.796	2.643	1.980	0.58	1.65	-1.36	2.49	0.690	0.070
40	7.416	0.3040	0.1814	1.981	2.774	2.625	1.964	0.18	1.72	-1.40	2.55	0.796	0.047
60	7.375	0.3035	0.1822	1.977	2.756	2.611	1.951	0.08	1.78	-1.44	2.60	0.863	0.032
80	7.341	0.3029	0.1828	1.974	2.742	2.597	1.940	0.05	1.81	-1.46	2.64	0.900	0.024
100	7.307	0.3025	0.1835	1.970	2.726	2.586	1.929	0.05	1.83	-1.49	2.67	0.922	0.019

Table 7.10 FM Results for the hybrids built on the PBE functional. All symbols and units are as in Table 7.1.

HM%	a_o	X_o	Y_o	R_{cu-o}	R'_{cu-o}	R_{cd-o}	R_{ti-o}	ΔE	q_{cu}	q_o	q_{ti}	$spin_{cu}$	$spin_o$
0	7.461	0.3052	0.1796	1.977	2.798	2.642	1.981	3.37	1.59	-1.31	2.40	0.559	0.091
20	7.404	0.3044	0.1806	1.971	2.773	2.621	1.963	0.60	1.66	-1.36	2.48	0.695	0.067
40	7.357	0.3040	0.1815	1.965	2.751	2.605	1.948	0.19	1.74	-1.40	2.53	0.799	0.045
60	7.318	0.3034	0.1825	1.963	2.733	2.591	1.935	0.08	1.79	-1.43	2.58	0.864	0.031
80	7.285	0.3029	0.1834	1.962	2.717	2.579	1.924	0.05	1.82	-1.46	2.61	0.901	0.023
100	7.256	0.3024	0.1839	1.959	2.705	2.568	1.915	0.03	1.84	-1.48	2.65	0.923	0.018

Observed trends and comparisons to experiment are discussed separately for structural and electronic properties in the following sub sections.

7.2.1.1 Structural Properties

Let us start by presenting the equilibrium lattice parameter and Cu-O, Ti-O and Cd-O bond distances in graphical form, highlighting and discussing the differences between these results and those obtained for CCTO.

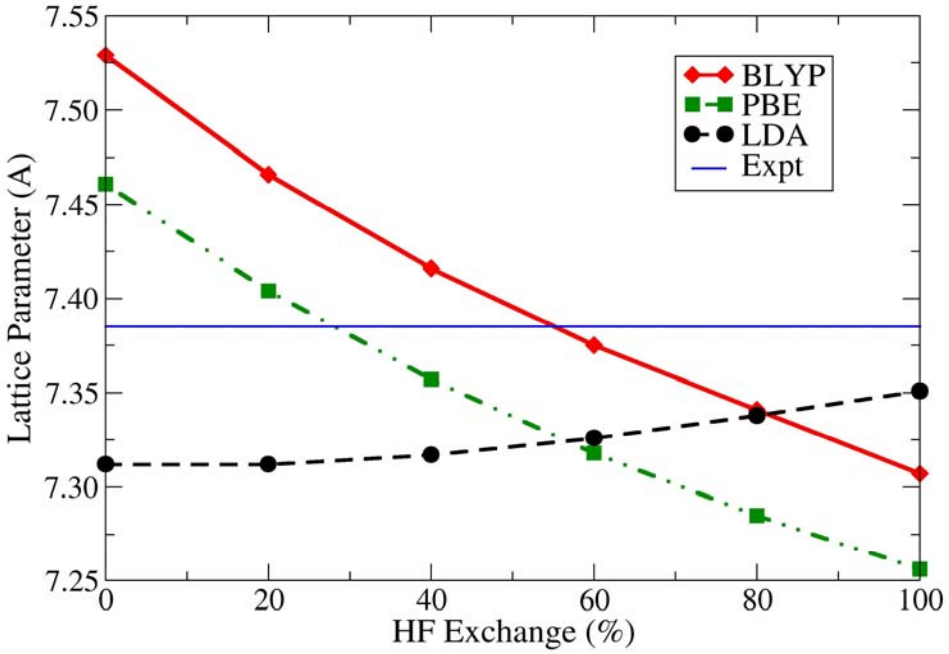

Figure 7.26 Equilibrium lattice paramater against HF mixing for the BLYP, PBE and LDA functionals.

The experimentally derived lattice constant of CCTO and CdCTO are very similar and we can see here that the hybrid functionals make almost identical predictions for the two cases, with the most accurate prediction achieved using the PBE and BLYP functionals between 20 and 60% HF exchange.

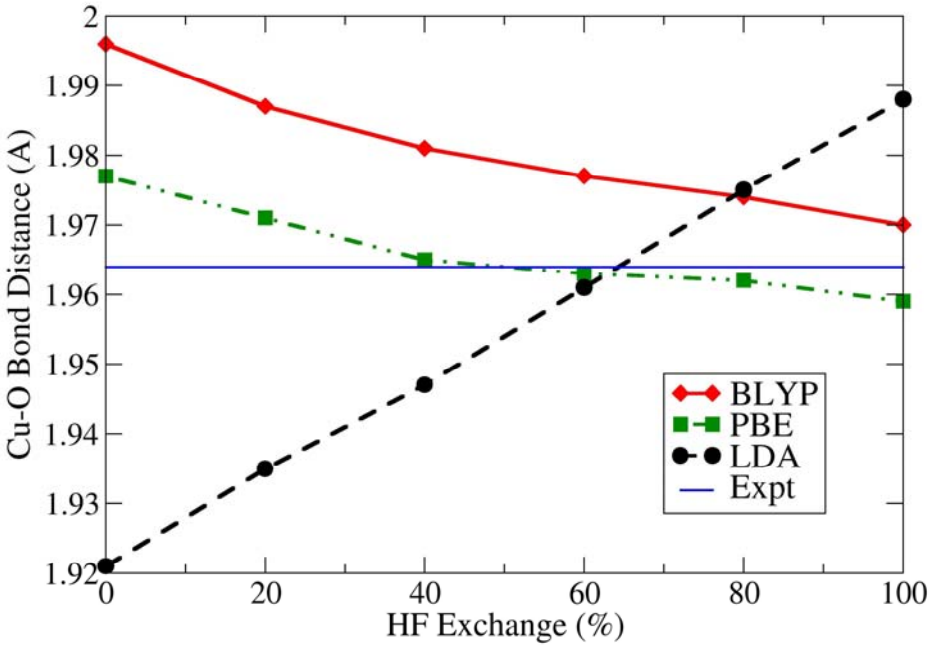

Figure 7.27 Shortest Copper-Oxygen bond distances against the fraction of HF exchange for the BLYP, PBE and LDA.

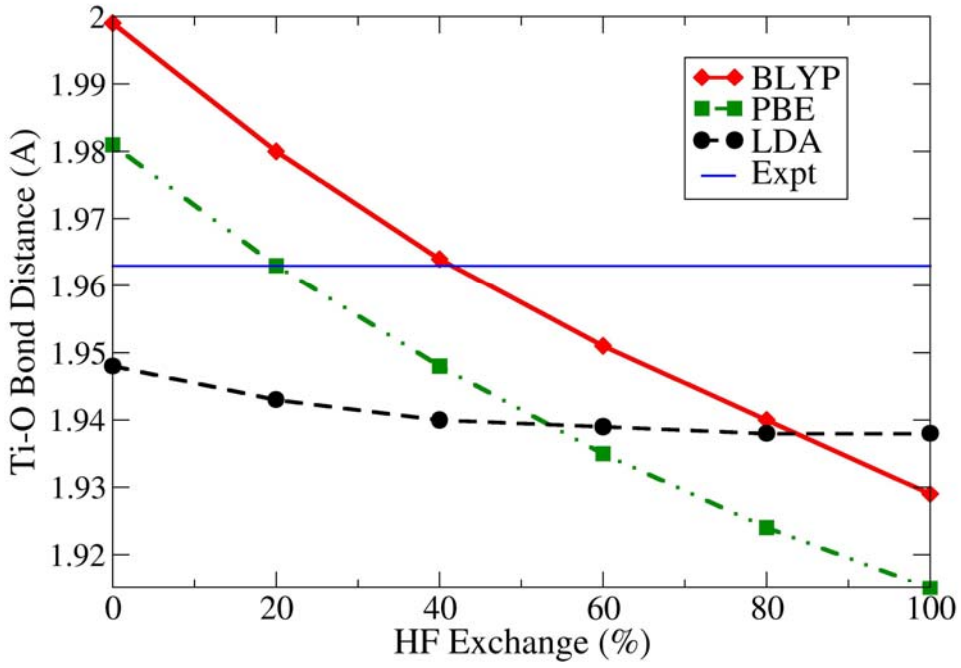

Figure 7.28 Titanium-Oxygen bond distances against the fraction of HF exchnage for the BLYP, PBE and LDA.

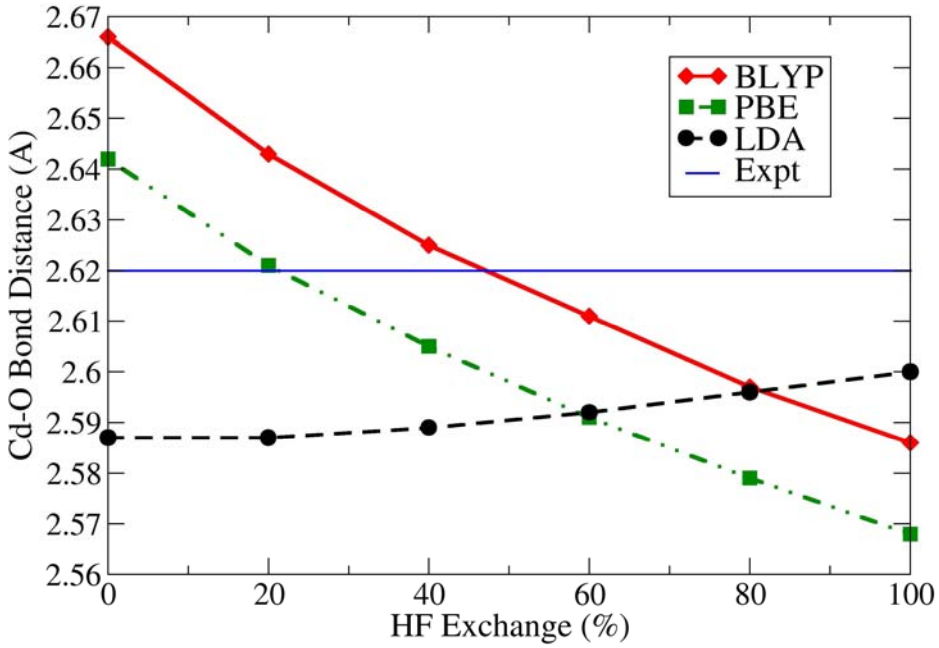

Figure 7.29 Cadmium-Oxygen bond distances against the fraction of HF exchange for the BLYP, PBE and LDA.

As was the case with CCTO, the structure was imposed in our calculations to belong to the Im3 space group. We however confirmed that this is a proper minimum via Γ-point phonon calculations.

The experimentally derived bond distances are very similar for the cases of CCTO and CdCTO. It can be seen from the above graphs that the PBE, BLYP and LDA functionals make almost identical predictions for the two materials. These findings are consistent with the literature[118, 119], which reports no structural difference between the two materials. There is therefore no structural consideration that could explain the intriguing difference between their dielectric constants.

The bulk modulus of CdCTO obtained using the PBE, BLYP and LDA functionals with 40% HF exchange are 249, 250 and 262GPa respectively, which are consistent with that derived experimentally by Yanzhang et al.[122] of 235±7 GPa. The corresponding values for CCTO are 220, 209 and 259 for the respective functionals and the experimentally derived value being 212GPa.

7.2.1.2 Electronic Properties

Similar electronic properties were observed in CdCTO as they were in CCTO. We start by looking at the energy difference between the FM and AFM phases, illustrated, for the full range of hybrid functionals, in Figure 7.30. Here the experimental value has been calculated from the experimentally known Neel temperature (25K) and by using the Ising model with the mean field approximation as outlined in section 7.1.1.4.

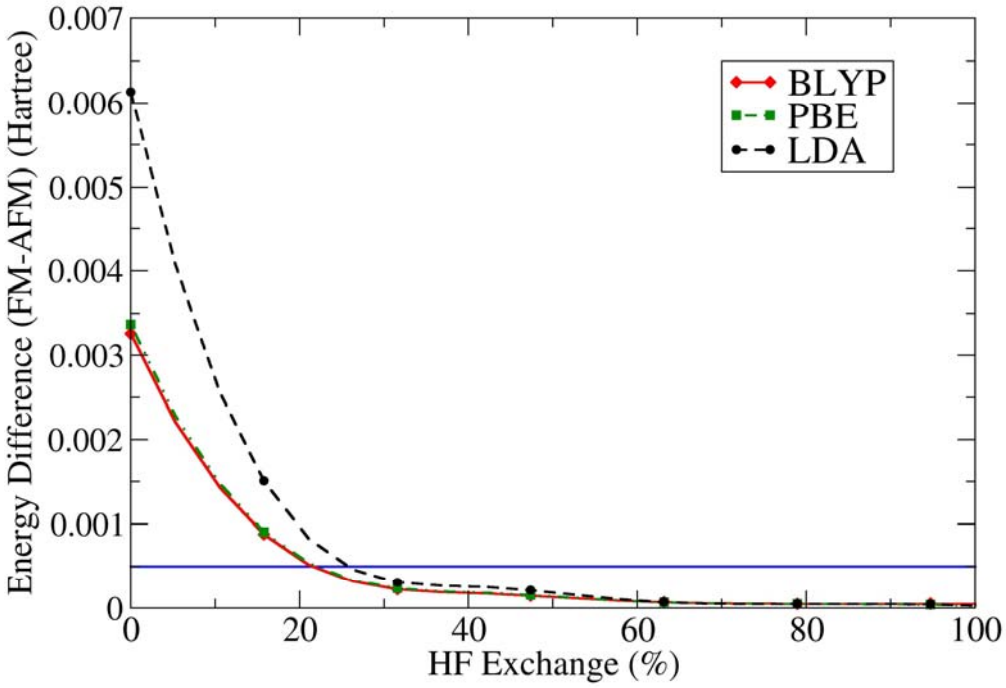

Figure 7.30 FM and AFM phase energy difference as a function of HF exchange for the BLYP, PBE and LDA functionals.

Our calculations confirm the AFM phase of CdCTO as the most stable. The results are also in agreement with those of CCTO, confirming that the choice of local DFT functional is not critical in describing the bulk electronic properties, however results are sensitive to the amount of HF exchange included. The best correspondence to experiment is found at approximately 25% HF exchange. We should also note here that similarly to the case of CCTO, the above trend for CdCTO is what we expect for a superexchange-type of interaction.

Let us now discuss the DOS calculated for CdCTO, limiting our discussion here to results obtained using the BLYP functional, and between 20-60% HF exchange. Results are shown in Figure 7.31.

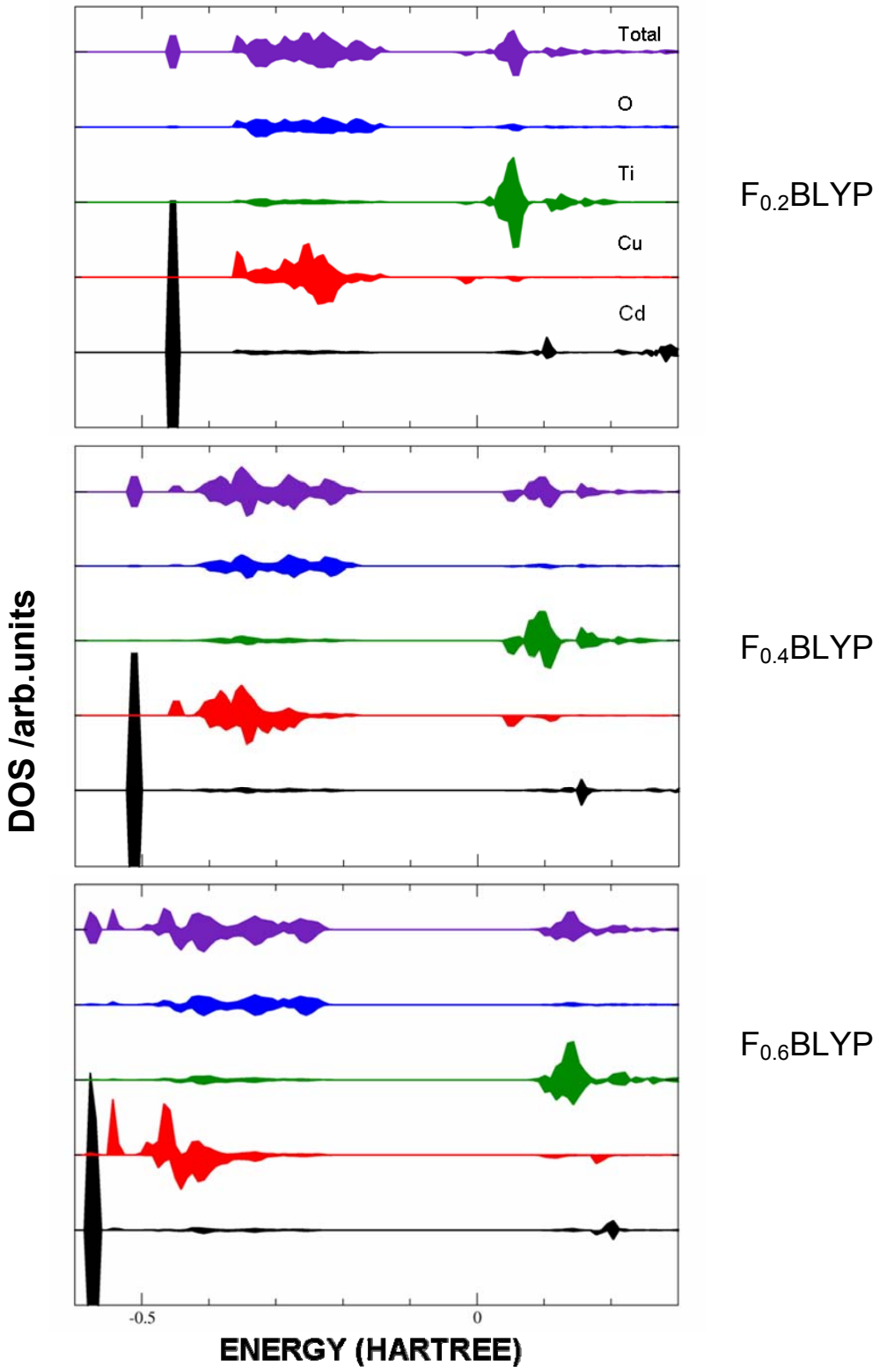

Figure 7.31 Density of States of bulk CdCTO using the BLYP hybrid functional at 20, 40 and 60% HF exchange from top to bottom. The contribution of Cd, Cu, Ti, O to the DOS and its total value are shown separately with the total divided by ten for ease of presentation.

The main difference between CCTO and CdCTO in terms of the density of states relates to the Ca/Cd contribution. In CCTO there is a large contribution to the conduction band by the calcium ions, while Cd has a semi-core band due to the 3d electrons which are relatively low in energy, but has a non-zero contribution to the valence and conduction bands. This feature, however, does not affect the Cu-Ti-O states that are virtually identical in CCTO and CdCTO. The calculated band gap has minor differences; for instance at the $F_{0.4}$PBE level it is calculated as 6.19eV in CCTO and 5.75eV in CdCTO. This is, however, unlikely to affect the electronic structure. The rest of the DOS states in CdCTO are almost identical to the case of CCTO with no significant differences.

One of the few differences between CCTO and CdCTO can be seen in the net atomic charge on the Ca/Cd ions, tabulated below for a range of functionals, which indicates a more covalent Cd-O than Ca-O interaction, consistently with the DOS analysis given earlier.

Table 7.11 Net atomic charges on the Ca and Cd atoms of CCTO and CdCTO respectively.

Functional	q_{Ca}	q_{Cd}
F0.2-PBE	1.718	1.387
F0.4-PBE	1.762	1.468
F0.6-PBE	1.798	1.538
F0.2-BLYP	1.715	1.389
F0.4-BLYP	1.759	1.468
F0.6-BLYP	1.794	1.537

.

The significant difference seen in the net atomic charges on the Ca/Cd atoms is consistent with that reported in the literature by Holmes et al.[118] and Matos et al. [123], although the difference reported in reference [123] was greater than that we found here (q_{Ca}-q_{Cd} ~1).

To conclude on the electronic properties of bulk CdCTO, we have first confirmed that the stable order is AFM. We have also shown that there are no intrinsic differences between CCTO and CdCTO which could rationalise the large difference in their dielectric constants.

In the same way as observed in our calculations on CCTO, the use of hybrid functionals has helped in gaining a better agreement with the experimentally observed properties of bulk CdCTO, than standard DFT.

Following the analysis of the structural and electronic properties we can conclude that the best range of theory consists in the use of either the BLYP or PBE functional in the range of 20-60% HF exchange. Therefore, in the same way as was done with CCTO, we shall use the BLYP functional with 20, 40 and 60% HF exchange for performing a study of the CdCTO 001 surface. We hope that this will shed light onto the redox chemistry we observed during our study of CCTO.

In agreement with other studies on bulk CdCTO, we have seen that there is little intrinsic difference between this material and CCTO. The fact that CCTO displays a very large dielectric constant and CdCTO does not, casts further support on the conlcusions that the mechanism behind this property is extrinsic, such as the formation of boundary-layer capacitors.

7.2.2 Surface Calculations

We used the same computational method as described for CCTO in section 7.1.2 to study the 001 surface of CdCTO. Let us begin by discussing the structural results from these calculations.

The structure of the first six layers of the surface is essentially the same as in the case of CCTO (with Ca replaced with Cd) and therefore, Figure 7.20 will serve the purpose of displaying the local environment of the outermost surface copper ions. The surface has been cleaved in the same way as for CCTO, leaving Cu(2) in square planar coordination and Cu(3) and Cu(4) with only two short bonds. We observed the same relaxation in the case of CdCTO as we did for CCTO, using all three hybrid functionals, and therefore have no substantial structural differences to note.

Let us now discuss the electronic properties. We start with those performed using the F-$_{0.2}$BLYP hybrid functional. The net atomic charges for Cu 2, 3 and 4 were predicted to be 1.669, 1.092 and 1.459 and the spins 0.043, 0.005, 0.492 respectively.

This is similar to the prediction for CCTO with a Cu^{3+}, Cu^{1+}, Cu^{2+} disproportionation observed at the 001 surface. Using the $F_{0.4}$BLYP functional the net charges were predicted to be 1.715, 1.538 and 1.608 with spins of 0.785, 0.594 and 0.667 for Cu 2, 3 and 4 respectively. Again this is similar to CCTO and a Cu^{2+}, Cu^{2+}, Cu^{2+} arrangement is observed. Finally, the results from calculations using the $F_{0.6}$BLYP functional predict the Cu ions to have 1.715, 1.034, 1.712 net charges with spins of 0.798, 0.003 and 0.781 respectively, yielding a Cu^{2+}, Cu^{1+}, Cu^{2+} arrangement which is identical to that of CCTO. This is seen more clearly in the DOS plot of figure 7.32.

Upon comparing the disproportionation energy at the 001 surface of CCTO with that achieved at the equivalent surface of CdCTO, described above, we do however find that the CCTO disproportionation energy is much larger (0.362eV) than that of CdCTO (0.113eV). Therefore the disproportionation observed at the surface of CCTO is energetically more stable than we predict for the CdCTO surface, indicating that the surface-layer effect is more pronounced in CCTO than in CdCTO. This is the only indication in support of the different dielectric constant observed for the two materials, and is once more consistent with the BLC model.

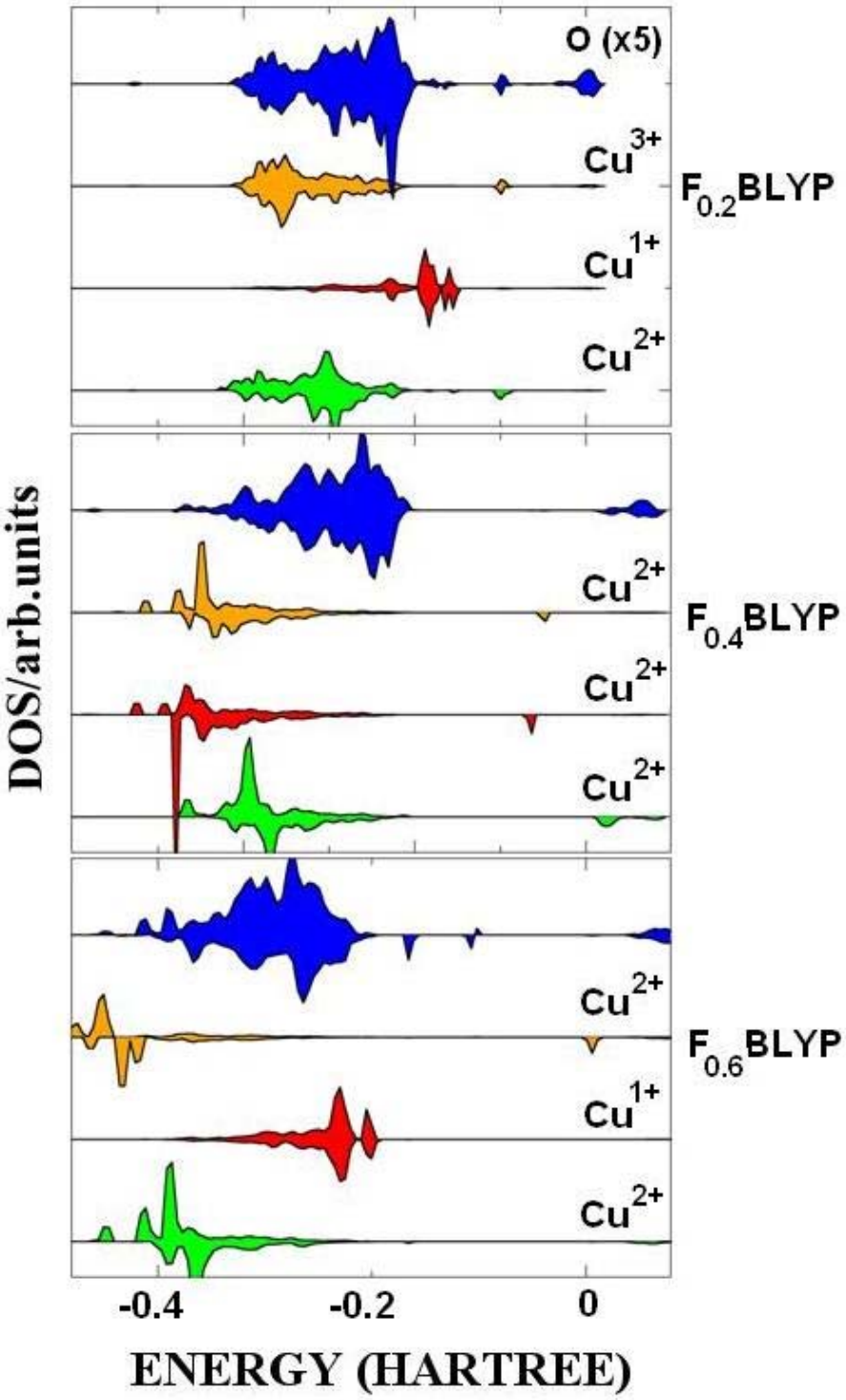

Figure 7.32 DOS calculated for the 001 surface of CdCTO using the BLYP functional with 20-60% HF exchange.

We can also compare the spin density on the 001 surface of CCTO and CdCTO. This is shown in Figure 7.33.

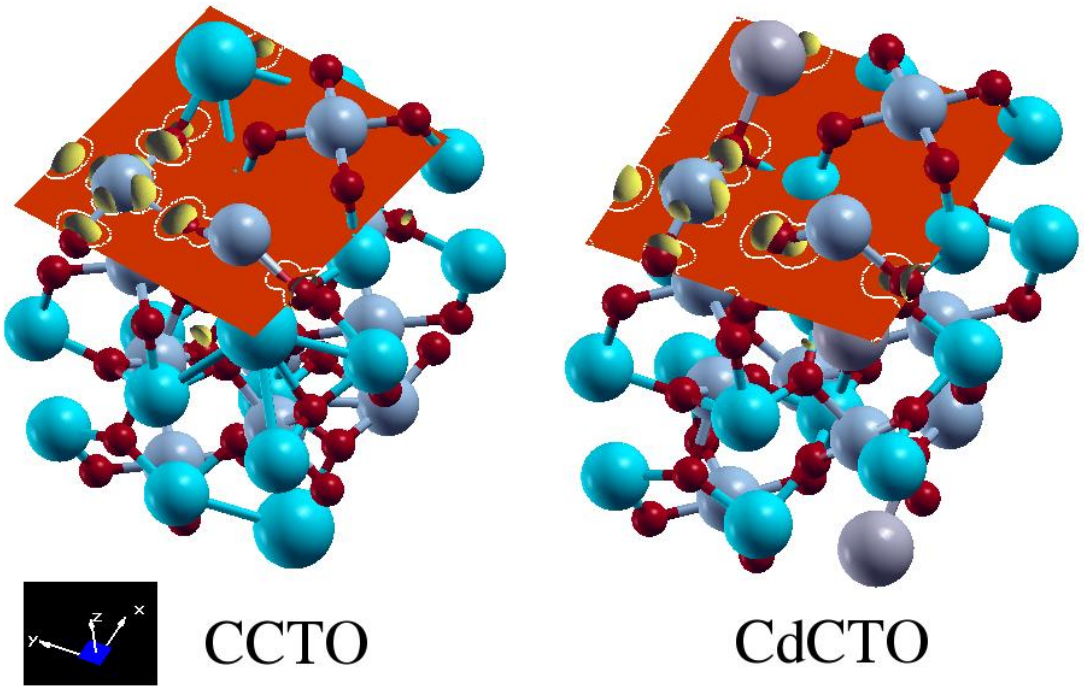

Figure 7.33 Spin density on the 001 Cu exposed surface of CCTO and CdCTO. Calculated with the $F_{0.2}$BLYP functional. The spin density with a value of 0.005 $e^-/Å^3$ is shown in yellow; a 2D projection parallel to the surface is also shown through a set of surface oxygens.

The figure confirms that there is little difference between the spin density at the surface of CCTO and CdCTO; however the Cd ion appears more polarisable than Ca; for instance the isodensity lines in the 2D projections on the oxygen between Cu(4) and Cd ions are more symmetric than between Cu(4) and Ca in CCTO. In figure 7.33 we can clearly see the spin density on the Cu(4) ion while the other two surface Cu ions are closed shell and with little spin density, providing further evidence of the surface disproportionation.

In our view the reduced stability of the surface disproportionation in CdCTO compared to CCTO is due to the higher polarisability of the Cd ions at the surface, that confer greater electronic flexibility to the 2+, 2+, 2+ structure of CdCTO compared to CCTO.

7.2.2.1 Conclusions on CdCTO

A similar study to that performed on the surface of CCTO was performed on the surface of CdCTO. The 001 surface was studied with a slab thickness of 19 layers. The same

dielectric behaviour is observed for bulk CCTO and CdCTO, but our calculations also show that the disproportionation of surface Cu^{2+} pairs into Cu^{1+} and Cu^{3+}, crucial for the BLC behaviour, is much more favourable for CCTO than for CdCTO. Therefore the different dielectric constant of CCTO and CdCTO may be attributed to the different surface chemistry. The chemical composition of surfaces and interfaces may further explain the difference; we consider that the difference in the dielectric constants could, at least in part, be attributed to the layer in which the stable surface terminates and depend on the relative amount of Cu ions directly exposed at the surface.

7.3 $CaCu_3Ge_4O_{12}$ (CCGO)

Another $AA'_3B_4Z_{12}$ type perovskite isostructural to CCTO and well characterised experimentally is $CaCu_3Ge_4O_{12}$ (CCGO)[124]. The specific interest in CCGO lies in its ferromagnetic ground state, with a Curie temperature of 13K [125]. No report of unusual dielectric properties exists for CCGO.

Ferromagnetism in CCGO was discovered experimentally and then confirmed by first principle calculations[125]. A FM ground state of the Cu^{2+} spins within the perovskite structure is of particular technological interest and is very rare in the literature.

CCGO is isostructural to CCTO and hence belongs to the Im3 space group with Ca and Cu ions occupying the A (at the ratio 1:3) site in a double cubic unit cell. The Cu ions form CuO_4 planes which are perpendicular to one another and Ge is octahedrally coordinated by O ions with the GeO_6 tilted to enable the square planar coordination of Cu^{2+}, as in CCTO.

7.3.1 Structural and electronic properties of Bulk CCGO

In earlier sections dedicated to AFM perovskite compounds, CCTO and CdCTO, the use of hybrid functionals has been shown to lead to better agreement with experiment than standard DFT with respect to the structural and electronic properties. In this section we extend our hybrid DFT study to the FM perovskite CCGO, and specifically aim to understand the reason for the different magnetic ground state. Comparison of CCTO

and CCGO may provide a useful additional test for the hybrid functionals. As for CCTO and CdCTO we shall examine the Cu-terminated 001 surface of CCGO to investigate if the same surface redox chemistry discussed for CCTO and CdCTO is also available for CCGO. It is further of interest to understand if the surface chemistry can disrupt the FM coupling among Cu^{2+} ions.

As for CCTO and CdCTO we shall employ a full range of HF exchange fraction in the study of bulk CCGO, but limit surface calculations to those providing the best match to experiment. The basis set for Ge is an all electron (97631/7631/61) contraction taken from the online database of the code and originally derived to study Ge^{4+} ions in framework oxides such as Ge-doped zeolites, GeS_2 and GeO_2[126].

Full geometry optimisations have been performed on bulk CCGO, and results summarised in Table 7.12-Table 7.14, divided by the choice of exchange-correlation functional. Results only cover the range of 0-60% HF exchange due to the difficulty in converging calculations employing a higher fraction of HF exchange. We have seen in previous sections, however, that the most relevant change is between 20 and 60% which is covered here for CCGO. Only the FM phase has been studied with hybrids built on the LDA.

Table 7.12 FM Results for the hybrids built on the BLYP functional. Symbols and units as in table 7.1.

HM%	a_0	X_O	Y_O	R_{Cu-O}	R'_{Cu-O}	R_{Ca-O}	R_{Ge-O}	ΔE	q_{Cu}	q_o	q_{Ge}	$Spin_{Cu}$	$Spin_O$
0	7.389	0.3014	0.1835	1.998	2.761	2.607	1.949	-0.49	1.57	-1.00	1.41	0.596	0.099
20	7.298	0.3010	0.1852	1.984	2.718	2.579	1.921	-0.16	1.64	-1.08	1.57	0.704	0.073
40	7.228	0.3005	0.1867	1.975	2.685	2.557	1.899	-0.04	1.72	-1.15	1.73	0.797	0.050
60	7.170	0.2998	0.1882	1.970	2.657	2.538	1.881	0.00	1.77	-1.22	1.87	0.860	0.035

Table 7.13 FM Results for the hybrids built on the PBE functional. Symbols and units as in table 7.1.

HM%	a_0	X_O	Y_O	R_{Cu-O}	R'_{Cu-O}	R_{Ca-O}	R_{Ge-O}	ΔE	q_{Cu}	q_o	q_{Ge}	$Spin_{Cu}$	$Spin_O$
0	7.312	0.3012	0.1844	1.982	2.727	2.582	1.926	-0.50	1.59	-1.00	1.38	0.602	0.097
20	7.230	0.3008	0.1859	1.970	2.689	2.557	1.902	-0.16	1.66	-1.07	1.54	0.710	0.071
40	7.166	0.3003	0.1873	1.962	2.658	2.536	1.882	-0.04	1.74	-1.15	1.69	0.803	0.049
60	7.114	0.2996	0.1887	1.958	2.634	2.519	1.865	0.00	1.84	-1.21	1.79	0.865	0.033

Table 7.14 FM Results for the hybrids built on the LDA functional. Symbols and units as in table 7.1.

HM%	a_0	X_O	Y_O	R_{Cu-O}	R'_{Cu-O}	R_{Ca-O}	R_{Ge-O}
0	7.159	0.3016	0.1834	1.935	2.675	2.527	1.889
20	7.138	0.3012	0.1849	1.938	2.659	2.523	1.880
40	7.125	0.3007	0.1865	1.945	2.647	2.521	1.873
60	7.119	0.2999	0.1881	1.955	2.638	2.520	1.868

Let us now compare these results to experimentally derived data, starting with the equilibrium structure. The lattice constant, Cu-O, Ge-O and Ca-O bond distances are presented in Figure 7.34-Figure 7.37. Not surprisingly, the overall behaviour is similar to what was already observed for CCTO and CdCTO; we shall therefore highlight only the differences between this case and the earlier results for the isostructural compounds.

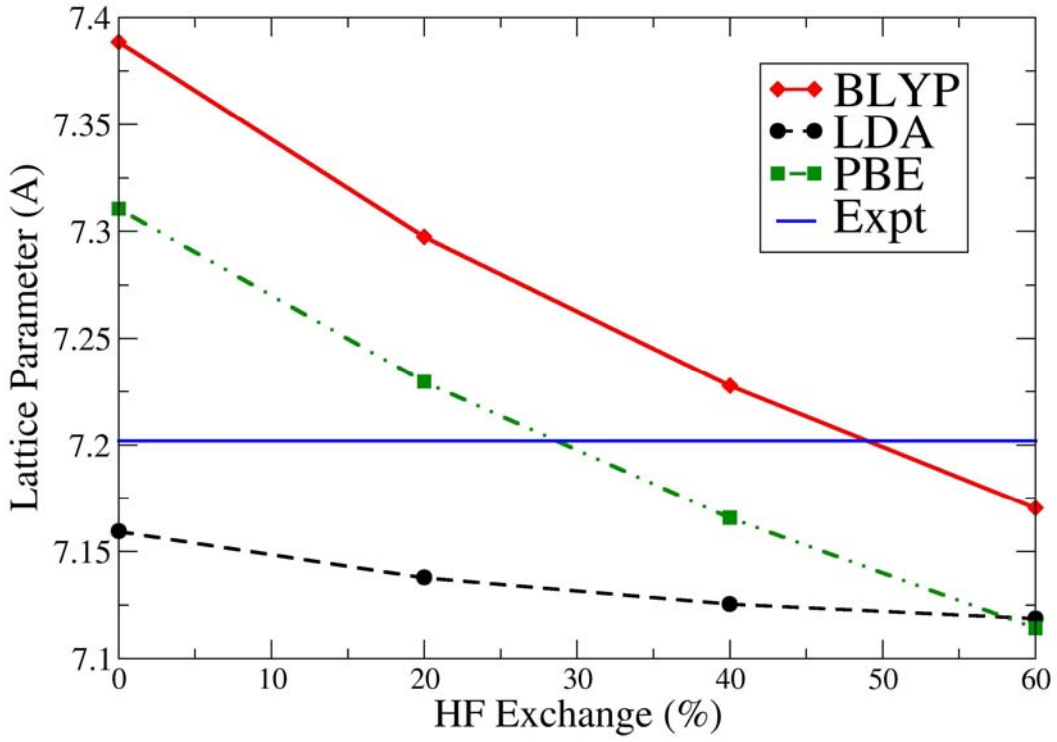

Figure 7.34 Equilibrium lattice parameter against the fraction of HF exchange for the BLYP, PBE and LDA functionals. The experimental value is displayed as a continuous blue horizontal line and was derived by Ozaki et al. [124].

The lattice parameter of CCGO known from experiment, 7.202Å[124], is more than 2% smaller than that for CCTO, 7.391Å and CdCTO, 7.348Å[84]; this difference is reproduced in our calculations. The hybrid functional comprising the PBE exchange-correlation functional and 20% HF exchange, for instance, yields an equilibrium value of 7.230Å for CCGO, 7.401Å for CCTO and 7.404Å for CdCTO. A small difference between the trends observed for CCTO and CCGO is shown by the hybrid functionals built on the LDA; pure LDA underestimates the CCGO lattice constant and the structure compresses further on increasing the fraction of HF exchange in the hybrid functional while for CCTO and CdCTO we observed a small expansion of the structure. It is encouraging to note that the experimental equilibrium lattice parameter of CCTO, CdCTO and CCGO is reproduced in our calculations using the same amount of HF exchange for all three materials; roughly 25% for PBE and 50% for BLYP.

Individual bond distances show the same trends already discussed for CCTO and CdCTO; in particular the Ge-O bond distances have the same behaviour observed earlier for the octahedral ions of CCTO and CdCTO, ie. Ti: there is a substantial decrease on increasing the fraction of HF exchange when using the GGA functionals, and a nearly constant value for the case of LDA. Results on CCGO also confirm that the change of Cu-O bond distances are much less pronounced than that of Ge-O and Ca-O, and overall agreement with experiment is achieved for the GGA functionals, using a fraction of HF exchange of 20-60%.

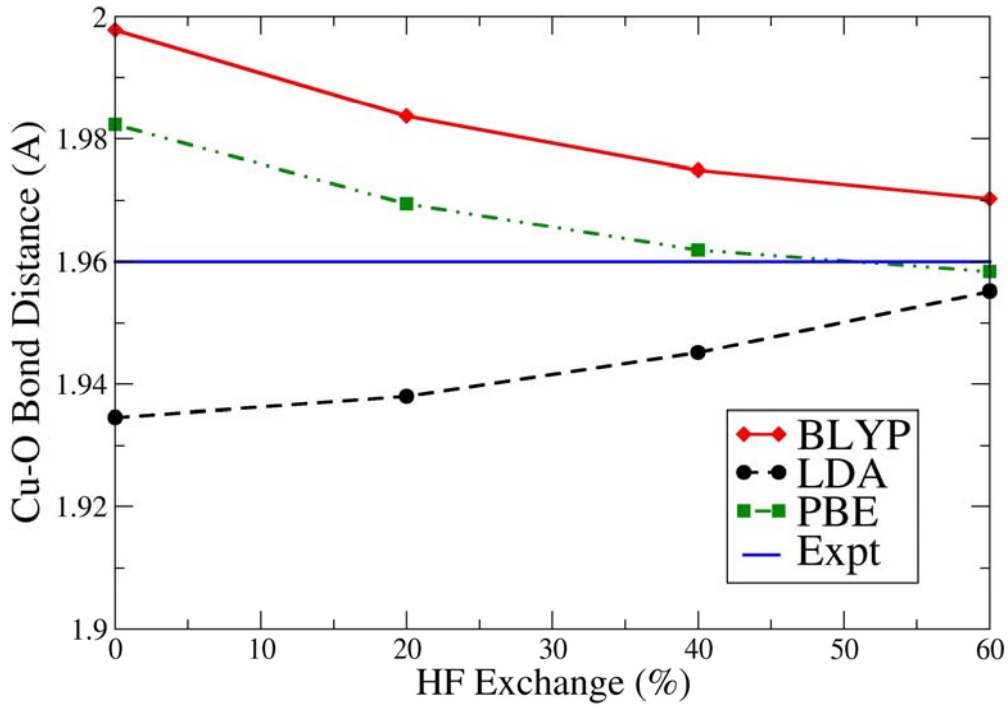

Figure 7.35 Shortest Copper-Oxygen bond distances against HF mixing for the BLYP, PBE and LDA functionals. The experimental value is shown as a continuous horizontal blue line.

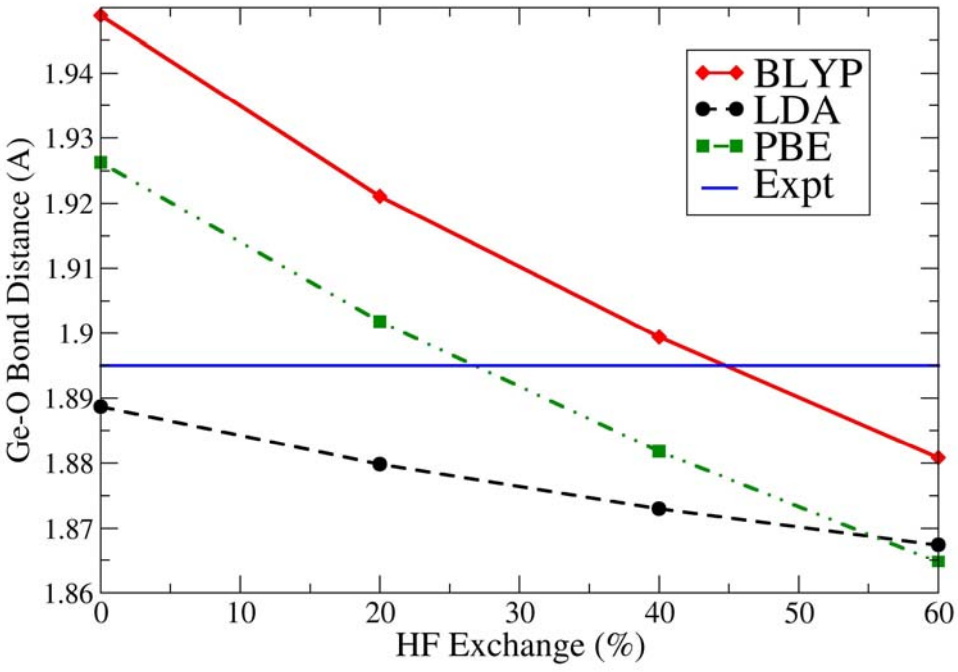

Figure 7.36 Germanium-Oxygen bond distances against HF mixing for the BLYP, PBE and LDA functionals. The experimental value is shown as a continuous horizontal blue line.

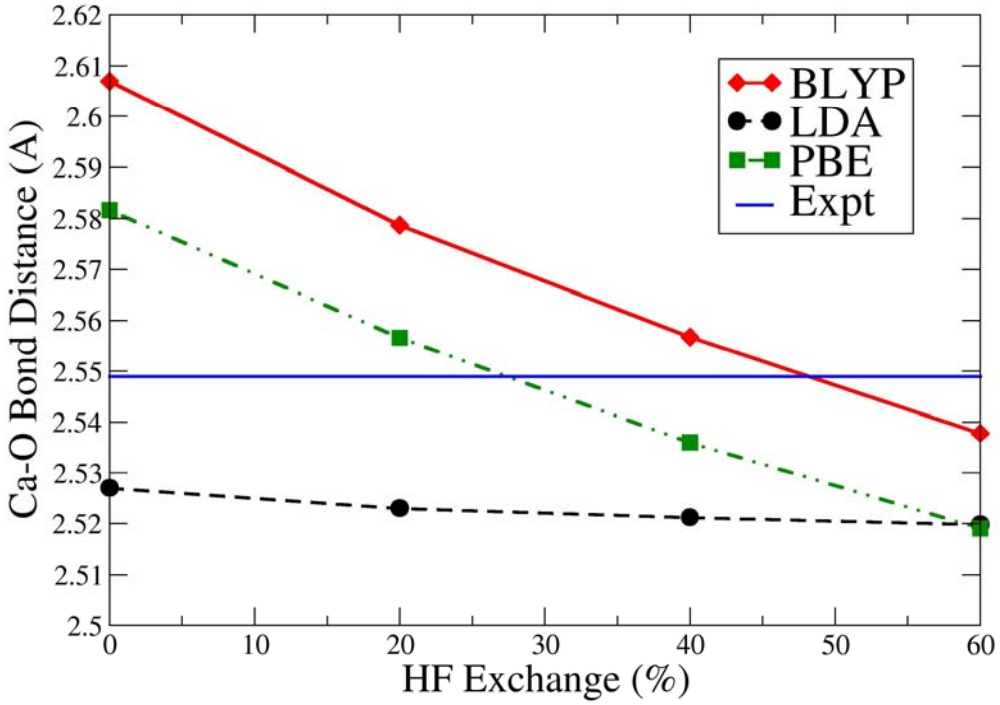

Figure 7.37 Calcium-Oxygen bond distances against HF mixing for the BLYP, PBE and LDA functionals. The experimental value is shown as a continuous horizontal blue line.

It is generally accepted that a set of rules, known as the Anderson-Goodenough-Kanemori (AGK)[2, 127] rules, can be used to rationalise whether a FM or AFM magnetic order is stable, by analysing the way in which superexchange depends on the angles between Cu ions mediated by an O ligand in the perovskite structure. It is generally assumed that a critical angle of 135° separates FM and AFM ordering. However it has been found that this angle can vary from material to material, with an example being in the continuous solid solution between $SeCuO_3$ and $SeTeO_3$ where Subramanian et al. found the stable magnetic order to change from FM to AFM at an angle of 127.5°[3]. Given that CCTO and CCGO have different magnetic ground states it is useful here to compare the Cu-O-Cu angles within the two structures and observe if any significant difference which could be used to rationalise this feature. In Table 7.15 we have summarised the three different Cu-O-Cu angles within the CCGO and CCTO crystal structures for a subset of the hybrid functionals employed. As mentioned before, the CCGO and CCTO structures are formed of tilted GeO_6 octahedra leading to a distorted Cu^{2+} environment in the 12-coordinated sites of the perovskite lattice, with four short (~2Å), four intermediate (~2.8Å) and four long (~3.2Å) Cu-O bond distances. In turn each O^{2-} ion has one Ca and three Cu nearest neighbour cations in the 12

coordinated sites. The three Cu ions correspond to one short, one intermediate and one long Cu-O bond. The Cu-O-Cu angles reported here are the angles formed between the short-medium (SM), short-long (SL) and medium long (ML) Cu-O bond distances. The experimental values in Table 7.15 are those derived by Boch et al.[102] and Ozaki et al.[124] for CCTO and CCGO respectively.

Table 7.15 Cu-O-Cu angles formed between short-medium, short-long and medium-long Cu-O differences.

Material-Method	SM (deg.)	SL (deg.)	ML (deg.)
CCGO-$F_{0.2}$PBE	100.7	176.8	76.1
CCGO-$F_{0.4}$PBE	100.6	177.0	76.4
CCGO-$F_{0.6}$PBE	100.5	177.2	76.7
CCGO-Expt.	100.7	176.9	76.1
CCTO-$F_{0.2}$PBE	100.7	175.8	75.0
CCTO-$F_{0.4}$PBE	100.7	175.9	75.2
CCTO-$F_{0.6}$PBE	100.7	176.1	75.4
CCTO-Expt.	100.9	175.7	74.8

The results in Table 7.15 show that there is very little difference in the Cu-O-Cu angles of CCGO and CCTO. The largest difference of approximately 1° is found between the two materials in the angles corresponding to the short-long and medium long Cu-O bonds. These values are however substantially different from the threshold value of 135° predicted by the AGK theory, and it is very unlikely that such a small change in the angle between CCTO and CCGO can account for the difference between the two magnetic ground states.

Let us now discuss the electronic properties, which are of particular interest for CCGO since it has a different magnetic ground state from CCTO and CdCTO. We limit attention here to the GGA functionals and start by examining the relative stability of the

FM and AFM phases. A plot of the energy difference between FM and AFM solutions is reported in Figure 7.38.

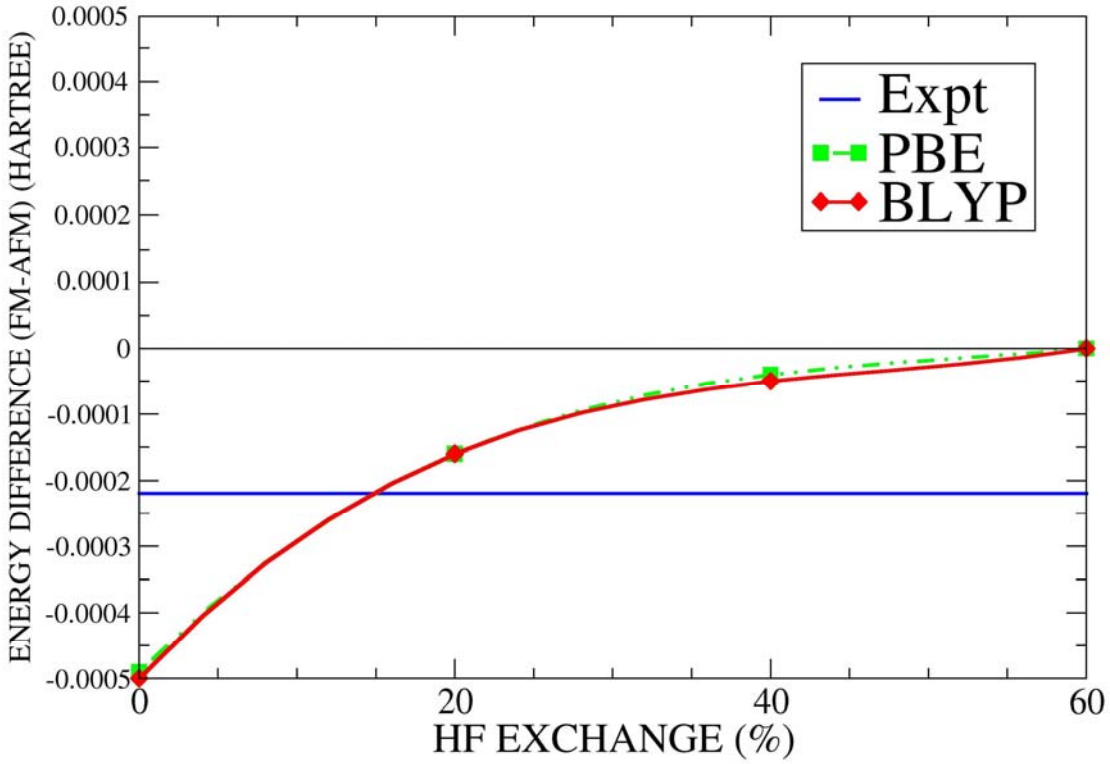

Figure 7.38 FM and AFM energy difference against the fraction of HF exchange for the BLYP and PBE functionals. The experimentally derived value is marked with a horizontal blue line.

The experimental value has been calculated as for CCTO, using the known Curie temperature of 13K[125] and using a mean-field approximation within an Ising model with a single magnetic coupling constant, J. Our calculations clearly predict the FM phase to be the correct ground state for CCGO, in agreement with experiment. The change of J as a function of HF exchange fraction is as we expect for a superexchange type of interaction, and is similar to that observed for CCTO. The choice of functional is again not important in predicting the electronic properties, with the PBE and BLYP functionals predicting nearly identical energy differences at each fraction of HF exchange.

Let us now further analyse the electronic properties by discussing the DOS calculated for CCGO bulk using the BLYP hybrid functional in the range of 20-60% HF exchange. This is plotted in Figure 7.39.

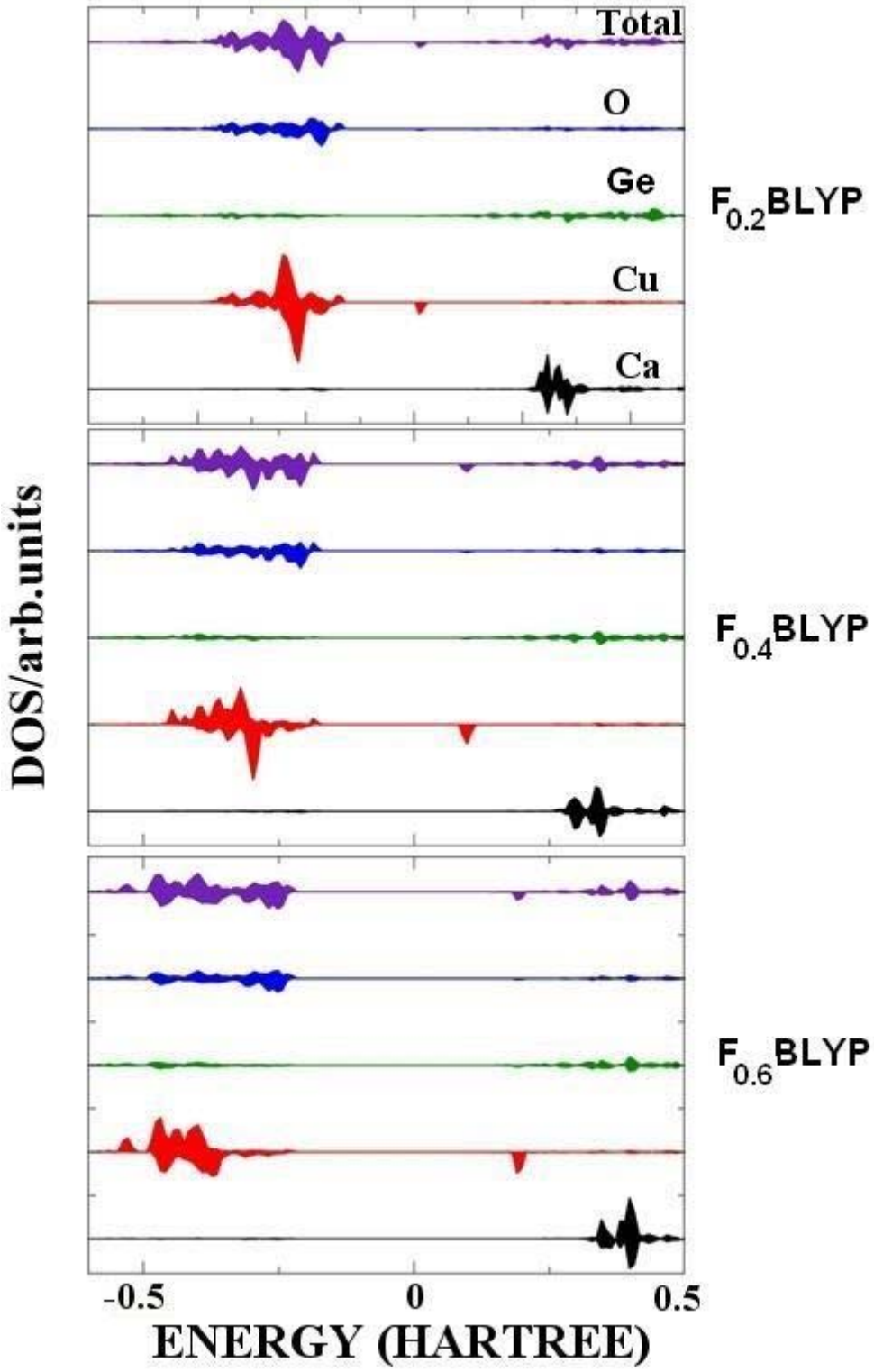

Figure 7.39 DOS calculated for CCGO using the BLYP functional and 20, 40 and 60% HF exchange.

Upon comparison to CCTO and CdCTO we observe a different band gap for CCGO. For example, using the $F_{0.4}$PBE functional we calculate the gap to be 7.31eV, 6.19eV and 5.75eV for CCGO, CCTO and CdCTO respectively. We also note that the Ge empty states are much higher in energy than the empty Ti 3d orbitals. This feature results in the states at the bottom of the conduction band using 60% HF exchange to be predicted of Cu character, and not of Ti character as in CCTO.

It has been claimed that the Ferromagnetism observed in CCGO can be attributed to the contribution of Ti in the superexchange interaction being different to that of Ge[128]. Our calculations appear to rule this out as a possibility, as we predict a negligible amount of spin polarisation on both the Ti ions of CCTO and Ge ions of CCGO. For example using the $F_{0.4}$PBE functional the spin polarisation calculated with a Mulliken analysis corresponds to 0.07 unpaired electrons on Ti and 0.003 unpaired electrons on Ge, which appears to be too low to invoke an effective involvement of either Ti or Ge in magnetic coupling across a Cu-O-Ti-O-Cu unit in which the two spin polarised ions are separated by four bonds. The negligible spin polarisation on Ti and Ge is further evidenced by the spin density plots shown in Figure 7.40, drawn in one of the equatorial planes of the TiO_6 octahedra in CCTO and GeO_6 octahedra in CCGO. The different ground magnetic state of CCTO and CCGO, albeit correctly reproduced by our calculations, cannot therefore be attributed to a specific chemical interaction, or structural feature of the two solids.

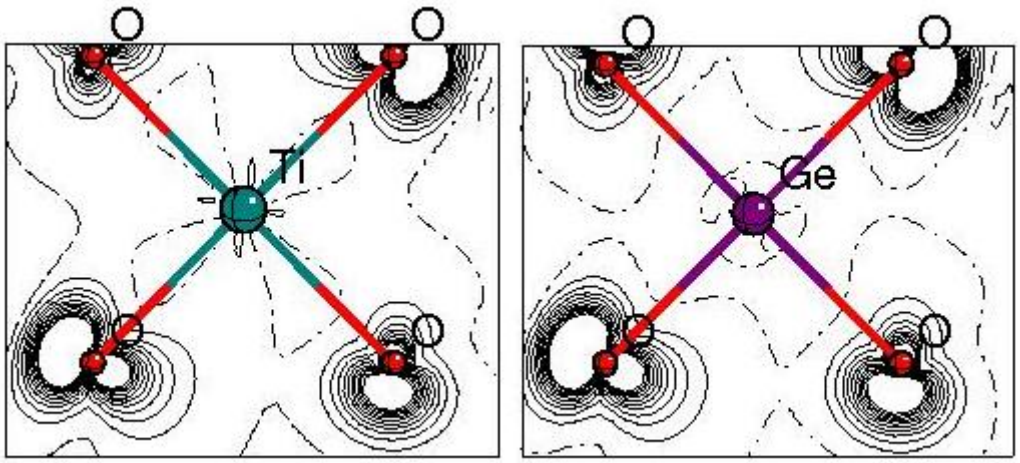

Figure 7.40 Spin density plot for the FM phases of CCTO and CCGO highlighting the contribution of the B-site ions (Ti and Ge). Isodensity lines drawn between -0.1 and 0.1 au. in intervals of 0.01.

7.3.1.1 Conclusions on bulk CCGO

The application of hybrid density functionals to the study of bulk CCGO enabled us to achieve good agreement with experiment. As was observed for CCTO, the geometry is too expanded when using the PBE and BLYP GGA functionals. Inclusion of HF exchange into the formulation yields better correspondence to experiment until the self-interaction error in local DFT is eventually overcorrected and the geometry is over compressed. The optimum amount of HF exchange for predicting the geometry is heavily dependent on the parameter in question and the functional used. The optimum value is however the same for CCTO, CdCTO and CCGO since trends are systematic across this class of isostructural compounds.

We predict the magnetic ground state of CCGO to be FM, in agreement with experiment, independently of the choice of hybrid exchange functional. We find very little difference in the Cu-O-Cu angles between CCTO and CCGO and hence rule out the dependence of the superexchange on the Cu-O-Cu (as defined by the AGK rules) angle as the reason for the difference in the magnetic ground state of the two compounds.

7.3.2 Surface Calculations

For consistency with the surface calculations on CCTO and CdCTO, also for CCGO we performed calculations on the 001 surface, employing the BLYP functional with 20, 40 and 60% HF exchange. All computational details were the same as those outlined in section 7.1.1.1. The 001 surface was cleaved to expose a $CaCu_3O_4$ plane and slabs with 19 layers of thickness were used to enable the convergence of all properties whilst minimising computational expense. The calculations were performed allowing both structural and electronic relaxation but the lattice parameters were constrained to those optimised in the bulk calculations. Details of the surface structure are identical to those of CCTO, illustrated in Figure 7.20. Perhaps not surprisingly, we find that both structurally and electronically, CCGO behaves in a very similar way to CCTO and CdCTO.

The net atomic charges for the surface Cu ions calculated with the $F_{0.2}$BLYP functional are +1.677, +1.072 and +1.496|e| with spin charges of 0.072, 0.038 and 0.541|e| respectively. We thus find a disproportionation similar to that observed in CCTO and CdCTO, which confirms the local environment of the outermost Cu ions as the chemical driving force for the chemical rearrangement. We performed calculations with this functional forcing a 2+, 2+, 2+ surface environment, and found that the difference in energy between this surface and the disproportionated one is 0.203eV, compared to 0.362eV for CCTO and 0.113eV for CdCTO.

Using the $F_{0.4}$BLYP functional we observed no disproportionation or charge transfer, a result that is consistent with that observed for CCTO and CdCTO. This is evidenced by charges of +1.717, +1.567 and +1.666|e| and spin charges of 0.787, 0.629 and 0.737|e| for the surface Cu ions.

We then used the $F_{0.6}$BLYP functional and again deduced results which are consistent with those obtained from the study of CCTO and CdCTO with an O to Cu charge transfer confirmed by net charges of +1.697, +1.030 and +1.751|e| and spin charges of 0.773, 0.007 and 0.827|e| for the surface Cu ions.

In conclusion, our surface calculations show that all three isostructural materials materials (CCTO, CdCTO and CCGO) show some redox chemistry at their 001

surfaces. Therefore, their different dielectric constants cannot be explained by this feature only. It could however be explained by a different surface termination of these materials and in particular by the type and number of Cu ions in different surface environments. We cannot investigate explicitly the relative stability of different surface terminations, as these would require slabs with different overall chemical composition and therefore leave this as a speculative conclusion open to further experimental or computational validations.

The sensitivity of the ground electronic state to the definition of forces in hybrid-exchange calculations is in our view indicative of the richness of surface redox chemistry of CCTO, CdCTO and CCGO. Such a sensitivity to the hybrid exchange formulation has not been observed for the bulk calculations. Other than the application-oriented conclusion discussed above, we would like to underline some important methodological implications of our results. We have proven that hybrid-exchange DFT does work for bulk solids with well-localised electrons (strongly correlated materials); we have further shown that the equilibrium structure of the solid is affected by both amount of HF exchange and choice of local DFT functional, while the electronic properties depend only on the amount of HF exchange and not on the local (LDA,GGA) exchange and correlation functional chosen. We have also shown that defects and surfaces pose less structural constraints than the bulk and are more stringent tests to the accuracy of hybrid-exchange calculations. Of course, any experimental characterisation work able to discriminate among different surface oxidation states of CCTO, CdCTO or CCGO would provide valuable detail, not only to assess the validity of our conclusions, but also in determining which hybrid-exchange formulation is best suited to study the electronic structure of complex ceramic surfaces.

7.4 Further Analysis of Magnetic Exchange in CCTO and CCGO

In previous sections we have presented details of the electronic structure of CCTO and CCGO, where we predict different magnetic ground states, AFM for CCTO and FM for CCGO. This difference between the two isostructural compounds is yet to be rationalised and here we aim to investigate the possible differences in magnetic exchange between the two materials. Although the energy differences between the FM and AFM phases plotted for CCTO in Figure 7.12 and CCGO in Figure 7.38 display a behaviour that we expect for a superexchange interaction involving a single J parameter, we aim to look in more detail here at other possible magnetic exchange mechanisms that could explain the observed magnetic behaviour.

To this goal, it is useful to start by examining the local environment and connectivity of Cu and O ions in CCTO and CCGO, responsible for superexchange interactions. The relevant features are shown in Figure 7.41, where only CCGO is shown for pictorial purposes. The local environment of Cu^{2+} has been amply discussed earlier for CCTO, and CCGO has similar qualitative features. The tilting of the $(Ti/Ge)O_6$ octahedra leads to a distorted Cu^{2+} environment in the 12-coordinated sites of the perovskite lattice, with four short (~2Å), four intermediate (~2.8Å) and four long (~3.2Å) Cu-O bond distances. In turn each O^{2-} ion has one Ca and three Cu nearest neighbour cations in the 12 coordinated sites. The three Cu ions correspond to one short, one intermediate and one long Cu-O bond. All oxygens are symmetry equivalent in CCTO and CCGO and hence have identical environment, at least when the magnetic phase is neglected. The single J Ising model adopted earlier to characterise the magnetic coupling in CCTO and CCGO, only considers the superexchange coupling between the Cu ions with short and intermediate Cu-O bond lengths, and implicitly neglects any involvement of the Cu^{2+} ions with the largest Cu-O bond distance (>3Å). The short-medium (SM), short-long (SL), and medium-long (ML) Cu-O-Cu angles are tabulated for CCTO and CCGO along with the corresponding short (S), medium (M) and long (L) Cu-O bond distances in Table 7.16. These distances have been calculated using the BLYP functional with 0-60% HF exchange.

Table 7.16 Cu-O-Cu angles and corresponding Cu-O bond distances of CCGO and CCTO, calculated using the BLYP functional with 0-60% HF exchange. The angles are in degrees and the distances in angstroms.

Functional	SM angle	SL angle	ML angle	S bond	M bond	L bond
CCGO-BLYP	100.6	176.3	75.7	1.998	2.761	3.229
CCGO-$F_{0.2}$BLYP	100.6	176.6	76.0	1.984	2.718	3.178
CCGO-$F_{0.4}$BLYP	100.6	176.9	76.3	1.975	2.685	3.138
CCGO-$F_{0.6}$BLYP	100.5	177.1	76.6	1.970	2.657	3.101
CCTO-BLYP	100.7	175.7	74.8	2.000	2.836	3.323
CCTO-$F_{0.2}$BLYP	100.7	175.8	75.0	1.991	2.807	3.290
CCTO-$F_{0.4}$BLYP	100.7	175.9	75.2	1.985	2.783	3.260
CCTO-$F_{0.6}$BLYP	100.7	176.1	75.4	1.981	2.764	3.236

The single J Ising model appears to work accurately for CCTO and CCGO. The coupling constant between the two Cu ions at short and medium distance is labelled as J1 in Figure 7.41. In this section we examine whether the single-J Ising model is sufficient to capture all details of magnetic coupling in CCTO and CCGO. The first extension that we considered consists in an Ising model in which magnetic coupling between Cu^{2+} ions is still pairwise additive, but superexchange through the long Cu-O bonds is no longer neglected. This leads to a model with three independent coupling constants (J's) associated with the short-medium Cu-O bonds (J1), short-long Cu-O bonds (J2) and medium-long Cu-O bonds (J3), as displayed in Figure 7.41. The energy of such a model will be given by an extension of equation (7.3) with three different values of J.

$$E_{FM} = E_0 + \sum_{J1\,pairs} J_1 S_1 S_2 + \sum_{J2\,pairs} J_2 S_1 S_2 + \sum_{J3\,pairs} J_3 S_1 S_2 \qquad (7.8)$$

where the sums extend to all unique pairs of Cu ions in the unit cell that are connected via an O ion with the correct bond distances (eg. short and intermediate for J1 etc.). In practice, because the environment of all the O ions is identical, each O of the unit cell is responsible for one J1, one J2 and one J3-type superexchange interaction. In the broken symmetry approach, the three values of J can be derived by calculating the energy of

four different magnetic orders (not linearly dependent on each other). The two magnetic phases already discussed, and used to produce the energy difference plots of CCTO and CCGO, correspond to a full FM order, and to an AFM phase in which the Cu ions in alternate 111 planes have opposite spins. We have chosen two additional AFM phases, in which the Cu ions have alternate spin along the 001 and 110 crystal planes; both are described by a double primitive unit cell and are therefore the simplest from a computational point of view.

The energy of the four magnetic phases examined, according to equation (7.8), above, is given by the following expressions in terms of J1-3, considering that each double-primitive unit cell contains 24 oxygens, and S for Cu^{2+} is ½.

$$E_{FM} = E_0 + 6J_1 + 6J_2 + 6J_3 \tag{7.9}$$

$$E_{AFM\,111} = E_0 - 6J_1 + 6J_2 - 6J_3 \tag{7.10}$$

$$E_{AFM\,001} = E_0 + 2J_1 - 2J_2 + 2J_3 \tag{7.11}$$

$$E_{AFM\,110} = E_0 - 2J_1 - 2J_2 - 2J_3 \tag{7.12}$$

We note here that the energy difference between two pairs of phases is linearly dependent. We have in fact:

$$E_{FM} - E_{AFM\,111} = 12J_1 + 12J_3 \tag{7.13}$$

$$E_{AFM\,001} - E_{AFM\,110} = 4J_1 + 4J_3 \tag{7.14}$$

This is not surprising, as in each pair one phase can be obtained from the other by reversing the spin of Cu ions in alternate 111 planes. A similar relation is found with the simplified one-J model (that corresponds to the assumption J2=0 and J3=0). An additional magnetic phase needs therefore to be considered if we want to employ our electronic structure calculations to estimate the value of each J. Before doing this, however, it is useful to examine results. By comparing the calculated energy of the four phases we have in fact a way of estimating simultaneously the numerical accuracy of our calculations, and whether the 3J model describes our results.

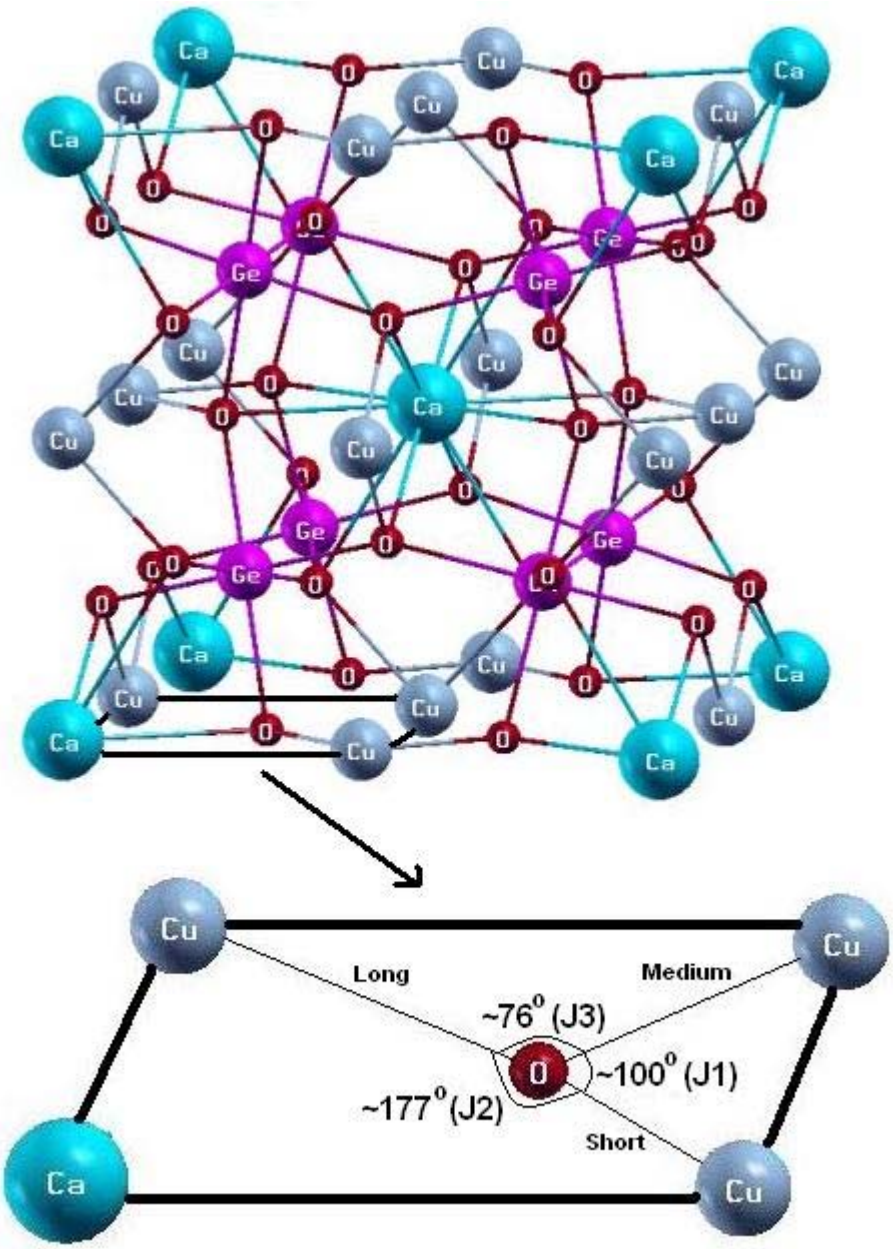

Figure 7.41 Local environment of the O^{2-} ions in CCGO. This displays the three Cu-O-Cu angles that are present throughout the structure.

The numerical results obtained for CCTO using the hybrid functional built on BLYP with 40% HF exchange are summarised in Table 7.17. We see using these data, that the energy difference E_{FM}-E_{AFM111} is 0.00018Ha while E_{AFM001}-E_{AFM110} is -0.00023Ha. Clearly the ratio between these two energy differences is not 3, as required by equations (7.13) and (7.14); they have roughly the same magnitude and opposite sign.

We can also look at the relevant energies obtained for CCGO, and we find that: E_{FM}-E_{AFM111}=-0.000040Ha, while E_{AFM001}-E_{AFM110}=0.00000062Ha. This is clearly in contrast with the results of equations 7.13-14 and hence the model does not provide numerically correct results for CCGO either.

The disagreement between model and calculated results may have two possible reasons; either the numerical accuracy of our data is insufficient (energy differences are small, of the order 10^{-4}Ha compared to the total unit cell energy of ~10^{4}Ha), or the Ising model based on the pair-wise additivity of three superexchange couplings does not describe CCTO and CCGO. We have first addressed the numerical accuracy issue: each magnetic phase has been calculated using different initial electronic configurations; in particular CRYSTAL enables us to obtain each AFM order by starting from the FM phase, and reversing the spin of selected Cu ions. Also, the energy of the FM phase has been calculated using the reduced symmetry of each of the AFM orders examined. The results obtained for CCTO are presented in Table 7.17 in rows entitled "SPINEDIT" and "symm." respectively. None of these changes introduce differences in the calculated energies; the largest change being of ~$3x10^{-6}$ Ha. Energy differences between magnetic phases are instead of $2x10^{-4}$ Ha and our results are therefore sufficiently accurate from a numerical point of view.

Having ruled out the numerical accuracy as the reason for the non-agreement of calculated results with the Ising model, we need to conclude that it is the 1-J and 3-J Ising model with pairwise additivity of interactions that is unsuitable to describe the subtleties of CCTO and CCGO.

Table 7.17 Energies of the various magnetic phases of CCTO considered for the 3 J analysis.

Magnetic Order	Energy (Hartree)
FM	-19800.83500813
FM double cell	-19800.83500687
FM-AFM111symm.	-19800.83500536
FM-AFM001symm.	-19800.83500590
FM-AFM110symm.	-19800.83500589
AFM111SPINEDIT	-19800.83518399
AFM001SPINEDIT	-19800.83504486
AFM110SPINEDIT	-19800.83481472

Table 7.18 Energies of the various magnetic phases of CCGO considered for the 3 J analysis.

Magnetic Order	Energy (Hartree)
FM	-29620.44460143
AFM111	-29620.44456154
AFM001	-29620.44445351
AFM110	-29620.44445413

This breakdown of pairwise addivity is known in other cuprates, for instance in the high T_c perovskite-related structure of La_2CuO_4[129, 130] often referred to as an anti-ferromagnet. Here, deviation from pairwise additivity in magnetism has been rationalised with a cyclic term (4-body interaction)[129, 131]. Such a cyclic term does not however appear to be relevant in the CCTO and CCGO structures.

Let us make reference to the O^{2-} environment shown in Figure 7.41. Because each O ion mediates between three Cu^{2+} ions, it is reasonable to explore a 3-body term in the magnetic Hamiltonian, J_{123}, that represents a magnetic energy through each O ligand of the CCTO and CCGO structure. Because the three Cu ions are differentiated by their Cu-O bond distances, we introduce different types of J_{123} constants in which spins identified as 1, 2 and 3 refer respectively to the spin of copper with the short, intermediate and long bond distances around the reference oxygen. The number of possible spin combinations is 2^3=8, which leads to 8 different 3-body coupling constants (J_{+++}, J_{++-}, J_{+-+}, J_{-++}, J_{+--}, J_{-+-}, J_{--+}, J_{---}); we can however assume symmetry with respect to inversion of all 3 spins around the same O (ie. $J_{+++}=J_{---}$, $J_{++-}=J_{--+}$ and $J_{+--}=J_{-++}$). This equivalence has actually been verified by running pairs of calculations in which the spin of all Cu ions has been reversed, which yield identical results (to 10^{-9} Ha) This leaves 4 distinct 3-body coupling constants, J_{+++}, J_{++-}, J_{+-+} and J_{-++} and we write a new spin-Hamiltonian in the form:

$$E = E_0 + n_{+++}J_{+++} + n_{++-}J_{++-} + n_{+-+}J_{+-+} + n_{-++}J_{-++} \qquad (7.15)$$

Where n_{ijk} is the number of oxygen ions in the unit cell with three Cu neighbours in spin i, j, k (or –i, -j, -k) in order of increasing Cu-O distance. We note here that S (spin of Cu) has disappeared from the model, as now the energy depends on the oxygen, not copper, ions that mediate the three-body superexchange interaction. Analysis of the calculated spin density of both CCTO and CCGO suggests that the new model is

reasonable; the multipolar expansion of the spin density on each O is complex, and has non-zero poles up to 6th order in a multipolar expansion of the charge density that depend on the magnetic environment of the oxygen.

To solve equation (7.15) we need to consider five different magnetic phases; there are now four spin exchange parameters and the hypothetical energy of a phase without magnetic coupling, E_o hence five equations are required to solve for all five variables. We still consider the four magnetic phases used for the multiple J analysis discussed earlier, E_{FM}, E_{AFM111}, E_{AFM110} and E_{AFM001}, and now introduce a fifth arbitrary magnetic phase in which the first five Cu ions in the crystallographic unit cell are spin up and the sixth copper is in a spin down state. We label the energy of this phase as E_{51}. Counting the number of different 3 body terms for these phases to obtain n_{+++}, n_{++-}, n_{+-+} and n_{-++} for each of the five magnetic orders we obtain:

$$E_{FM} = E_0 + 3J_{+++} \tag{7.16}$$

$$E_{111} = E_0 + 3J_{+-+} \tag{7.17}$$

$$E_{110} = E_0 + 1J_{++-} + 1J_{+-+} + 1J_{-++} \tag{7.18}$$

$$E_{001} = E_0 + 1J_{+++} + 1J_{++-} + 1J_{-++} \tag{7.19}$$

$$E_{51} = E_0 + 1.5J_{+++} + 0.5J_{++-} + 0.5J_{+-+} + 0.5J_{-++} \tag{7.20}$$

Unfortunately, the determinant of the matrix of the above equations is zero and hence we do not have a unique solution to J_{+++}, J_{++-}, J_{+-+} and J_{-++}. Further analysis of these expressions yields the linear dependences:

$$3E_{AFM\,001} = E_{FM} - E_{AFM\,111} + 3E_{AFM\,110} \tag{7.21}$$

and

$$2E_{AFM\,51} = E_{FM} + E_{AFM\,110} \tag{7.22}$$

By considering all possible permutations of spin up and down on the six Cu ions of the unit cell we can define a crystallographic cell with 2 Cu's with spin up and 4 Cu's with

spin down; if we label the six Cu ions as Cu1-6, this phase is found when the Cu ions 1 and 2 are in the spin up and all others in the spin down state. We label this phase as E_{42}.

$$E_{42} = E_0 + 0.5J_{+++} + 0.5J_{++-} + 1.5J_{+-+} + 0.5J_{-++} \quad (7.23)$$

However, also this new phase is linearly dependent on the E_{FM} and E_{AFM110} phases such that:

$$2E_{42} = \frac{E_{FM}}{3} + E_{AFM110} \quad (7.24)$$

The linear dependence relationship is retained also when considering larger unit cells of the structure; therefore we cannot form enough non-linearly dependent equations to solve for unique solutions of J_{+++}, J_{++-}, J_{+-+} and J_{-++}. However, at this stage we can put the calculated energies for the aforementioned magnetic phases into the equalities expressed by equations (7.21), (7.22) and (7.24) to check if, in principle, this 3-body exchange model provides numerically accurate results for CCTO and CCGO. Results can be seen in Table 7.19 and 7.20.

Table 7.19 Value of the left hand side (LHS) and right hand side (RHS) of equations 7.21, 7.22 and 7.24 for CCGO, in Hartrees. The energies were calculated using the $F_{0.4}$PBE functional.

Equation	LHS	RHS
7.20	-59240.889047	-59240.889055
7.21	-88861.333360	-88861.333402
7.24	-88861.333532	-88861.333543

Table 7.20 Value of the left hand side (LHS) and right hand side (RHS) of equatons 7.21, 7.22 and 7.24 for CCTO, in Hartrees. The energies were calculated using the $F_{0.4}$PBE functional.

Equation	LHS	RHS
7.21	-59402.505134	-59402.505268
7.22	-39601.669965	-39601.669822
7.24	-39601.669629	-39601.669672

Here we find that the identities 7.21, 7.22 and 7.24 are reproduced with much higher numerical accuracy than that achieved for the pairwise Ising model, to approximately 10^{-5} Hartree for CCTO and CCGO. As discussed earlier, 10^{-5} Ha is the intrinsic accuracy of our calculations, as demonstrated earlier with results presented in Table 7.17. The 3-body superexchange model seems to work for both CCTO and CCGO, and is certainly more successful than the 3 J analysis in describing the magnetic coupling. However, to find unique solutions to J_{+++}, J_{++-}, J_{+-+} and J_{-++} more linearly independent equations are required. To this goal we have considered triple unit cells, in which the primitive unit cell is tripled in one lattice direction. This cell contains nine Cu ions and the possible spin up and down permutations lead to 15 unique solutions. All the solutions allowed are still linear combinations of those given by equations 7.16-7.20. The underlying symmetry of CCTO and CCGO, in fact, does not enable us to obtain the individual values of the 3-body coupling constants, however large cell and complex magnetic order we may set in our calculations. While this conclusion may appear not entirely satisfactory, the fact that the identities 7.21-7.24 are satisfied by CCGO indicates, at least in a semi-quantitative way, that magnetic coupling in this material is not pairwise additive, and requires many-body interaction terms. It is our understanding that the different ground magnetic state between CCTO and CCGO is linked to the three body terms, which we cannot evaluate individually but are able to explain the different behaviour calculated and observed experimentally.

7.5 New Compositions: $CaCu_3Zr_4O_{12}$, $SrCu_3Zr_4O_{12}$ and $SrCu_3Ti_4O_{12}$.

The class of $AA'_3B_4Z_{12}$ perovskites has shown rich electronic behaviour, leading to useful functional properties (dielectric, magnetic, surface redox chemistry). We now extend our computational study predictively to new compositions not yet synthesised experimentally, and to observe if novel properties can be introduced. In particular we replace the Ca and Ti ions of CCTO with larger ones (Calcium with Strontium and Titanium with Zirconium) to obtain $CaCu_3Zr_4O_{12}$ (CCZO), $SrCu_3Zr_4O_{12}$ (SCZO) and $SrCu_3Ti_4O_{12}$ (SCTO). Following the prediction from section 7.1.2.3 we consider that an

increase in lattice parameter may lead to different surface behaviour of Cu^{2+}. Another goal is to identify new materials with a FM ground state, which are extremely rare in the literature and are of considerable academic and technological interest.

We start by discussing results obtained from calculations on the perovskite structure of $CaCu_3Zr_4O_{12}$ (CCZO), which has not yet been synthesised and is not reported either experimentally or theoretically in the literature. We limit the DFT study here to the hybrid functionals built on the GGA definitions and omit the LDA which has consistently proven worse in CCTO, CdCTO and CCGO. Convergence criteria and other computational details were consistent with those used for all previous calculations and the basis set for Zr and Sr were taken from the online database for the CRYSTAL code. As there are no experimental structural parameters to start from, we used the cell parameters derived by Subramanian et al.[84] for CCTO as a starting point. We also force the structure to belong to the Im3 space group making it isostructural to CCTO, CdCTO and CCGO.

As there is no experimental data on this compound, we studied the FM and AFM phases with spins alternating along the 111, 110 and 001 planes in order to determine the stable magnetic structure.

Table 7.21 Results for CCZO, using the hybrids built on the PBE functional

HM%	a_0	X_O	Y_O	R_{Cu-O}	R'_{Cu-O}	R_{Ca-O}	R_{Zr-O}	$\Delta E_{FM-AFM111}$	$\Delta E_{FM-AFM110}$	$\Delta E_{FM-AFM001}$	q_{Cu}	q_o	q_{Zr}	$Spin_{Cu}$	$Spin_O$
0	7.846	0.3088	0.1668	1.991	3.014	2.754	2.118	2.44	-2.20	2.10	1.59	-1.47	2.81	0.581	0.096
20	7.801	0.3091	0.1675	1.981	2.991	2.742	2.105	0.45	-0.29	0.28	1.66	-1.53	2.91	0.699	0.071
40	7.763	0.3091	0.1682	1.975	2.972	2.732	2.093	0.15	-0.14	0.05	1.74	-1.58	3.00	0.797	0.048
60	7.733	0.3089	0.1689	1.972	2.956	2.723	2.083	0.07	-0.07	0.00	1.79	-1.62	3.08	0.863	0.033
80	7.705	0.3086	0.1695	1.970	2.943	2.713	2.094	0.06	-0.06	0.00	1.83	-1.66	3.15	0.901	0.024

Table 7.22 Results for CCZO, using the hybrids built on the BLYP functional

HM%	a_0	X_O	Y_O	R_{Cu-O}	R'_{Cu-O}	R_{Ca-O}	R_{Zr-O}	$\Delta E_{FM-AFM111}$	$\Delta E_{FM-AFM110}$	$\Delta E_{FM-AFM001}$	q_{Cu}	q_o	q_{Zr}	$Spin_{Cu}$	$Spin_O$
0	7.917	0.3087	0.1673	2.012	3.039	2.780	2.136	2.40	-2.15	2.09	1.57	-1.47	2.82	0.575	0.098
20	7.867	0.3091	0.1678	2.000	3.015	2.767	2.122	0.43	-0.27	0.26	1.65	-1.53	2.92	0.693	0.072
40	7.826	0.3092	0.1683	1.992	2.995	2.755	2.110	0.14	-0.13	0.04	1.72	-1.58	3.01	0.793	0.049
60	7.793	0.3090	0.1690	1.987	2.978	2.745	2.099	0.06	-0.06	0.00	1.78	-1.62	3.09	0.859	0.034
80	7.763	0.3088	0.1695	1.984	2.964	2.734	2.089	0.05	-0.05	0.00	1.82	-1.66	3.16	0.898	0.025

Let us now discuss these results, beginning with the structural parameters.

Our calculations impose CCZO to belong to the body centred cubic space group Im3. We have performed Γ-point calculations for each case and can confirm that this choice is a proper minimum with respect to symmetry lowering distortions. Let us first examine the trend in the equilibrium lattice parameter as a function of HF exchange. This was predicted to be between 7.705Å and 7.917Å depending on the choice of theory. This range is shown in Figure 7.42.

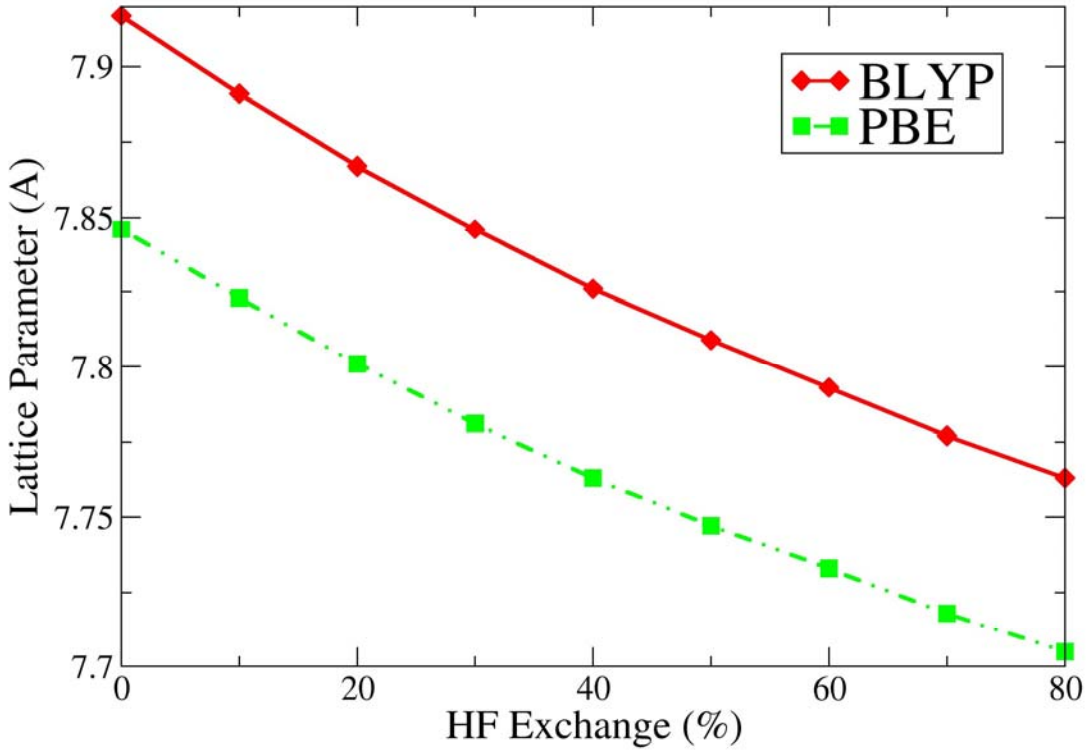

Figure 7.42 Equilibrium lattice parameter of CCZO against HF exchange for the BLYP and PBE functionals.

The BLYP and PBE functionals behave very similarly to the cases of CCTO, CdCTO and CCGO: they predict a larger unit cell with pure DFT and they both compress the geometry with similar gradients upon inclusion of more HF exchange. Making the assumption that the hybrid functionals act similarly in describing CCZO as they do for CCTO and CCGO, we predict the actual lattice parameter to be approximately 7.80Å. This is a 6% increase from the case of CCTO whose lattice parameter is 7.39Å.

Let us now examine the bond lengths calculated using the $F_{0.4}$PBE functional. The Zr cations are sixfold coordinated by equidistant oxygens with a bond length predicted to be 2.110Å for CCZO, 8% larger than the equivalent for CCTO (Ti-O = 1.947Å). The Zr-O distance as a function of HF exchange is plotted for CCZO in Figure 7.43. The Ca atoms are surrounded by 12 equidistant O atoms with bond lengths predicted to be 2.732Å and 2.592Å for CCZO and CCTO respectively (a 5% increase). Due to the tilting of the ZrO_6 octahedra, each Cu atom is coordinated by a planar arrangement of 4 nearest oxygen atoms with distances predicted to be 1.992Å and 1.971Å for CCZO and CCTO (a 1% increase), 4 oxygens at a further distance of 2.995Å and 2.761Å for

CCZO and CCTO respectively (an 8% increase) and 4 oxygens at a much further distance.

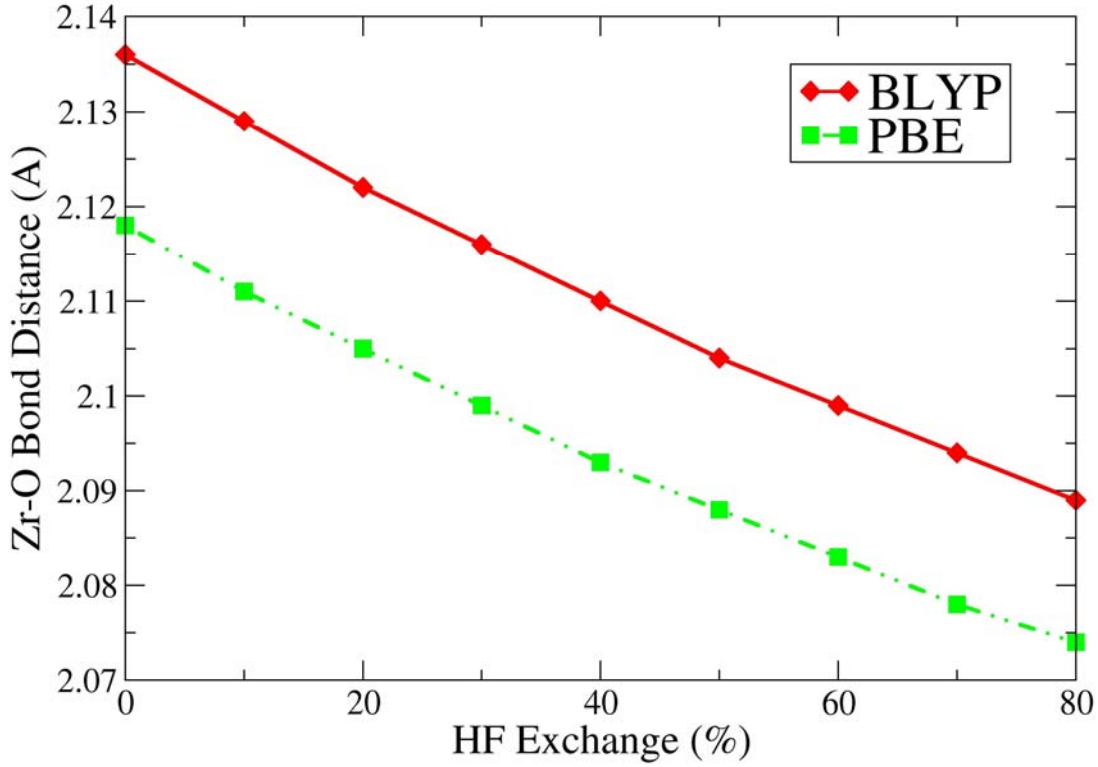

Figure 7.43 Zirconium-Oxygen bond distances as a function of HF exchange for the BLYP and PBE functionals.

The Zr substitution has an effect also on the tilting of the octahedral: for CCTO we obtain tilt angles of 19.14° when using the $F_{0.4}$PBE functional. When using the same functional for CCZO the distortion is predicted to be larger, with a tilt angle of 22.0°, due to the larger size mismatch between Ca^{2+} and Cu^{2+} and the octahedral ion Zr^{4+}. It is reasonable to expect such a distortion to have important effects on the magnetic order.

Let us now examine the electronic properties of CCZO. All the values in this section refer to the equilibrium structure for each of the hybrid functionals examined. Calculations were performed on the FM phases and a set of AFM phases, including those having up and down spins alternating along the 111, 001 and 110 planes. The energy difference between FM and AFM (111, 110 and 001) phases as a function of the HF percentage in the hybrid functional is shown in Figure 7.44. The energies calculated

using the PBE and BLYP functionals were very similar and we therefore plot only the PBE data here.

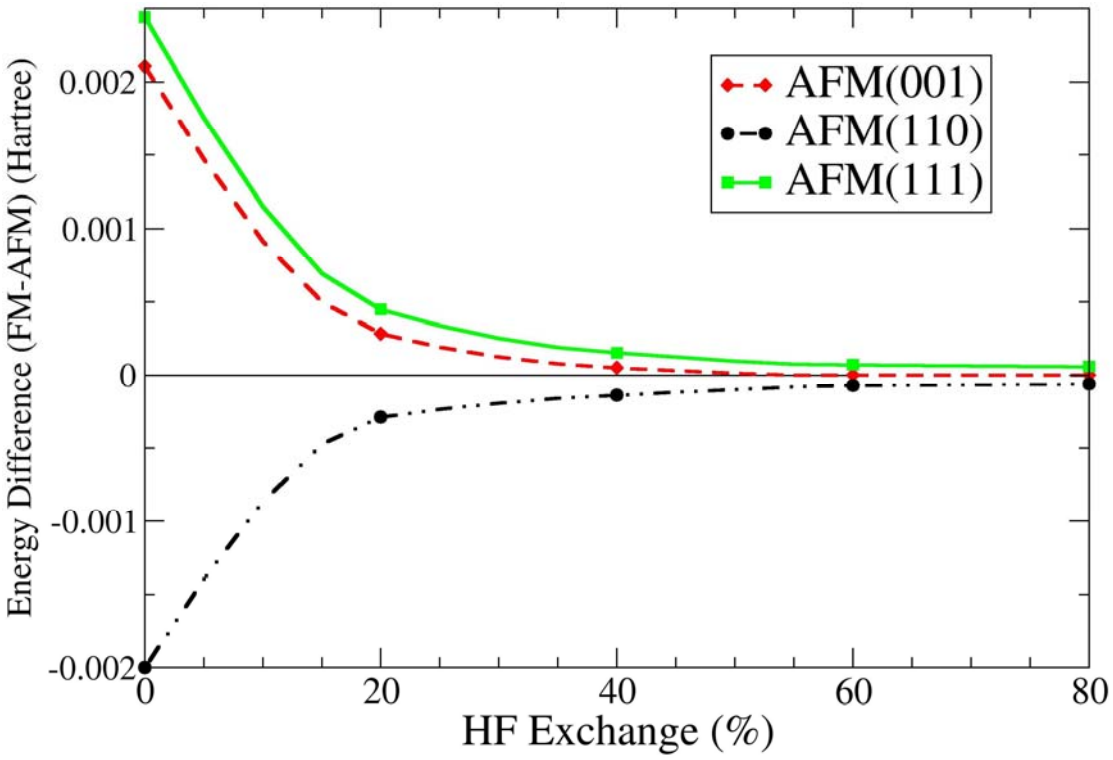

Figure 7.44 Relative energy of different magnetic phases of CCZO, with respect to the FM state taken as a reference, plotted as a function of HF exchange for the PBE functional.

We predict the magnetic ground state to be AFM, with spins alternating along the 111 planes. The AFM phase with spins aligned along the 001 planes is energetically the second most stable phase and the FM phase is more stable than the AFM110 phase. The dependence of the energy on the percentage of HF exchange display the behaviour that we expect for a superexchange-type mechanism.

Let us now examine the DOS calculated for CCZO using the PBE functional with 20, 40 and 60% HF exchange.

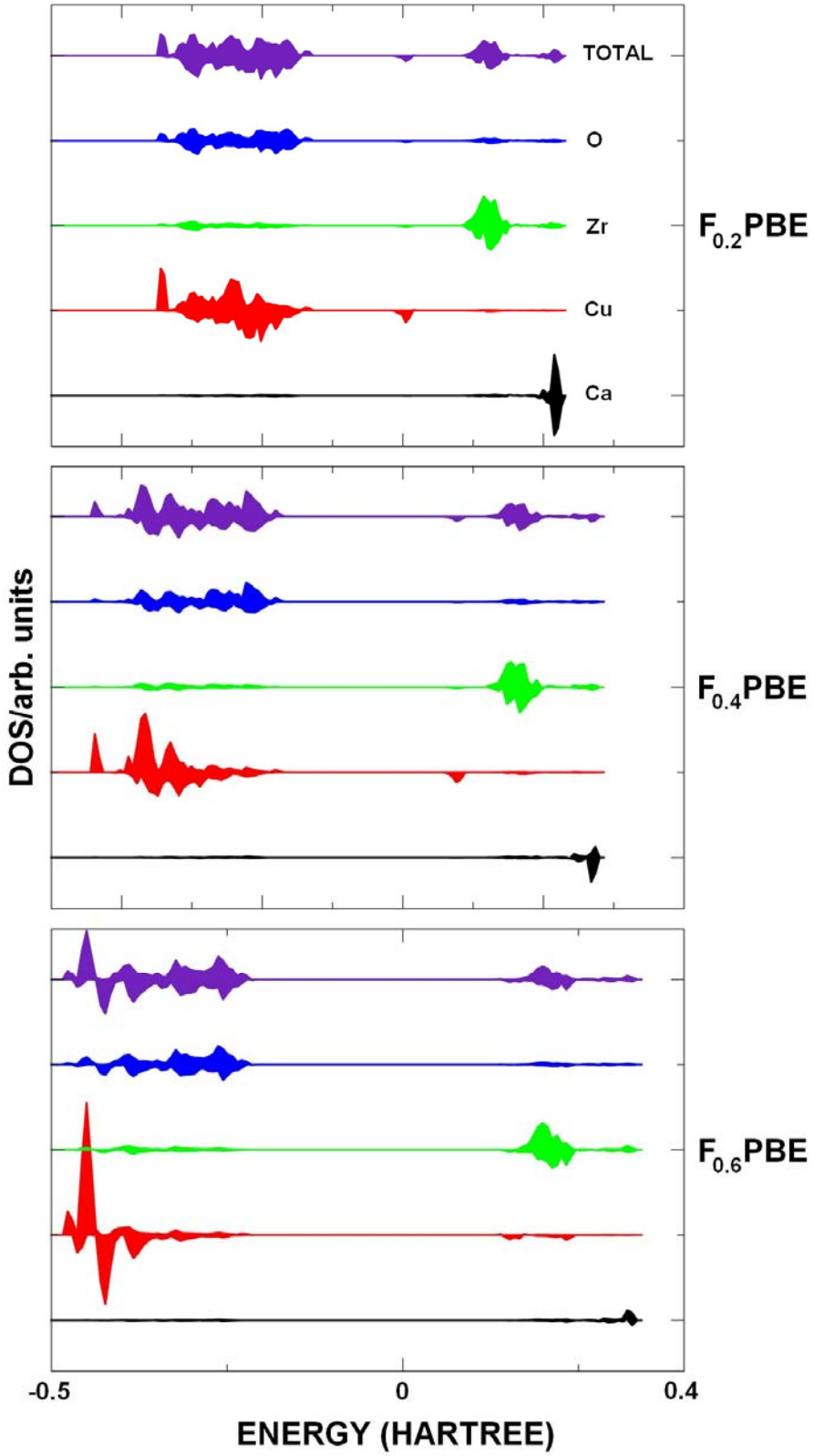

Figure 7.45 Density of states calculated using the PBE functional with 20, 40 and 60% HF exchange from top to bottom. The DOS of the Ca, Cu, Zr and the total are displayed. The total is divided by ten for ease of presentation.

The most noticeable effect from these results is a significant increase in valence electron density on the Cu^{2+} ions as we increase HF exchange. The bottom of the conduction band is still Cu using the $F_{0.6}$PBE functional, a result similar to what we observed for CCGO and due to the Zr 4d states being higher in energy compared to the Ti-3d states. This feature also causes an increase of the calculated band gap, which using the $F_{0.4}$PBE functional is of 6.84eV in CCZO compared with 6.19eV, 5.75eV and 7.31eV for CCTO, CdCTO and CCGO respectively.

Let us now introduce a new system, where Calcium (Ca^{2+}) is replaced by Strontium (Sr^{2+}) on the A site to yield $SrCu_3Zr_4O_{12}$, or SCZO. Similarly to CCZO, this perovskite has not yet been synthesised, so we performed a geometry optimisation in the Im3 space group followed by Γ-point frequency calculations to confirm the chosen symmetry. We used the all electron Sr basis set taken from the online database for the CRYSTAL code. We present the structural and electronic results for BLYP and PBE functionals in Table 7.23 and Table 7.24 respectively. We consider here the FM, AFM111, AFM001 and AFM110 phases in the range of 0-80% HF exchange.

Table 7.23 FM results for hybrids built on the PBE functional.

HM (%)	a0 (Å)	Xo	Yo	Rcu-o (Å)	R'cu-o (Å)	Rca-o (Å)	Rzr-o (Å)	$\Delta E_{FM-AFM111}$	$\Delta E_{FM-AFM001}$	$\Delta E_{FM-AFM110}$	qcu (a.u)	qo (a.u)	qzr (a.u)	spincu	spino
0	7.874	0.3098	0.1681	1.999	3.012	2.776	2.124	2.25	2.02	-2.11	1.59	-1.48	2.81	0.584	0.095
20	7.827	0.3101	0.1688	1.988	2.989	2.764	2.111	0.42	0.27	-0.28	1.66	-1.54	2.91	0.702	0.070
40	7.789	0.3102	0.1695	1.982	2.969	2.753	2.099	0.14	0.05	-0.13	1.74	-1.59	3.00	0.801	0.047
60	7.758	0.3100	0.1701	1.978	2.953	2.743	2.089	0.08	0.00	-0.06	1.80	-1.63	3.08	0.866	0.032
80	7.730	0.3097	0.1707	1.976	2.940	2.734	2.079	0.03	0.00	-0.01	1.83	-1.67	3.15	0.903	0.023

Table 7.24 FM results for hybrids built on the BLYP functional.

HM (%)	a0 (Å)	Xo	Yo	Rcu-o (Å)	R'cu-o (Å)	Rca-o (Å)	Rzr-o (Å)	$\Delta E_{FM-AFM111}$	$\Delta E_{FM-AFM001}$	$\Delta E_{FM-AFM110}$	qcu (a.u)	qo (a.u)	qzr (a.u)	spincu	spino
0	7.947	0.3097	0.1686	2.020	3.037	2.802	2.143	2.22	2.00	-2.10	1.57	-1.48	2.82	0.578	0.097
20	7.896	0.3101	0.1690	2.007	3.013	2.789	2.129	0.40	0.25	-0.27	1.65	-1.54	2.92	0.696	0.072
40	7.854	0.3103	0.1696	1.999	2.992	2.777	2.116	0.14	0.04	-0.12	1.73	-1.59	3.01	0.797	0.048
60	7.820	0.3102	0.1703	1.994	2.975	2.767	2.105	0.07	0.00	-0.06	1.79	-1.63	3.09	0.863	0.033
80	7.790	0.3100	0.1708	1.990	2.961	2.757	2.096	0.02	0.00	-0.01	1.82	-1.67	3.16	0.900	0.024

We start by examining the structural properties, and in particular the lattice parameter and the bond distances involving the newly introduced element, ie Sr^{2+}, which are displayed in Figure 7.46 and Figure 7.47.

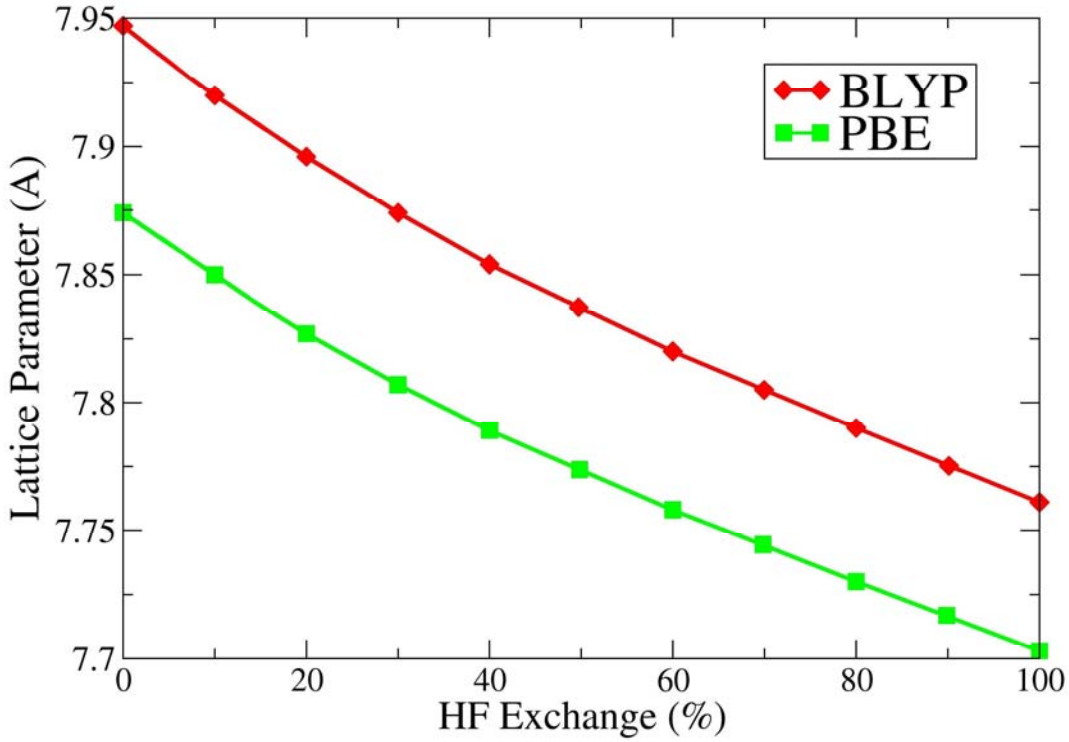

Figure 7.46 Equilibrium lattice parameter as a function of HF exchange for the BLYP and PBE functionals.

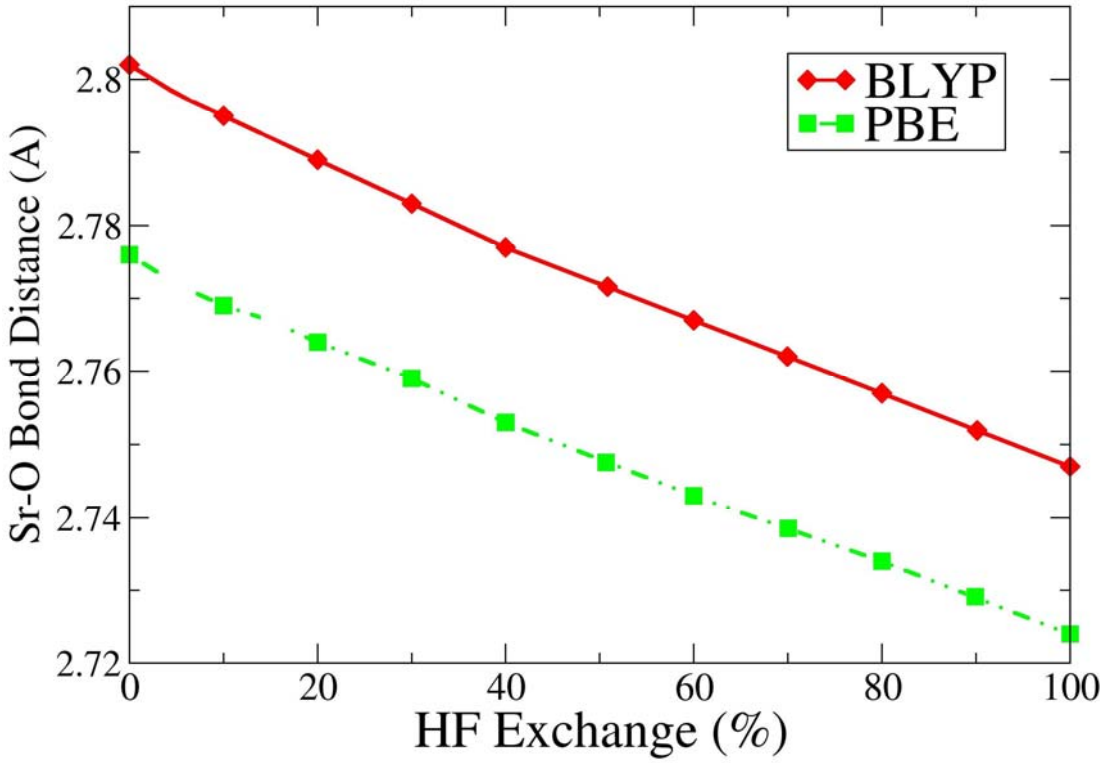

Figure 7.47 Sr-O bond distance as a function of HF exchange for the BLYP and PBE functionals.

Structurally we find little difference between CCZO and SCZO. Perhaps surprisingly replacing Ca^{2+} with the much larger Sr^{2+} ion causes a very small expansion of the lattice parameter, of only 0.02Å. The lattice parameter and bond distances show identical trends to the isostructural materials discussed earlier.

The tilting of the octahedra is increased upon comparison to CCTO by the substitution of Ca and Ti with Sr and Zr. For example, using the $F_{0.4}$PBE functional the tilt is predicted to be 19.1° for CCTO and 21.9° for SCZO. The tilting predicted for SCZO in this case is smaller than for CCZO (22.0°) following the substitution of Ca with Sr, due to the larger Sr being a better match than Ca for Zr in the octahedral site.

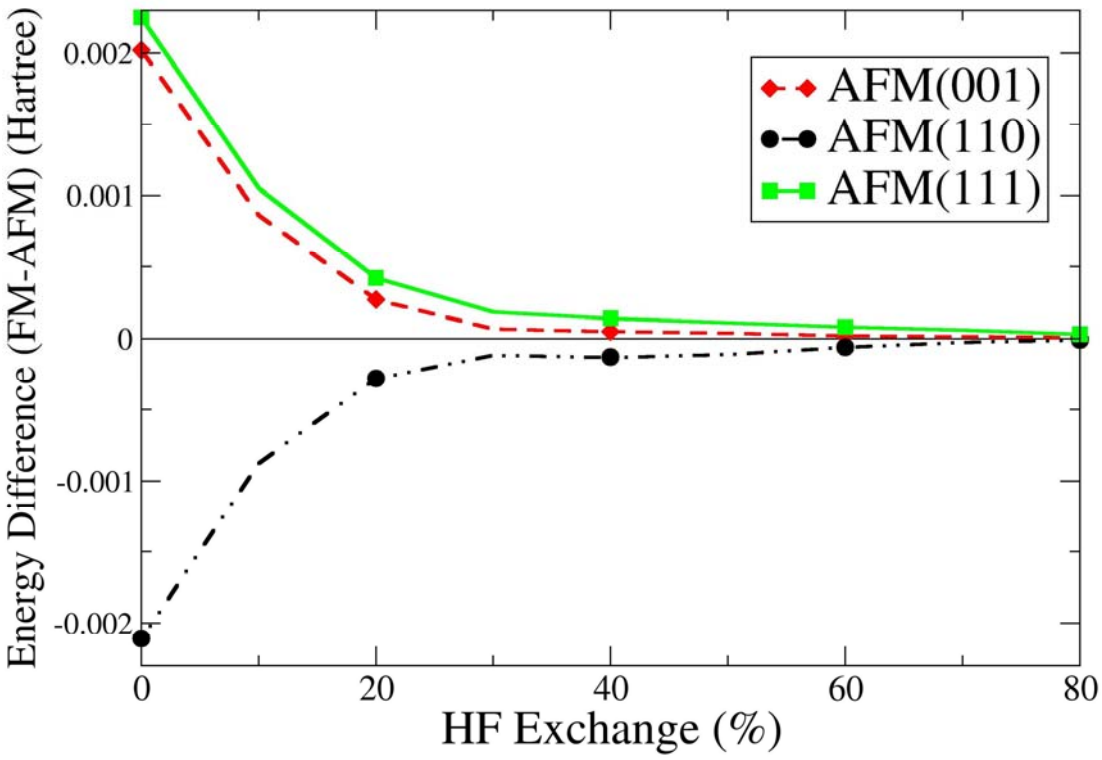

Figure 7.48 Energy difference between the FM and AFM phases against the fraction of HF exchange for SCZO calculated using the PBE functional.

We start our analysis of the electronic properties by examining the difference in energy between the FM and AFM(111, 110 and 001) phases which is presented in Figure 7.48. Results are similar to those for CCZO: the AFM phase with spin alternating along the 111 planes is the most stable phase. The AFM001 phase is more stable than the FM phase which is in turn more stable than the AFM110 phase. The magnitude of the energy differences between the FM and AFM phases is almost identical in CCZO and SCZO, but about 50% smaller than in CCTO, suggesting very small values for the Neel temperature (less than 15K). The trend in energy difference is as we expect for a superexchange type of interaction.

Let us now discuss the DOS calculated for SCZO using the PBE functional, shown in Fig 7.49.

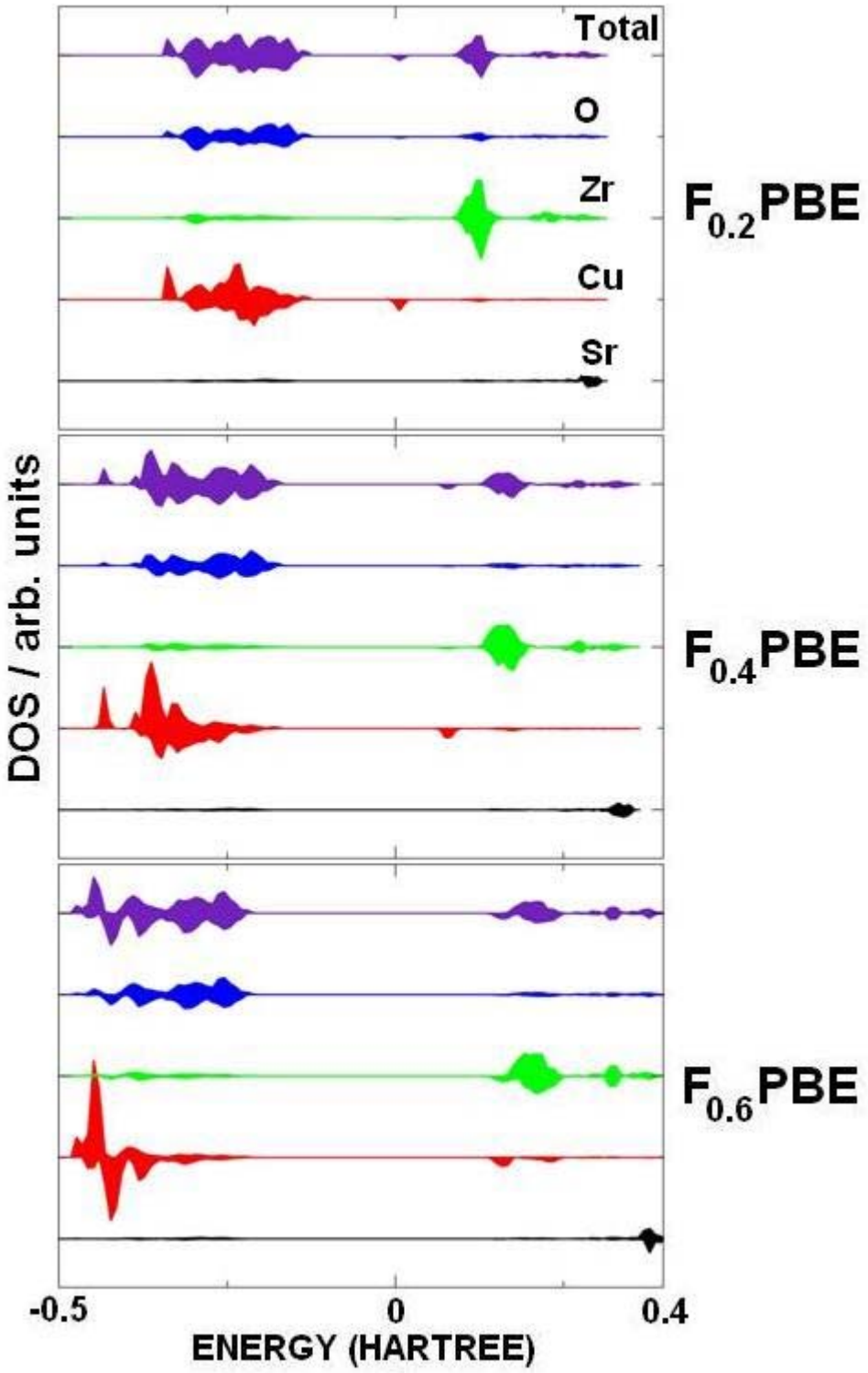

Figure 7.49 Density of states of SCZO calculated using the PBE functional with 20, 40 and 60% HF exchange from top to bottom. The projected DOS of the Ca, Cu, Zr ions and the total DOS are displayed. The total is divided by ten for ease of presentation.

Here we note very little difference in the band gap upon comparison with CCZO (6.84eV and 6.83eV for CCZO and SCZO respectively). The comparison of structural and electronic properties suggest that Ca and Sr behave in an identical fashion in the CCZO/SCZO matrix and may be expected to form readily a solid solution of the two phases.

The final cation replacement that we examine in this class of materials is SCTO, obtained from CCTO by replacing Ca with Sr. Similarly to CCZO and SCZO, also SCTO has not yet been synthesised, and hence the aim of our study was to screen its behaviour. We applied the PBE and BLYP functionals to this study in the range of 0-80% HF exchange. The results are summarised in Table 7.25 and Table 7.26.

Table 7.25 FM results for hybrids built on the PBE functional.

HM (%)	a0 (Å)	Xo	Yo	Rcu-o (Å)	R'cu-o (Å)	Rsr-o (Å)	Rti-o (Å)	$\Delta E_{FM-AFM111}$	$\Delta E_{FM-AFM001}$	$\Delta E_{FM-AFM110}$	qcu (a.u)	qo (a.u)	qti (a.u)	spincu	spino
0	7.491	0.3048	0.1805	1.992	2.805	2.654	1.987	2.97	2.68	-1.42	1.59	-1.35	2.41	0.565	0.091
20	7.436	0.3045	0.1816	1.984	2.778	2.637	1.969	0.53	0.31	-0.20	1.67	-1.40	2.49	0.701	0.066
40	7.389	0.3042	0.1829	1.980	2.754	2.623	1.954	0.16	0.03	-0.13	1.74	-1.44	2.55	0.804	0.044
60	7.352	0.3037	0.1838	1.977	2.736	2.610	1.942	0.07	0.01	-0.08	1.79	-1.47	2.61	0.869	0.030
80	7.319	0.3033	0.1846	1.975	2.721	2.599	1.931	0.03	0.00	-0.04	1.83	-1.50	2.66	0.905	0.022

Table 7.26 FM results for hybrids built on the BLYP functional.

HM (%)	a0 (Å)	Xo	Yo	Rcu-o (Å)	R'cu-o (Å)	Rsr-o (Å)	Rti-o (Å)	$\Delta E_{FM-AFM111}$	$\Delta E_{FM-AFM001}$	$\Delta E_{FM-AFM110}$	qcu (a.u)	qo (a.u)	qti (a.u)	spincu	spino
0	7.560	0.3047	0.1806	2.011	2.830	2.678	2.005	2.90	2.57	-1.38	1.57	-1.35	2.42	0.557	0.094
20	7.500	0.3045	0.1816	2.001	2.802	2.659	1.986	0.49	0.28	-0.17	1.65	-1.40	2.50	0.694	0.069
40	7.450	0.3042	0.1826	1.995	2.778	2.644	1.971	0.14	0.02	-0.1	1.73	-1.44	2.57	0.801	0.046
60	7.409	0.3039	0.1836	1.991	2.758	2.631	1.958	0.06	0.00	-0.07	1.78	-1.47	2.61	0.864	0.032
80	7.374	0.3034	0.1844	1.987	2.742	2.618	1.946	0.02	0.00	-0.03	1.81	-1.50	2.67	0.902	0.023

We begin by presenting the lattice parameter as a function of HF exchange, shown in Figure 7.50. The trend is similar to that observed for CCTO; the geometry is compressed as more HF exchange is included and the BLYP functional predicts a larger unit cell than the PBE functional. The equilibrium lattice parameter for SCTO (extrapolating from the trend of CCTO, CdCTO and CCGO) is of 7.43Å; this represents an expansion from 7.38Å of CCTO due to the larger Sr^{2+} ion compared to Ca^{2+}. We note however that the effect of the Ca/Sr replacement on the lattice parameter is much smaller than that of the Ti/Zr substitution in CCZO/SCZO. Tilting of the TiO_6 or ZrO_6

octahedra enables the perovskite lattice to partially accommodate a strain introduced by the size mismatch on the A site.

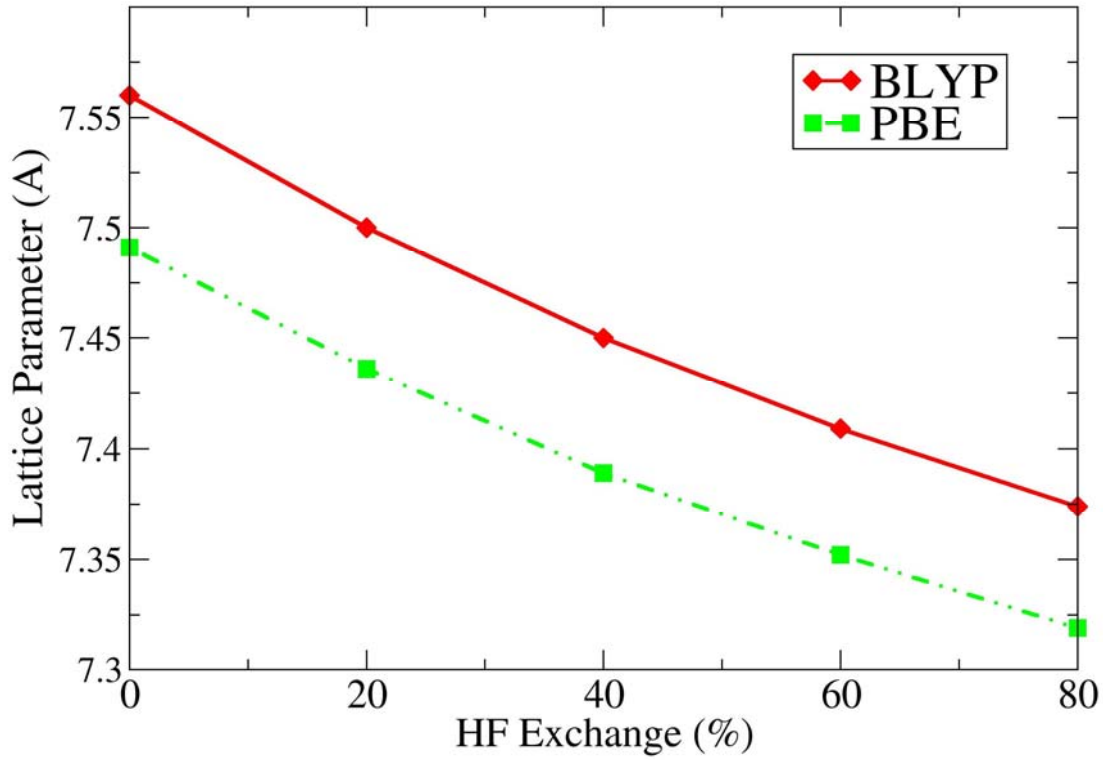

Figure 7.50 Lattice parameter of SCTO calculated using the BLYP and PBE functionals with between 0 and 60% HF exchange.

The difference in energy between the FM and AFM111, AFM110 and AFM001 magnetic phases of SCTO is shown in Figure 7.51.

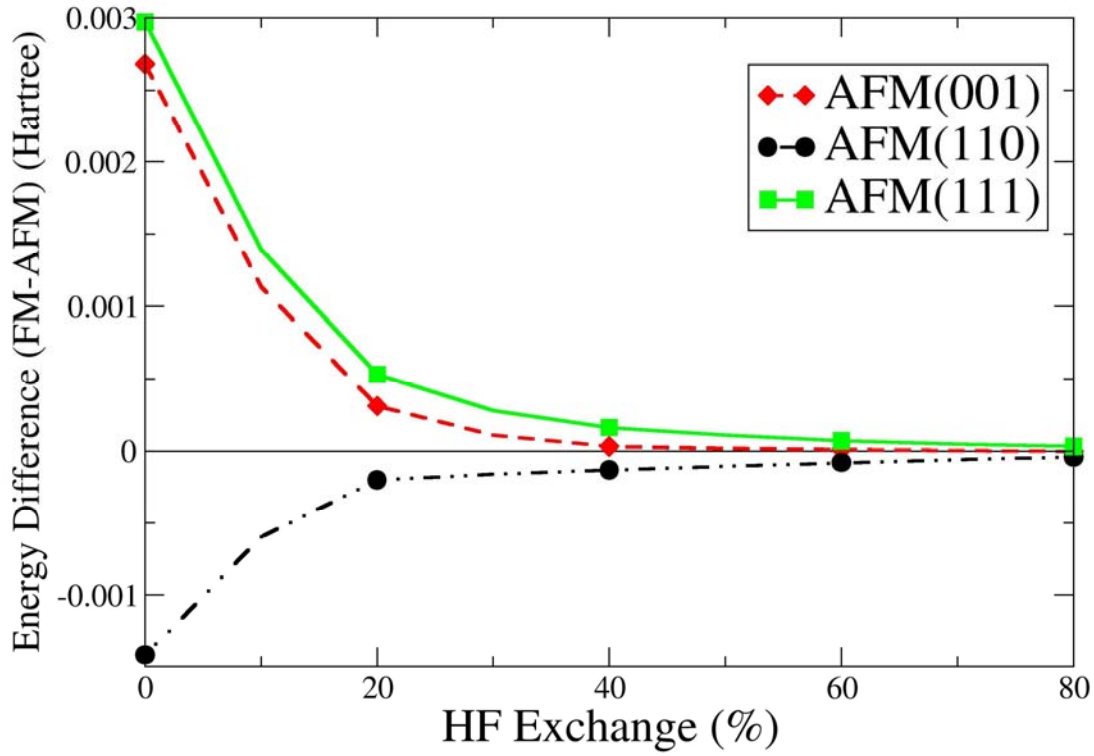

Figure 7.51 Energy difference between the FM and AFM phases of SCTO against the fraction of HF exchange calculated using the PBE functional.

The relative order of the four phases is the same as observed for CCZO and SCZO, but the energy difference is comparable to that calculated for CCTO. Comparison therefore of the four compositions indicates that magnetic coupling is more effective for the Ti-containing solids than for the Zr analogues.

The DOS calculated for SCTO using the PBE functional with 20-60% HF exchange is reported in figure 7.32 for completeness, but it shows no relevant feature to address.

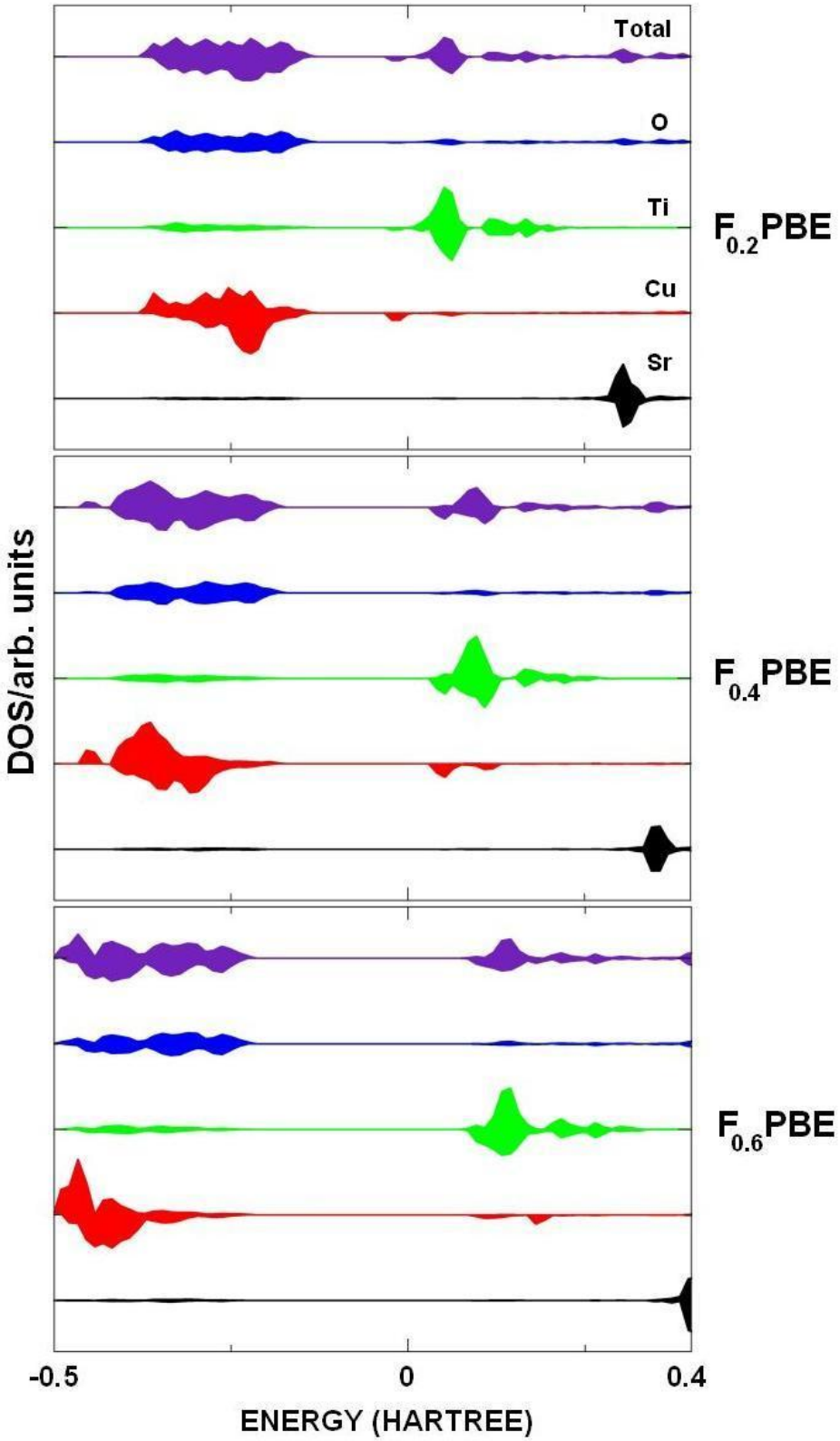

Figure 7.52 Density of states of SCTO calculated using the PBE functional with 20, 40 and 60% HF exchange from top to bottom. The DOS of the Sr, Cu, Ti, O and the total are displayed. The total is divided by ten for ease of presentation.

7.5.1 Conclusions on the study of CCZO, SCZO and SCTO

We performed predictive calculations on the perovskite compounds CCZO, SCZO and SCTO, obtained from CCTO by replacing Ca with Sr and/or Ti with Zr. These materials are isostructural to CCTO; the unit cell parameters vary considerably, especially upon introduction of Zr in the octahedral site. CCZO and SCZO are approximately 7% larger than CCTO and SCTO due to the relatively large Zr^{4+} ions. The substitution of Ca with Sr has instead a less pronounced effect, of less than 0.5%, on the lattice parameter.
The introduction of Sr^{2+} and Zr^{4+} into the A and B sites of the perovskite lattice, does not affect the magnetic ground state; CCZO, SCZO and SCTO were predicted to be AFM111 as CCTO. Replacement of Ti by Zr reduces by approximately 50% the value of the magnetic coupling constants (J_S), while replacement of Ca with Sr has no effect on magnetic coupling. Overall the electronic properties of the new compositions are expected to be similar but inferior to those of CCTO due to the decreased value of the J's.

7.6 Study of $CaCu_3Ti_4S_{12}$ (CCTS)

In the previous section we have investigated the properties of new perovskites obtained from CCTO by cation replacements; it is also possible for anions other than O^{2-} to adopt the Z site of the perovskite structure, although perovskites with other anions are far less studied than oxides. One alternative of potential interest for CCTO is the sulphide anion, S^{2-}, which is isoelectronic with the oxide ion and thus enables a 1:1 substitution. In this section we report results on the study of $CaCu_3Ti_4S_{12}$ (CCTS), where we aim to investigate the substitution of O^{2-} with the larger S^{2-} on the structural and electronic properties. Sulfides usually have smaller band gaps than oxides, a condition that leads to more extreme dielectric properties; it is also unclear whether Cu^{2+} and S^{2-} can coexist in the same lattice, or if the lower oxidation states Cu^{1+}/S^{1-} are stable. These features are suitable for a computational study, and here we apply the expertise gained in the earlier sections to the CCTS sulphide.

In Table 7.27 and Table 7.28 we present a summary of results for CCTS, obtained using the BLYP and PBE functionals and between 0-60% HF exchange. The basis set used for S is an all-electron 8-63111G developed by Bredow et al[132].

Table 7.27 FM results for hybrids built on the PBE functional.

HM (%)	a0 (Å)	Xs	Ys	Rcu-s (Å)	R'cu-s (Å)	Rsr-s (Å)	Rti-s (Å)	$\Delta E_{FM-AFM111}$	$\Delta E_{FM-AFM001}$	$\Delta E_{FM-AFM110}$	qcu (a.u)	qs (a.u)	qti (a.u)	spincu	spins
0	8.987	0.3095	0.1706	2.298	3.420	3.176	2.417	21.65	21.58	12.00	1.45	-1.13	1.87	0.239	0.129
20	8.967	0.3090	0.1728	2.310	3.397	3.175	2.405	5.70	5.60	2.50	1.47	-1.17	1.96	0.387	0.114
40	8.954	0.3088	0.1747	2.319	3.378	3.177	2.396	2.80	2.58	0.19	1.54	-1.22	2.05	0.537	0.093
60	8.936	0.3082	0.1765	2.329	3.361	3.173	2.386	1.10	1.00	0.05	1.66	-1.28	2.12	0.700	0.061

Table 7.28 FM results for hybrids built on the BLYP functional.

HM (%)	a0 (Å)	Xs	Ys	Rcu-s (Å)	R'cu-s (Å)	Rsr-s (Å)	Rti-s (Å)	$\Delta E_{FM-AFM111}$	$\Delta E_{FM-AFM001}$	$\Delta E_{FM-AFM110}$	qcu (a.u)	qs (a.u)	qti (a.u)	spincu	spins
0	9.132	0.3092	0.1706	2.338	3.477	3.225	2.456	21.53	21.47	11.86	1.42	-1.12	1.86	0.233	0.133
20	9.101	0.3087	0.1729	2.347	3.449	3.220	2.440	5.65	5.54	2.45	1.44	-1.16	1.95	0.375	0.120
40	9.075	0.3085	0.1746	2.352	3.426	3.217	2.428	2.77	2.54	0.17	1.51	-1.21	2.03	0.518	0.100
60	9.055	0.3081	0.1762	2.359	3.408	3.214	2.418	1.08	0.96	0.04	1.63	-1.26	2.11	0.682	0.066

Let us first examine the structure, in particular the equilibrium lattice parameter which is plotted in Figure 7.53. As already observed for all the cation replacements, an increase in HF exchange causes a contraction of the equilibrium lattice spacing; there are however substantial differences between CCTO and CCTS. First, the unit cell size has a very large expansion, from 7.38Å in CCTO to 8.97Å in CCTS, (using the PBE functional at 25% HF exchange) an increase of over 1.5Å (or over 20%). Second, the difference between the BLYP and PBE series of hybrid functionals is more pronounced than for the oxides; this result is in line with observations in the literature, that indicate that the performance of BLYP degrades rapidly on increasing atomic number of the anion, while PBE is more robust across groups of the periodic table. Third, the decrease in lattice parameter is less pronounced for the sulphide than the oxide; in the PBE series, the compression upon increasing the HF fraction from 0-60% in CCTO is of 1.8%, and only of 0.56% in CCTS. The BLYP series yield analogous results.

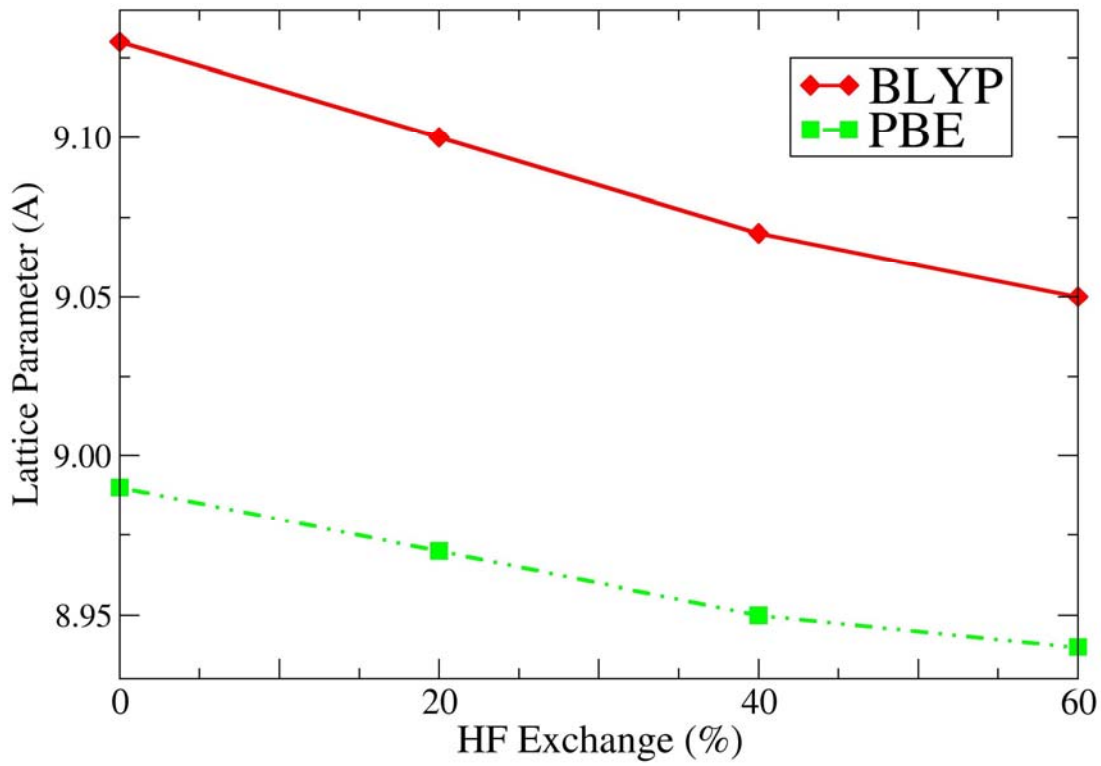

Figure 7.53 Equilibrium lattice parameter of CCTS calculated using the BLYP and PBE hybrid exchange functionals with between 0-60% HF exchange.

Let us now examine the electronic properties, beginning with the DOS calculated for CCTS using the PBE functional with 20, 40 and 60% HF exchange, shown in Figure 7.54.

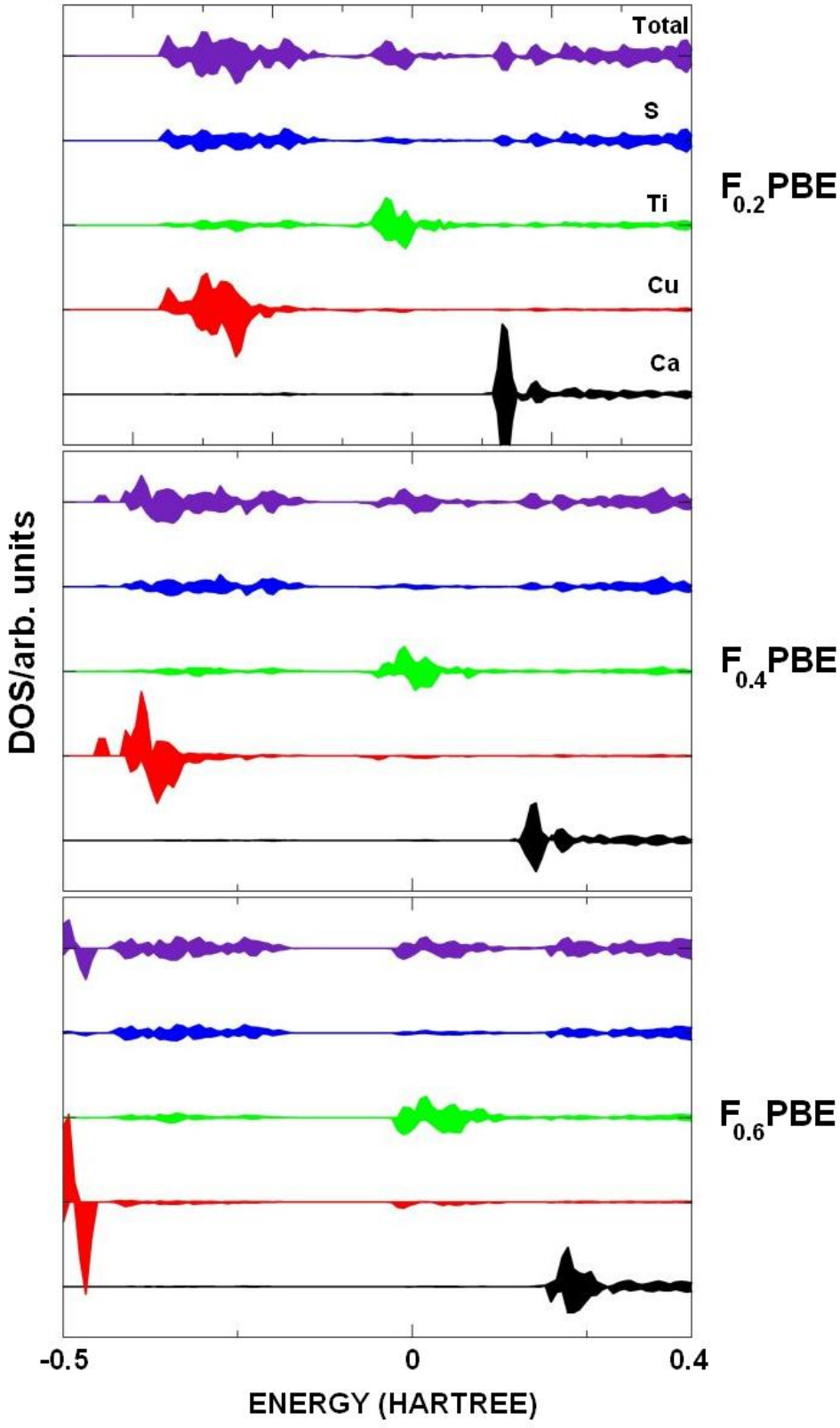

Figure 7.54 Density of states calculated using the PBE functional with 20, 40 and 60% HF exchange from top to bottom. The DOS of the Ca, Cu, Ti, S and the total are displayed. The total is divided by ten for ease of presentation.

Plotted on the same energy scale as for our previously described perovskites, we notice the relatively small band gap of CCTS. This gap also opens relatively little upon increasing the amount of HF exchange. Using 40% and 60% HF exchange we observe a band gap and hence an insulating state. In these cases we obtain Cu^{2+} and S^{2-} states. The situation at 20% HF exchange is much less clear. To understand this better we look at a more detailed DOS with 20% HF shown in Figure 7.55.

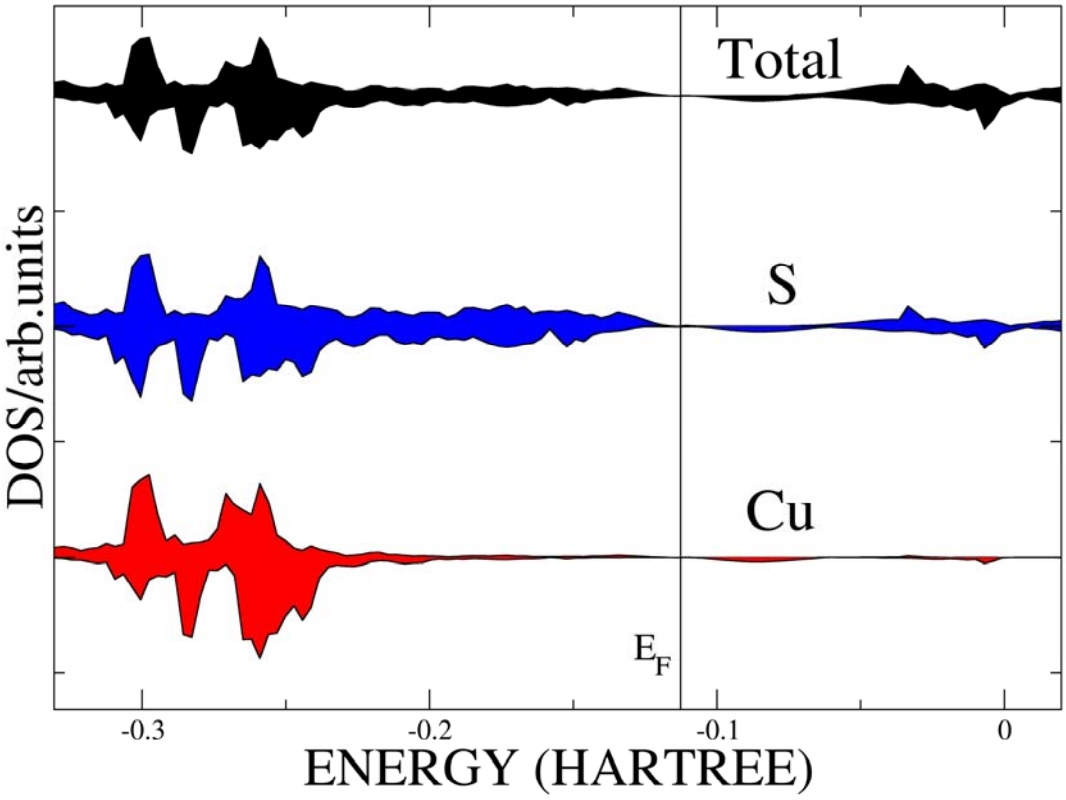

Figure 7.55 Density of states calculated using the PBE functional with 20% HF exchange. The DOS of the Cu, S and the total are displayed. The total is divided by ten for ease of presentation.

Here it looks as if S, at the top of the valence band, overlaps slightly with the Cu^{2+} empty d-level at the bottom of the conduction band. This can be seen more clearly from the band structure in Figure 7.56.

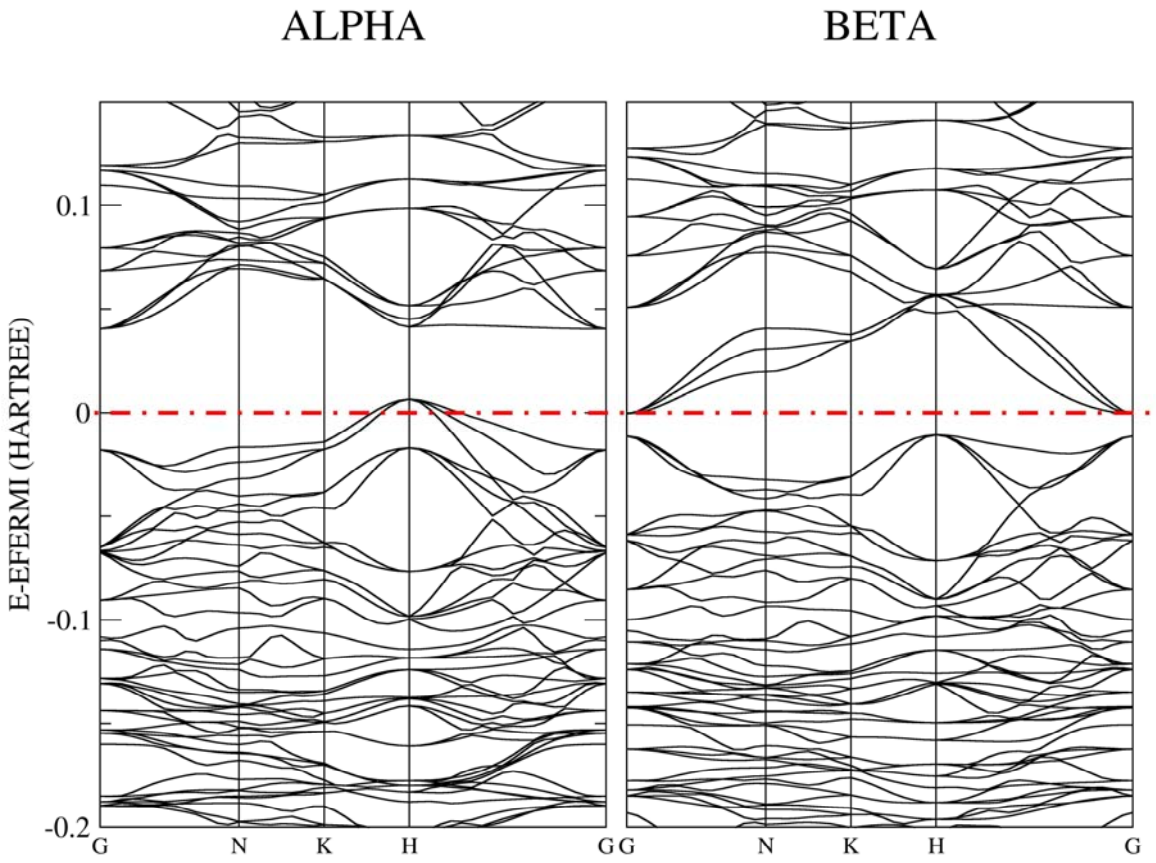

Figure 7.56 Band structure of CCTS calculated using the PBE functional with 20% HF exchange. The Fermi level is indicated by the dashed red line.

When starting from DFT and increasing the amount of HF exchange in the hybrid functional, the S level overlaps with the Cu level yielding a metallic state, when we use 20% HF exchange we get a slight overlap, which disappears with higher fractions of HF exchange until we achieve the insulating states observed with 40% and 60% HF exchange.

Let us now examine the difference in energy between the FM and possible AFM phases. This is shown in Figure 7.57.

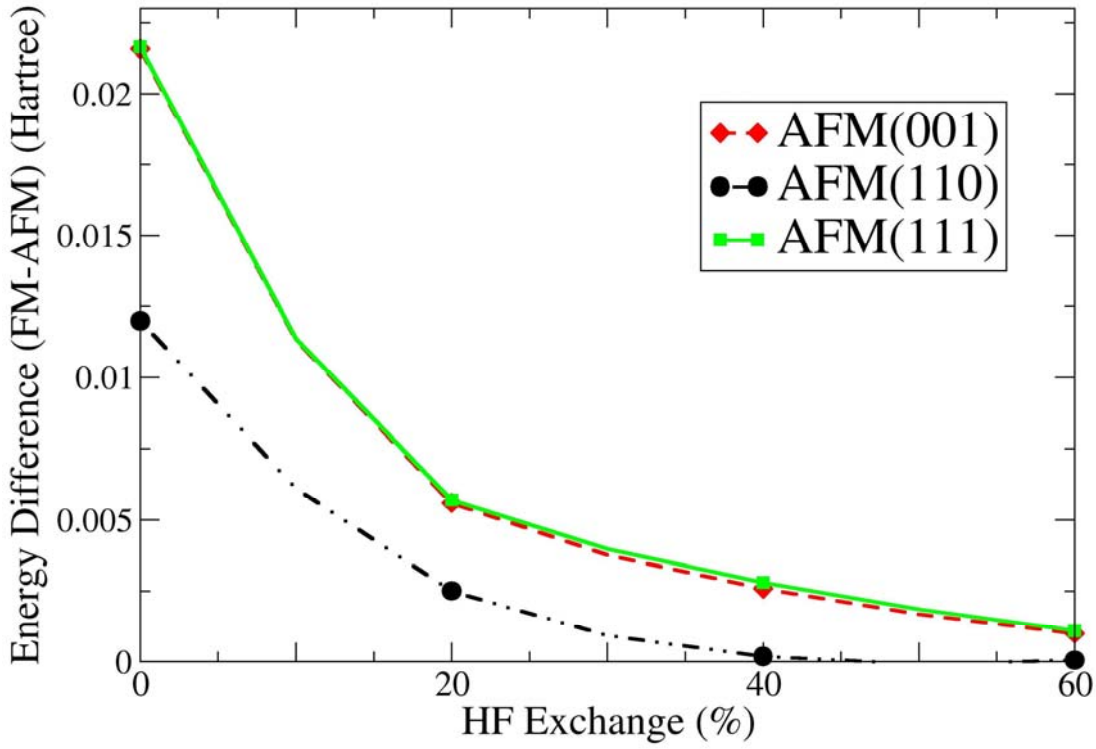

Figure 7.57 Energy difference between the FM and AFM phases against the fraction of HF exchange for SCTO calculated using PBE functional.

Here we predict the ground state to be the AFM111 phase. The FM phase is the least stable of all phases considered. Thus the replacement of O with S does not alter the magnetic properties. However, the difference in energy between the FM and AFM states is far larger in CCTS than CCTO, with an almost 7-fold increase. This feature could mean the material could find practical use in device applications as the order temperature is expected to be substantially higher.

7.7 Conclusions on Chapter 7

In this chapter we have presented the results from calculations on the perovskite compound CCTO and various isostructural compounds with different electronic properties. We have employed hybrid density functionals for this study, and by systematically increasing the fraction of HF exchange we have shown an improvement in both structural and electronic results with respect to experiment. In general we found that an increase in HF exchange led to a decrease in bond distances when using the BLYP and PBE GGA functionals but an increase when using the LDA. Using the BLYP and PBE functionals, agreement to experiment was usually achieved with between 20-60% HF exchange whereas the LDA often failed to find agreement to experiment at any amount of hybrid exchange mixing. A similar behaviour was observed for the electronic properties, but in this case the LDA and GGA results were very similar. We also noted that the choice of functional does affect the predicted structural parameters but has little effect on the electronic properties.

The surface of CCTO was studied in order to investigate its colossal dielectric constant and the possible existence of a barrier layer mechanism. We found that the behaviour of the surface was very sensitive to the choice of theory but we did observe redox chemistry, with the surface Cu ions disproportionating or undergoing a charge-transfer reaction with the surface oxygens. The surface redox activity generates trap states that prevent the mobility of charge carriers and kill the n-type conductivity of CCTO; our findings are thus in support of the Barrier Layer effect.

We studied several compounds isostructural to CCTO, such as CCGO, which despite their structural similarity show very different magnetic behaviour; CCTO is AFM and CCGO has a FM ground state. The behaviour of the parameters of bulk CCGO as a function of HF exchange was qualitatively similar to that observed for CCTO. We then studied the surface of CCGO and found a similar disproportionation to that observed for CCTO. This study was also extended to CdCTO and a similar disproportionation was also observed. However, the difference in disproportionation energy for the three materials showed that CCTO is more likely than CdCTO and CCGO to undergo surface redox steps.

We extended our study to new compositions, where Ca^{2+} and Ti^{4+} were replaced with Sr^{2+} and Zr^{4+} to form CCZO, SCZO and SCTO, none of which has previously been

studied. These compounds were found to be stable within the Im3 space group with respect to symmetry lowering distortions. We found an expansion of the cell compared to CCTO, as expected for the larger Zr^{4+} and Sr^{2+} ions. Our calculations predicted the ground state to be AFM for all three compounds. The AFM phase with spins alternating along the 111 planes was found to be most stable.

We also investigated the effect of replacing O with S in the CCTO structure. As a result we observed a large increase in the unit cell lengths but also a 7-fold increase of magnetic coupling, which makes CCTS a material of practical interest.

Chapter 8 - ABZ_3 Type Perovskites

We have discussed the perovskite structure (Chapter 4) and how its flexibility allows many elements to fit within its structural framework, to give rise to a large variety of properties. In the majority of materials, the charge of the B-site cation is equal or higher than that of the A-site cation; commonly observed valence combinations of the A and B cations are 3-3 (eg. $YAlO_3$ and $BiCoO_3$), 2-4 ($CaTiO_3$) and 1-5 ($KNbO_3$). However, there are also a small number of perovskite oxides with the valence combination 4-2, containing divalent transition metal oxides on the B, site that make reference to $SeCuO_3$. Such 4-2 perovskites are rare, and other possible combinations such as $ThCuO_3$ and $CeZnO_3$ have never been achieved experimentally. The few 4-2 Perovskites described so far contain a p element on the A site ie. Se^{4+}, Te^{4+}. The covalent A-O bonds and the lone pair electrons of Se^{4+} and Te^{4+} which are able to fill the space on the A site, contribute to the stability of the crystal structure.

In this chapter we present results on a set of 4-2 perovskites, containing Se^{4+} as the A-site cation. The parent compound is $SeCuO_3$, that has recently been shown to have magnetoelectric behaviour[84]. Examples with other 2+ transition metal ions also known experimentally are given for comparison.

The aims and objectives of this chapter are to shed further light on the ferroelectric, ferromagnetic and multiferroic properties of $SeCuO_3$.

8.1 $SeCuO_3$

Copper selenite ($SeCuO_3$) was first synthesised at high pressure in 1975 by Kohn et al[133]. X-ray powder patterns showed that the unit cell is orthorhombic and has been assigned to the Pnma space group. This has been more recently confirmed by Subramanian et al.[3]. The structure is that of a highly distorted perovskite, where the Se^{4+} ions occupy the larger A sites with the transition metal ion Cu^{2+} on the B sites. We stress here that Cu was in the A site in the CCTO structure and now occupies the B site. We shall therefore examine the effect this has on the materials properties. The $SeCuO_3$ structure is composed of corner shared CuO_6 octahedra forming a 3D network, with the

Se^{4+} in the 12 coordinated cavities. The ideal perovskite structure contains A cations in 12 fold coordination, however the small size and strong covalent nature of Se^{4+} pulls in 3 of the 12 oxygen atoms, producing SeO_3 groups which tilt the CuO_6 octahedra and bend M-O-M angles (M=Cu in this case) away from the ideal 180° to a range of 120° - 130°. This is the smallest observed for any perovskite. There is also a large distortion in Cu-O distances varying in the range from 1.9-2.6Å due to the Jahn-Teller effect caused by the d^9electronic configuration of Cu^{2+}.

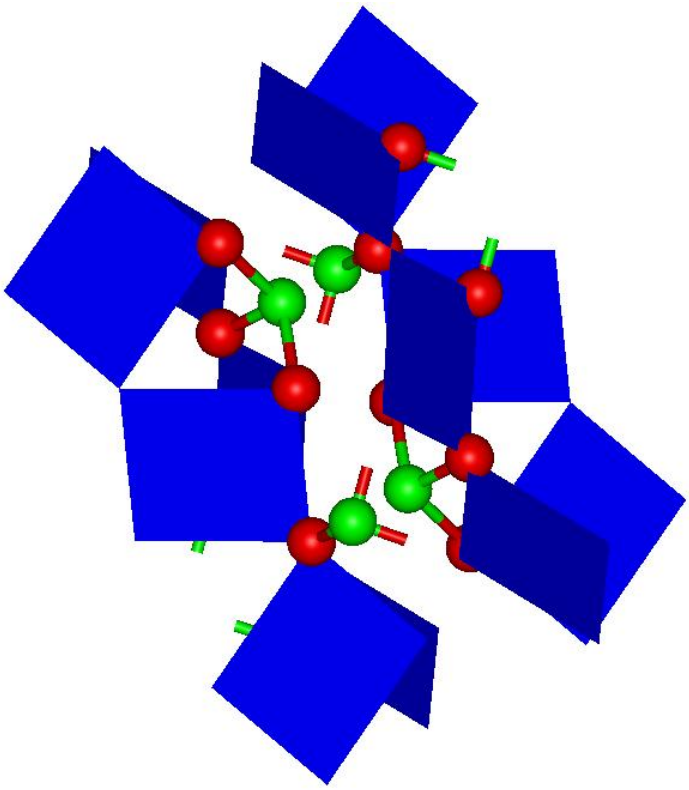

Figure 8.1 $SeCuO_3$ unit cell displaying the tilting of the CuO_6 octahedra and the $[SeO_3]^{2-}$ groups. Oxygen is in red, Selenium in green and Copper in blue. The figure also displays the copper chains.

The magnetic ground state of $SeCuO_3$ has been found to be ferromagnetic, with a Curie temperature of T_C=25K[133]. All subsequent studies have found agreement with this claim, however the reason for the ferromagnetic ordering is subject to debate.

The unit cell contains two symmetry unique O atoms, which we label as O(1) and O(2). Each oxygen is involved in a Cu-O-Cu bridge which can be distinguished by the Cu-O(1)-Cu and Cu-O(2)-Cu angles. In a magnetic oxide of transition-metal ions possessing unpaired electrons (in this case Cu^{2+}), the spin exchange interactions

between adjacent Cu^{2+} ions are either of superexchange type (involving Cu-O-Cu paths) or of the direct exchange type. A set of rules known as the Anderson-Goodenough-Kanemori (AGK) rules can be employed to provide approximate values for the superexchange interaction sign and strength considering the electronic configuration of the M ions (in this case Cu^{2+}) and the M-O-M angle only[2, 127, 134, 135]. From the AGK rules it results that for Cu^{2+} an M-O-M angle greater than ~135° will lead to an AFM ground state, with a FM ground state for values of the M-O-M angle below this critical value. According to the AGK rules, the cut off angle of 135° can be used to explain the FM ground state of $SeCuO_3$ since both the Cu-O(1)-Cu (or α_1) and Cu-O(2)-Cu (or α_2) angles are below the threshold value and have been experimentally measured as 122° and 127.1° by Subramanian et al[3]. The same authors also investigated a continuous solid solution between $SeCuO_3$ and the isostructural $TeCuO_3$, which has an AFM ground state. By substituting Selenium by Tellerium on the A sites they were the first to show a FM-AFM transformation controlled by a single microscopic parameter. They reported that α_1 remained approximately constant at ~123° for both materials and thus FM in both cases. They found however that α_2 changed from 127° to 130.5° from x=0 to x=1 in the continuous solution of $Se_{1-x}Te_xCuO_3$. They were also able to determine a crossover angle between the FM and AFM superexchange of 127.5°, significantly lower than the aforementioned AGK value and thus suggesting that the AGK rules have at most a qualitative application. Subramanian et al. proposed therefore that it is the effect of α_2 on the superexchange that determines the magnetic ground state. However, there have since been two computational studies involving a spin exchange analysis that contradict this assignment. Villesuzanne. et al[136] studied the difference in the spin exchange parameters of both FM $SeCuO_3$ and FM $TeCuO_3$, considering the spin exchange associated with the α_1 and α_2 Cu-O-Cu angles as well as direct contributions within the unit cell. The spin exchange associated with α_1 and α_2 can be called J_1 and J_2 respectively. They found that there was virtually no difference in J_2 between the two materials; it was instead J_1 that displayed a change of sign from FM to AFM when moving from $SeCuO_3$ and $TeCuO_3$. This result suggests that it could be the dependence of the superexchange on α_1 that is responsible for the observed FM-AFM transition and not α_2 as suggested in ref. [3]. In agreement with the aforementioned experiment conducted by Subramanian et al, the angle that J_1 relates to (α_1) remains almost constant from $SeCuO_3$ to $TeCuO_3$. This suggests that perhaps it is not the

dependence of the superexchange on any Cu-O-Cu angle but in fact an entirely different reason for the observed ferromagnetism. Iniquez et al.[137] performed a similar computational study of the $SeCuO_3$ and $TeCuO_3$ perovskites using the PBE functional within DFT and also the LDA+U method, to provide a more accurate treatment of the 3d electrons of Cu^{2+}. They found agreement with the conclusions of Villesuzanne et al, ie. the superexchange angles have little influence on the magnetic couplings of these systems. Furthermore, they considered both the $SeCuO_3$ solid in the $TeCuO_3$ structure and vice versa and found evidence that it is the structure and not the chemical composition that determines the magnetic ground states of these two systems. The authors propose that the observed FM to AFM transition is due to the position of the Se or Te cations relative to the superexchange Cu-O-Cu paths, and show reasonable evidence of this by the way of variable Se/Te-O distances and their effect on the magnetic ground state. As the Se/Te cation approaches the O(1) atom it acts like a 'magnetic valve' and reduces the superexchange contribution to the magnetic coupling, as illustrated in Fig 8.2.

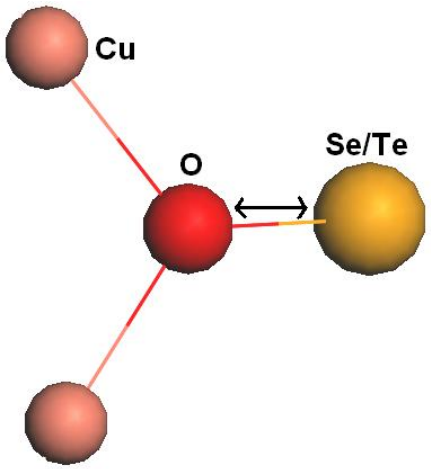

Figure 8.2 Se/Te-O bond distance which has been suggested as the parameter that controls the ground magnetic state of $Cu(Se/Te)O_3$.

It should also be noted that there are different AFM phases available to the $SeCuO_3$ and $TeCuO_3$ structures; these are commonly labelled as A-AFM, C-AFM and G-AFM phases, in which the spins are ordered as shown in Figure 8.3, where we also display the FM phase for completeness. The two aforementioned theoretical works by Villesuzanne and Iniquez agree with each other, but disagree with the experimental work of ref [3] on

the most stable magnetic phase for $CuTeO_3$. The computational studies predict the FM phase as the ground state for $SeCuO_3$ and A-AFM for $TeCuO_3$, while experiment indicates FM and C-AFM respectively. Further to this, Yu et al[138] studied the two perovskites computationally within the LSDA regime and found agreement with the earlier computational studies on the A-AFM ground state of $TeCuO_3$. We should also mention here the experimental work of Escamilla et al[139], who studied the substitution of Cu^{2+} with Mn^{2+} to form a continuous solid solution $SeCu_{1-x}Mn_xO_3$, which changed magnetic ground state from FM to AFM. They found that all Cu/Mn-O-Cu/Mn angles remained constant throughout the solution, further suggesting that the ferromagnetic behaviour is not due to the effect of the M-O-M angle on the superexchange.

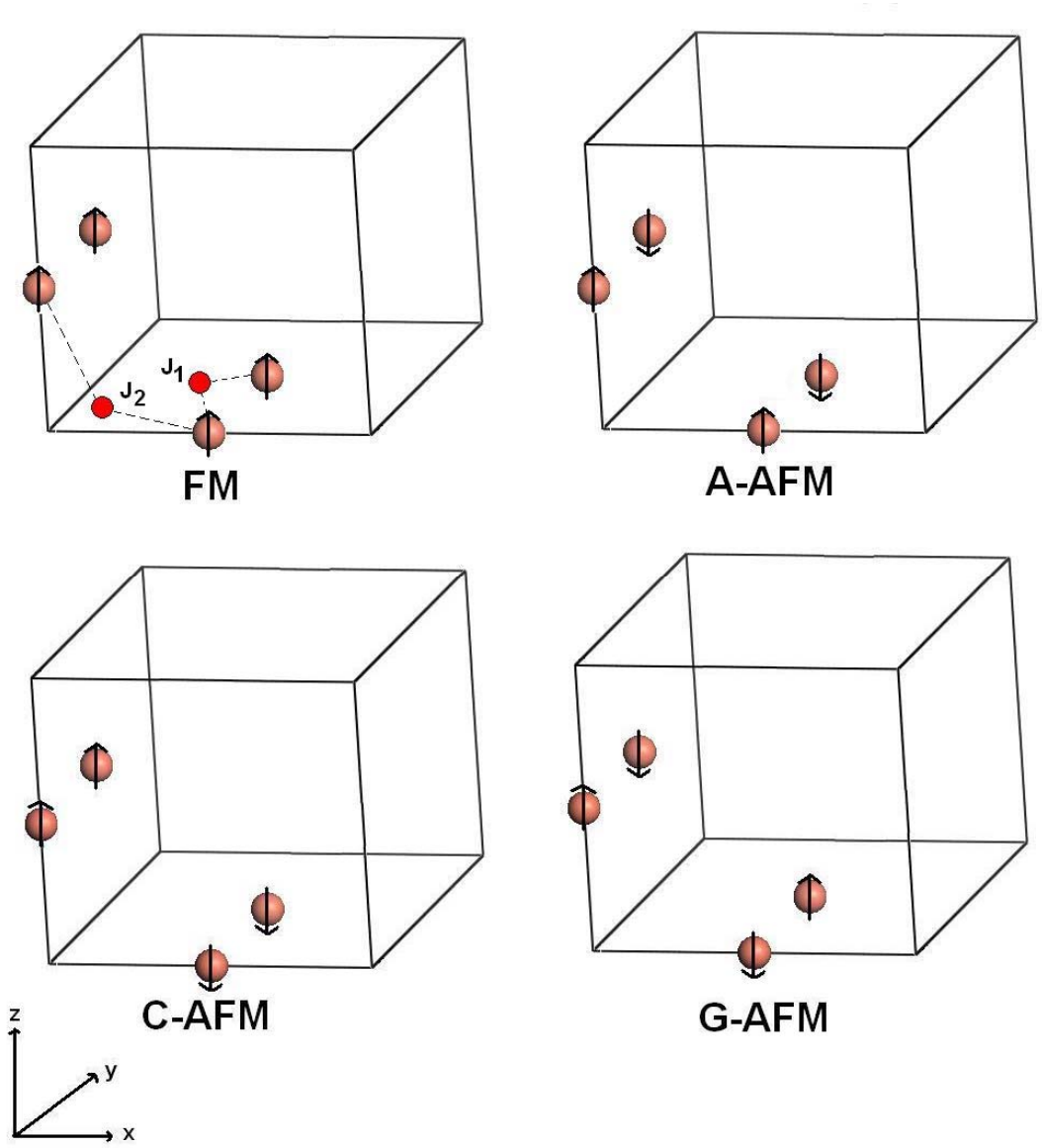

Figure 8.3 The FM and AFM spin phases considered for the ABZ_3 perovskites in this PhD. For this purpose, only the Cu atoms are shown in the unit cell. The FM diagram also displays the J_1 and J_2 exchange parameters that are considered (relating to the Cu-O(1)-Cu and Cu-O(2)-Cu angles respectively.

One of the most interesting suggestions found in the literature is that made by Lawes et al. [92]. They suggest that the perovskite $SeCuO_3$ could exhibit multiferroic behaviour. Also Subramanian et al.[3] suggest that there is magnetoelectric coupling in $SeCuO_3$. However, ferroelectricity is formally forbidden by the Pnma centrosymmetric space group of $SeCuO_3$, which clearly leaves open questions on the interplay between structural and electronic degrees of freedom in $SeCuO_3$ and related materials that we aim to study computationally.

8.1.1 Aims of the Study and Computational Details

As discussed in the introduction to this chapter, the perovskite structured $SeCuO_3$ displays interesting magnetic properties which are not only of academic interest but also make the material potentially useful for technological applications. In order to maximise the potential of this structure it is important to fully understand its electronic and magnetic properties, both of which are subject to debate. The high pressure conditions required to synthesise this material are no doubt among the reasons for the lack of good quality experimental data. The strongly correlated Cu^{2+} ions of $SeCuO_3$ also make an accurate analysis difficult for computational methods based on local DFT. We therefore studied the structural, electronic and magnetic properties of $SeCuO_3$ using hybrid density functionals. Through this study we aimed to tackle the uncertainties of the structure, particularly the magnetic structure, whilst providing a good test for the hybrid functionals.

The computational details were similar to those reported in Chapter 5 for CCTO. It is necessary to make an appropriate choice of k points as to limit computational expense but represent the properties accurately. We found that k-point nets of 4x4x4 were sufficient to converge all properties as shown Table 8.1, which displays the unit cell parameters calculated with the $F_{0.4}$PBE functional for k-point nets of 4x4x4 and 8x8x8. The Gaussian basis sets used to describe the crystalline orbitals were obtained from the online library of the CRYSTAL code[105] other than that used for selenium which was developed by Towler [140]. The accuracy of this basis set was confirmed by repeating calculations using an independent basis set derived by Ahlrichs[141]. The comparison of the unit cell parameters calculated with the two independent basis sets and the $F_{0.4}$PBE functional is shown in Table 8.2. The initial lattice parameter and fractional coordinates of the unit cell employed in full geometry optimisations were those derived by Subramanian et al[3].

Table 8.1 Comparison of unit cell parameters calculated with the $F_{0.4}$PBE functional with k-point nets of 4x4x4 and 8x8x8.

HF%	a	b	c	Se(X)	Se(Z)	O1(X)	O1(Z)	O2(X)	O2(Y)	O2(Z)
4x4x4	5.830	7.367	5.253	0.0344	0.0005	0.0712	0.3233	0.1983	0.0742	-0.1080
8x8x8	5.833	7.365	5.254	0.0346	0.0005	0.0713	0.3232	0.1983	0.0742	-0.1080

Table 8.2 Comparison of unit cell parameters calculated with the $F_{0.4}$PBE functional with two independent basis sets developed by Towler and Alrichs.

Method	a	b	c	Se(X)	Se(Z)	O1(X)	O1(Z)	O2(X)	O2(Y)	O2(Z)
Towler	5.830	7.367	5.253	0.0344	0.0005	0.0712	0.3233	0.1983	0.0742	-0.1080
Alrichs	5.844	7.387	5.224	0.0344	0.0005	0.0713	0.3242	0.1993	0.0752	-0.1070

8.1.2 Structural Results

Similarly to our work on CCTO discussed in chapter 7, also for $SeCuO_3$ we studied the FM and three AFM phases shown in Figure 8.3 using hybrid exchange functionals built on the PBE, BLYP and LDA functionals within DFT and a range of HF exchange between 0 and 100% in 20% increments. Some gaps exist in our results at high fractions of HF exchange due to the difficulty in achieving SCF convergence. All three AFM structures shown in Figure 8.3 were studied across the range of HF exchange to investigate if the ground magnetic state is sensitive to this parameter. We begin by presenting and discussing the structural results. The structure was constrained to belong to the experimentally derived Pnma space group; we have however performed Γ-point phonon calculations to confirm that this choice represents a proper minimum, at least with respect to symmetry lowering distortions within the primitive unit cell (composed of 4 formula units or 20 atoms). An example of phonon frequencies, calculated with the $F_{0.4}$PBE hybrid functional, is tabulated in Table 8.3. Clearly there is no imaginary mode and the three rigid translations are calculated to have a frequency of $5cm^{-1}$ that indicates good numerical accuracy.

Table 8.3 Phonon analysis for $SeCuO_3$ calculated using the $F_{0.4}$PBE functional. The 60 modes are tabulated with the corresponding frequencies.

Mode	Freq. (cm^{-1})	Mode	Freq. (cm^{-1})	Mode	Freq. (cm^{-1})
1	5	21	242	41	508
2	5	22	244	42	510
3	2	23	265	43	527
4	118	24	274	44	559
5	133	25	302	45	565
6	141	26	304	46	574
7	145	27	309	47	576
8	152	28	335	48	597
9	176	29	338	49	764
10	176	30	347	50	772
11	183	31	381	51	780
12	184	32	424	52	787
13	191	33	431	53	793
14	196	34	438	54	803
15	201	35	445	55	811
16	208	36	451	56	865
17	216	37	456	57	875
18	235	38	465	58	876
19	238	39	467	59	886
20	240	40	479	60	904

Within the Pnma space group there are four symmetry unique atoms at the following fractional coordinates: Cu (0, 0, 0.5), Se (X_{Se}, 0.25, Z_{Se}), O(1) ($X_{O(1)}$, 0.25, $Z_{O(1)}$) and O(2) ($X_{O(2)}$, $Y_{O(2)}$, $Z_{O(2)}$). The optimised parameters and bond distances are reported in tables 6.4-6, where the symbols and units are as described for CCTO in Chapter 5. The gaps in the experimental data are due to these particular parameters not being available.

Table 8.4 Equilibrium structure for $SeCuO_3$, calculated using hybrid exchange functionals built on the PBE local formulation.

HF%	a	b	c	Se(X)	Se(Z)	O1(X)	O1(Z)	O2(X)	O2(Y)	O2(Z)
0	5.910	7.504	5.295	0.0323	-0.0018	0.0739	0.3291	0.1981	0.0721	-0.1171
20	5.882	7.400	5.312	0.0360	0.0027	0.0732	0.3274	0.1998	0.0727	-0.1074
40	5.830	7.367	5.253	0.0344	0.0005	0.0712	0.3233	0.1983	0.0742	-0.1080
60	5.794	7.330	5.207	0.0324	-0.0012	0.0690	0.3202	0.1963	0.0752	-0.1084
Expt.	5.970	7.331	5.290							

CuO6 octahedra			SeO8 polyhedra						
Cu-O1 x2	Cu-O2 x2	Cu-O2 x2	Se-O1	Se-O1	Se-O2 x2	Se-O2 x2	Se-O2 x2	Cu-O1-Cu	Cu-O2-Cu
2.128	2.403	1.965	1.769	2.859	1.765	3.123	2.845	123.64	129.30
2.109	2.454	1.932	1.738	2.868	1.730	3.169	2.817	122.60	128.87
2.104	2.424	1.927	1.709	2.855	1.707	3.125	2.804	122.18	128.41
2.096	2.399	1.928	1.687	2.845	1.690	3.093	2.786	121.89	128.00
2.090	2.521	1.919	1.607	2.842	1.843	3.081	2.682	122.00	127.10

Table 8.5 Equilibrium structure for $SeCuO_3$, calculated using hybrid exchange functionals built on the BLYP local formulation.

HF%	a	b	C	Se(X)	Se(Z)	O1(X)	O1(Z)	O2(X)	O2(Y)	O2(Z)
0	6.007	7.630	5.409	0.0400	0.0025	0.0749	0.3304	0.2024	0.0731	-0.1108
20	5.961	7.513	5.401	0.0410	0.0051	0.0737	0.3278	0.2030	0.0738	-0.1039
40	5.913	7.464	5.340	0.0396	0.0036	0.0721	0.3242	0.2016	0.0752	-0.1034
60	5.874	7.423	5.285	0.0376	0.0016	0.0703	0.3211	0.1996	0.0762	-0.1039
80	5.837	7.379	5.238	0.0354	-0.0001	0.0681	0.3187	0.1975	0.0768	-0.1045

CuO6 octahedra			SeO8 polyhedra						
Cu-O1 x2	Cu-O2 x2	Cu-O2 x2	Se-O1	Se-O1	Se-O2 x2	Se-O2 x2	Se-O2 x2	Cu-O1-Cu	Cu-O2-Cu
2.164	2.494	1.966	1.786	2.936	1.775	3.228	2.922	123.64	129.59
2.142	2.520	1.939	1.754	2.928	1.741	3.242	2.884	122.59	128.42
2.132	2.494	1.932	1.723	2.913	1.717	3.204	2.865	122.15	127.87
2.123	2.465	1.933	1.699	2.901	1.697	3.166	2.845	121.86	127.48
2.113	2.437	1.933	1.681	2.888	1.682	3.133	2.822	121.66	127.19

Table 8.6 Equilibrium structure for $SeCuO_3$, calculated using hybrid exchange functionals built on the LDA local formulation.

HF%	a	b	c	Se(X)	Se(Z)	O1(X)	O1(Z)	O2(X)	O2(Y)	O2(Z)
0	5.738	7.164	5.172	0.0172	-0.0041	0.0676	0.3310	0.1927	0.0677	-0.1215
20	5.757	7.208	5.221	0.0271	0.0000	0.0690	0.3283	0.1969	0.0705	-0.1108
40	5.783	7.280	5.223	0.0318	0.0005	0.0691	0.3247	0.1980	0.0733	-0.1077
60	5.818	7.341	5.235	0.0351	0.0007	0.0691	0.3212	0.1984	0.0755	-0.1049
80	5.854	7.396	5.254	0.0380	0.0010	0.0691	0.3180	0.1989	0.0774	-0.1021

CuO6 octahedra			SeO8 polyhedra						
Cu-O1 x2	Cu-O2 x2	Cu-O2 x2	Se-O1	Se-O1	Se-O2 x2	Se-O2 x2	Se-O2 x2	Cu-O1-Cu	Cu-O2-Cu
2.030	2.300	1.934	1.757	2.731	1.757	2.987	2.656	123.40	130.29
2.052	2.382	1.907	1.731	2.785	1.722	3.069	2.708	122.96	129.40
2.076	2.407	1.911	1.707	2.828	1.703	3.097	2.760	122.47	128.57
2.099	2.432	1.920	1.689	2.867	1.688	3.126	2.802	121.93	127.67
2.121	2.461	1.930	1.676	2.905	1.676	3.157	2.840	121.66	127.19

The dependence of the equilibrium lattice parameters, a, b and c of the orthorhombic unit cell on the hybrid exchange definition are displayed in Figure 8.4. They show a trend similar to what was discussed earlier for CCTO, with a cell contraction on increasing HF exchange for the GGA functionals, and a small expansion for hybrids built on the LDA. The structural anisotropy is slightly overestimated computationally, with a and c lattice parameters underestimated, and b overestimated, with respect to experiment.

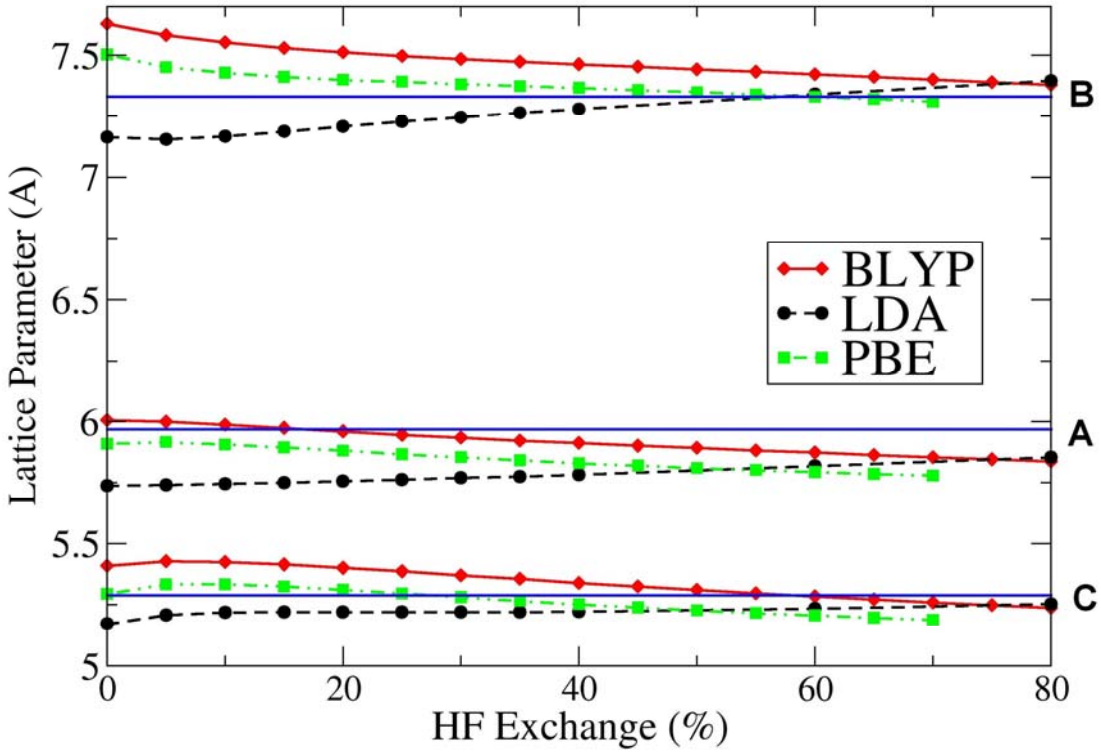

Figure 8.4 Equilibrium lattice parameters of $SeCuO_3$ as a function of HF exchange, calculated using the BLYP, PBE and LDA functionals.

As discussed earlier in this section, in the $SeCuO_3$ structure the A cation is not in the usual perovskite 12-fold coordination, as the Se^{4+} pulls in 3 of the 12 oxygens forming $[SeO_3]^{2-}$ trigonal pyramidal units, inducing a large tilt of the CuO_6 octahedra.

Our results indicate that Se^{4+} in $SeCuO_3$ is best described not as an isolated ion in the perovskite lattice, but as part of a molecular ion $[SeO_3]^{2-}$ (selenite). The three short Se-O bonds, for instance, have a large Mulliken overlap population (0.100|e| at the $F_{0.4}$PBE level) while the other Se-O bonds have negligible or even negative overlap population.

The main structural difference between theory and experiment is noticed in the bond lengths within the $[SeO_3]^{2-}$ units. This molecular ion is found experimentally to have two longer (1.843Å) and one shorter (1.607Å) bonds while theory predicts three almost identical bond lengths, with intermediate values between the experimental measurements (see Figure 8.5, eg. using the $F_{0.4}$PBE functional we obtain 2x 1.707Å and 1x 1.709Å). Se-O bond distances are shown schematically in Figure 8.6 as a function of HF exchange.

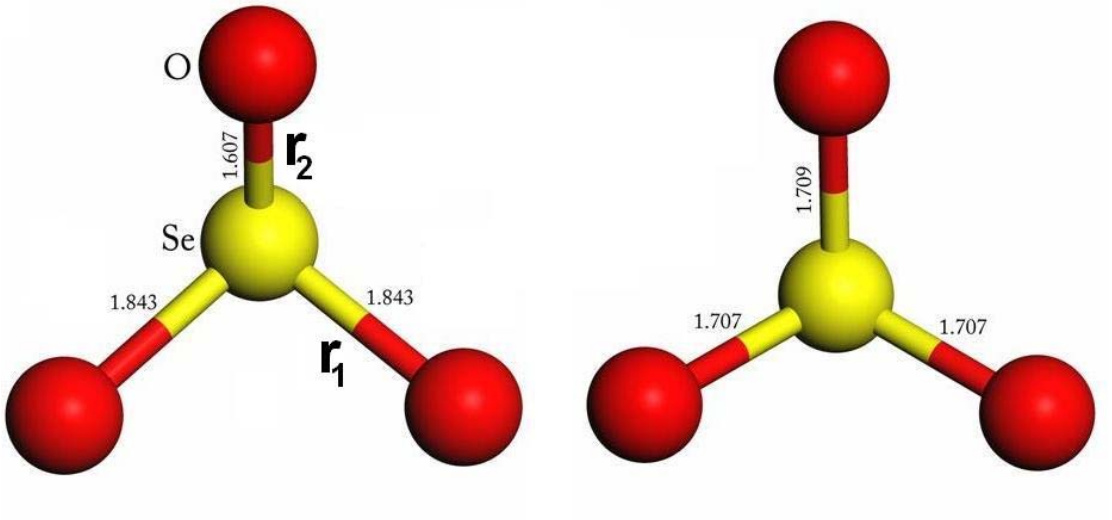

Figure 8.5 Experimentally derived (left) and calculated (right) $[SeO_3]^{2-}$ unit in $SeCuO_3$. Calculation was performed using the $F_{0.4}$PBE functional.

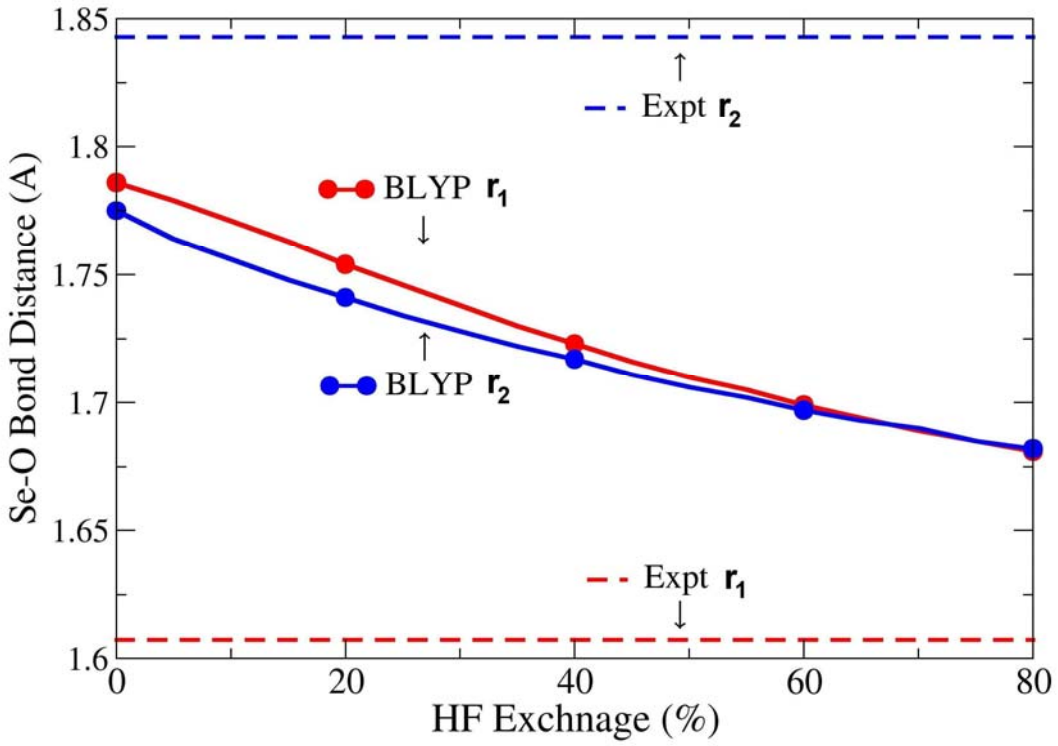

Figure 8.6 Se-O bond distances involved in the $[SeO_3]^{2-}$ formation. The unit is formed of two equal length Se-O bonds (in blue) and one different length Se-O bond (in red).

Theory favours therefore a higher symmetry than experiment regarding the Se-O bonds lengths. The relevant bond distances are not presented in the earlier computational papers[136-138] and hence we cannot make a comparison here.

Since Se has received relatively little attention in solids studied computationally with local orbital basis sets, we have repeated our initial calculations (obtained with Towler's basis set) with the one proposed by Ahlrichs[141] to make sure that such disagreement in Se-O bond distances is not an artefact of the basis set. We found very good internal consistency between the two basis sets. For example, if we compare the Se-O bonds (r_1 and r_2) calculated with the $F_{0.4}$PBE functional, we predict 1.707Å and 1.709Å using Towler's basis set and 1.707Å and 1.712Å with Ahlrichs.
Having eliminated the basis set as a source of error, our results suggest that it may be worth to revisit the experimental structural determination of the $[SeO_3]^{2-}$ units. We have seen earlier that the position of Se or Te relative to the oxygens may play a role in the Cu-O-Cu superexchange, and this is therefore an important feature of the solid.

We have previously discussed that there are two Cu-O-Cu angles within the $SeCuO_3$ orthorhombic unit cell that could possibly contribute towards a superexchange mechanism that would rationalise the stable FM state. These angles are labelled Cu-O(1)-Cu and Cu-O(2)-Cu, and our relevant calculated results compared to experiment are displayed in Figure 8.7.

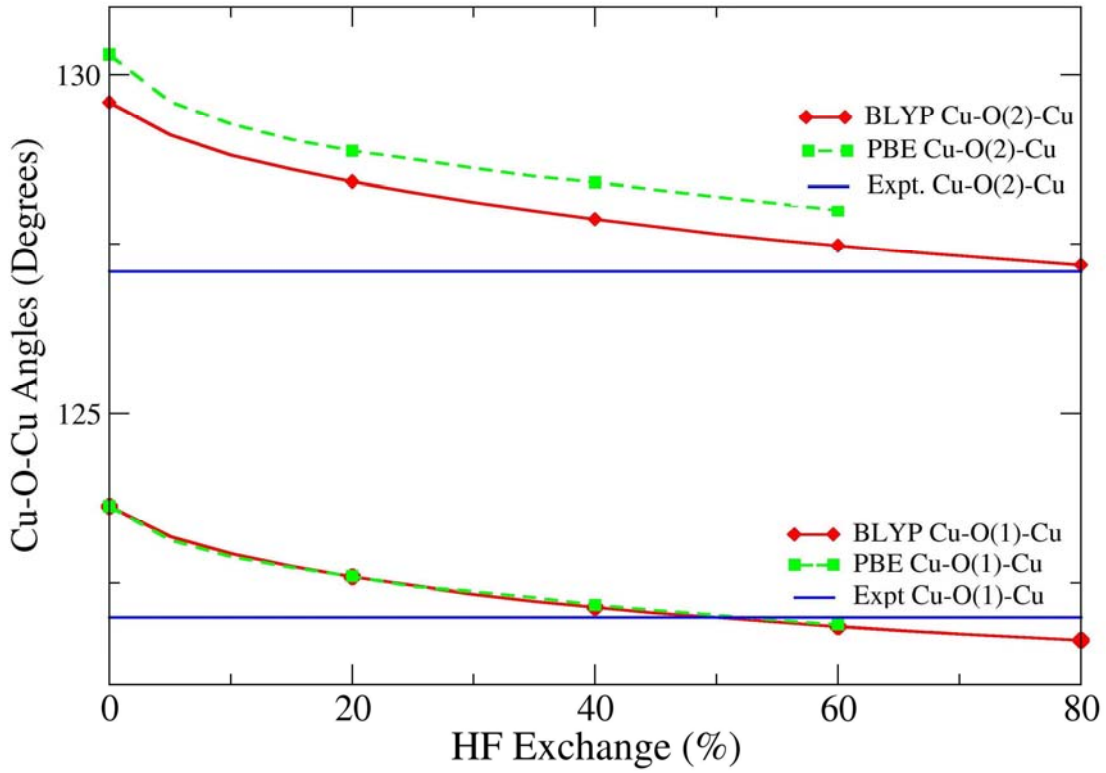

Figure 8.7 Cu-O(1)-Cu and Cu-O(2)-Cu angles within the $SeCuO_3$ unit cell calculated using the BLYP and PBE functionals between 0-80% HF exchange. The experimental values are those experimentally derived by Subramanian et al.[3].

The agreement with experiment is overall satisfactory, particularly for the Cu-O(1)-Cu angle which is best reproduced using the $F_{0.5}$BLYP/PBE functionals. We find reasonable agreement with the Cu-O(2)-Cu angle given the highly distorted nature of the perovskite, although its value is overestimated by up to 3° at the local DFT limit. We note however that the Cu-O(2)-Cu angle decreases by approximately 3° in the range of HF exchange considered in our work. If this parameter does effectively control the FM/AFM nature of superexchange, as suggested in ref.[3], we expect the calculated ground magnetic state of $SeCuO_3$ to have a pronounced dependence on the hybrid functional choice, a feature that we shall investigate in greater detail in the following discussion.

Before moving on to examine the electronic properties, the Jahn-Teller distortion inside the CuO_6 octahedra deserves analysis. This distortion results in very different Cu-O distances, as shown in Figure 8.8. Cu^{2+} is clearly in a square planar environment, as

expected for a d^9 ion, with two trans Cu-O(2) bonds substantially longer than the four equatorial Cu-O bonds. Comparison of the calculated Cu-O distances in the CuO_6 octahedra against experimentally derived values are displayed in Figure 8.9.

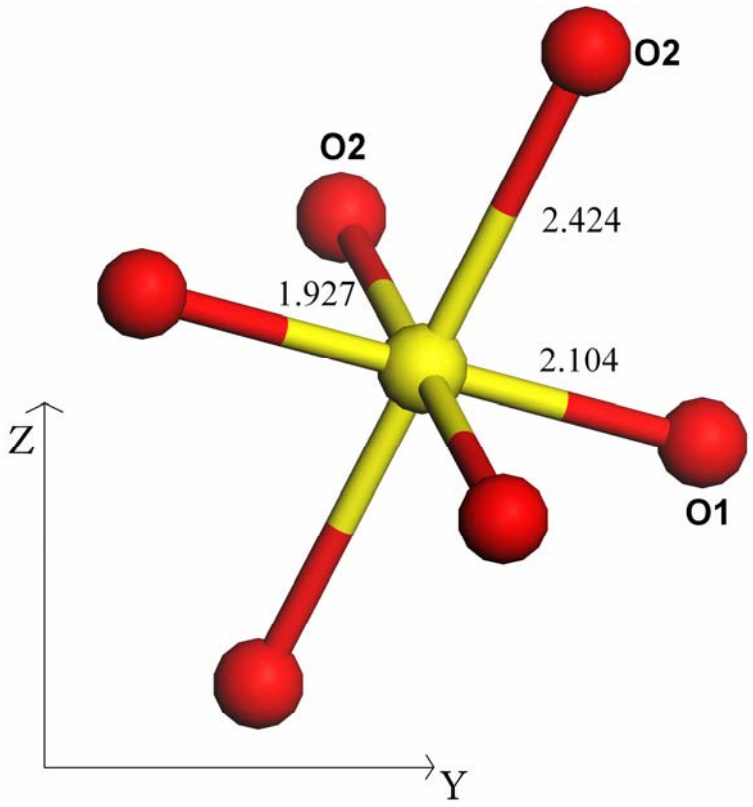

Figure 8.8 Jahn-Teller distorted CuO_6 octahedra calculated using the $F_{0.4}$PBE functional.

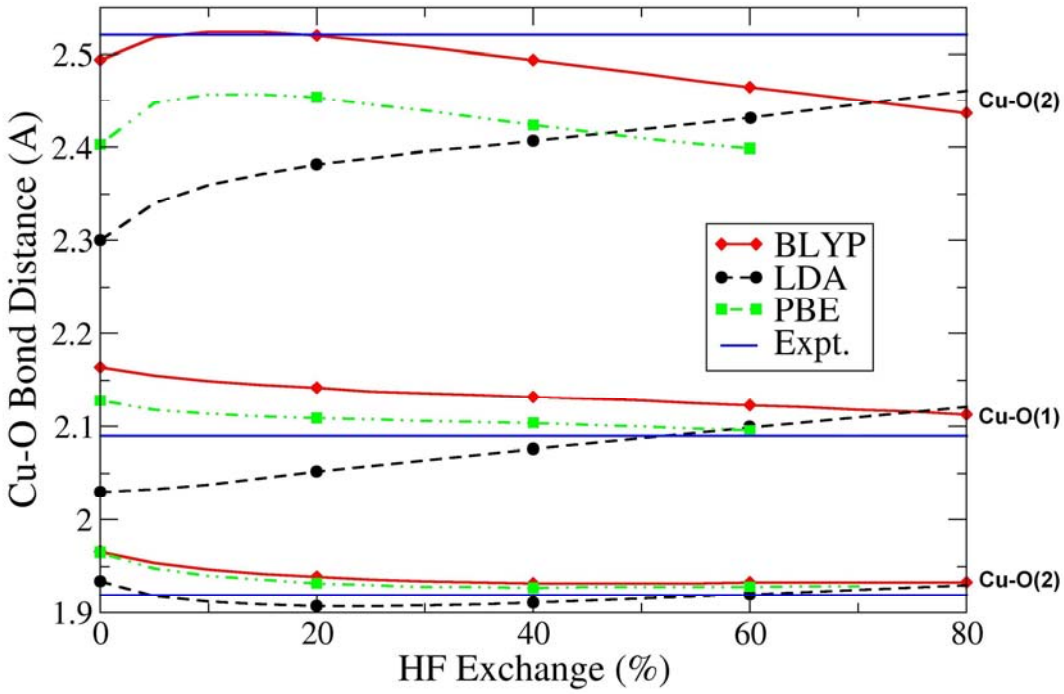

Figure 8.9 Cu-O bond distances of the Jahn-Teller distorted CuO_6 octahedra. The experimental values are displayed as continuous horizontal blue lines.

We observe a relatively small error in the equatorial bonds, with the features already discussed in detail for CCTO: a small underestimation of the bond lengths at pure LDA level, and overestimation in GGA; with hybrid exchange corrections these distances change in the right direction towards the experimental data. The longer Cu-O(2) distances are instead underestimated, by as much as 10% at pure LDA level, but also at GGA level. The longest Cu-O bonds generated by the Jahn-Teller distortion are weak interactions in the solid; LDA is well known to overbind such non-bonded pairs, but also the decrease of Cu-O distances at GGA level may be a direct result of BSSE (see Chapter 3).

8.1.3 Electronic Properties

Let us now examine the electronic properties of $SeCuO_3$, and in particular the magnetic ground state. We have calculated the FM and three different AFM phases, indicated as A, C and G-type as shown in Figure 8.3. We limit our discussion here to calculations performed using hybrid exchange built on the BLYP and PBE GGA functionals.
Results are summarised in Table 8.7, while the relative energies of the magnetic phases examined are shown in Figure 8.10.

Table 8.7 Electronic Properties of $SeCuO_3$ calculated using the BLYP and PBE hybrid functionals; ΔE is the energy difference between FM and AFM structures in mH per double unit cell; q are the net atomic charges and Spin are the spin atomic charges both in |e| for each ion calculated with a Mulliken partition scheme.

Functional	$\Delta E_{FM\text{-}G\text{-}AFM}$	$\Delta E_{FM\text{-}C\text{-}AFM}$	$\Delta E_{FM\text{-}A\text{-}AFM}$	q_{Cu}	q_{Se}	$q_{O(1)}$	$q_{O(2)}$	$Spin_{Cu}$	$Spin_{Se}$	$Spin_{O(1)}$	$Spin_{O(2)}$
PBE	-2.30	-2.05	-1.71	1.576	1.823	-1.212	-1.093	0.575	0.033	0.096	0.148
F0.2-PBE	-1.12	-0.97	-0.92	1.661	1.951	-1.277	-1.167	0.713	0.021	0.070	0.098
F0.4-PBE	-0.40	-0.34	-0.32	1.744	2.060	-1.337	-1.234	0.822	0.014	0.046	0.059
F0.6-PBE	-0.16	-0.15	-0.10	1.796	2.156	-1.348	-1.284	0.883	0.011	0.031	0.037
BLYP	-2.44	-2.11	-1.85	1.561	1.851	-1.213	-1.099	0.571	0.031	0.098	0.150
F0.2-BLYP	-1.14	-1.05	-0.97	1.648	1.978	-1.279	-1.173	0.708	0.020	0.072	0.100
F0.4-BLYP	-0.41	-0.36	-0.34	1.732	2.087	-1.340	-1.240	0.818	0.014	0.048	0.060
F0.6-BLYP	-0.16	-0.15	-0.14	1.786	2.184	-1.388	-1.291	0.880	0.011	0.033	0.038
F0.8-BLYP	-0.08	-0.08	-0.07	1.818	2.271	-1.428	-1.330	0.913	0.009	0.024	0.027

The magnetic ground state of $SeCuO_3$ is found to be the FM phase in both the BLYP and PBE series, and independently on the amount of HF exchange employed in the hybrid functional formulations. The relative energy of the FM and AFM phases does depend on the amount of HF exchange, and the behaviour is similar to that discussed in Chapter 5 for CCTO, with the energy difference decreasing in a hyperbolic-like fashion on increasing the HF exchange fraction. As already discussed in Chapter 5, this behaviour is typical of superexchange interactions. In this respect, the variation of the Cu-O-Cu angles (see Figure 8.7) as a function of HF exchange appears to play no role in the sign of superexchange coupling between Cu ions; the value of 127° for Cu-O(2)-Cu suggested as a threshold for a FM/AFM switch in the experimental work of Subramanian[3] is not observed in our calculationss, which therefore agree with the

earlier computational studies[136-138]. We can confirm therefore that $SeCuO_3$ has a FM ground state, independently on the Cu-O-Cu angles, at least in the range of 120-130° observed in our calculations with different hybrid functionals. Results for the hybrid functionals built on PBE or BLYP formulations are virtually identical, again as already observed for CCTO; in Figure 8.10 we have only plotted the BLYP results, for clarity.

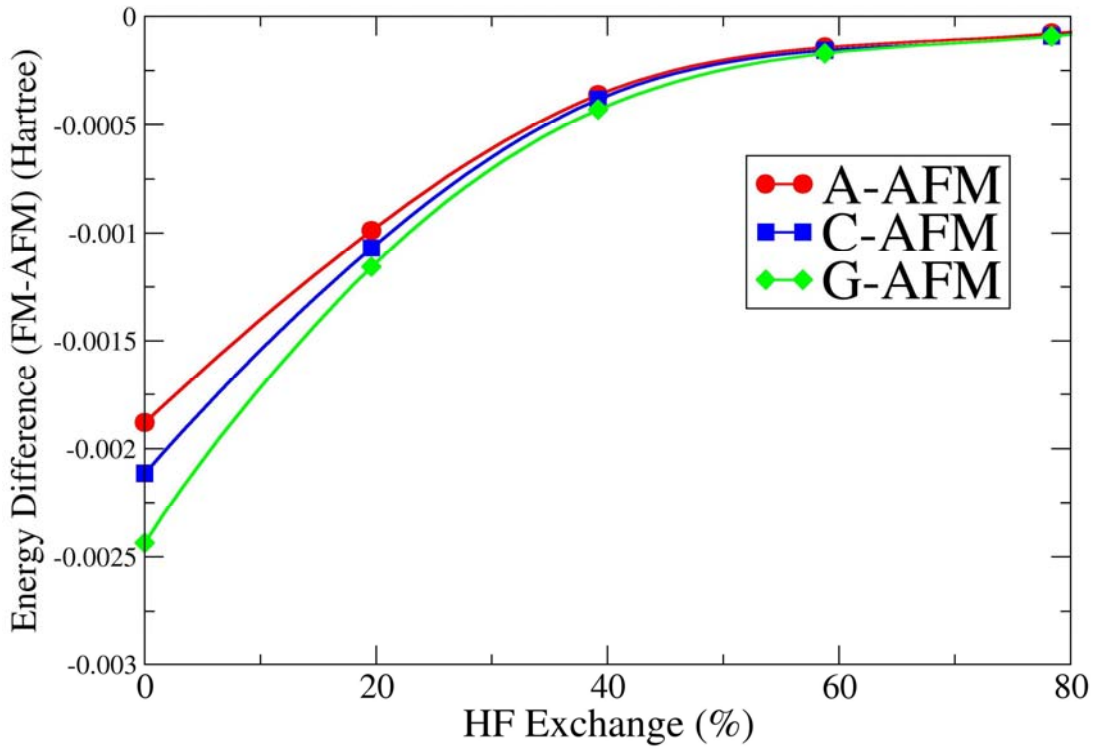

Figure 8.10 Energy difference (Hartree per double unit cell) between the FM and AFM (A, C and G-type) phases calculated using the BLYP functional between 0% and 80% HF exchange.

Let us now consider the relative energy of the three AFM phases, and the effective coupling parameters J_1 and J_2 between Cu ions introduced earlier (see Figure 8.3). Among the AFM phases, the relative energy is found to vary in the order of A<C<G; the energy differences are small and again decay rapidly on increasing the HF exchange fraction. No reversal of phase stability is observed on varying the HF exchange. Of the previous computational studies of $SeCuO_3$, only Villesuzanne[136] reports the relative

energy of the three AFM phases, indicating the A-type as the stable AFM order, in agreement with our work.

The spin polarisation in each symmetry unique atom of the structure, calculated with a Mulliken partition scheme, is shown in Table 8.7. It is important to notice that the spin polarisation is higher on O(2) than O(1), approximately by a factor of 1.5. On the basis of the relative spin polarisation of O(1) and O(2), it is reasonable to expect magnetic coupling to be stronger via the Cu-O(2)-Cu bridge than via O(1), or in other words to have $|J_2|>|J_1|$.

In order to quantify magnetic coupling in $SeCuO_3$ we performed a J analysis of the unit cell, using an Ising effective spin Hamiltonian containing the two coupling parameters J_1 (corresponding to superexchange through O(1)) and J_2 (superexchange through O(2)), and making the assumption that these will be the largest contributors to the magnetic order. We neglect direct exchange and super exchange involving the longest Cu-O bond distances, ie. the axial ones in the Jahn-Teller distorted CuO_6 octahedra. The energies of three different ordered spin states ie. FM, A-AFM, and C-AFM will be expressed as a 2-J Ising Hamiltonian, as:

$$E = E_0 + \sum_{J1} J_1 S_1 S_2 + \sum_{J2} J_2 S_1 S_2 \tag{8.1}$$

The sums extend to all unique pairs of Cu ions in the primitive unit cell linked via O(1) and O(2) bridges. There are four Cu and twelve O atoms in the unit cell, four O atoms are of O(1) type involved in the J_1 coupling, and eight of O(2) type involved in the J_2 coupling. We take S=±1/2 and analyse the spin states (up or down) in each Cu-O-Cu path for the considered magnetic phases to obtain:

$$E_{FM} = E_0 + J_1 + 2J_2 \tag{8.2}$$

$$E_{A-AFM} = E_0 - J_1 + 2J_2 \tag{8.3}$$

$$E_{C-AFM} = E_0 + J_1 - 2J_2 \tag{8.4}$$

which provides:

$$E_{FM} - E_{C-AFM} = 4J_2 \quad (8.5)$$

$$E_{C-AFM} - E_{A-AFM} = 2J_1 - 4J_2 \quad (8.6)$$

and also:

$$E_{FM} - E_{A-AFM} = 2J_1 \quad (8.7)$$

Which can be solved to give:

$$J_1 = \frac{E_{FM} - E_{A-AFM}}{2} \quad (8.8)$$

$$J_2 = \frac{(E_{FM} - E_{C-AFM})}{4} \quad (8.9)$$

Table 8.8 Spin exchange parameters (mH) of $CuSeO_3$ calculated using the BLYP and PBE functionals with between 0 and 80% and 0 and 60% HF exchange respectively.

Functional	J1	J2
BLYP	-0.93	-0.53
F0.2-BLYP	-0.49	-0.26
F0.4-BLYP	-0.17	-0.08
F0.6-BLYP	-0.07	-0.04
F0.8-BLYP	-0.04	-0.02
PBE	-0.89	-0.51
F0.2-PBE	-0.46	-0.24
F0.4-PBE	-0.16	-0.09
F0.6-PBE	-0.05	-0.04

Despite the spin polarisation being higher on O(2) than O(1) we find here that the strength of J_1 is approximately twice that of J_2. If we examine the Cu-O-Cu angles in Tables 8.4-6 we see that the Cu-O(1)-Cu is always smaller than Cu-O(2)-Cu, by

approximately 5.7°. According to the AGK rules of superexchange, decreasing the angle away from the threshold AFM/FM value favours more and more an FM superexchange. Our results are therefore in qualitative agreement with the AGK rules. Even if the spin polarisation appears higher for O(2) than O(1), FM type superexchange is stronger through the O(1) bridges in the $SeCuO_3$ structure. Therefore, despite the claims of ref. [3], where it is suggested that the Cu-O(2)-Cu angle is the reason behind the ferromagnetism of $SeCuO_3$, if the dependence of superexchange on the Cu-O-Cu angles can rationalise ferromagnetism in $SeCuO_3$ it would be mostly via a Cu-O(1)-Cu bridge. We find qualitative agreement with the previous computational study which reports a J analysis ie. that of Villesuzzane et al.[136], in that both spin exchange parameters favour a FM ground state. However, the authors find a similar magnitude to the strength of J_1 and J_2 but our calculations predict J_1 to be approximately twice as strong as J_2.

Let us now discuss the density of states; the example calculated using the $F_{0.4}$PBE hybrid functional is shown in Figure 8.11, including separate projections on the symmetry unique Cu, Se, O(1) and O(2) atoms of the $SeCuO_3$ unit cell.

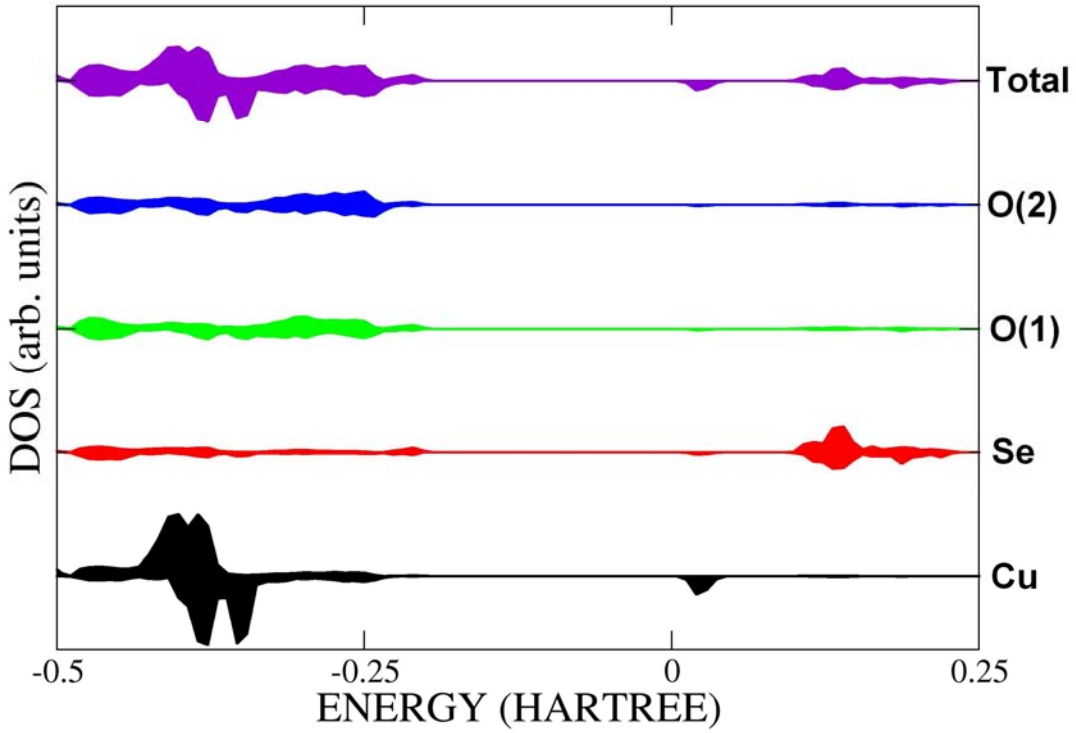

Figure 8.11 DOS for $SeCuO_3$, calculated using the $F_{0.4}$BLYP hybrid functional.

The band gap calculated with this functional is 6.06eV, and corresponds to an insulating ground state. The Cu(d) levels overlap with the O(2p) states in the middle of the valence band, while the first unoccupied level corresponds to the empty d atomic orbital of Cu^{2+}. These results yield a charge-transfer type insulator, similar to what was observed in CCTO when using 40% HF exchange. The empty Se states are approximately 1.2eV above the empty Cu-d level.

It has been suggested that $SeCuO_3$ exhibits multiferroic (magnetoelectric) behaviour. However a ferroelectric behaviour is not compatible with the centrosymmetric space group that $SeCuO_3$ has been found to adopt.

While the magnetic order in $CuSeO_3$ is clearly due to the localised spin on the Cu^{2+} d^9 ions, the origin of possible ferroelectric distortions are related to the electronic structure of the Se^{4+} ions. Se^{4+} is one of a number of ions that occupy the 12-coordinated sites known to favour ferroelectric-like distortions; others are Pb^{2+} and Bi^{3+}. The polarisable s valence shell generates an electric dipole in the structure when the Pb^{2+}, Bi^{3+} or Se^{4+} ions are displaced off-centre in the 12-coordinated site. $Pb^{2+}$and Bi^{3+} are more ionic than

Se^{4+}, and their off-centering is small and driven only by electrostatic forces. In the case of Se^{4+} examined here, instead, the formation of a molecular ion $[SeO_3]^{2-}$ involves covalent Se-O bonding and generates more pronounced distortions. It is possible that the valence 5s electrons on selenium play an important part in the polarisation of the structure. To characterise this feature we have calculated three-dimensional charge density plots around the $[SeO_3]^{2-}$ pyramidal units, which are shown in Figure 8.12. The polarisation of the s electrons away from the Se-O bonds is clearly visible and suggests that indeed Se^{4+} may give rise to ferroelectric like polarisations, although this is not present in the centrosymmetrical Pnma space group determined experimentally. In fact, the different (but symmetry equivalent) Se ions in each unit cell displace in opposite directions in a fashion more similar to an antiferroelectric, rather than ferroelectric distortion. It is not unreasonable however to imagine that a displacement of Se (induced by an external field) modifies both polarisation and magnetic coupling, and hence that $SeCuO_3$ is indeed magneto-electric, although a direct calculation of such effect requires a geometry optimisation in the presence of a field, which is at present not possible to perform.

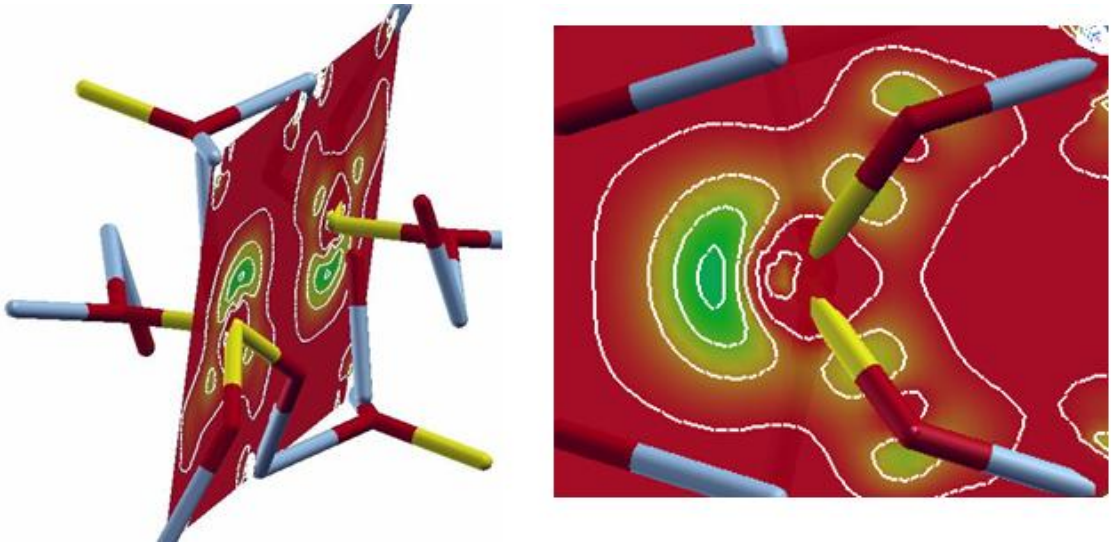

Figure 8.12 3D charge density maps highlighting the unshared electron pair of selenium in the $[SeO_3]^{2-}$ unit.

8.1.4 Conclusions on $SeCuO_3$

We have applied hybrid exchange density functional theory to the study of $SeCuO_3$. Our structural results find good agreement with experiment and the trend in structural parameters as a function of HF exchange shows a similar behaviour to that reported in Chapter 7 for CCTO. The largest structural difference between our theory and experiment lies in the relative bond distances within the Selenite ions. Also the Cu-O(2)-Cu angle is overestimated, by up to 3° with respect to experiment; this is significant as experimental work suggests that the FM ground state of $SeCuO_3$ can be explained by the Cu-O(2)-Cu angle, with an angle of less than 127.5° required to yield an FM rather than an AFM ground state. Despite our results achieving higher angles than the proposed 127.5° FM-AFM cut-off angle, we predict a FM ground state for $SeCuO_3$ and agree on the relative stability of the FM, A,C and G-type AFM states with the earlier theoretical work of Villesuzanne et al.[136]. A spin exchange analysis of $SeCuO_3$ shows that the strength of the superexchange interaction is twice as strong via the Cu-O(1)-Cu than the Cu-O(2)-Cu bridge, a result that can be explained via the AGK rules and the equilibrium values of the Cu-O-Cu angles.

In order to investigate the difference in the magnetic couplings between the isostructural FM $SeCuO_3$ and AFM $TeCuO_3$ we attempted to apply our hybrid exchange functionals to the study of $TeCuO_3$. Unfortunately this study was problematic due to the difficulty in defining a reliable basis set for Te. We were unable to achieve good enough convergence on the properties to comment on the small energy differences between the different magnetic phases of $TeCuO_3$.

8.2 $SeBO_3$ (B=Ni, Mn and Co)

As an extension to the study of $SeCuO_3$, in this section we consider the case where Se^{4+} occupies the A site and Ni^{2+}, Mn^{2+} and Co^{2+} individually occupy the octahedral B site to

form $SeNiO_3$, $SeMnO_3$ and $SeCoO_3$ respectively, all of which have been synthesized experimentally, but have received little attention, despite the interest generated by the observation of magnetoelectric effects in the isostructural $SeCuO_3$. Experimentally, this is probably due to the high pressure (6-8GPa) and temperature conditions required to synthesise these pervoskites. Computationally the problem lies in the strong on-site Coulomb and exchange interactions between neighbour transition metal ions due to the localised nature of the d electrons and the associated self-interaction error in DFT. Our hybrid exchange DFT calculations are aimed at filling this gap.

In the following sections we discuss the study of $SeNiO_3$, $SeMnO_3$ and $SeCoO_3$. Nickel, Manganese and Cobalt Selenites ($SeNiO_3$, $SeMnO_3$ and $SeCoO_3$) were originally synthesised over 30 years ago by Kohn et al. [133, 142]. These perovskites have more recently been studied experimentally by Munoz et al. [143, 144]. These studies implemented neutron diffraction data complemented by susceptibility and magnetisation measurements. The neutron diffraction patterns are described by the authors as "reasonably good" in spite of the relatively small amount of sample (0.5g). Kohn et al. and Munoz et al. believe the $SeNiO_3$, $SeMnO_3$ and $SeCoO_3$ structures to be isostructural to $SeCuO_3$ and thus belong to the orthorhombic Pnma space group. All three compounds are described by the authors as having AFM ground states (T_N=104K for $SeNiO_3$ and T_N=54K for $SeCoO_3$ [143]). Munoz et. al.[143] found the most stable AFM order to be the G-AFM phase for all three compounds. This was more recently confirmed by Cao et al.[145] for $SeNiO_3$ in a computational study via the LSDA+U method. There has yet to be a computational study of either $SeMnO_3$ or $SeCoO_3$. The G-type AFM ground state of $SeMnO_3$ was however confirmed experimentally by Escamilla et al.[139] who studied the continuous solid solution $Se(Cu_{1-x}Mn_x)O_3$.

Similarly to $SeCuO_3$ there is a large distortion and tilting of the $(Ni/Mn/Co)O_6$ octahedra. This tilting has been reported to be larger in $SeMnO_3$ than $SeNiO_3$ due to a higher tolerance factor (t, defined in chapter 6). The lattice parameters were also found to be larger in the Mn case due to the larger ionic radii of the high spin Mn^{2+} ion (0.83Å) compared to Ni^{2+} (0.69Å). Similarly to what we observed earlier for $SeCuO_3$ the Se^{4+} is responsible for pulling three oxygen atoms out of the SeO_{12} polyhedra to form short covalent bonds and yielding $[SeO_3]^{2-}$ trigonal pyramidal units in which the three short Se-O bonds involved (~1.7Å for each compound) are highly covalent in

character. Thus the SeO_3 units form discrete molecular ionic entities, hence from a chemical point of view the $SeMO_3$ perovskites examined here should be referred to as metal selenites. Similarly to the case of $SeCuO_3$ the $[SeO_3]^{2-}$ trigonal pyramidal units contain a highly polarisable lone $4s^2$ electron pair on Se. Let us now examine our results for each of the $SeMO_3$ compounds. In all of the calculations discussed in the following sections, we performed full geometry optimizations, starting from the most recent structure refinements obtained in the neutron diffraction studies of Munoz et al.[144]. The space group has been chosen as Pnma, but Γ-point phonon calculations were performed to check that the choice of space group was correct.

8.2.1 $SeNiO_3$

For this study we compare our calculated results summarised in Table 8.9 with the more recent structural parameters refined by Munoz et al. The first observation when comparing the structure of $SeNiO_3$ with $SeCuO_3$ discussed earlier is the absence of Jahn Teller-like distortions in the NiO_6 octahedra. This result is consistent with the high spin d^8 electronic configuration of Ni^{2+}, that is stable in an undistorted octahedral environment. The spread of Ni-O bond distances in $SeNiO_3$, in both calculated and experimental results, is less than 0.1Å, compared with over 0.5Å for the Cu-O bond lengths in $SeCuO_3$.

The Se^{4+} ions are involved in selenite molecular ions; we notice in fact three very short Se-O bonds of approximately 1.7Å, while the nine remaining Se-O distances are above 2.7Å. As in $SeCuO_3$, our calculations predict three similar Se-O bond lengths; for instance using the $F_{0.4}$PBE hybrid functional we obtain two Se-O(2) bonds of 1.723Å and one Se-O(1) bond of 1.714Å. These results compare very favourably with the high quality neutron diffraction data, that yield bond distances of 1.728Å and 1.716Å. They also reinforce our conclusion in section 8.1.4 that the disagreement between theory and experiment on the relative Se-O bond distances in $SeCuO_3$ should be attributed to the poor quality of the experimental diffraction pattern and subsequent structural refinement, and not to the theory results.

As in $SeCuO_3$, also in $SeNiO_3$ there are two non symmetry equivalent oxygen ions in the unit cell, labelled as O(1) and O(2), that are responsible for superexchange coupling with different Ni-O-Ni angles. In the experimental structure refinement the Ni-O-Ni angles are 123° and 131° around the oxygen atoms O(1) and O(2) respectively. This distorted structure is consistent with that of $SeCuO_3$ and can be rationalised by the abnormally small Se^{4+} cation (0.64Å) on the A site of the perovskite lattice, engaged in Selenite molecular ions $[SeO_3]^{2-}$ that cause a large off-centre displacement of Se in the 12-coordinated site of the perovskite lattice. The M-O-M angles are similar in $SeCuO_3$ and $SeNiO_3$; the large tilting of octahedra observed in these materials is therefore driven primarily by the chemistry of the Se^{4+} ions, and not by the eventual Jahn-Teller distortion of the MO_6 octahedra.

Let us now consider magnetism in $SeNiO_3$. As mentioned earlier, despite the similar structure, $SeNiO_3$ has a different ground magnetic state from $SeCuO_3$, the latter being FM while $SeNiO_3$ has a G-AFM order. In our work, we have studied the FM and the three AFM phases already introduced for $SeCuO_3$ (see Figure 8.3). Separate geometry optimisations have been performed for each magnetic order, but no relevant difference is found on the nuclear coordinates for different magnetic phases. We therefore present the results obtained from the FM phase only.

Table 8.9 Structural Paramaters for $SeNiO_3$ calculated using the LDA, BLYP and PBE functionals with between 0-60% HF exchange.

				NiO_6 octahedra			SeO_8 polyhedra						
Functional	a	b	c	Ni-O1 x2	Ni-O2 x2	Ni-O2 x2	Se-O1	Se-O1	Se-O2 x2	Se-O2 x2	Se-O2 x2	Ni-O1-Ni	Ni-O2-Ni
LDA	5.714	7.260	4.900	2.033	2.089	2.015	1.754	2.665	1.763	2.805	2.675	126.40	132.48
$F_{0.2}$-LDA	5.741	7.349	4.900	2.063	2.107	2.034	1.718	2.719	1.730	2.843	2.734	125.87	131.37
$F_{0.4}$-LDA	5.775	7.413	4.915	2.088	2.129	2.051	1.697	2.761	1.707	2.878	2.777	125.20	130.21
$F_{0.6}$-LDA	5.813	7.462	4.932	2.108	2.152	2.066	1.682	2.799	1.690	2.910	2.811	124.51	129.27
PBE	5.893	7.537	5.010	2.113	2.155	2.081	1.766	2.791	1.773	2.915	2.813	125.95	131.70
$F_{0.2}$-PBE	5.860	7.515	4.975	2.114	2.152	2.077	1.728	2.794	1.738	2.913	2.816	125.44	130.71
$F_{0.4}$-PBE	5.832	7.481	4.948	2.109	2.149	2.072	1.702	2.793	1.711	2.910	2.809	124.90	129.90
$F_{0.6}$-PBE	5.807	7.436	4.922	2.102	2.144	2.066	1.681	2.789	1.690	2.903	2.796	124.35	129.39
BLYP	5.968	7.684	5.077	2.153	2.196	2.102	1.780	2.846	1.786	2.968	2.885	126.25	131.45
$F_{0.2}$-BLYP	5.928	7.644	5.036	2.148	2.188	2.096	1.742	2.842	1.751	2.959	2.880	125.65	130.42
$F_{0.4}$-BLYP	5.896	7.597	5.005	2.141	2.183	2.090	1.714	2.837	1.723	2.951	2.868	125.00	129.65
$F_{0.6}$-BLYP	5.867	7.549	4.978	2.133	2.177	2.084	1.692	2.831	1.701	2.943	2.852	124.49	129.09
Experiment	5.879	7.525	4.937	2.116	2.158	2.069	1.716	2.793	1.728	2.920	2.838	125.55	130.52

Table 8.10 Electronic properties of $SeNiO_3$ calculated using the PBE functional with between 0-60% HF exchange.

Functional	$\Delta E_{FM-(A-AFM)}$	$\Delta E_{FM-(G-AFM)}$	$\Delta E_{FM-(C-AFM)}$	q_{Ni}	q_{Se}	$q_{O(1)}$	$q_{O(2)}$	$Spin_{Ni}$	$Spin_{Se}$	$Spin_{O(1)}$	$Spin_{O(2)}$
PBE	3.48	11.28	7.85	1.632	1.943	-1.203	-1.185	1.606	0.038	0.121	0.117
F0.2-PBE	0.90	3.64	2.53	1.730	2.065	-1.276	-1.259	1.756	0.020	0.075	0.075
F0.4-PBE	0.32	1.58	1.13	1.792	2.171	-1.331	-1.316	1.840	0.013	0.049	0.049
F0.6-PBE	0.12	0.84	0.63	1.830	2.268	-1.375	-1.362	1.886	0.009	0.035	0.035

Let us now discuss the energy difference between the FM and AFM phases, which is reported in Table 8.10 and shown in Figure 8.13. Calculations have only been performed with hybrid functionals built on the PBE formulation, as we have seen several times already that energy differences between magnetic phases are identical when using the BLYP and PBE functionals, and only depend on the fraction of HF exchange employed.

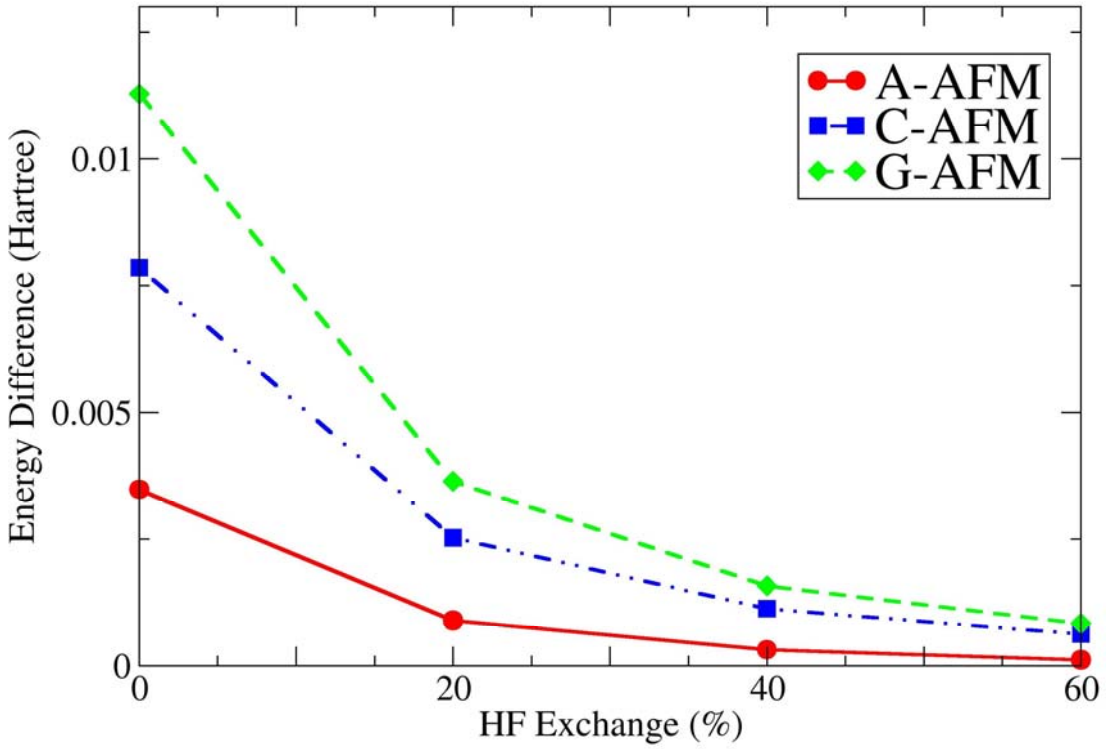

Figure 8.13 Difference in Energy between the FM and 010, 101 and 111 AFM phases calculated for $SeNiO_3$ using the PBE functional between 0-60% HF exchange.

Our results clearly predict an AFM order, with the ground state represented by the G-AFM phase. This in agreement with both the experimental work of Munoz et al.[143] and the theoretical data published by Cao et al[145]. We also predict the FM phase to be

the least stable magnetic phase among those studied and the A-AFM phase to be the least stable among the AFM magnetic orders.

By applying the same Ising spin Hamiltonian described for $SeCuO_3$ (see equations 8.8 and 8.9) we calculate effective coupling parameters J_1 and J_2 as reported in Table 8.11.

Table 8.11 J values calculated using the PBE functional. The values are in mH.

Functional	J1	J2
PBE	1.74	2.82
F0.2-PBE	0.45	0.91
F0.4-PBE	0.16	0.40
F0.6-PBE	0.06	0.21

These results show that J_2 is roughly twice as strong as J_1 and both exchange parameters favour an AFM ground state. This result is in contrast to $SeCuO_3$ where J_1 is calculated to be approximately twice the strength of J_2 and both exchange parameters favour an FM ground state. Again, the relative value of J_1 and J_2 in in qualitative agreement with the AGK rules, in that an increase of the M-O-M angle makes an AFM interaction stronger. It is however unclear why similar coordination geometries and M-O-M angles promote a FM superexchange in $SeCuO_3$ and an AFM superexchange in $SeNiO_3$. It is also of interest to note that the spin polarisation of O(1) and O(2) is similar in $SeNiO_3$, while it was higher on O(2) for $SeCuO_3$.

8.2.2 $SeMnO_3$

Let us now discuss the third isostructural $SeMO_3$ material, ie. the manganese selenite $SeMnO_3$ for which our calculated results are compared with the most recently derived experimental structural parameters [143] in Table 8.12. Interestingly Escamilla et al. found that the Cu-O-Cu angles involving the two non-equivalent oxygen atoms, O(1) and O(2), did not change throughout the $Se(Cu_{1-x}Mn_x)O_3$ series of solid solutions, which is consistent with our belief that the interesting magnetic properties of these materials do not depend on small changes of the M-O-M angles. $SeMnO_3$ has been

reported to have a G-type AFM ground state. The Neel temperature of 53.5K is about half that measured for $SeNiO_3$.

As with Nickel Selenite we studied not only the FM phase of $SeMnO_3$ but also the three AFM phases (A-AFM, C-AFM and G-AFM). We used the LDA, BLYP and PBE functionals with 0, 20, 40 and 60% HF exchange. However we limit to the $F_{0-0.6}$PBE functional range for our study of the electronic properties. All other computational details remain the same as for previous calculations.

Table 8.12 Structural results for $SeMnO_3$ calculated using the LDA, BLYP and PBE funcitonals with between 20-60% HF exchange.

				MnO_6 octahedra			SeO_8 polyhedra						
Functional	a	b	c	Mn-O1 x2	Mn-O2 x2	Mn-O2 x2	Se-O1	Se-O1	Se-O2 x2	Se-O2 x2	Se-O2 x2	Mn-O1-Mn	Mn-O2-Mn
LDA	5.904	7.566	5.130	2.153	2.211	2.108	1.742	2.793	1.758	2.949	2.828	121.31	129.25
$F_{0.2}$-LDA	5.961	7.657	5.128	2.191	2.232	2.139	1.709	2.843	1.723	3.000	2.887	121.76	128.14
$F_{0.4}$-LDA	6.001	7.722	5.133	2.160	2.250	2.160	1.690	2.882	1.701	3.031	2.930	121.20	127.09
$F_{0.6}$-LDA	6.041	7.773	5.142	2.235	2.270	2.175	1.676	2.922	1.686	3.060	2.965	120.81	126.32
PBE	6.097	7.897	5.219	2.242	2.284	2.169	1.756	2.932	1.769	3.061	2.996	123.12	128.50
$F_{0.2}$-PBE	6.088	7.856	5.183	2.244	2.276	2.179	1.720	2.929	1.732	3.068	2.988	122.10	127.57
$F_{0.4}$-PBE	6.064	7.800	5.157	2.238	2.269	2.180	1.694	2.921	1.705	3.063	2.970	121.20	126.89
$F_{0.6}$-PBE	6.035	7.742	5.136	2.229	2.262	2.176	1.675	2.912	1.685	3.055	2.947	120.56	126.43
BLYP	6.171	8.049	5.281	2.282	2.328	2.181	1.771	2.990	1.783	3.111	3.075	123.71	128.35
$F_{0.2}$-BLYP	6.155	7.991	5.237	2.278	2.313	2.194	1.734	2.980	1.746	3.109	3.056	122.54	127.39
$F_{0.4}$-BLYP	6.127	7.924	5.204	2.269	2.302	2.195	1.707	2.968	1.717	3.100	3.032	121.67	126.68
$F_{0.6}$-BLYP	6.095	7.857	5.177	2.257	2.291	2.192	1.686	2.955	1.695	3.089	3.005	121.03	126.20
Experiment	6.093	7.864	5.143	2.249	2.275	2.173	1.695	2.928	1.721	3.067	3.003	122.30	127.30

Table 8.13 Electronic properties of $SeMnO_3$ calculated using the PBE funcitonal with between 20-60% HF exchange.

Functional	$\Delta E_{FM\text{-}A\text{-}AFM}$	$\Delta E_{FM\text{-}G\text{-}AFM}$	$\Delta E_{FM\text{-}C\text{-}AFM}$	q_{Mn}	q_{Se}	$q_{O(1)}$	$q_{O(2)}$	$Spin_{Mn}$	$Spin_{Se}$	$Spin_{O(1)}$	$Spin_{O(2)}$
PBE	4.00	7.66	5.00	1.670	1.847	-1.180	-1.165	4.722	0.060	0.069	0.074
F0.2-PBE	1.11	3.06	1.94	1.720	1.970	-1.238	-1.225	4.813	0.037	0.048	0.051
F0.4-PBE	0.81	2.09	1.09	1.758	2.079	-1.287	-1.275	4.861	0.026	0.036	0.038
F0.6-PBE	0.39	1.25	0.75	1.787	2.178	-1.329	-1.318	4.890	0.019	0.029	0.031

From Table 8.12 it can be seen that we find good agreement with experiment with respect to all structural parameters. The lattice parameters of $SeMnO_3$ are larger than in $SeNiO_3$ due to an increase in ionic radii. We also find that with Mn on the B site the structure is more distorted than with Ni and the Cu-O-Cu angles lie somewhere between the case of B=Mn and B=Ni. For instance, using the $F_{0.4}$PBE functional the B-O(1)-B angle is 121°, 122° and 125° for B=Mn, Cu and Ni respectively. The B-O(2)-B angle is predicted to be 127°, 128° and 130° for the same order of ions on the B site. These angles are remarkably similar in the cases of B=Cu or Mn, yet $SeMnO_3$ is not reported to have the same ground state magnetic order as $SeCuO_3$. This adds further curiosity to the role of the Cu-O-Cu superexchange in the ferromagnetism of Copper Selenite.
In a comparative computational study of FM $SeCuO_3$ and AFM $TeCuO_3$ Iniquez et al.[137] found evidence that the exchange parameters J_1 and J_2 are largely independent of their respective Cu-O-Cu angles. They rationalised the difference in magnetic ground state by the distance between the O-Se/Te ions (Figure 8.2) which increases upon Te substitution (Cu-Se=1.75 Å, Cu-Te=1.90Å). They suggested that the substitution of these ions acted like a magnetic valve switching on and off the ferromagnetism. In the cases studied here, namely $SeMO_3$ where M=Cu, Ni and Mn, we can eliminate this effect as a rationalisation of the difference in magnetic properties in these materials. Our calculations predict the relevant O-Se distances as being almost identical in these cases (1.709Å, 1.711Å and 1.705Å respectively).

To discuss the electronic properties of $SeMnO_3$ we begin by examining the difference in energy calculated for the A-AFM, C-AFM and G-AFM phases. We present here the results obtained using the PBE functional with between 0-60% HF exchange.

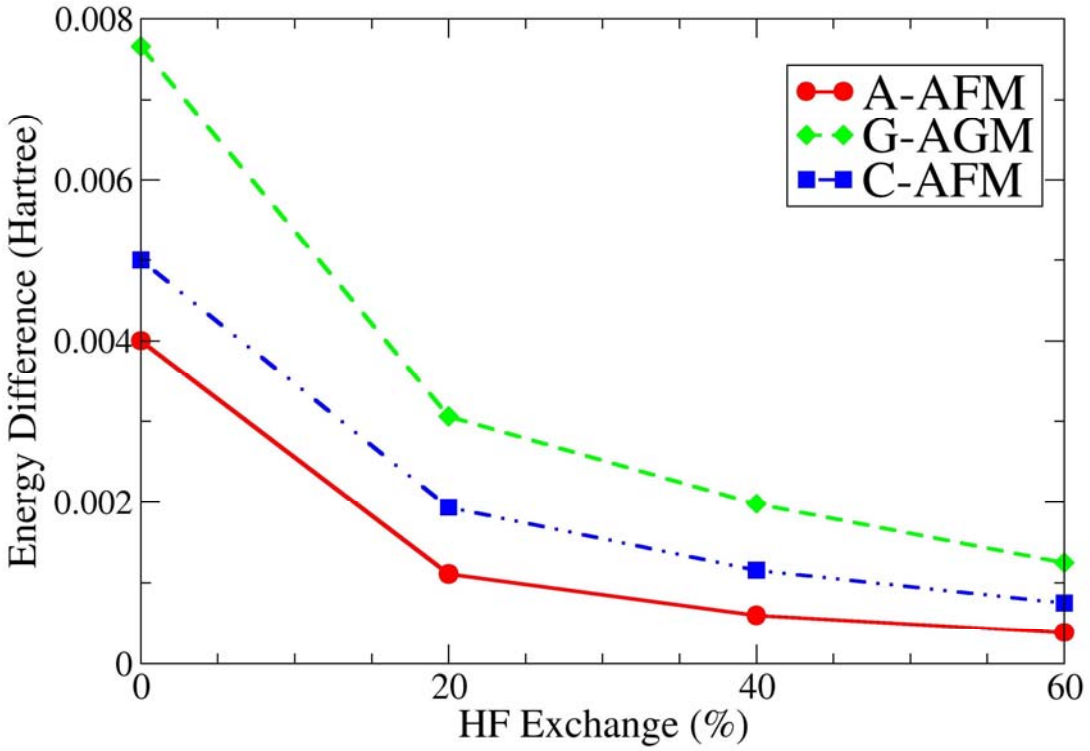

Figure 8.14 Difference in energy between the FM and AFM 010, 111 and 101 phases of $SeMnO_3$ calculated using the PBE hybrid functional with 0-60% HF exchange.

We find agreement here with all experimental and computational literature, with a G-AFM ground state for $SeMnO_3$. There is no published experimental work comparing the relative stability of the different AFM phases to make reference to. However, our results predict all the AFM phases to be more stable than the FM phase and the A-AFM to be the least stable phase. This is consistent with our finding for $SeNiO_3$.

The effective coupling constants, J_1 and J_2, as calculated for $SeCuO_3$ and $SeNiO_3$ are reported in Table 8.14.

Table 8.14 Efffective coupling constants calculated using the PBE functional. All values mH.

Functional	J1	J2
PBE	2.00	1.92
F0.2-PBE	0.56	0.49
F0.4-PBE	0.41	0.27
F0.6-PBE	0.20	0.19

These results show that both effective exchange parameters favour an AFM order, similarly to $SeNiO_3$; however the two exchange parameters have similar strength in this case. The values of J_1 and J_2 in $SeMnO_3$ and in particular of J_2 are smaller in $SeMnO_3$ than in $SeNiO_3$ (for instance, using the $F_{0.4}$PBE hybrid functional exchange, J_2 was 0.40 mHa in $SeNiO_3$ and 0.27 mHa in $SeMnO_3$), an effect which is roughly proportional to the ratio of Neel temperatures in $SeNiO_3$ and $SeMnO_3$ known from experiment. Superexchange is therefore stronger for Ni^{2+} than for Mn^{2+} ions.

8.2.3 $SeCoO_3$

.

Only one experimental study on $SeCoO_3$ is available, the lack of experimental studies of this compound is due to the high pressure and temperature conditions required to synthesise the structure. There is yet to be any computational study of this perovskite and thus we decided to examine its structural and electronic properties.

We used the PBE DFT functional with 40% HF exchange to perform a full geometry optimization of the crystallographic unit cell. We limit to this hybrid functional as it has performed well in our previous studies of perovskites.

Co^{2+} is a d^7 ion that can exist in low spin (t_{2g}^6 eg^1, with 1 unpaired electron) and high spin (t_{2g}^5 eg^2, with 3 unpaired electrons) electronic configuration, so we initially performed calculations on both to conclude on the most stable. The high spin configuration was found to be significantly more stable than the low spin one, by ~0.5eV per unit cell, and therefore we present the results only for calculations of $SeCoO_3$ with high spin Co^{2+}. As in previous sections, we performed calculations not

only on the FM but also on the A-AFM, C-AFM and G-AFM phases. The structural results are displayed in Table 8.15 along with the experimental values.

Table 8.15 Structural results for $SeCoO_3$ calculated using the $F_{0.2}$-PBE functional.

				CoO_6 octahedra			SeO_8 polyhedra						
Method	a	b	C	Co-O1 x2	Co-O2 x2	Co-O2 x2	Se-O1	Se-O1	Se-O2 x2	Se-O2 x2	Se-O2 x2	Co-O1-Co	Co-O2-Co
$F_{0.4}$-PBE	5.894	7.544	5.037	2.139	2.201	2.093	1.701	2.846	1.710	2.965	2.845	123.75	129.06
Experimental	5.930	7.596	5.029	2.151	2.214	2.083	1.715	2.861	1.715	2.981	2.878	123.96	129.55

Structurally we find excellent agreement with experiment and a Γ point phonon analysis confirmed that the orthorhombic Pnma space group is the correct choice. The M-O-M angles are, on average, only ~1° larger in $SeCoO_3$, compared to $SeCuO_3$, with M-O(1)-M predicted to be 122.2° and 123.8° and M-O(2)-M predicted as 128.4° and 129.1° for Cu and Co respectively.

The electronic properties are presented in Table 8.16.

Table 8.16 Electronic structure of $SeCoO_3$ calculated using the $F_{0.2}$-PBE functional.

Functional	$\Delta E_{FM-(A-AFM)}$	$\Delta E_{FM-(G-AFM)}$	$\Delta E_{FM-(C-AFM)}$	J_1	J_2	q_{Co}	q_{Se}	$q_{O(1)}$	$q_{O(2)}$	$Spin_{Co}$	$Spin_{Se}$	$Spin_{O(1)}$	$Spin_{O(2)}$
F0.4-PBE	0.32	1.27	1.26	0.15	0.32	1.777	2.140	-1.315	-1.301	2.833	0.008	0.0528	0.0528

In agreement with the experimental study by Munoz et al.[144] we find the G-AFM ground state to be the most stable. The effective exchange parameters, J_1 and J_2, are both AFM. We predict the A-AFM to be the least stable AFM phase with all AFM phases more stable than the FM phase.

8.2.4 Conclusion on the $SeBO_3$ Compounds (B=Ni, Mn and Co)

In conclusion we have studied the structural and electronic properties of the highly distorted perovskites $SeNiO_3$, $SeMnO_3$ and $SeCoO_3$. We performed our study using

hybrid functionals with the strongly correlated Ni/Mn/Co^{2+} ions providing a suitable test. For $SeNiO_3$, we found excellent agreement with experiment regarding the structure. The M-O-M angles are observed to vary very little from M=Cu to Ni (Cu-O(1/2)-Cu ~ 122° and 128°, Ni-O(1/2)-Ni ~ 124° and 129° respectively) thus we find it unlikely that the ferromagnetism of $SeCuO_3$ can be rationalised by the angular dependence of superexchange. We find agreement with previous experimental and theoretical studies on the correct ground state of $SeNiO_3$ (G-AFM). For $SeMnO_3$ we also found good structural agreement with experimental studies. There were no structural observations that could rationalise the difference in magnetic properties between $SeMnO_3$ and $SeCuO_3$. Electronically we found the ground state to be the G-AFM type, consistent with previous experimental studies.

8.3 $SeBS_3$ (B=Cu, Ni and Mn)

In the previous section we have discussed the structural, electronic and magnetic properties of $SeBO_3$ perovskites with different transition metal ions on the B site. There have been no studies to date on the effect of substituting other anions in place of O^{2-} in these pervoskites. This is due to the difficult task of synthesising these materials at high pressure. It is however, a field where ab-initio modelling can investigate predictively whether such materials would be of any practical interest.

We studied the substitution of O^{2-} with S^{2-} to form the series of perovskites $SeBS_3$ where B=Cu, Ni and Mn, and investigated the effect of the substitution on the structural, electronic and magnetic properties. Here we limited our study to using the $F_{0.4}$PBE functional, which has generally found the best correspondence to experiment during our studies. In each sulphide material we started from the structure of the equivalent oxide as no other data is available. We kept the same starting tolerances and computational parameters as for our previous studies.

We start our discussion here by presenting the structural results, which are summarised with comparison to their oxide equivalents.

Table 8.17 Structural results for the $SeBS_3$ (B=Cu, Mn, Ni) perovskites calculated using the $F_{0.4}$PBE functional.

				BZ_6 octahedra			SeZ_8 polyhedra						
Material	A	b	c	B-Z1 x2	B-Z2 x2	B-Z2 x2	Se-Z1	Se-Z1	Se-Z2 x2	Se-Z2 x2	Se-Z2 x2	B-Z1-B	B-Z2-B
$SeCuS_3$	7.253	8.823	6.308	2.478	2.877	2.317	2.250	3.423	2.190	3.839	3.337	125.74	135.19
$SeCuO_3$	5.830	7.367	5.253	2.104	2.424	1.927	1.709	2.855	1.707	3.125	2.804	122.18	128.41
$SeNiS_3$	7.199	9.009	5.861	2.522	2.532	2.443	2.222	3.255	2.205	3.516	3.355	126.54	137.79
$SeNiO_3$	5.832	7.481	4.948	2.109	2.149	2.072	1.702	2.793	1.711	2.910	2.809	124.90	129.90
$SeMnS_3$	7.526	9.347	6.101	2.661	2.667	2.586	2.210	3.411	2.202	3.730	3.528	122.37	134.81
$SeMnO_3$	6.064	7.800	5.157	2.238	2.269	2.180	1.694	2.921	1.705	3.063	2.970	121.20	126.89

Optimisations of the thioselenite compounds were performed in the Pnma space group, but as for the corresponding oxide compounds, we performed Γ-point phonon calculations to confirm that this was a proper minimum with respect to symmetry lowering distortions.

Due to the larger sized S^{2-} anion compared to O^{2-} we expect an increase in the structural parameters upon substitution of S for O. This is exactly what we observe, eg. we observe a ~24% increase for lattice parameter a, ~20% increase for b and ~18% increase for c for each perovskite. The perovskites exhibit different distortions with a smaller tilting of the BS_6 octahedra. For example for $SeCuO_3$ and $SeCuS_3$ the Cu-O-Cu angles open up by as much as 10°. The bond distances in the BS_6 octahedra are also all enlarged by approximately 20% compared to BO_6. The structures contain $[SeS_3]^{2-}$ trigonal pyramidal units and the effect of S replacing O in all of the compounds results in ~30% increase in the bond lengths involved in these units. Three Se-S bonds are still substantially shorter than the others, and their bond population is high, so that in the $SeBS_3$ perovskites we can identify a thioselenite ion SeS_3^{2-} analogous to the selenite SO_3^{2-} present in the oxides. The B-S(2)-B angle is increased by approximately 8° in each sulfide, however, the B-S(1)-B angle increases by a different amount in each case and we find ~3°, ~2° and ~1° increases for Cu, Ni and Mn respectively.

We should note here that according to ref. [3], where it is claimed that it is an increase in the Cu-O-Cu angle that switches the magnetic ground state from FM to AFM, we should find an AFM ground state for $SeCuS_3$. Upon substitution of O with S the Cu-S(2)-Cu angle increases significantly, to 135°, well above the cut off angle of 127.5° that is suggested for the FM/AFM crossover.

Let us now examine the electronic properties, starting with a comparison of the relative energy of FM and AFM phases. These results are shown in Table 8.18.

Table 8.18 Electronic properties of $SeCuS_3$, $SeNiS_3$ and $SeMnS_3$ calculated using the PBE functional with 40% HF exchange.

Material	ΔE_{FM-111}	ΔE_{FM-101}	ΔE_{FM-010}	q_B	q_{Se}	$q_{O(1)}$	$q_{O(2)}$	$Spin_B$	$Spin_{Se}$	$Spin_{O/S(1)}$	$Spin_{O/S(2)}$
$SeCuO_3$	-0.40	-0.34	-0.32	1.744	2.060	-1.337	-1.234	0.822	0.014	0.046	0.059
$SeCuS_3$	-1.23	-2.63	-0.97	1.523	0.749	-0.895	-0.688	0.546	0.008	0.167	0.139
$SeNiS_3$	7.48	6.31	1.10	1.696	0.756	-0.808	-0.822	1.718	0.006	0.107	0.085
$SeMnS_3$	7.18	5.82	5.18	1.596	1.696	-0.923	-0.893	4.801	0.024	0.057	0.059

The effective coupling constants J_1 and J_2 can also be calculated via equations 8.8 and 8.9. These are shown with comparison to $SeCuO_3$, in Table 8.19.

Table 8.19 Effective coupling constants calculated using the $F_{0.4}$PBE functional.

Functional	J1	J2
$SeCuO_3$	-0.16	-0.09
$SeCuS_3$	-0.49	-0.66
$SeNiS_3$	0.55	1.58
$SeMnS_3$	2.59	1.46
$SeNiO_3$	0.16	0.40
$SeMnO_3$	0.41	0.27

Interestingly the ground state of $SeCuS_3$ is FM. The substitution of S^{2-} for O^{2-} has increased the structural parameters by approximately 20% and significantly altered the Cu-Z(2)-Cu angle. Despite this change, the magnetic ground state is the same in $SeCuO_3$ and $SeCuS_3$. It therefore seems unlikely that any change in magnetic order upon cation or anion substitution in the perovskite structure can be attributed to a change in the Cu-O(2)-Cu angle as suggested in ref. [3]. It rather seems an intrinsic property of Cu-Cu superexchange mediated by a selenite or thioselenite ion.

Upon comparing results for $SeCuO_3$ and $SeCuS_3$ we notice that S is much more covalent; there is much more spin on S than O and therefore there is a much stronger superexchange. We observe an increase in the FM/AFM energy difference by at least a factor of three. This much larger energy difference for S leads to a much higher T_c and hence $SeCuS_3$ could be extremely promising for practical device applications.

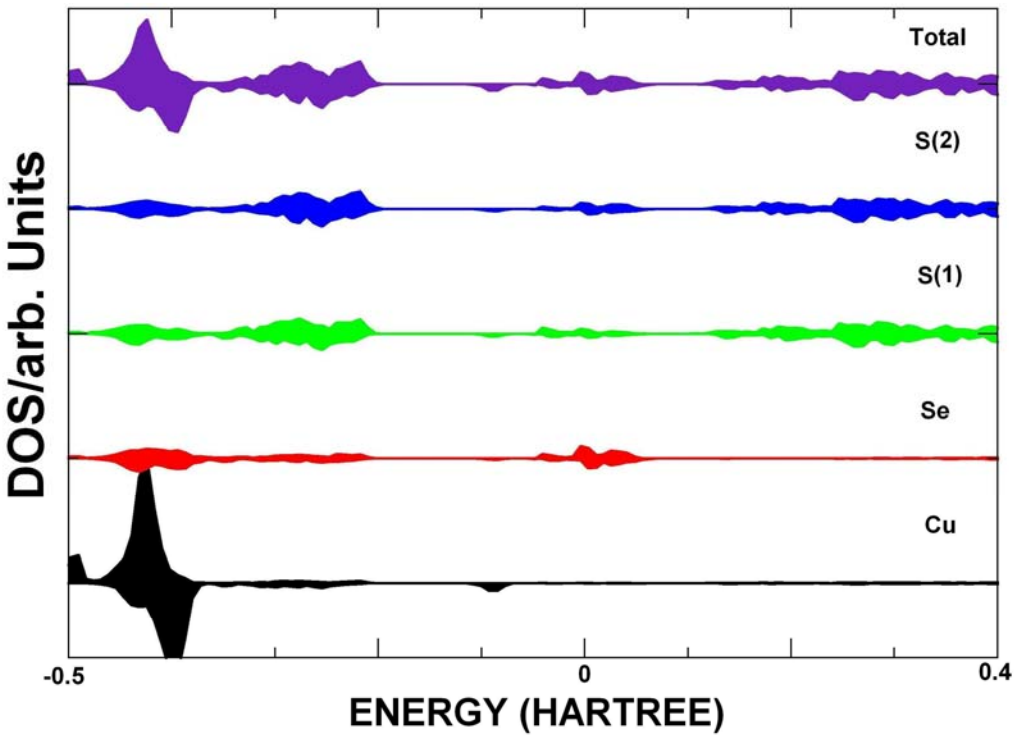

Figure 8.15 DOS for $SeCuS_3$ with projections on the Se, Cu, S(1) and S(2) atoms. The total is shown divided by ten.

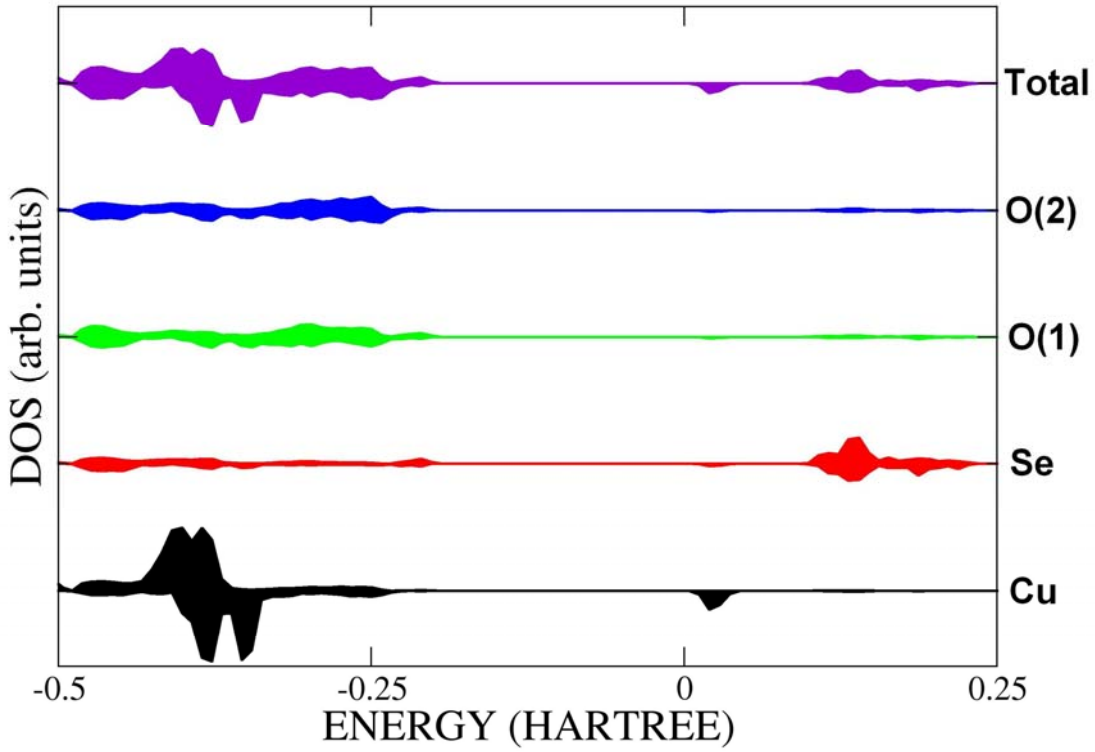

Figure 8.16 DOS for $SeCuO_3$ with projections on the Se, Cu, O(1) and O(2) atoms. The total is shown divided by ten.

Let us now examine the DOS for SeCuS3, calculated using the BLYP functional with 40% HF exchange, shown in Figure 8.15 DOS for SeCuS3 with projections on the Se, Cu, S(1) and S(2) atoms. The total is shown divided by ten.

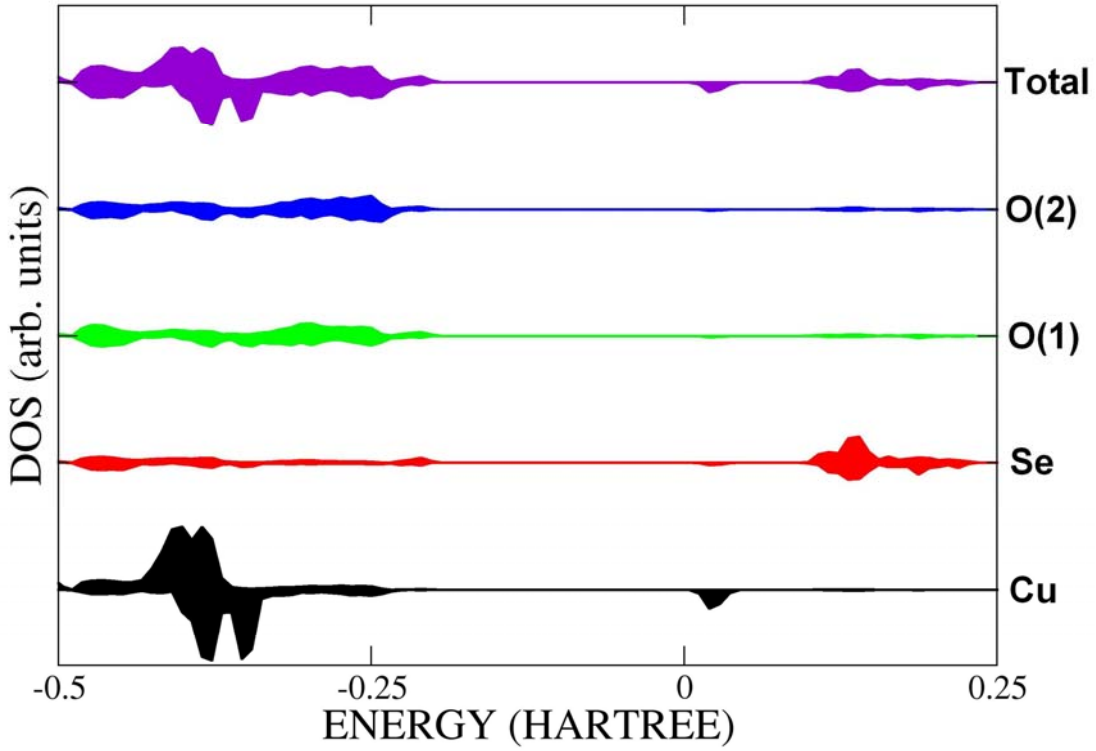

Figure 8.16 DOS for SeCuO3 with projections on the Se, Cu, O(1) and O(2) atoms. The total is shown divided by ten.

which can be compared with that of $SeCuO_3$ in Figure 8.11 (and repeated in Figure 8.16 for easier comparison). We notice a much smaller gap for $SeCuS_3$ than was observed for $SeCuO_3$, however $SeCuS_3$ is still insulating. The occupied Cu^{2+} band is below the anion levels, while the bottom of the conduction band is formed by the empty Cu^{2+}-d level but less separated from the empty S levels than from O in $SeCuO_3$.

In conclusion, we studied the effect of replacing O with S on the structural and electronic properties of the $SeBS_3$ perovskite family (B=Cu Mn and Ni). The effect of this substitution on the structure was to increase bond distances and lattice parameters by approximately 20%. This also led to a decrease in the octahedral distortion with angles opening up by as much as 10°. Electronically we obtain some interesting results with each material predicted to have the same magnetic ground state as its oxide

equivalent but magnetic coupling increased threefold. The retention of the same magnetic ground state in Oxides and Sulfides is particularly interesting for the case of $SeCuS_3$ where the Cu-S(1)-Cu and Cu-S(2)-Cu angles open up by 4° and 7° respectively. In the experimental works of Subramanian et al.[3] a change in Cu-O-Cu angle of approximately 1° (from the continuous solid solution of FM $SeCuO_3$ and AFM $TeCuO_3$) is discussed as being important in explaining the different magnetic ground states. Here, for $SeCuO_3$ and $SeCuS_3$ we predict a FM ground state for both materials despite the relatively large change in Cu-O-Cu angle.

One of the most interesting observations was the large increase (by a factor of at least 3) in the energy difference between FM and AFM phases from $SeCuO_3$ to $SeCuS_3$. This larger energy difference will result in a much higher T_c which gives this perovskite large potential for use in technological devices.

8.4 Conclusions on Chapter 8

In this chapter we described calculations performed on the isostructural compounds ABZ_3 (where A=Se, B=Cu, Ni, Mn, Co and Z=O, S). We initially discussed calculations on copper selenite $SeCuO_3$ where we found the magnetic ground state to be FM, in agreement with experiment. Following an analysis of $SeNiO_3$, $SeMnO_3$ and $SeCoO_3$ we find the AFM phase to be the most stable for all three perovskites. The difference in the magnetic ground state between these perovskites and $SeCuO_3$ has been attributed in the literature to the superexchange dependence on the Cu-O(1)-Cu and/or Cu-O(2)-Cu angles. Our studies have shown that this explanation is not satisfactory to rationalise such large differences in magnetic behaviour. It has also been reported in ref.[2] that it is the Cu-O(2)-Cu and not the Cu-O(1)-Cu angle which is responsible for the difference in magnetic order. An analysis of the two relevant coupling constants contradicts this claim and we find that superexchange is stronger via the Cu-O(1)-Cu bridge by a factor of two.

We performed studies into the aforementioned perovskites with O replaced by S. This resulted in considerably expanded geometries with respect to their oxide equivalents (by

approximately 20%). We found $SeCuS_3$ to be FM, however the Cu-S(2)-Cu and the Cu-S(1)-Cu angles opened up by more than 5° which provided further suggestion that the FM ground state cannot be rationalised simply by the superexchange dependence on these angles.

Chapter 9 - Conclusion

This PhD thesis has been concerned with the computational study of copper containing perovskites using modern electronic structure methods, and in particular we have performed an extensive test of hybrid exchange functionals within DFT. Applications cover two main classes of materials, discussed separately in chapters 7 and 8: both are perovskite-structured and have general composition $AA_3'B_4Z_{12}$ and $ASeZ_3$.

Let us first summarise the major results obtained from the study of the $AA_3'B_4Z_{12}$ perovskites; the reference compound for this family is $CaCu_3Ti_4O_{12}$ (CCTO), of technological interest for its very large dielectric constant. We initially studied bulk CCTO, whose structure is well characterised by experiment, with a range of different hybrid functionals. The aim here was to provide a reliable test for the performance of the hybrid functionals and determine the functional in best agreement with experiment to apply to the study of more complex structures, such as surfaces and interfaces. The mechanism enabling the high dielectric constant of CCTO is still not entirely understood, but it is believed to be linked to surface and interface effects via a barrier-layer capacitor model. In terms of the bulk material, we found excellent agreement with experiment. The hybrid functionals built on the GGA (PBE and BLYP) DFT functionals, in the range of 20-60% HF exchange found best agreement with experiment; hence we employed these functionals to study CCTO surfaces. At the 001 surface of CCTO we observed interesting redox chemistry, whose details however depend crucially on the amount of HF exchange used: a disproportionation of Cu^{2+} into Cu^{1+} and Cu^{3+} is observed when using 20% HF exchange, while 60% HF leads to charge transfer from surface Cu to surface O ions. Both surface redox reactions yield surface states able to effectively trap mobile charge carriers and hence kill the n-type conductivity of bulk CCTO. This finding is in agreement with the barrier layer model used to rationalise the dielectric properties of CCTO. We then extended our study to the isostructural CdCTO and CCGO to see if the same surface disproportionation was observed in cases where the large dielectric constant is not observed experimentally. The same disproportionation was found in all the isostructural materials, which suggests

that it is an intrinsic property of materials exposing under coordinated Cu ions in different surface environments. However we did find that the disproportionation energy is much more favourable in CCTO than CdCTO or CCGO. We considered different magnetically ordered phases in bulk CCTO, and applied Ising models to derive the magnetic coupling constants of the material. The single J model on which our initial energy analysis was based, is not correct; extension to multiple J models and especially three-body coupling parameters are required to describe magnetism in CCTO.

We extended our study to new isostructural compositions which have not yet been synthesised. These are $SrCu_3Ti_4O_{12}$, $SrCu_3Zr_4O_{12}$ and $CaCu_3Zr_4O_{12}$. These materials were found to be stable in the Im3 space goup. The unit cell parameters are found to vary considerably in these new compounds, especially upon introduction of Zr in the octahedral site. We find CCZO and SCZO to be approximately 7% larger than CCTO and SCTO. SCTO is only slightly larger (approx. 0.5%) than CCTO. We found that the substitution of Sr^{2+} and Zr^{4+} into the A and B sites of the perovskite lattice does not affect the magnetic ground state and SCTO, SCZO and CCZO were all predicted to be AFM. Replacement of Ti by Zr reduces the magnetic coupling constants by a factor of 1/2, while replacement of Ca with Sr has no effect on the magnetic coupling. Overall the electronic properties of these new compositions are expected to be similar, but inferior to those of CCTO.

We also looked at the effect of substituting O^{2-} with S^{2-} on the Z site of the perovskite, to form $CaCu_3Ti_4S_{12}$ (CCTS). The result here was that CCTS has a large increase in lattice parameters compared with CCTO, but more interestingly it exhibits a 7-fold increase in the magnetic coupling. This gives it potential use for practical applications.

We extended our study of perovskites by examining various structures of the form ABZ_3 where the charge on the A site cation is larger than the B site cation with a 4-2 valence combination. We started by examining the structural and electronic properties of $SeCuO_3$. Structurally we found a large disagreement with experiment in terms of the relative bond distances within the selenite ions. Experiment predicts two long and one short bond distance where as our calculations find that three similar length bond distances are more stable. Our calculations also predict the Cu-O(2)-Cu angle to be 3° larger than reported by experimental studies. This is a significant difference as the experimental study rationalises the FM ground state of $SeCuO_3$ by the value of the Cu-

O-Cu angles, according to the Goodenough-Kanemori rules. In the experimental study the authors identify a cut-off angle between FM and AFM ground magnetic states as 127.5°. We find instead a FM ground state to be stable for $SeCuO_3$ using a wide range of hybrid functionals with different equilibrium values of the Cu-O-Cu angles, contradicting the rationalisation proposed by Subramanian et al.

We also studied of $SeMnO_3$, $SeNiO_3$ and $SeCoO_3$. For these materials we found excellent agreement to experiment with respect to the materials structure. We found that these compounds all have a FM ground state in agreement with the literature. We found very little difference in the Cu-O-Cu angles between the $SeBO_3$ (B=Cu, Mn, Ni and Co). Thus we concluded that it is unlikely that such a small change in angle can be responsible for the large difference in the magnetic structure of these compounds.

Our research was then directed towards the structural and electronic properties of $SeCuS_3$, $SeMnS_3$ and $SeCoS_3$. A study of these materials has never been performed before and therefore we deemed it of interest to examine their potential properties. The results of these calculations are very promising; the materials were found to be stable within the Pnma space group. Structurally we observe a large increase of the lattice parameters of approximately 20% compared to the respective oxides. Interestingly we find the same FM ground state for $SeCuS_3$ and $SeCuO_3$ despite the S substitution significantly increasing the Cu-S(1/2)-Cu angles. This confirms that the Cu-S-Cu angles cannot rationalise the difference in magnetic structures. One of the most interesting results from this study is in the threefold increase of the FM/AFM energy. This energy difference results in a much larger T_c which gives the $SeCuS_3$ perovskite a considerable potential as a FM material.

Some very useful general learning outcomes were achieved during this PhD. One of the most encouraging results was the general success of the hybrid functionals which provided both quantitatively and qualitatively good results throughout the materials investigated.

From a methodological perspective, we have clearly shown that in the computational study of bulk compounds, the equilibrium structure depends on both amount of HF exchange employed and choice of 'local' exchange and correlation (xc) functional in DFT. Instead, when the electronic properties of bulk systems are concerned, the main features depend *only* on the amount of HF exchange used, and not on the particular choice of DFT xc functional. Hybrids built on PBE, BLYP and LDA choices yield nearly identical results for the electronic properties of each bulk materials studied. Defects and surfaces pose more stringent tests to the accuracy of hybrid-exchange calculations: even small variations in the amount of HF exchange may cause a different ground electronic state (as observed for the CCTO surfaces). This result is somewhat indicative of the rich surface and defect chemistry of transition metal oxides, where several electronic states of comparable energy are often present; even a small variation in the definition of forces may reverse their relative stability and converge the solution to a different state.

The accuracy of results with respect to experiment were very promising and hence we moved to the study of materials which have not yet been experimentally synthesised, 'predictively'. An example of these are the Sulfides. These materials proved to be extremely promising for their magnetic and dielectric properties. The results from these materials have provided some useful data and set some clear targets for experimental studies.

Despite the wealth of useful results produced during this PhD, there are of course areas of study which we could have approached, given more time. An example of this lies in our study of CCTO. Our study of the 001 surface unveiled some interesting redox chemistry. However, this study could be extended to investigate other surfaces and grain boundaries. Future studies could be useful in shedding further light on the interesting dielectric properties displayed by CCTO. Future work also appears of interest for perovskite-structured sulfides, where our initial calculations revealed the potential for new and improved dielectric and magnetic properties.

Chapter 10 - Bibliography

[1] H. Jahn and E. Teller, **161**, 220 (1937).
[2] J. Kanemori, J. Phys. Chem. Solids **10**, 87 (1959).
[3] M. A. Subramanian, A. P. Ramirez, and W. J. Marshall, Physical Review Letters **82**, 1558 (1999).
[4] S. A. Zumdahl and S. S. Zumdahl, *Chemistry* (Brookes Cole, 2006).
[5] C. Hammond, *Introduction to Crystallography* (Oxford University Press, 1992).
[6] R. Tilley, *Crystals and Crystal Structures* (John Wiley & Sons, Ltd., 2006).
[7] P. J. Brown and J. B. Forsyth, *The Crystal Structure of Solids* (Edward Arnold, 1973).
[8] H. J. Monkhorst and J. D. Pack, Phys. Rev. B **13**, 5188 (1976).
[9] G. S. Rohrer, *Structure and Bonding in Crystalline Materials* (Campridge University Press, 2001).
[10] P. Weiss, J. Phys. **6**, 661 (1907).
[11] E. C. Stoner, Philos. Mag. **15**, 1080 (1933).
[12] N. A. Hill, J. Phys. Chem. **104**, 6694 (2000).
[13] E. Schrodinger, Annalen der Physik **384**, 489 (1926).
[14] P. Atkins and R. Friedman, *Molecular Quantum Mechanics* (Oxford University Press, 2005).
[15] W. Pauli, Z. Phys. **31**, 373 (1925).
[16] J. C. Slater, Phys. Rev. **35**, 210 (1930).
[17] D. Hartree, Proc. Cambridge Phil. Soc. **24**, 111 (1927).
[18] V. Fock, Z Phys **61**, 126 (1930).
[19] D. Hartree, Proc. Cambridge Phil. Soc. **24**, 426 (1928).
[20] D. Hartree, Proc. Cambridge Phil. Soc. **25**, 310 (1929).
[21] L. H. Thomas, Proc. Cambridge Phil. Soc. **23**, 542 (1927).
[22] E. Fermi, Z. Phys. **48**, 73 (1928).
[23] P. A. M. Dirac, Proc Cambridge Phil Soc **26**, 376 (1930).
[24] Slater, Phys. Rev. **81**, 385 (1951).
[25] E. P. Wigner, Trans. Faraday Soc. **34**, 678 (1938).
[26] P. Hohenberg and W. Kohn, Phys. Rev. B **136**, 864 (1964).
[27] R. M. Martin, *Electronic Structure* (Cambridge University Press, 2004).
[28] J. P. Perdew, Phys. Rev. Lett. **55**, 1665 (1985).
[29] A. D. J. Becke, Phys. Rev. A, 3098 (1988).
[30] C. Lee, W. Yang, and P. R. G., Phys. Rev. B **37**, 785 (1988).
[31] J. P. Perdew, K. Burke, and M. Ernzerhof, Phys. Rev. Lett. **77**, 3865 (1996).
[32] J. C. Cramer, *Essentials of Computational Chemistry* (John Wiley & Sons Ltd, 2002).
[33] J. P. Perdew and A. Zunger, Phys. Rev. B **23**, 5048 (1981).
[34] R. O. Jones and O. Gunnarsson, Rev. Mod. Phys. **61**, 689 (1989).
[35] J. B. Krieger, Y. Li, and G. J. Iafrate, Phys. Rev. A **45**, 101 (1992).
[36] V. I. Anisimov, J. Zaanen, and O. K. Anderson, Phys. Rev. B **44**, 943 (1991).
[37] A. D. J. Becke, J. Phys. Chem. **98**, 1372 (1993).
[38] A. D. J. Becke, J. Chem. Phys. **98**, 5648 (1993).

[39] F. Cora, M. Alfredsson, G. Mallia, et al., Structure and Bonding **113**, 171 (2004).
[40] W. Koch and M. C. Holthausen, *A Chemists Guide to Density Functional Theory* (Wiley, 2001).
[41] M. D. Segall, P. L. D. Lindan, M. J. Probert, et al., J. Phys.: Cond. Matt. **14**, 2712 (2002).
[42] S. F. Boys, Proc. Roy. Soc. London **200**, 542 (1950).
[43] J. Kohanoff, *Electronic Structure Calculations for Solids and Molecules* (Cambridge University Press, 2006).
[44] P. Blaha, K. Schwarz, G. Madsen, et al., 2001).
[45] G. Kresse and J. Hafner, Phys Rev. B **B49**, 14251 (1994).
[46] G. Kresse and J. Hafner, Phys Rev. B **B47**, 558 (1993).
[47] G. Kresse and J. Furthmuller, Comput. Mater. Sci. **6**, 16 (1996).
[48] M. F. Guest, J. H. van Lenthe, J. Kendrick, et al., 1980).
[49] R. Dovesi, V. R. Saunders, C. Roetti, et al., Universita di Torino, 2006).
[50] C. G. Broyden, Math. Comput. **19**, 577 (1965).
[51] C. G. Broyden, J. Inst. Math. Appl. **6**, 76 (1970).
[52] M. L. Boas, *Mathematical Methods in the Physical Sciences* (John Wiley & Sons.
[53] G. P. Srivastava, J. Phys. A **17**, L317 (1984).
[54] D. Vanderbilt and S. G. Louie, Phys. Rev. B **30**, 6118 (1984).
[55] D. D. Johnson, Phys. Rev. B **38**, 12807 (1988).
[56] R. S. Mulliken, J. Chem. Phys. **23**, 1833 (1955).
[57] B. Wul and I. M. Goldman, C. R. Acad. Sci. **46**, 139 (1945).
[58] P. K. Davies, H. Wu, A. Y. Borisevich, et al., Annu. Rev. Mater. Res. **38**, 369 (2008).
[59] M. A. Pena and J. L. G. Fierro, Chem. Rev. **101**, 1981 (2001).
[60] A. S. Bhalla, G. Ruyan, and R. Rustum, Materials Research Innovations **4**, 3 (2000).
[61] R. E. Schaak and T. E. Mallouk, Chem. Mater. **14**, 1455 (2002).
[62] A. N. Vasil'ev and O. S. Volkova, Low Temperature Physics **33**, 896 (2007).
[63] M. Kunz and I. D. Brown, J. Solid State Chem. **115**, 395 (1995).
[64] U. Opik and M. H. L. Pryce, Proc. Roy. Soc. London **A238**, 425 (1957).
[65] R. F. W. Bader, Mol. Phys. **3**, 137 (1960).
[66] R. F. W. Bader, Can. J. Chem. **40**, 1164 (1962).
[67] R. G. J. Pearson, J. Am. Chem. Soc. **91**, 4947 (1969).
[68] R. G. J. Pearson, J. Mol. Structure **103**, 25 (1983).
[69] R. A. Wheeler, M.-H. Whangbo, T. Hughbanks, et al., J. Am. Chem. Soc. **108**, 2222 (1986).
[70] G. W. Watson and S. C. Parker, J. Phys. Chem. B **103**, 1258 (1999).
[71] G. W. Watson, S. C. Parker, and G. Kresse, **59**, 8481 (1999).
[72] I. Lefebvre, M. Lannoo, G. Allan, et al., Phys. Rev. Lett. **59**, 2471 (1987).
[73] I. Lefebvre, M. A. Szymanski, J. Olivier-Fourcade, et al., Phys. Rev. B **58**, 1896 (1998).
[74] R. Seshadri and N. A. Hill, Chem. Mater. **13**, 2892 (2001).
[75] U. V. Waghmare, N. A. Spaldin, H. C. Kandpal, et al., Phys. Rev. B **67**, 12511 (2003).

[76] G. Hollinger, F. J. Himpsel, B. Reihl, et al., Solid State Communications **44**, 1221 (1982).
[77] Y. Tokura, Physica B **1**, 237 (1997).
[78] P. D. Battle, T. C. Gibb, and P. Lightfood, J. Solid State Chem. **84**, 271 (1990).
[79] H. B. Krausse and D. L. Gibbon, Z. Kristallogr. **134**, 44 (1971).
[80] T. Nagakawa, J. Phys. Soc. Japan **24**, 806 (1968).
[81] G. Shirane, S. Hosino, and K. Suzuki, ibid. **80**, 1105 (1950).
[82] S. Pilgrim, A. Sutherland, and S. Winzer, J. Am. Ceram. Soc. **70**, 3122 (1990).
[83] B. Deschanvres, B. Raveua, and F. Tollemer, Bull. Soc. Chim. Fr., 4077 (1967).
[84] M. A. Subramanian, D. Li, B. Duan, A., et al., Solid State Chem. **151**, 323 (2000).
[85] A. P. Ramirez, M. A. Subramanian, M. Gardel, et al., Solid State Commun. **115**, 217 (2000).
[86] C. C. Homes, T. Vogt, S. M. Shapiro, et al., Science **293**, 673 (2001).
[87] S. Garcia-Martin, A. Morata-Orrantia, M. H. Aguirre, et al., Applied Physics Letters **86**, 043110 (2005).
[88] J. G. Bednorz and K. A. Muller, Phys. Rev. Lett. **52**, 2289 (1984).
[89] B. T. Matthias, Phys. Rev. **75**, 1771 (1949).
[90] F. Cora and C. R. A. Catlow, Faraday Discuss. **114**, 421 (1999).
[91] E. Ascher, H. Rieder, H. Schmid, et al., J. Appl. Phys. **37**, 1404 (1966).
[92] G. Lawes, A. P. Ramirez, C. M. Varma, et al., Phys. Rev. Lett. **91**, 257208 (2003).
[93] J. G. Bednorz and K. A. Muller, Physik B Condensed Matter **64**, 189 (1986).
[94] M. Houssa, *High-k Gate Dielectrics* (CRC Press, 2004).
[95] M. Depas, B. Vermeire, P. W. Mertens, et al., Solid-State Electron **38**, 1465 (1995).
[96] S. H. Lo, D. A. Buchanan, Y. Taur, et al., Electron Dev. Lett. **18**, 209 (1997).
[97] A. T. Fromhold, *Quantum Mechanics for Applied Physics and Engineering*, 1981).
[98] J. Liu, C. Duan, W. N. Mei, et al., Journal of Applied Physics **98** (2006).
[99] R. Wernicke, American Ceramic Society **1**, 261 (1981).
[100] S. Waku, Electr. Commun. Lab. **15** (1967).
[101] C.-F. Yang, Jpn. J. Appl. Phys. **35**, 1806 (1995).
[102] B. Bochu, M. N. Deschizeaux, J. C. Jouburt, et al., Journal of Solid State Chemistry **29**, 291 (1979).
[103] C. Pisani, R. Dovesi, and C. Roetti, **48** (1988).
[104] C. Pisani, **67** (1996).
[105] http://www.crystal.unito.it.
[106] F. Birch, Phys. Rev. **71**, 809 (1947).
[107] P. W. Anderson, Phys. Rev. **115**, 2 (1959).
[108] A. Collomb, D. Samaras, B. Bochu, et al., Phys. Stat. Solidi. **41**, 459 (1977).
[109] A. Koitsch, Phys. Rev. B **65**, 052406 (2002).
[110] Y. J. Kim, Solid State Commun. **121**, 625 (2002).
[111] N. Ashcroft and N. Mermin, *Solid State Physics* (WB Saunders and Co., Philadelphia, 1976).
[112] M. Mizumaki, T. Saito, H. Shiraki, et al., Inorg. Chem. **48**, 3499 (2009).
[113] D. C. Sinclair, T. B. Adams, F. D. Morrison, et al., Applied Physics Letters **80**, 2153 (2002).

[114] W. Kobayashi and I. Terasaki, Physica B **329-333** (2003).
[115] J. Li, M. A. Subramanian, H. D. Rosenfeld, et al., Chem. Mater. **16**, 5223 (2004).
[116] L. Ni and X. M. Chen, Solid State Communications **149**, 379 (2009).
[117] H.-S. Hong, D.-Y. Kim, H.-M. Park, et al., J. Am. Ceram. Soc. **90**, 2118 (2007).
[118] C. C. Homes, T. Vogt, S. M. Shapiro, et al., Phys. Rev. B **67**, 092106 (2003).
[119] L. X. He, J. B. Neaton, D. Vanderbilt, et al., Phys. Rev. B **67**, 012103 (2003).
[120] Y. Ma and R. Aksoy, Solid State Communications **142**, 376 (2007).
[121] L. He, J. B. Neaton, M. H. Cohen, et al., Phys. Rev. B **65**, 214112 (2002).
[122] M. Yanzhang and A. Resul, Solid State Communications **142**, 376 (2007).
[123] M. Matos and L. Walmsley, J. Phys. Condens. Matter **18**, 1793 (2006).
[124] Y. Ozaki, M. Ghedira, J. Chenavas, et al., Acta. Cryst. **B33**, 3615 (1977).
[125] A. Shiraki, T. Saito, T. Yamada, et al., Phys. Rev. B **76**, 140403 (2007).
[126] R. Eliseo, M. Llunell, and P. Alemany, Journal of Solid State Chemistry **176**, 400 (2003).
[127] J. B. Goodenough, Phys. Rev. **100**, 564 (1995).
[128] Y. Shimakawa, H. Shiraki, and T. Saito, Journal of the Physical Society of Japan **77**, 113702 (2008).
[129] S. Sugai, Phys. Rev. **B42**, 1405 (1990).
[130] J. D. Perkins, Phys. Rev. Lett. **71**, 1621 (1993).
[131] J. Lorenzana, J. Eroles, and S. Sorella, Phys. Rev. Lett. **83**, 5122 (1999).
[132] T. Bredow, H. P., and W. M., Phys Rev. B **70** (2004).
[133] K. Kohn, S. Akimoto, K. Inoue, et al., J. Phys. Soc. Japan **38**, 587 (1975).
[134] H. A. Kramers, Physica **1**, 182 (1934).
[135] P. W. Anderson, Phys. Rev. **79**, 705 (1950).
[136] A. Villesuzanne, M.-H. Whangbo, M. A. Subramanian, et al., Chem. Mater. **17**, 4350 (2005).
[137] J. Iniquez and T. Yildirim, Phys. Rev. B **71**, 180415 (2005).
[138] U. Yu, J. H. Shim, B. H. Kim, et al., Journal of Magnetism and Magnetic Materials **310**, 1660 (2007).
[139] R. Escamilla, A. Duran, M. I. Rosales, et al., J. Phys. Condens. Matter **15**, 1951 (2003).
[140] M. D. Towler, A. Zupan, and M. Causa, Computer Physics Communications **98**, 181 (1996).
[141] R. Ahlrichs and K. May, Phys. Chem **2**, 943 (2000).
[142] K. Kohn, K. Inoue, O. Horie, et al., Journal of Solid State Chemistry **18**, 27 (1976).
[143] A. Munoz, J. A. Alonso, M. J. Martinez-Lope, et al., Dalton Trans., 4936 (2006).
[144] A. Munoz, J. A. Alonso, M. J. Martinez-Lope, et al., Physical Review B **73**, 104442 (2006).
[145] Y. L. Cao, M. Q. Cai, and Y. G. W., Applied Physics Letters **92**, 132914 (2008).